Doctoral Theses at NTNU 2005:46

Kjersti Omdahl Christensen

Steam Reforming of Methane on Different Nickel Catalysts

ISBN 82-471-6960-6 (printed ver.)
ISBN 82-471-6959-2 (electronic ver.)
ISSN 1503-8181

NTNU

Kjersti Omdahl Christensen

NTNU
Norwegian University of
Science and Technology
Doctoral thesis
for the degree of doktor ingeniør
Faculty of Natural Sciences and Technology
Department of Chemical Engineering

Doctoral thesis 2005:46

NTNU

Kjersti Omdahl Christensen

Steam Reforming of Methane on Different Nickel Catalysts

Trondheim, March 2005

Doctoral thesis for the degree of doktor ingeniør

Norwegian University of Science and Technology
Faculty of Natural Sciences and Technology
Department of Chemical Engineering

NTNU

Acknowledgements

First of all I would like to thank Professor Anders Holmen, Professor De Chen and Dr. Rune Lødeng for support and inspiring supervision. Before I began the work with this thesis, Professor Anders Holmen gave me an enthusiastic description of the dr.ing scholarship. Without his knowledge, encouragement and positivism I would probably not even have started.

I thank my colleges at the Department of Chemical Engineering and at Sintef Materials and Chemistry for support and friendship during the last five years. The “coffee-breakers” are especially appreciated for contributing to the social environment.

The financial support from Hydro, Statoil, the Research Council of Norway and the Norwegian University of Science and Technology is greatly acknowledged.

Last, I would like to thank my husband Pål for support, encouragement and love, and also our daughter Anna for giving me the best hugs.

Abstract

The effect of crystal size on carbon formation and sintering was studied on nickel catalysts at steam reforming conditions. Different nickel supported catalysts were examined. As support three commercial hydrotalcites were used: HT30 (MgO/Al_2O_3 = 3/7), HT50 (MgO/Al_2O_3 = 5/5) and HT70 (MgO/Al_2O_3 = 7/3). These supports were compared with $CaO\text{-}Al_2O_3$ and $\alpha\text{-}Al_2O_3$. For the sintering experiments an industrial $Ni/CaAl_2O_4$ catalyst was used for comparison. The hydrotalcite derived catalysts had different Mg/Al ratios and the lowest Mg/Al ratio gave the highest Ni dispersion. The hydrotalcite derived catalysts also had a higher dispersion than $NiO/CaO\text{-}Al_2O_3$, $NiO/\alpha\text{-}Al_2O_3$ and $Ni/CaAl_2O_4$.

Carbon formation studies were performed in the tapered element oscillating microbalance (TEOM) at 823K, total pressure of 20 bar and steam to carbon (S/C) ratios of 0.08 to 2.4. The TEOM is a powerful tool for *in situ* catalyst characterization. All the feed gases pass through the catalysts bed and the TEOM offers a high mass resolution and a short response time. With an on-line gas chromatograph or mass spectrometer, catalyst activity and selectivity can be determined as a function of time. From the TEOM experiments it seemed that the Ni crystal size had a large effect on the carbon threshold value (S/C ratio where the carbon gasification rate equals the carbon deposition rate). Increased crystal size gave an increased carbon threshold value. It was concluded that small nickel crystals resulted in a large saturation concentration of carbon giving a low driving force for carbon diffusion and hence a lower coking rate. TOF increased with increasing Ni crystal size. This could be explained by surface inhomogeneities on the large crystals. Sintering experiments were

performed at 903K and 20 bar in a fixed-bed reactor system. For all the catalysts the sintering mechanism involving particle migration seemed to be dominating. Due to a higher degree of wetting of the substrate by the nickel particle, the catalysts with smallest nickel particles showed the highest resistance towards sintering.

Hydrogenolysis of methane was used as a probe reaction for testing the catalysts activity. An increased TOF with increased Ni particle size was observed. This result coincides with results from the steam methane reforming experiments in the TEOM.

The characteristics of the hydrotalcite derived catalysts prepared by impregnation of commercial hydrotalcite supports were compared with hydrotalcite derived catalysts prepared by the co-precipitation method. An improved dispersion with decreasing Mg/Al ratio in the hydrotalcite was found. The catalysts prepared by the co-precipitation method maintained a high dispersion at increased nickel loadings. Different techniques were used to determine the Ni particle size. The results showed an excellent correlation between the Ni particle size found by chemisorption, X-ray diffraction (XRD), transmission electron microscopy (TEM) and scanning transmission electron microscopy (STEM).

Table of contents

List of publications

I. K. O. Christensen, D. Chen, R. Lødeng, A. Holmen: "Effect of crystal size on carbon formation and sintering of hydrotalcite derived Ni-catalysts" *Submitted*

II. K. O. Christensen, E. Ochoa-Fernández, D. Chen, R. Lødeng, A. Holmen: "Nickel crystal size and distribution of hydrotalcite derived catalysts prepared by different methods" *Submitted*

III. E. Bjørgum, D. Chen, K. O. Christensen, R. Lødeng, A. Holmen: "*In situ* catalyst characterization by the oscillating microbalance catalytic reactor (TEOM)" *Submitted*

IV. D. Chen, R. Lødeng, K. Omdahl, A. Anundskås, O. Olsvik, A. Holmen: "A model for reforming on Ni catalysts with carbon formation and deactivation" *Stud. Surf. Sci. Catal*. 139 (2001) 93.

V. D. Chen, K. O. Christensen, E. Ochoa-Fernández, Z. Yu, B. Tøtdal, N. Latorre, A. Monzón, A. Holmen: "Synthesis of carbon nanofibers: effects of Ni crystal size during methane decomposition" *J. Catal*. 229 (2004) 87

VI. D. Chen, E. Bjørgum, R. Lødeng, K. O. Christensen, A. Holmen: "Microkinetic model assisted design for steam methane reforming" *Stud. Surf. Sci. Catal.* 147 (2004) 139

VII. E. Bjørgum, D. Chen, M. G. Bakken, K. O. Christensen and A. Holmen: Energetic mapping of Ni catalysts by detailed kinetic modeling. *J. Phys. Chem. B* **109** (2005) 2360

The thesis is based on results presented in paper I to IV. Copies of these papers are given in Appendices.

Presentations:

1. D. Chen, R. Lødeng, K. Omdahl, A. Anundskås, O. Olsvik, A. Holmen: *A Model for Carbon Formation and Deactivation of Ni Catalyst during Methane Reforming.* Keynote lecture. 9th International Symposium on Catalyst Deactivation, USA, October 7-10, 2001

2. D. Chen, R. Lødeng, K. Omdahl, A. Anundskås, O. Olsvik, A. Holmen: *Microkinetical Modeling of Methane Reforming,* Lecture. Eurokin Villeurbanne Meeting, France, October 18-19, 2001

3. D. Chen, R. Lødeng, K. Omdahl, Morten Rønnekleiv, Ola Olsvik, Karina H. Hofstad, A. Anundskås, Henrik S. Andersen, A. Holmen: *Carbon formation and deactivation of steam reforming catalysts*, Lecture. Europacat-V, Ireland, September 2-7, 2001

4. K. Omdahl, De Chen, R. Lødeng, A. Holmen*: Hydrogenolysis of ethane over Ni-catalysts.* Poster. Nordic Summer School: Trends in Industrial Catalysis, Espoo, Finland, May 28-June 1 2001

5. D. Chen, H. Svendsen, R. Lødeng, K.O. Christensen, A. Anundskås, O. Olsvik, A. Holmen. "*A multiscale approach to steam methane reforming: Carbon potential mapping in a steam reforming reactor*". Extended abstract & poster at ISCRE17, Hong Kong, september 2002.

6. K.O. Christensen, D. Chen, R. Lødeng, A. Holmen: *A study of carbon formation on different Ni-catalysts during steam methane reforming*, Oral presentation, 10th Nordic Symposium on Catalysis, Helsingør, Denmark, June 2-4 2002

7. D. Chen, R. Lødeng, K. O. Christensen, A. Anundskås, O. Olsvik, A. Holmen: *Microkinetical modeling of steam reforming in the presence of transport limitations,* Poster. NICE9, Durdent Court, London, England, February 11-12, 2003

8. D. Chen, K. O. Christensen, R. Lødeng, M. Rønnekleiv, H. S. Andersen, A. Holmen: *A study of natural gas prereforming kinetics,* Lecture. EuropaCat-VI, Innsbruck, Austria, August 31-September 4, 2003

.

9. D. Chen, E. Bjørgum, R. Lødeng, K.O. Christensen and A. Holmen: *Microkinetic model assisted design for steam methane reforming.* Lecture. 7th Natural Gas Conversion Symposium. Dalian, China, June 6 -10, 2004

The author's contribution

The author had an active part in all stages of the work presented in this thesis. In Paper I the author has planned, conducted, interpreted the experiments and done the writing. In Paper II the preparation of the impregnated catalysts and most the experiments with these catalysts were done by the author. The writing was also mostly done by the author. Esther Ochoa-Fernández prepared the co-precipitated catalysts, did all experiments involving these catalysts and performed the Fourier X-ray diffraction on the impregnated NiO/HT30. In Paper III the author had an active part in writing of the general literature survey. In Paper IV the author contributed mainly to the discussions during the work with the paper.

List of symbols and abbreviations

A	Atomic weight [g/mol]
a_{Ni}	Specific surface area of Ni [nm^2]
$C_{C\_Ni,f}$	Carbon concentration at the front of the Ni particle [mol_C/m^3]
$C_{C\_Ni,r}$	Carbon concentration at the rear of the Ni particle [mol_C/m^3]
C_{CH4}	Methane concentration [mol/m^3]
$C_{CH4\ eq}$	Methane concentration at equilibrium [mol/m^3]
$C_{fil,sat}$	Saturation concentration of carbon in the filament [$mol_C/m^3{}_f$]
$C_{Ni,f}$	Concentration of carbon at the front of a Ni particle [$mol_C/m^3{}_{Ni}$]
$C_{Ni,r}$	Concentration of carbon at the rear of a Ni particle [$mol_C/m^3{}_{Ni}$]
D	Dispersion [%]
d	Particle diameter [nm]
D	Dispersion [%]
D_0	Initial dispersion [%]
D_C	Effective carbon diffusivity
D_{eff}	Effective diffusivity
d	Particle size [nm]
d_{Ni}	Effective length of carbon diffusion in a Ni particle [nm]
d_{NiO}	NiO particle size [nm]
$d_{p,s}$	Particle size [nm]
E_a	Apparent activation energy [kJ/mol]
EDX	Energy dispersive X-ray
f	Fraction of the active surface which is effectively exposed to reactants during a catalytic reaction
f_{TEOM}	Natural frequency of the spring-mass system in the TEOM [s^{-1}]

FID	Flame ionization detector
GC	Gas chromatograph
HT	Hydrotalcite
K	Sherrer constant
k	Rate constant [mol/g_{cat},s]
k_{TEOM}	Spring constant from tapered element (TEOM) [g/s^2]
K_{CO}	Equilibrium constant
K_{eq}	Equilibrium constant
K_{H_2O}	Equilibrium constant
k_i	Instric rate constant [mol/g_{cat},s]
k_s	Sintering rate constant
L	Crystal dimension [nm]
m	Hydrogen number
m_{TEOM}	Oscillating mass in the TEOM reactor [g]
N	Avogadro's number [mol^{-1}]
n	Number of moles [mol]
n	Order of reflection
n	Carbon number
n	Sintering order
n	Hydrogen number
P_{CH_4}	Partial pressure of CH_4
P_{CO}	Partial pressure of CO
P_{H_2}	Partial pressure of H_2 [bar]
P_{H_2O}	Partial pressure of H_2O [bar]
R	Gas constant [kJ/K,mol]
r	Reaction rate [mol/g_{cat},s]

r_v	Effective reaction rate [mol/g_{cat},s]
S	Surface area of the active fraction [nm^2]
spc	Solid phase crystallization
SEM	Scanning electron microscopy
STEM	Scanning transmission electron microscopy
T	Temperature [K]
t	time [h]
TCD	Thermal conductivity detector
TEM	Transmission electron microscopy
TEOM	Tapered element oscillating microbalance
TPR	Temperature programmed reduction
V	Total volume of the active fraction [nm^3]
x_1	Ethane conversion at temperature 1
x_2	Ethane conversion at temperature 2
x_b	The weight fraction of carbon [g carbon / g Ni]
XRD	X-ray diffraction
y	Hydrogen number
*	Surface site

Greek symbols

β	Full breadth at half maximum [nm]
ΔG	Gibbs free energy [kJ/mol]
ΔG_{seg}	Gibbs free energy for segregation [J/mol]
$\Delta G°$	Gibbs free energy at standard conditions [kJ/mol]
ΔH^{o}_{298}	Heat of reaction at 298 K [kJ/mol]
θ	Bragg angle
θ_C	Surface coverage of carbon
λ	Wavelength
ρ	Specific mass of active phase [g/nm]
σ	Average surface area occupied by one active atom at the surface [nm^2]
φ	Degree of deactivation

1 Introduction

1.1 Thesis overview

The thesis is organized as a collection of four papers dealing with steam methane reforming. Some hydrogenolysis experiments have been performed during the work with this thesis. These results are not included in the papers, and will therefore be presented in chapter 4.

1.2 Natural gas

"Fact Sheet 2004 Norwegian Petroleum Activity" [1] has been used for information about natural gas. Natural gas consists of methane, ethane, propane, pentanes, natural gasoline and condensate. Norway produced 262.2 mill scm oil equivalent in 2003, of which 73 mill scm was gas. European consumption of dry gas has grown strongly in recent decades, also at the expense of other energy bearers – primarily oil and coal. Europe used about 490 bn scm natural gas in 2002. The biggest consumer nations are the UK, Germany, Italy, the Netherlands and France. Norwegian dry gas exports was 71.1 bn scm in 2003. 14% of the total European gas consumption is supplied from the Norwegian continental shelf. This makes Norway the second largest gas exporter to Europe and the third biggest on a world basis. Discovered and undiscovered resources on the Norwegian continental shelf are expected to total roughly 12.9 bn scm oil equivalents from 2003. Production to date amounts to 29% of total resources.

1.3 Synthesis gas

Historical review

One of the early studies on the reforming reactions was carried out by Fischer and Tropsch [2]. They reported that nickel and cobalt were active for CO_2 reforming of methane and that methane in coking gas was equally well converted by CO_2 and H_2O. In 1912 Mittasch and coworkers had the first patent on supported nickel catalysts for steam reforming [3]. The first tubular reformer using natural gas was installed by Standard Oil in Baton Rouge in 1930 [4], but the breakthrough of the steam reformer technology came in 1962 with ICI's two tubular reformers operating at 15 bar [4]. Recent years have shown progress in steam reformer technologies due to improved materials for reformer tubes, better understanding of carbon limits, better catalysts and higher feedstock flexibility [5].

Synthesis gas production in general

Natural gas can be converted in to liquid fuels, hydrogen or ammonia. This is done by first producing synthesis gas. Synthesis gas is a mixture of H_2, CO and CO_2. The property of the synthesis gas varies with the final products that will be produced. Ideally the synthesis gas will have the same stoichiometry as the final product [6]. The cost of a synthesis gas production unit is large, normally in the range of 60% of a large-scale conversion plant based on natural gas. Because of the high investment cost for synthesis gas production there is grate interest of optimizing the process schemes.

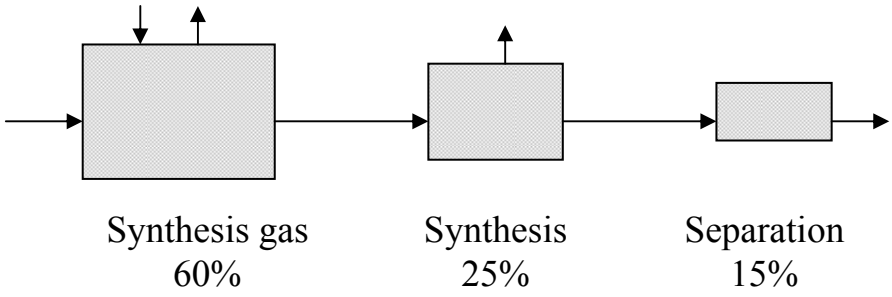

Figure 1: Relative investments of indirect conversion of natural gas [6]

Synthesis gas can be produced by different routes: Steam reforming, CO_2 reforming, autothermal reforming (ATR) and catalytic partial oxidation (CPO). The choice of technology depends on the scale of operation and also the desired product stoichiometry [6]. Steam reforming is the established process for converting natural gas and other hydrocarbons into synthesis gas [3]. The steam reforming process converts two stable molecules into the more reactive synthesis gas, hence the overall reaction is strongly endothermic.

$$C_nH_m + nH_2O = nCO + (n + {}^{m}/_{2})H_2 \qquad -\Delta H^{\circ}_{298} < 0 \qquad (1.1)$$

$$CH_4 + H_2O = CO + 3H_2 \qquad -\Delta H^{\circ}_{298} = \text{-206 kJ/mol} \qquad (1.2)$$

Water-gas shift:

$$CO + H_2O = CO_2 + H_2 \qquad -\Delta H^{\circ}_{298} = 41 \text{ kJ/mol} \qquad (1.3)$$

Steam may be replaced by CO_2 for a more favorable H_2/CO ratio for many syntheses:

$$CH_4 + CO_2 = 2CO + 2H_2 \qquad -\Delta H^{\circ}_{298} = \text{-247 kJ/mol} \qquad (1.4)$$

Methane may also be converted by means of oxygen into synthesis gas through partial oxidation:

$CH_4 + ½\ O_2 = CO + 2H_2$ $\quad -\Delta H^{\circ}_{298} = 36$ kJ/mol (1.5)

A nickel supported catalyst is typically used for the reactions (1.1)-(1.4), while the reactions (1.5) may be non-catalytic or use a supported nickel, platinum or rhodium catalyst [7].

1.4 Scope of the work

Synthesis gas production from natural gas has been extensively studied by several research groups. The catalysts are dictated by severe conditions with high pressure and high temperature. This involves several challenges concerning loss of catalytic activity.

In this study methane has been used as a simplified form of natural gas. The scope of this work has been to gain an understanding of the carbon formation and sintering taking place during steam methane reforming at industrial conditions.

The catalysts used in this study have been made in-house. In addition one industrial reformer catalyst has been used for comparison.

Experiments have been preformed in different small scale apparatuses. The TEOM (Tapered element oscillating microbalance) has been used to study carbon on the catalyst. The TEOM has low internal volume and fixed-bed characteristics. A high pressure reactor system was built for sintering studies. The fixed-bed reactor was designed for easy catalyst outtake, which made the sintering studies with a long time scale possible. Catalyst probe reactions were done in a hydrogenolysis setup.

"Carbon formation from syngas production" was the title of a joint project between Hydro, Statoil, SINTEF and NTNU, which started in 1995 and ended in 2003. The project was financed by Hydro, Statoil and the Research Council of Norway. The thesis has been a part of the joint project.

2 Literature

2.1 The steam reforming process

Traditionally, steam reforming of the hydrocarbon feedstock was performed in a single fired tubular reformer (primary reformer). Today a prereformer upstream the tubular reformer is common. All higher hydrocarbons are converted in the prereformer in the temperature range of 623-823K, and the methane reforming and shift reactions are brought into equilibrium. With the use of prereformer, it is possible to preheat the feed to the tubular reformer to temperatures around 923K, thus reducing the size of the tubular reformer [8]. The prereformer also allow higher feedstock flexibility [9]. Downstream the tubular reformer an autothermal reformer (secondary reformer) could be placed [10]. A flow diagram of a steam reforming process with prereformer, tubular reformer and secondary reformer is shown in Figure 2.

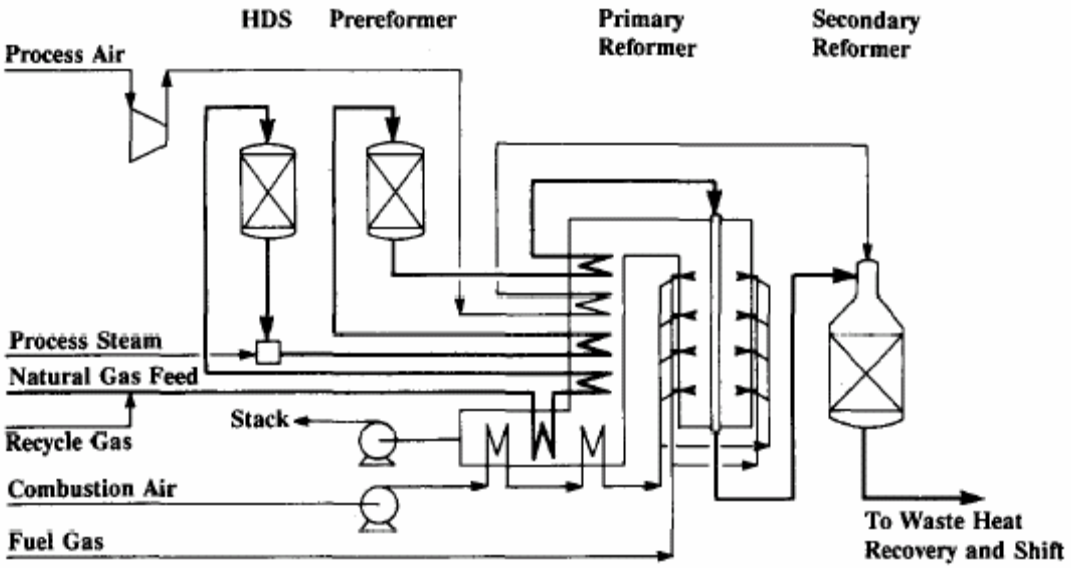

Figure 2. “State-of-the-art” reforming section for production of ammonia synthesis gas [11]

In order to supply the heat to the tubular reformer for the overall endothermic steam reforming reaction, the catalyst is loaded into a number of high-alloy tubes placed inside a furnace equipped with side burners. Typical inlet temperatures are 723-923K, and the product gas leaves the reformer at 973-1223K [7].

In a typical reformer furnace 50% of the heat produced by combustion in the burners is transferred though the reformer tube walls and absorbed by the process. The other half of the fired duty is available in the hot flue gas and is recovered in the waste heat section of the reformer for preheat duties and for steam production. This makes the overall thermal efficiency of the reformer approaching 95% [4, 7].

2.2 The steam reforming catalyst

The steam reforming catalyst is normally based on nickel. Cobalt and noble metals are also active, but more expensive [7, 8]. The catalysts are dictated by severe operating conditions, including temperatures in the range of 723-1223K and pressures up to 30 bar. The catalyst must have sufficient activity, resistance to carbon formation and mechanical strength to meet the requirements for the reformer operation listed below [12].

- Full conversion of the higher hydrocarbons and a close approach to equilibrium for the methane steam reforming reaction at the reformer exit
- Low tube wall temperatures to ensure a long life
- Constant pressure drop to maintain full process flow equally distributed through all reformer tubes

A commercial catalyst has normally sufficient activity to achieve complete conversion within the limits given by the mechanical design. The approach to equilibrium for steam reforming (1.2) is inversely proportional to the effective catalyst activity above 973K.

The Ni particle size seems to be an important factor for steam reforming catalyst activity. Smaller particles will provide a larger surface for reaction and hence improved catalyst activity. But also other aspects concerning the particle size are important. Smaller NiO crystals are known to have more steps and kinks on the surface than larger crystals, and hence a larger turnover rate [13]. Also Goula et al. reported that smaller crystals have a more open metal surface [14]. When it comes to carbon formation, smaller particles have been reported to be more resistant. Carbon formation is a structure sensitive reaction and not able to proceed at all when the crystals are below a critical size [13]. Borowiecki [15] reported a higher carbon deposition rate on larger Ni particles during steam reforming of butane. The author explains the correlation between particle size and coking rate with a model where spillover of steam adsorbed on the surface of the support is the key point. Chen et al. [16] found that the size of the nickel crystal had an influence on both coking rate and the ability of initiation or nucleation of carbon nano-fibers (CNF) from methane decomposition. The results indicated a lower coking rate on the smaller sized Ni particles. They also reported that initiation or nucleation of CNF was more difficult on the smaller sized Ni particles.

The steam reforming catalysts can be modified in order to be more carbon resistant. Both MgO and CaO in the support material could favor the coke gasification and hence decrease the carbon formation. Houruchi et al. [17] reported that basic metal oxides make the catalyst suppress the

carbon deposition. Borowiecki et al. [18, 19] found that an introduction of small amounts of molybdenum compounds (less than or equal to 0.1 wt%) reduced the detrimental effect of carbon deposit formation and increased the activity of methane steam reforming. With larger amounts, the authors observed a decrease in the catalyst activity. Su et al. [20] reported the stability and the high temperature steam resistance of Ni/α-Al_2O_3 catalysts doped with rare earth oxides investigated by means of an accelerated aging test. They found that the addition of rare earth oxides resulted in great improvements in the stability and high temperature steam resistance of the catalysts trough suppressing the growth of Ni-particle, the oxidation of the active component Ni and the formation of $NiAl_2O_4$. The effect of heavy rare oxides was shown to be more distinct than that of light ones. Choudhary et al. [21] found that supported nickel catalysts precoated with MgO, CaO or rare earth oxide showed much higher activity, selectivity and productivity in methane to syngas conversion reactions, than the catalysts prepared without any precoating.

Hydrotalcites are presented by the following general formula (2.1) [22]:

$$[M_n^{2+}M_m^{3+}(OH)_{2(n+m)}]^{m+}A_{m/x}^{x-}\times yH_2O \qquad (2.1)$$

where: M^{2+} and M^{3+} are metal cations, A is an anion, x is charge of the anion, n>m and y is the number of interlayer water molecules. When heated, the hydrotalcites dehydrates and loose their characteristic structure. At about 473K, the interlayer water leaves and about 723K, the layer hydroxides dehydrate. The dehydrated material retains the memory of the layered structure, but if the material is heated above 1023K an irreversible

change occurs and a complex mixture of oxides, mixed oxides, spinels, etc. begins to form [22]. The mixed oxide obtained by calcination has high surface area, basic properties and form homogenous mixtures of oxides with small crystal size, which by reduction form small and thermally stable crystals [23]. Clause et al. [24, 25] reported that the nature of the nickel oxide particles obtained by decomposition of Ni/Al_2O_3 hydrotalcite-type precipitates was related to the nature of the trivalent ion present. Calcination temperatures below 1100K gave formation of small and stable NiO particles, even at high Ni loadings. Trifirò et al. [26] have investigated the nature and properties of Ni–containing mixed oxides from hydrotalcite-type (HT) anionic clays. They found that in HT precursors all ions were homogenously distributed in brucite-type sheets. No correlation between the crystal size of the HT phases and that of the NiO particles formed upon calcination was found. Fornasari et al. [27] reported high surface area and low reducibility for the Ni^{2+} ions for Ni/Al/Mg mixed oxides calcinated up to 1023K. The low reducibility was explained by the presence of a surface spinel-type phase. Ni-rich samples gave increased Ni^{2+} reducibility, while Mg-rich samples showed reduced reducibility.

As early as in 1975 Ross [28] published a review article where he recognized that coprecipitated Ni, Al based catalysts satisfied all the requirements for steam reforming of methane. Later work has shown remarkable properties for hydrotalcite catalysts. In the review article written by Cavani et al. [23] an overview of catalytic activity during steam reforming is given, where catalysts from hydrotalcite precursors are reported to be both active and stable. Morioka et al. [29] reported high activity and high sustainability against coke formation during partial oxidation of methane to syngas. The hydrotalcite catalysts were stable and

had highly dispersed Ni. Bhattachatyya et al. [30] compared hydrotalcite caly-derived catalysts with Ni/Al_2O_3 and $Ni/MgAl_2O_4$ during CO_2 reforming of methane to syngas. Under severe reaction conditions (H_2O/CH_4=0.5, 1133K, 20 bar) the clay-derived catalysts exhibited superior activity and stability. Aging studies showed that clay-derived catalysts were more stable and coke resistant than commercial catalysts. Shishido et al. [31] prepared Ni-supported catalysts by the solid phase crystallization (spc) method starting from Mg-Al hydrotalcite anionic clay as the precursor. Activity and selectivity of Ni catalysts prepared by the spc method (spc-Ni/Mg-Al) and Ni impregnated on Mg-Al hydrotalcite (imp-Ni/Mg-Al) were compared with activity and selectivity of $Ni/-Al_2O_3$ and Ni/MgO during partial oxidation of methane to syngas. The spc-Ni/Mg-Al catalyst showed high activity and selectivity to synthesis gas, even at a high space velocity. For imp-Ni/Mg-Al the activity was higher than for $Ni/-Al_2O_3$ and Ni/MgO, while it was close to the activity for spc-Ni/Mg-Al. Takehira et al. [32] prepared spc-Ni/MgAl catalysts with Mg–Al hydrotalcite-like compounds as the precursors. The catalysts were tested for steam reforming of CH_4 into synthesis gas. The activity of spc-Ni/MgAl catalyst was high when Ni/Mg was larger than 0.2, and the most suitable ratio of Mg/Al was 1/3. During activity tests spc-Ni0.5/Mg2.5Al showed high CH_4 conversion following thermodynamic equilibrium even at a high space velocity. No deterioration in the catalytic activity was observed for 600 h of reaction time, while a commercial Ni/Al_2O_3 catalyst showed a clear activity decline during the same period of time on stream.

2.3 Kinetics and mechanism

Various approaches have been applied to establish intrinsic kinetics of steam reforming of hydrocarbons [33].

Table 1: Different approaches for intrinsic kinetics of steam reforming of hydrocarbons

Authors	Form of kinetics
Bodrov et al. [34]	Langmuir Hinshelwood
Khomenko et al. [35]	Temkin identity
Rostrup-Nielsen [4]	Two-step kinetics power law
Tøttrup [36]	Pellet kinetics
Xu and Froment [37]	Langmuir Hinshelwood
Aparicio [38]	Microkinetic analysis
Chen et al. [39, 40]	Microkinetic model

Early work on steam reforming of methane was based on the assumption that methane adsorption was rate determining, which was in agreement with the assumption of first-order dependence on the methane concentration. For example, Bodrov et al. [34] assumed methane adsorption to be rate limiting and proposed the following expression based on experiments conducted over a nickel foil:

$$r = \frac{kP_{CH_4}}{1 + a\left(P_{H_2O}/P_{H_2}\right) + bP_{CO}} \tag{2.2}$$

Under some conditions it has been observed that H_2 can retard the reaction [38] and this can not be explained by the above expression.

Later work avoided the discussion of a rate determining step and used the quasi steady-state approximation in terms of the Temkin identity instead. Khomenko et al. [35] proposed the following rate expression:

$$r = \frac{kP_{CH_4}P_{H_2O}\left(1-\left(P_{CO}\left(P_{H_2}\right)^3 \middle/ K_{eq}P_{CH_4}P_{H_2O}\right)\right)}{f\left(P_{H_2O},P_{H_2}\right)\left(1+\left(K_{H_2O}P_{H_2O}/P_{H_2}\right)\right)} \qquad (2.3)$$

where K_{eq} is the equilibrium constant for the overall reaction and $f\left(P_{H_2O},P_{H_2}\right)$ is a polynomial in P_{H_2O} and P_{H_2}. However, this expression was tested at high pressure over a nickel foil and the rate constant was found to be a function of pressure [38].

Xu and Froment [37] established a complex Langmuir-Hinshelwood expression on the basis of 280 measurements made with a $Ni/MgAl_2O_4$ catalyst. Unfortunately, the model was only valid within the temperature range of 773-848K, pressures between 3 and 15 bar and a H_2O/CH_4 ratio of 3-5. A detailed reaction scheme was presented, with three main reactions: Steam reforming of methane to CO and H_2 (1.2), steam reforming of methane to CO_2 and H_2 (2.4) and the water gas shift reaction (1.3).

$$CH_4 + 2H_2O = CO_2 + 4H_2 \qquad -\Delta H^{\circ}_{298} = \text{-165 kJ/mol} \qquad (2.4)$$

The proposed reaction scheme has a rate determining step for each of the three reactions, these rate determining steps are all surface reactions. Xu and Froments proposed rate expression for reaction (1.2) was:

$$r = \frac{\left(kP_{CH_4}P_{H_2O}/P_{H_2}^{2.5}\right)\left(1-\left(P_{CO}\left(P_{H_2}\right)^3/K_{eq}P_{CH_4}P_{H_2O}\right)\right)}{1+K_{CO}P_{CO}+K_{H_2}P_{H_2}+K_{CH_4}P_{CH_4}+\left(K_{H_2O}P_{H_2O}/P_{H_2}\right)} \quad (2.5)$$

The limitations in the applicability of the rate expressions (2.2), (2.3) and (2.5) suggest that there is no single rate determining step in the reforming of methane and that no simple analytical expression can be valid over a wide range of conditions [38]. Aparicio used microcinetic analysis to describe the steam methane reforming reactions. Parameters were obtained from the surface science literature or from fitting the results of transient kinetics experiments, no rate determining step was assumed. Aparicio used a set of 16 reactions (32 rate constants) and data from Xu and Froment [37] to adjust the model. The model predicts that for surface reactions involved in methane adsorption and dehydrogenation, the formation of a C-O bond and the formation of a OC-O bond can all be slow steps. Under most condition a combination of these reactions determines the rate.

Chen et al. [39, 40] used Aparichios microkinetic model [38] as basis for a new model which also included carbon formation and deactivation. The model described both dry and steam reforming of methane on Ni/MgO-Al_2O_3 and Ni/CaO-Al_2O_3 at a pressure range of $0.1 \cdot 10^{-5}$ to 20 bar and a temperature range of 773 to 923K.

2.4 Deactivation of catalyst

With time on stream industrial catalysts loose activity. There are three primary causes for catalyst deactivation in steam reforming:

- Carbon formation
- Sintering
- Poisoning

Carbon formation

Steam reforming generally involves the risk of carbon formation and the tendency to carbon formation increases with carbon number, unsaturation and aromaticity in the feed [4, 41, 42]. The main carbon formation reactions are:

$CH_4 = C + 2H_2$ $-\Delta H^{\circ}_{298} = -75$ kJ/mol (2.6)

$2CO = C + CO_2$ $-\Delta H^{\circ}_{298} = 172$ kJ/mol (2.7)

$CO + H_2 = C + H_2O$ $-\Delta H^{\circ}_{298} = 131$ kJ/mol (2.8)

$C_nH_m = nC + {}^{m}/_{2}\ H_2$ (2.9)

C_nH_m = olefins = coke (2.10)

$C_nH_m = (CH_2)_n$ = gum (2.11)

The carbon formation reactions can be categorized in three groups, which give the main routes for carbon formation. These routes are given in Table 2.

Table 2: Routes to carbon [4]

Carbon type	Reaction	Phenomena	Critical parameters
Gum	(2.11)	Blocking of Ni surface	Low H_2O/C ratio, absence of H_2, low temperature
Whisker carbon	(2.6) - (2.9)	Breakup of catalyst pellet	Low H_2O/C ratio, high temperature, precence of olefins, aromatics
Pyrolytic coke	(2.10)	Encapsulation of catalyst pellet, deposits on tube wall	High temperature, residence time, presence of olefins, Sulphur poisoning

Whisker carbon is the principal product of carbon formation in steam reforming [4]. The carbon whiskers have high mechanical strength, and the catalyst particle is destroyed when the whiskers hit the pore walls. This process may result in increasing pressure drop and hot tubes, which complicates the operation [8]. The mechanism for carbon whiskers has been described with carbon transport through the bulk of the nickel [43-45]. Recently Helveg et al. [46] suggested that the carbon is transported along the graphene-Ni interface. Both mechanisms will be presented here.

Carbon transport through the bulk of the nickel particles

Methane is adsorbed on the surface, and is through surface reactions converted into adsorbed carbon. These steps are followed by segregation of surface carbon into the layers near the surface. The carbon diffuses through the Ni and precipitates on the rear side of the Ni particle. The growing

whisker will lift the Ni particle at the tip. The nickel particle changes shape into a pear-like particle, leaving small fragments of nickel behind in the whisker [8].

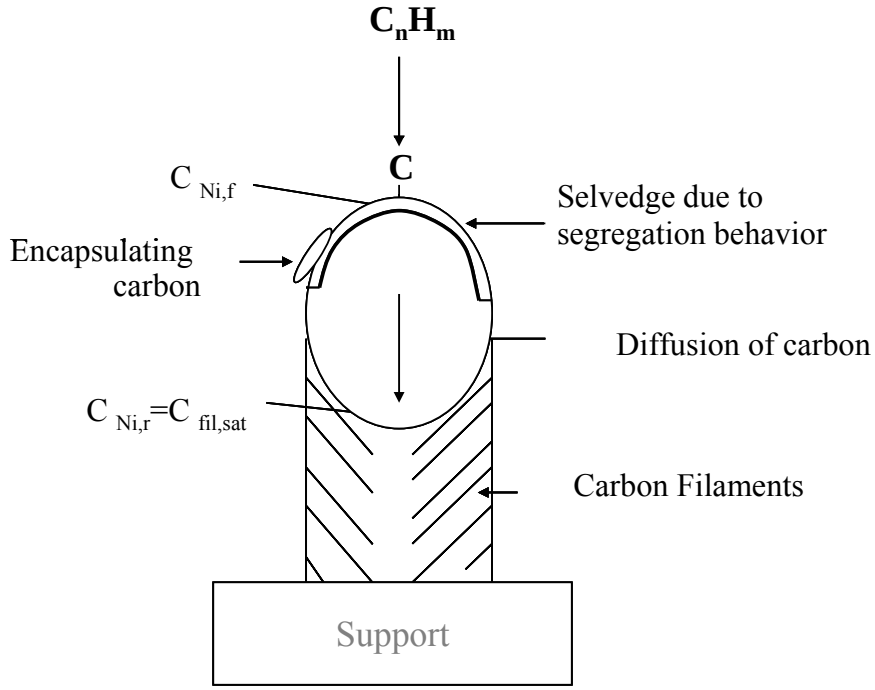

Figure 3. Schematic drawing of the carbon formation mechanism [47]. $C_{Ni,f}$ is the concentration of carbon at the front of the particle, just below the selvedge. $C_{Ni,r}$ is the concentration of carbon dissolved in nickel at the rear of the particle on the support side. $C_{fil,sat}$ is the saturation concentration of the filament.

At steady-state the coking rate equals the rate of carbon diffusion through the metal (Ni) particles which can be described by the following expression [16]:

$$r=\frac{D_C}{d_{Ni}} a_{Ni}\left(C_{C\_Ni,f}-C_{C\_Ni,r}\right) \qquad (2.12)$$

where D_C is the effective diffusivity for carbon diffusion through the nickel particle, d_{Ni} is the effective length of carbon diffusion in the Ni particles, a_{Ni} is the specific surface area of Ni, $C_{C\_Ni,f}$ is the carbon concentration on the front side of the Ni particles and $C_{C\_Ni,r}$ is the carbon concentration on the rear side of the Ni particles.

Carbon transport along the graphene-Ni interface

Helveg et al. [46] performed *in situ* transmission electron microscopy (TEM) observations of the formation of carbon nanofibers from methane decomposition over supported nickel nanocrystals. They observed an elongation/contraction of the nickel crystal during the carbon growth, Figure 4.

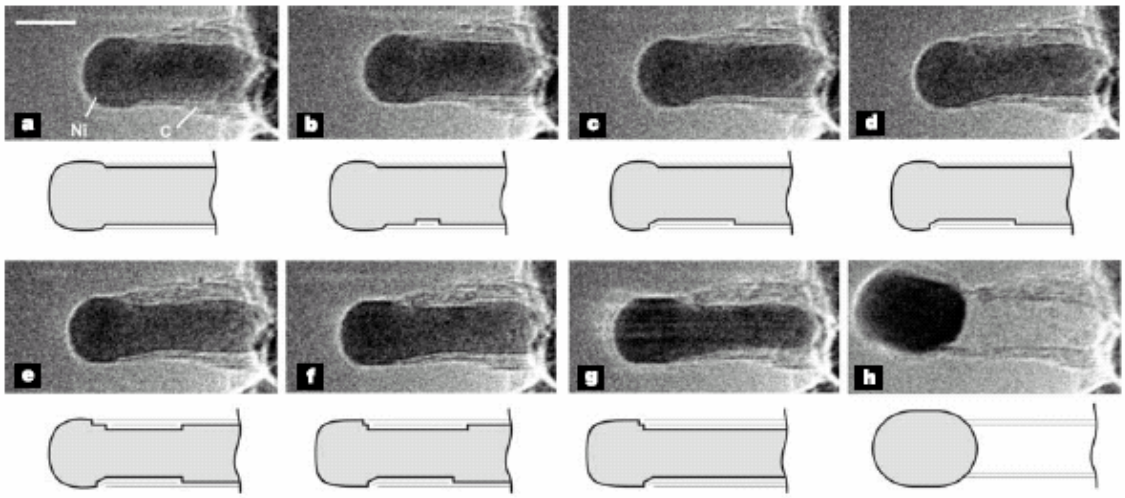

Figure 4. Image sequence of a growing carbon nanofibre [46]. Images (a-h) illustrate the elongation/contraction process. Drawings are included to guide the eye in locating the positions of mono-atomic Ni steps edges at the C-Ni interface. The images are acquired *in situ* with CH_4:H_2=1:1 at a total pressure of 2.1 mbar with the sample heated to 809K. Scale bar, 5nm.

Graphene layers were formed around the nickel crystal leading to a change in the adsorption energy of C and Ni adatoms. The graphene overlayer helped the formation of Ni steps, and hence, the release of Ni adatoms, which could diffuse along the interface towards the free surface. C adatoms at the interface were destabilized. The transport of C adatoms from the free surface to sites at the graphene-Ni interface was described by the following steps: Breaking of the C-bond to the Ni-step on the free surface, incorporation under the graphene sheet and diffusion at the graphene-Ni interface.

The difference in the two mechanisms, "Carbon transport through the bulk of the nickel particles" and "Carbon transport along the graphene-Ni interface", could perhaps be explained by the different pressures. It is possible that the study of Helveg et al. [46] only is valid at low pressures, while the mechanism concerning carbon transport through the bulk of the nickel particles is valid for high pressures.

Steam reforming of methane proceeds via the dissociative adsorption of hydrocarbons on the catalyst surface [45]:

$$CH_4 + * = CH_x * + \frac{(4\text{-}x)}{2} H_2 \tag{2.13}$$

$$CH_x * = C * + \frac{x}{2} H_2 = [C,Ni]_{bulk} \rightarrow \text{whisker carbon} \tag{2.14}$$

$$H_2O + * = O* + H_2 \tag{2.15}$$

$$C * + O* = CO + 2 * \tag{2.16}$$

Beebe et al. [48] found that the activation energy for dissociative adsorption of methane was structure sensitive, with an activation energy for adsorption on Ni(110) and Ni (111) being higher than on Ni (100).

The coke formation can be minimized by ensemble size control and by preventing carbide formation [45]. From reaction (2.13) to (2.16) it is clear that steam reforming of methane requires the dissociative adsorption of a hydrocarbon to form carbonaceous intermediates and that the carbon formation origins from the same carbonaceous intermediates [45]. Rostrup-Nielsen [49] reported that carbon formation requires a larger ensemble of surface sites than steam reforming. The ensemble size can be controlled by careful addition of sulphur in the feed [50]. The rate of steam reforming was reduced, but carbon formation was essentially eliminated [51]. Carbide is suggested to be the essential intermediate route to coke and it is assumed that prevention of carbide formation on the surface slows down the carbon formation process [45]. Due to the formation of carbide, metals like Fe and Ni are prone to carbon deposition [42, 43, 52]. Both ruthenium and rhodium are more effective catalysts [44] on which carbon formation seems to occur via a different mechanism [43]. Neither ruthenium nor rhodium dissolve carbon in the same extent as nickel and iron and are therefore more resistant to carbon formation [44]. Trimm [45] reported that dopants such as Sn, Sb, Bi and Zn can decrease coke formation, while having little effect on the steam reforming.

Minimizing the carbon formation is also a function of the support. Promoting the catalyst with alkali has been known to enhance the carbon resistance. A spillover of steam (or OH-species) from the catalyst support to the nickel surface [4, 6] is assumed to occur during steam reforming. The spillover effect is illustrated in Figure 5. Alkali promoted catalysts have ten

times larger surface coverage of H_2O* and OH* than non promoted catalysts [38]. It has been reported [53] that equilibrium coverages and heats of adsorption were lower on magnesia, with high spill over effect, than on non promoted catalysts. The rate of dissociation of steam was most pronounced on magnesia. Rostrup-Nielsen et al. [54] reported that the control of the degree of methane dissociation may be as important as enhanced steam adsorption in order to increase the catalyst coking resistance.

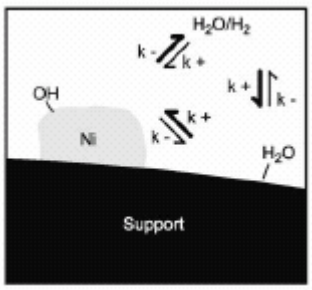

Figure 5. Spillover of steam on supported Ni-catalyst [6]

Hydrotalcites or mixed oxides have shown to be more resistant to coke formation than conventional steam reforming catalysts [22, 29]. The formation of small and stable Ni particles in hydrotalcite derived catalysts could explain the enhanced carbon resistance.

Sintering

Sintering is an important cause of deactivation of nickel containing steam reformer catalysts. A good understanding of the sintering mechanism is crucial, both for the prediction of the extent of deactivation and for design of catalysts that maintain high activity [8]. Sintering of nickel particles has been extensively studied by several groups [10, 32, 55-76].

There are many parameters which can effect the sintering: Reaction temperature, reaction atmosphere, catalyst composition and structure and support morphology. Elevated temperatures and the presence of water seem to accelerate the sintering and be the two most important contributors to sintering [64].

Two different sintering mechanisms have been proposed [76]: The atom migration mechanism and the particle migration and coalescence mechanism. Atom migration refers to the process where metal atoms are emitted from one metal particle and captured by another metal particle. In the particle migration process, the particles themselves move over the support and collide to form larger particles. The driving force for both processes is the difference in surface energy, which varies inversely with the particle size.

Particle growth is fast in the beginning of the sintering process, but slows down with time, resulting in a semi-stable state. The asymptotic particle size is characteristic for the semi-stable particle size. An example of this is shown in Figure 6.

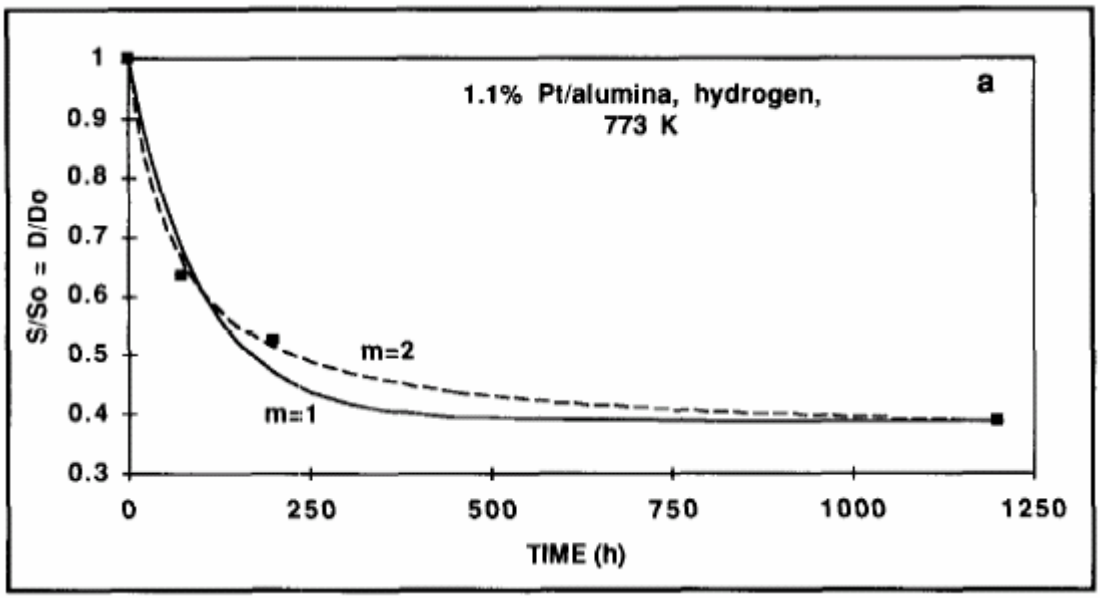

Figure 6: Normalized surface area for sintering of 1.1% Pt/γ-Al_2O_3 in hydrogen [77].

The shape of the particle size distribution is characteristic for the different sintering mechanisms. The atom migration mechanism results in a particle size distribution with a tail towards small particle sizes and a steep slope towards larger particles. For the particle migration process on the other hand, the log normal distribution of particle sizes with a tail towards larger particles is observed.

Another way of determining the sintering mechanism is to look at sintering kinetics [64]. The sintering rate data is expressed by an empirical rate equation involving dispersion.

$$-d(D/D_0)/dt=k_s(D/D_0)^n \qquad (2.17)$$

where k_s is the sintering rate constant, D_0 the initial dispersion and (n+1) is the sintering order. Lower values for n indicate atomic migration, while

$2<n<8$ usually indicates particle migration. A higher value for n could also indicate particle migration if a diffusion controlled process is assumed [73]. Generally high values for n are observed for sintering at low temperatures, and the reverse at high temperatures [64, 73, 74].

Hydrotalcite derived catalysts have showed a better resistance towards sintering than conventional steam reforming catalysts [23, 27]. Cavani et al. [23] studied reported results from different patents concerning hydrotalcite derived catalyst. A coprecipitated Ni/Al/Na catalyst showed superior performance compared to a conventional K doped catalyst supported on Al_2O_3 during steam reforming of naphta [78]. The resistance toward sintering was reported to be enhanced by introduction of Cr^{3+} into the precursor in substitution for Al^{3+} [79]. Christensen et al. [80] reported that a strong Ni particle-support interaction due to incorporation of Ni in the hydrotalcite structure makes hydrotalcite derived catalysts more resistant to sintering than Al_2O_3 supported catalysts.

Poisoning

The most important poison for steam reforming catalysts is sulphur. Sulphur in the feed leads to formation of hydrogen sulfide and a too large supply will result in a total deactivation of the catalyst [45]. It is important that sulphur in the feed gas is removed, this can be done by reaction with zinc oxide [8]. Under the reforming condition sulphur compounds will be converted into hydrogen sulfide, which is chemisorbed on transition metal surfaces by the following reaction:

$$H_2S + Me = Me\text{-}S + H_2 \qquad (2.18)$$

Reaction (2.18) takes place when the H_2S/H_2 ratio is less than those required for the formation of bulk sulfides [8]. It is possible to regenerate the poisoned catalyst by the reverse of reaction (2.18), but the driving force is extremely low [8]. Steam has been showed to have no influence on the chemisorption equilibrium. However, steaming results in complete oxidation of the nickel and the sulphur on non-promoted nickel catalysts is removed easily at temperatures above 873K [81]. Sulphur may be removed by oxidation and controlled re-reduction of the catalyst [4].

2.5 Hydrogenolysis as a probe reaction for steam reforming

Linear hydrocarbons having two to four carbon atoms react with H_2 by hydrogenolysis, giving smaller alkanes. Rostrup-Nielsen and Alstrup [82] have correlated the rates of steam ethane reforming and hydrogenolysis of ethane and found indications of a common rate determining step. A strong direct correlation of several orders of magnitude of activity for ethane hydrogenolysis and steam ethane reforming was found. They also reported that the turnover frequencies for steam methane reforming correlated directly with that of steam ethane reforming [82].

The general mechanism of ethane hydrogenolysis (the Sinfelt–Taylor mechanism), includes the following main steps [83-85]:

- Chemisorption of H_2
- Dehydrogenation of ethane on the catalyst surface to form adsorbed C_2H_x species
- C–C bond scission in C_2H_x (x = 5-0) to form the CH_y species (y = 3–0)
- Hydrogenation of CH_y to form methane, which then desorbs from the surface

The most frequent assumption is that the C–C bond scission step is rate-determining and that other steps are at pseudo equilibrium [84, 86]. Therefore, any C_2H_x or CH_y species is at equilibrium with either the reactants or the products of the reaction:

$$C_2H_6 + (6 - x)* = C_2H_x*_{6-x} + (3\text{-}0.5x)H_2 \quad (2.19)$$

$$CH_y*_{4-y} + (2\text{-}0.5y)H_2 = CH_4 + (4\text{-}y)* \quad (2.20)$$

where * is an adsorption site.

Reported apparent activation energy for hydrogenolysis of ethane over nickel catalysts are in the range of 170-191kJ/mol [83, 87, 88].

3 Experimental techniques

3.1 Catalyst preparation

Catalysts were prepared by incipient wetness impregnation of different supports with an aqueous solution of $Ni(NO_3)_2 \cdot 6H_2O$ to obtain 12.5 wt% Ni. As supports three different commercial hydrotalcites from Condea were used: HT30 (MgO/Al_2O_3 = 3/7), HT50 (MgO/Al_2O_3 = 5/5) and HT70 (MgO/Al_2O_3 = 7/3). These supports were compared with CaO-Al_2O_3 and α-Al_2O_3. CaO-Al_2O_3 was prepared by mechanical mixing, and the molar ratio was CaO/Al_2O_3=1/2. The mixture was calcined at 1423K at a heating-rate from ambient of 200K/h. α-Al_2O_3 was prepared by heating γ-Al_2O_3 at a rate of 200K/h up to 1423K. The final temperature was held for five hours. After impregnation the catalysts were dried overnight at 373K and calcined at 873 or 1173K at a heating rate of 4K/min, the final temperature was held for 4 hours. Ni/$CaAl_2O_4$ is an industrial reforming catalyst with 11 wt% nickel supported on $CaAl_2O_4$. This catalyst has only been used in the sintering experiments. The composition and calcination temperature of the different catalysts are given in Table 3.

Table 3: An overview of catalyst composition and calcination temperature, T_C. The MgO, CaO and Al_2O_3 content for the HT catalysts are from CONDEA, the remaining figures are calculated from the preparation of the catalysts.

Catalyst	NiO [%]	MgO [%]	CaO [%]	Al_2O_3 [%]	T_C [K]
NiO/HT30	15.9	24.5	-	59.6	873
NiO/HT50	15.9	42.6	-	41.5	873
NiO/HT70 (873)	15.9	59.5	-	24.6	873
NiO/HT70 (1173)	15.9	59.5	-	24.6	1173
NiO/CaO-Al_2O_3	15.9	-	39.27	44.8	1173
NiO/α-Al_2O_3	15.9	-	-	84.1	1173
Ni/$CaAl_2O_4$	11	-	8	81	-

3.2 Tapered element oscillating microbalance (TEOM)

The TEOM is produced by Rupprecht and Patashnick Co., Albany NY. A schematic drawing of the feeding system, TEOM and analysis unit is given in Figure 7 [40, 89, 90].

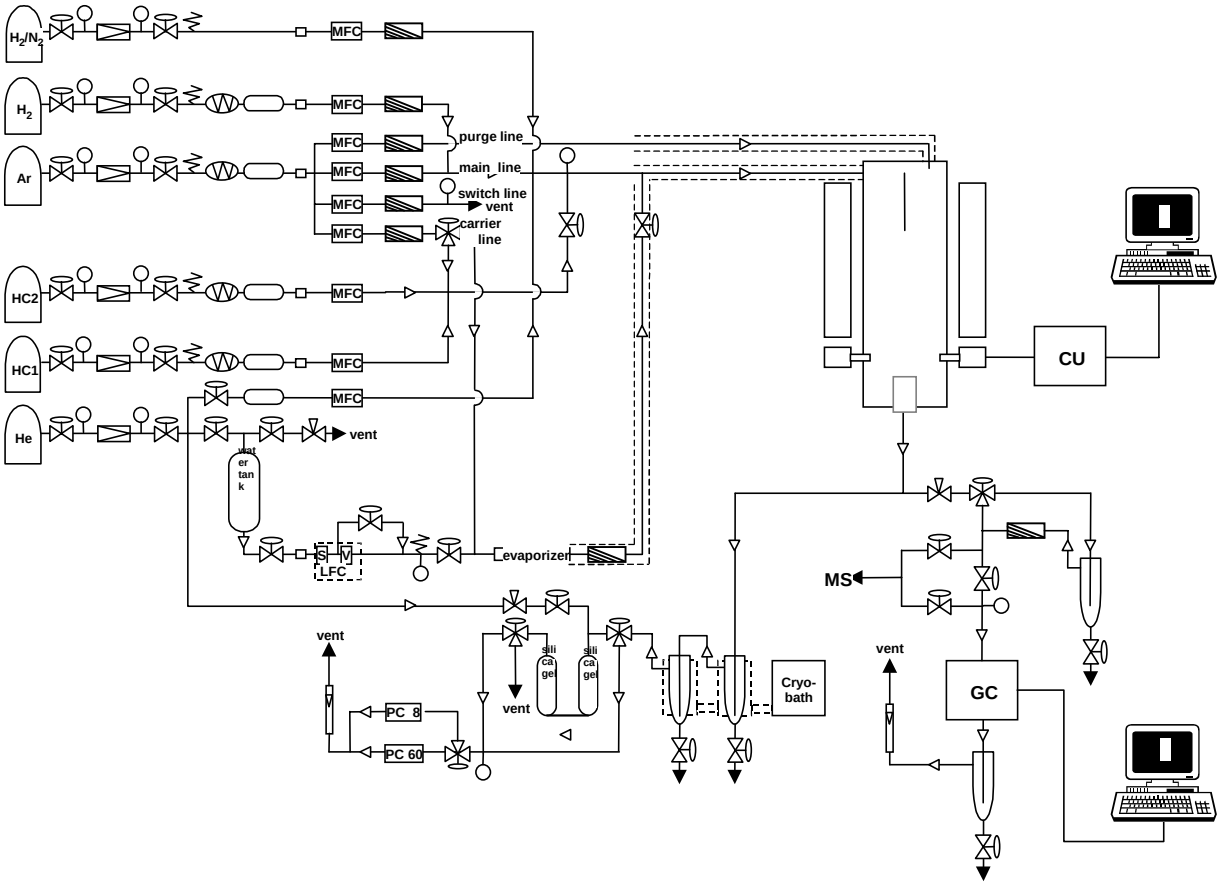

Figure 7. Schematic drawing of the tapered element oscillating microbalance [40, 89, 90]

The outlet of the reactor was heated to 523K to avoid condensation of water. The product composition was monitored by an on-line HP 5890 gas chromatograph (GC) which was equipped with a flame ionization detector (FID) and a GS-Q capillary column (30m, 0.543 mm). The TEOM consists of a hollow tapered quartz tube with a material test-bed in the end, and the internal volume is 0.17 ml. The tapered element is about 16 cm long, has an approximate inner diameter of 4mm and outer diameter of 6 mm. During experiments the test-bed is filled with catalyst diluted by an inert solid and held in place by α-Al_2O_3-wool and a metal cap.

Change of mass as the gas flows through the tapered element and catalyst bed are recorded by the system. A feed amplifier makes the tapered element oscillate at its natural frequency.

$$f_{TEOM}^2 = \frac{k_{TEOM}}{m_{TEOM}} \tag{3.1}$$

where f_{TEOM} is the frequency of oscillation, m_{TEOM} is the oscillating mass and k_{TEOM} is the spring constant of the tapered element. Equation (3.1) can be rearranged to the following form:

$$m_{TEOM,1} = k_{TEOM}\left(\frac{1}{f_{TEOM,1}^2}\right) \tag{3.2}$$

Changes in mass will be recorded by changes in the frequencies of the oscillation at different times, and the different masses are not needed.

$$\Delta m_{TEOM} = k_{TEOM}\left(\frac{1}{f_{TEOM,2}^2} - \frac{1}{f_{TEOM,1}^2}\right) \tag{3.3}$$

where $f_{TEOM,1}$ and $f_{TEOM,2}$ are frequencies at time 1 and 2 and Δm_{TEOM} is the change in mass. The upper end of the tapered element is fixed, while the end of the tapered element with the catalyst bed oscillates freely. A sensitive electronic feedback amplifier control circuit is connected to a mechanical drive to supply the necessary energy to maintain an oscillation with the natural frequency for the element and the catalyst. Due to the free vibration of the tapered element the outlet can not be directly attached to a gas chromatograph for analysis. A purge gas flowing outside the reactor collects the product gas before it reaches the gas chromatograph.

The major advantages of the TEOM compared to a conventional microbalance are:

- Direct real time mass change measurements of sample bed
- All the reaction gas goes through the packed sample bed, no bypass
- Time resolution of 0.1 seconds
- Mass sensitivity of 1μg
- The gas streams are only in contact with quartz and stainless steel
- A temperature capability of 973K
- A pressure capability of 60 bar
- 50mg sample maximum capacity
- High flow rates and better control of gas solid contact

A detailed description of the TEOM is given in Paper III.

Procedure for the TEOM experiment

The catalyst loading was about 8mg and it was diluted with approximately 100mg α-Al_2O_3. Both catalyst and diluent had a particle size in the range of 0.25-0.50mm. The effects of solid dilution are twofold: Minimizing the temperature gradient in the catalyst bed and reducing the potential for agglomeration of growing filamentous carbon and hence the potential for pressure drop. Because of the steam, α-Al_2O_3 wool was chosen instead of quarts wool to hold the catalyst bed in place. In the presence of steam volatilization and transport of SiO_2 from Si containing material to the catalysts surfaces caused fouling of the catalyst function [90]. α-Al_2O_3 is a stable and inert material at the conditions used in the experiments. Reduction of the catalyst was done in a mixture of 1/1 H_2/Ar at increasing

temperature from ambient to 923K at a rate of 2K /min. The final reduction temperature was held for 6 hours before it was lowered to reaction temperature at 823K or 873K.

The steam reforming reaction was started after first stabilizing the flow of steam in presence of a sufficient amount of H_2 to keep the catalyst reduced. At stable conditions the hydrocarbon was fed and the flow of H_2 stopped. Steam reforming was studied at 823K and 873K, a total pressure of 20 bar and steam to carbon ratios of 0.08 to 2.4. Space velocity was 12.5 $mol_{CH4}/g_{cat}h$ in all experiments.

Dynamical experiments were performed to study the effect of S/C on carbon formation at a constant temperature. Coke formation was initiated at a low S/C ratio. Thereby the S/C ratio was stepwise increased until net coke gasification was observed. Carbon threshold value is defined as the steam to carbon ratio that gives zero net carbon formation; the gasification rate equals the rate of the carbon formation [47].

3.3 High pressure sintering

A high pressure sintering setup has been built and used for catalyst activity and deactivation studies. A schematic drawing of the setup is shown in Figure 8.

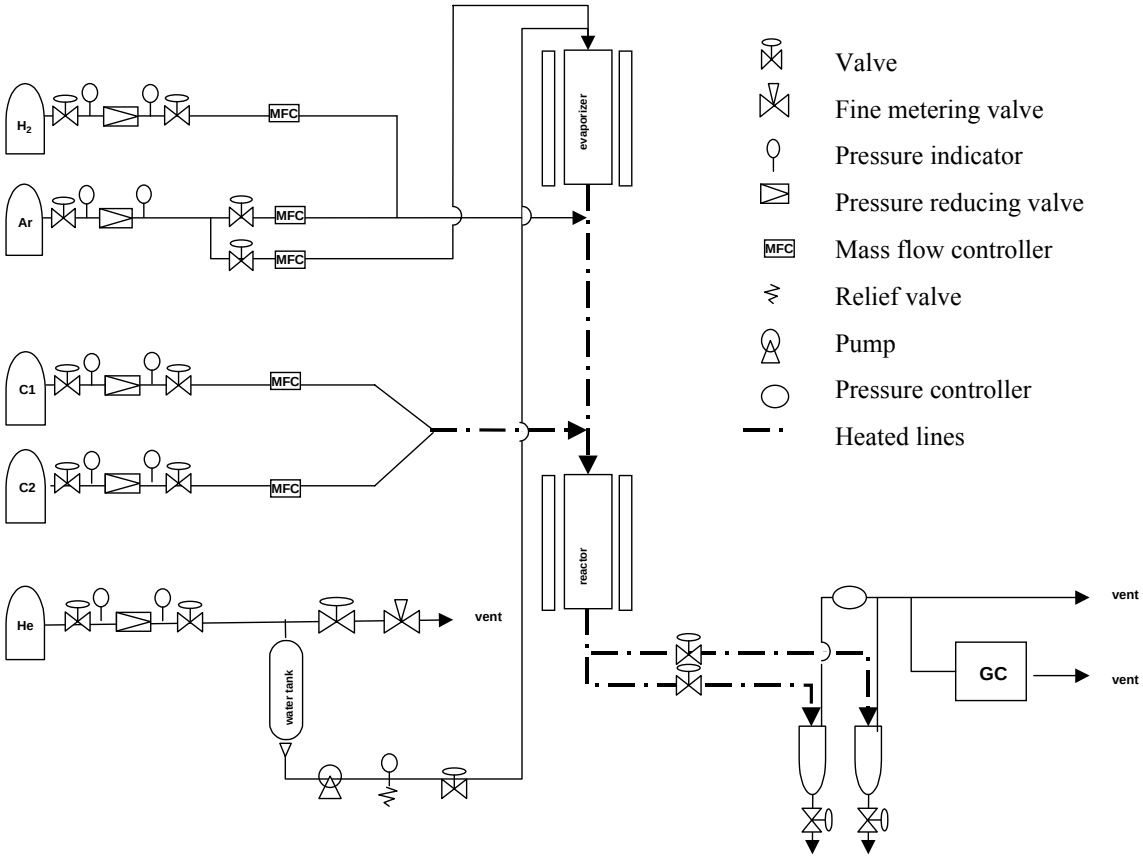

Figure 8: Schematic drawing of the high pressure sintering equipment

The reactor was a fixed-bed stainless steel tube reactor (length: 410 mm, inner diameter: 7 mm and outer diameter: 10 mm) and the catalyst was held in place by a stainless steel grid and Al_2O_3 wool. The temperature gradient over the catalyst bed was measured by a movable thermocouple and considered to be neglectable. The gas feed was controlled by mass flow controllers. N_2 was bubbled through the water tank to reduce the content of oxygen in the water. The water from the tank was pressurized by a pump, diluted by Ar and led in to the vaporizer before it was mixed with the rest of the feed gasses. An electronic pressure controller regulated the pressure

in the reactor. The product gas was analyzed by a gas chromatograph with a thermal conductivity detector (TCD).

Procedure for the sintering experiment

A catalyst loading of about 3g, with particle size in the rage of 0.25-0.50 mm was used. The catalyst was held in place by Al_2O_3 wool. Prior to the sintering experiments the catalyst was reduced in a mixture of 1/1 H_2/Ar and a total flow of 0.008 mol/min at increasing temperature from ambient to 943K. The heating rate was 3 K/min and the final reduction temperature was held for about 14 hours before it was lowered to the reaction temperature 903K. During start-up of the sintering experiments steam was introduced in a carrier flow of Ar and in the presence of hydrogen to avoid oxidation of the catalyst. Sintering experiments were performed both with ($H_2O/CH_4/Ar$=1/0.51/0.57) and without methane ($H_2O/H_2/Ar$=1/0.23/0.85) in the reaction mixture, at a total pressure of 20 bar. The total flow and steam partial pressure was kept constant at 0.03 mol/min and 9.6 bar, respectively.

In order to examine the sintered catalyst 1g of the catalyst was removed from the reactor after every 24th hour (approximately). After each catalyst removal, the remaining catalyst was reduced and sintered at the conditions described above.

3.4 Hydrogenolysis

A fixed bed hydrogenolysis setup was built for performing experiments at atmospheric pressure. A schematic drawing of the setup is shown in Figure 9.

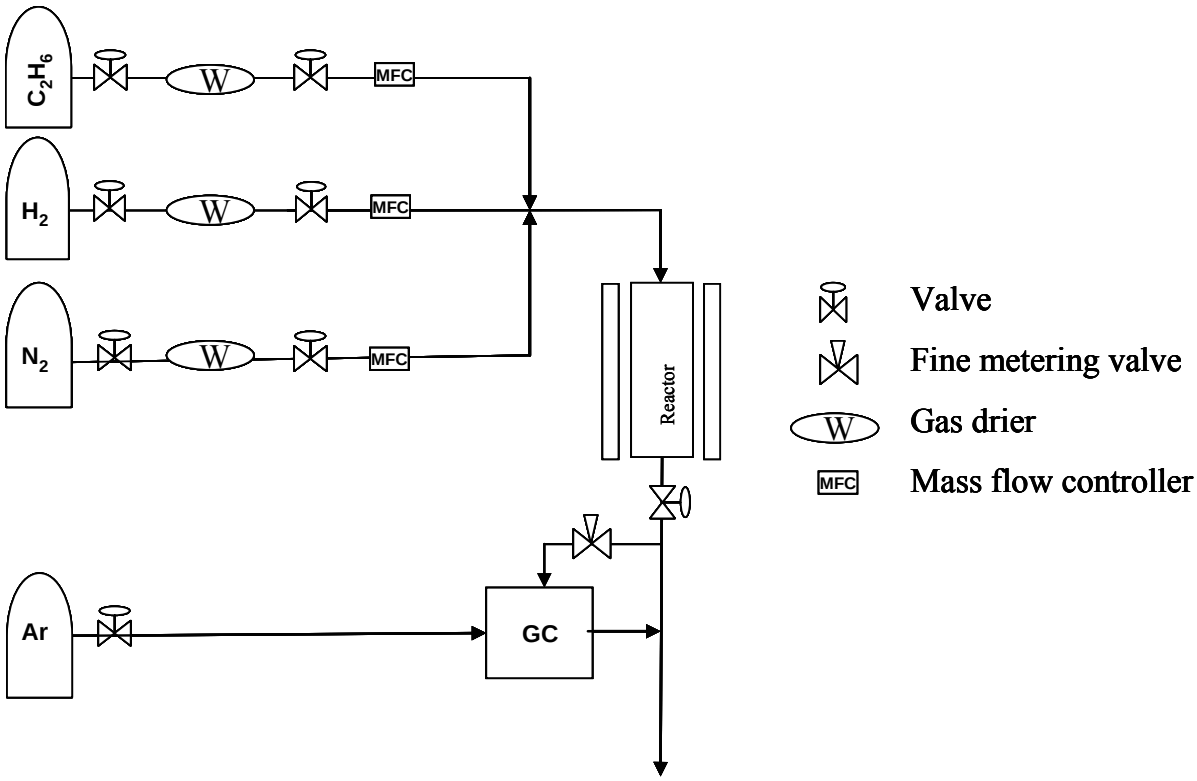

Figure 9: Schematic drawing of the hydrogenolysis setup

The reactor was an u-shaped quartz tube reactor and the catalyst was held in place by quartz wool. The feed gas was dried by gas driers, controlled by mass flow controllers and the product gas was continuously analyzed by a mass spectrometer and every half hour by a gas chromatograph with thermal conductivity detector (TCD).

Procedure for the hydrogenolysis experiment

Prior to the hydrogenolysis experiments the catalyst was reduced in a flow of H_2/Ar=1/1.3 at a temperature increase of 4K/min from ambient to 873K, before the temperature was reduced to the hydrogenolysis start-temperature at 473K. Hydrogenolysis was performed in a gas feed of $H_2/Ar/C_2H_6$=1.4/2.2/1 with a space time of 2.0 $mol_{C_2H_6}/g_{cat}h$. During the hydrogenolysis experiments the temperature increased with 3K/min from 473 to a maximum temperature at 873K, before it decreased with 3K/min back to 473K.

3.5 H_2 chemisorption measurements

The principle of volumetric chemisorption is to measure the adsorbed amount of gas as a function of the equilibrium pressure and in this way generate an adsorption isotherm. This is done by recording the pressure decrease when a known amount of gas expands into a known volume containing the catalyst sample. The isotherm is obtained by measuring this pressure decrease for a number of increments of increasing pressure. Sufficient time is given for adsorption equilibrium to establish at each measurement. The adsorbed amount corresponding to one monolayer is determined by extrapolating the linear part of the isotherm to zero pressure. A second isotherm could be measured after evacuation of the sample. The second isotherm, giving the amount of weakly “reversibly” adsorbed gas, is subtracted from the total amount adsorbed (first isotherm) to give the amount of irreversibly adsorbed species. The difference between the two isotherms gives the chemisorbed amount.

For Ni catalysts the total amount of adsorbed H_2 and a stoichiometry of H:Ni=1 are used to calculate the dispersion.

Procedure for the chemisorption measurement

H_2 adsorption isotherms were measured at 308K in an ASAP 2000. Prior to the measurements the catalysts were reduced in flowing H_2 with temperature programming from ambient temperature to 903K at a rate of 10 K/min, and kept at this temperature for 12h. The samples were then evacuated for 0.5h at 903K before cooling to 308K and the adsorption isotherm between 5 and 300 Torr was measured. Strongly and weakly held hydrogen where separated by measuring a second isotherm after pumping for 30 min.

The dispersion (D) can be calculated from the following formula [91]:

$$D=\frac{f\times A}{\rho\times\sigma\times N}\times\frac{S}{V} \qquad (3.4)$$

where: D - Dispersion

f - The fraction of the surface of the active phase which is effectively exposed to the reactants during the catalytic reaction.

A - Atomic weight of the active atoms

ρ - Specific mass (or density) of the active phase

σ - Average surface area occupied by one active atom at the surface

N - Avogadro's number

S - Surface area of the active fraction

V – Total volume of the active fraction

The dimension of V/S is a length that is proportional to some size characterizing the active particles contained in the catalyst. For a catalyst with all supported particle shaped as identical spheres of diameter d f=6 and S/V=6/d, hence:

$A = 58.69$ g, mol^{-1}

$\rho = 8.9 \cdot 10^{-21}$ g, nm^{-1}

$\sigma = 0.065$ nm^2 (Atomic cross-sectional area in the ASAP)

$N = 6.022 \cdot 10^{23}$ mol^{-1}

From the above formula and constants the following relation between dispersion and particle size is obtained:

$$d=\frac{101}{D} \qquad [d = nm, D = \%] \qquad (3.5)$$

3.6 Temperature programmed reduction (TPR)

Temperature programmed reduction (TPR) is an experimentally simple technique for the characterization of heterogeneous catalysts. An oxidic catalyst precursor is submitted to a programmed temperature rise, while exposed to a reducing gas mixture. The reduction of a metal oxide (MO) by hydrogen to form metal (M) and water vapor may be described by the general formula:

$$MO(s) + H_2(g) \rightarrow M(s) + H_2O \quad (3.6)$$

Thermodynamics predict under which conditions a catalyst can be reduced. The reduction will proceed when ΔG in equation (3.7) is negative.

$$\Delta G = \Delta G^{\circ} + nRT \ln\left(\frac{P_{H_2O}}{P_{H_2}}\right) \quad (3.7)$$

where ΔG is the change in Gibbs free energy for the reduction, ΔG˚ is Gibbs free energy under standard conditions, n is the stoichiometric coefficient for reaction (3.6), T is the temperature and P is the partial pressure. During TPR experiments the water formed is removed effectively and the second term in (3.7) is therefore always negative. For nickel ΔG˚ is also negative and the reduction is thermodynamically feasible [92].

The rate of reduction is continuously measured by monitoring the composition of the reducing gas at the outlet of the reactor. The gas flow is kept constant during the experiment and the changes in hydrogen concentration are therefore proportional to the rate of reduction. Reduction peaks appear when the reduction rate passes through a maximum. The interpretation of the TPR profile is usually confined to the discussion of peak maximum temperatures, the number of peaks and to the hydrogen consumption from which the extent of reduction can bee determined. The chemical nature and the environment of the reducible species will determine the positions of the peaks appearing in the TPR.

Procedure for the TPR experiment

An apparatus built at NTNU by Vada was used for the TPR experiments and has previously been described by Blekkan et al. [93]. The TPR experiments were performed in a quartz micro-reactor heated by an electrical furnace. The experiments involved heating of 0.2g catalyst at a rate of 4K/min to 1173K with a gas consisting of 7% H_2 in Ar. The H_2 consumption was measured by analyzing the effluent gas with a thermal conductivity detector. The steam formed during the reduction was removed by a cooling trap.

3.7 X-Ray diffraction (XRD)

X-rays have wavelengths in the angstrom range and are therefore sufficiently energetic to penetrate solids and probe their internal structure [92]. XRD is used to identify bulk phases, monitor kinetics of bulk transformations and to estimate particle sizes. Diffraction of X-rays by crystal planes allows one to derive lattice spacing by using the Bragg relation:

$$n\lambda=2d\cdot\sin\theta \tag{3.8}$$

where n is the order of the reflection, λ is the wavelength, d is the distance between two lattice planes and θ is the Bragg angle. By using a certain wavelength (λ) Sherrer showed that the broadening of the diffraction line corresponding to the Bragg angle (θ) is related to the crystal size [92].

$$<L>=\frac{K\lambda}{\beta\cos\theta} \tag{3.9}$$

where: L is a measure of the dimension of the crystal in the direction perpendicular to the reflecting plane, λ is the X-ray wave length, β is the peak with and θ is the angle between the beam and the normal reflecting plane. K is the Sherrer constant and equals 0.89 [91].

Procedure for the XRD experiment

X-ray diffraction studies were performed on a Simens D5005 X-ray diffractometer using monochromatic CuKα radiation. Phase identifications were carried out by comparing the collected spectra in the database. The measurements were done on calcined catalysts and average crystal sizes were calculated using the Scherrer formula, equation (3.9), based on peak broadening.

3.8 Transmission electron microscopy (TEM) and scanning transmission electron microscopy (STEM)

Electron microscopy is a technique used to determine the size and shape of supported particles. By detecting characteristic X-rays produced in the interaction of the electrons with matter, information on the composition and internal structure of the particles can be revealed. In Figure 10 the interaction between the primary electron beam and the sample is shown [92].

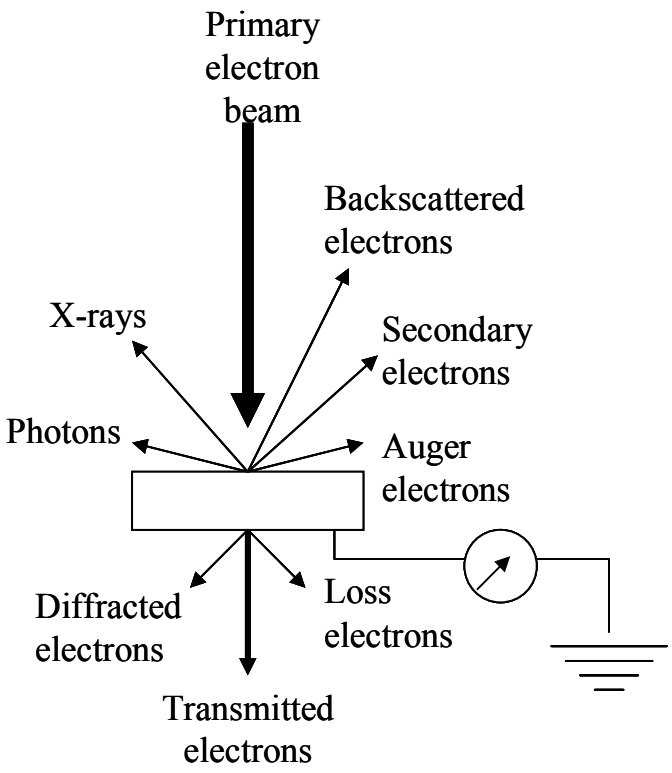

Figure 10: Interaction between primary electron and the sample in an electron microscope [92]

Transmission electron microscopy (TEM) uses transmitted and diffracted electrons. In TEM a primary electron beam of high energy and high intensity passes through a condenser to produce parallel rays. As the attenuation of the beam depends on the density and the thickness, the transmitted electrons form a two-dimensional projection of the sample mass. This projection is magnified by the electron optics and produces bright field images. The dark field image is obtained from the diffracted electron beams, which are slightly off angle from the transmitted beam. A bright field and a dark field image are presented in Figure 11. Typical operating conditions are 100-200 keV electrons, 10^{-6} mbar vacuum, 0.5nm resolution and a magnification of $3 \cdot 10^5$-10^6.

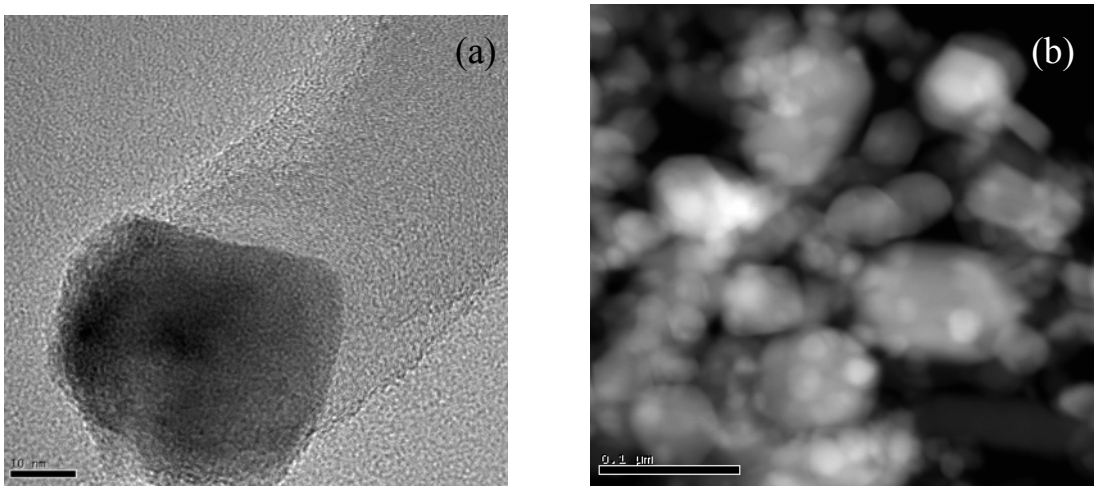

Figure 11: (a) Bright field image of a carbon whisker growing from a nickel catalyst supported on hydrotalcite derived material (NiO/HT50). (b) Dark field image of the same catalyst sample. The catalyst has been sintered for 50 hours at steam methane reforming conditions.

For scanning transmission electron microscope (STEM) scanning coiles connected to the TEM makes it possible to illuminate a small area of the sample from which either bright or dark field images are obtained.

Emitted X-rays are characteristic of an element and allow for a determination of the chemical composition of a selected part of the sample. This technique is referred to as energy dispersive X-ray analysis (EDX).

Procedure

The diameter of the Ni-particles was studied by a JEOL 2000EXII high resolution transmission electron microscopy. TEM specimens were prepared by ultrasonic dispersion of the slightly ground catalyst samples in chloroform, and a drop of the suspension was applied to a holey carbon copper grid.

The Ni catalysts have also been examined by means of STEM, which is preformed with JEOL 2000EXII electron microscope equipped with a field emission gun capable of giving a lattice resolution of 0.14 nm. Both bright field and dark field images were performed to get a better contrast of Ni particles against support materials.

Both TEM and STEM was performed by John Walmsley at SINTEF Materials and Chemistry.

4 Results and discussion

4.1 Hydrogenolysis

Ethane hydrogenolysis is a classical reaction that has been used to illustrate the effects of structure on catalytic activity [94]. In this study ethane hydrogenolysis was used as a probe reaction for the catalysts activity. Rostrup-Nielsen and Alstrup [82] reported that the rates for steam reforming of ethane and hydrogenolysis of ethane are closely related. It is therefore assumed that the activity for one catalyst with respect to the other catalysts will be the same for hydrogenolysis and steam reforming. The hydrogenolysis experiments were fast and easy to perform, and were therefore chosen as a probe reaction for testing different prepared catalysts. The procedure for the hydrogenolysis, and the reduction prior to the hydrogenolysis experiments are described in chapter 3.4. Examples of C_2H_6 conversion as a function of temperature are given in Figure 12.

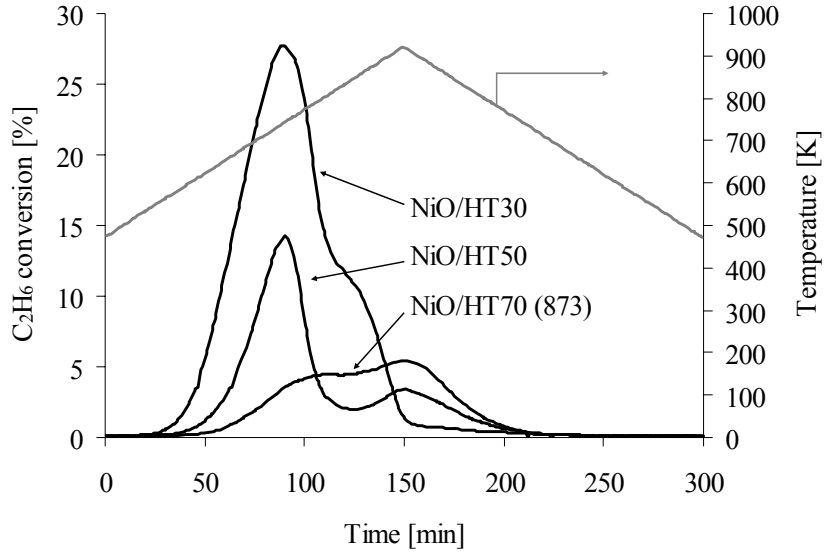

Figure 12. Ethane conversion over NiO/HT30, NiO/HT50 and NiO/HT70 (873) at a total flow of 0.006 mol/min, $H_2/Ar/C_2H_6 = 1.4/2.2/1$

The hydrogenolysis profiles in Figure 12 show that the C_2H_6 conversion passes through a maximum with increasing temperature. This could be due to carbon formation on the catalysts. Jackson et al. [87] reported a non steady-state behavior for reduced catalysts in contact with reactant gas for hydrogenolysis. They observed an initial activation/deactivation of the catalyst before reaching steady-state and related this to the formation of a reactive carbonaceous overlayer on the nickel surface. Carbon formation on the prepared catalysts is thoroughly discussed in Paper I.

Figure 13 shows a linear relation between temperature and TOF. At temperatures above 700K this linearity was lost, probably due to carbon formation.

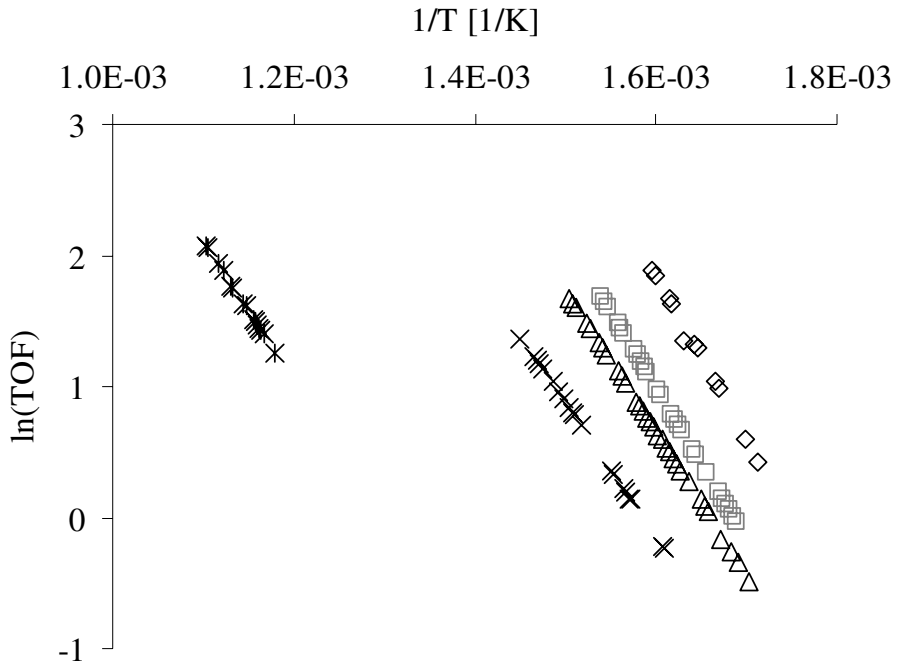

Figure 13. Hydrogenolysis of ethane at a total flow of 0.006 mol/min and $H_2/Ar/C_2H_6$ = 1.4/2.2/1. ◊: NiO/HT30, □: NiO/HT50, X: NiO/HT70 (873), Δ: NiO/HT70 (1173) and *: NiO/α-Al_2O_3.

The apparent activation energies are calculated from the Ahrenius plot in Figure 13.

Table 4: Apparent activation energies, E_a, for the different catalysts

Catalyst	E_a [kJ/mol]
NiO/HT30	103
NiO/HT50	96
NiO/HT70 (873)	85
NiO/HT70 (1173)	90
NiO/α-Al_2O_3	98

The values in Table 4 are in correlation with the apparent activation energy reported by Goodman [95], E_a = 100 kJ/mol on a Ni(100) surface.

The average particle size for the different catalysts, given in Table 5, are calculated from X-ray diffraction and discussed in Paper I.

Table 5: Particle size of different Ni catalysts from XRD

Catalyst	NiO crystal size [nm]
NiO/HT30	12
NiO/HT50	24
NiO/HT70 (873)	29
NiO/HT70 (1173)	29
NiO/α-Al_2O_3	32

Figure 14 shows the relation between Ni particle size and TOF.

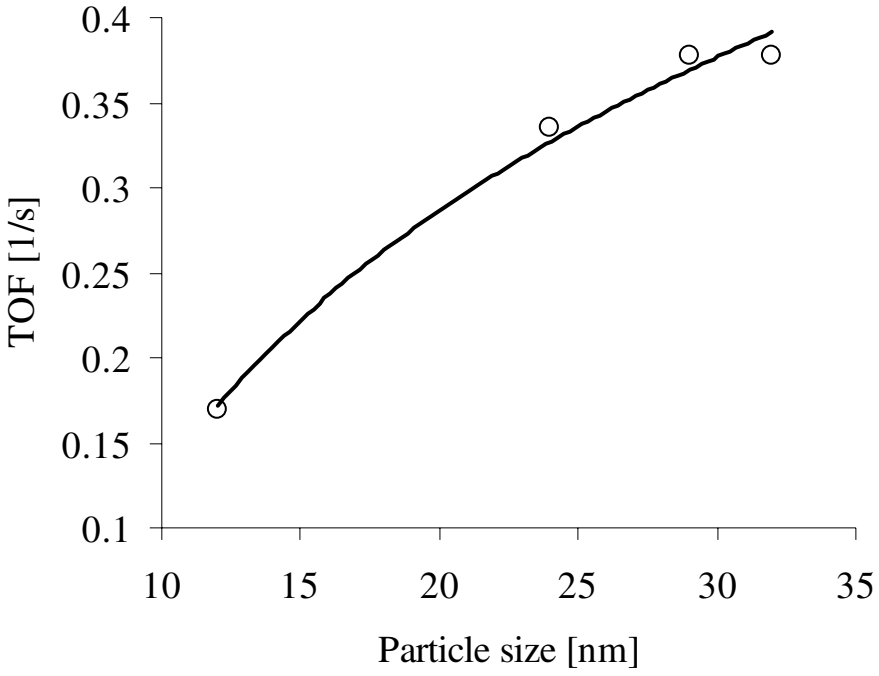

Figure 14. TOF as a function of particle size at 510K. The dots are experimental results, while the line indicates a trend. The hydrogenolysis experiments were performed at a total flow of 0.006 mol/min and $H_2/Ar/C_2H_6$ = 1.4/2.2/1

An increasing TOF with increasing Ni particle size is observed. These results are according with the results obtained on steam methane reforming, Paper I. Che et al. [96] states that hydrogenolysis of ethane generally is considered to be structure sensitive. C-C bonds are broken and a site would probably consist of several surface atoms. This implies that the site density is strongly affected by the particle diameter. Increased TOF with increased particle size could be explained by an increased site density with increased particle size [96].

The relation between TOF for ethane hydrogenolysis and methane steam reforming is shown in Figure 15.

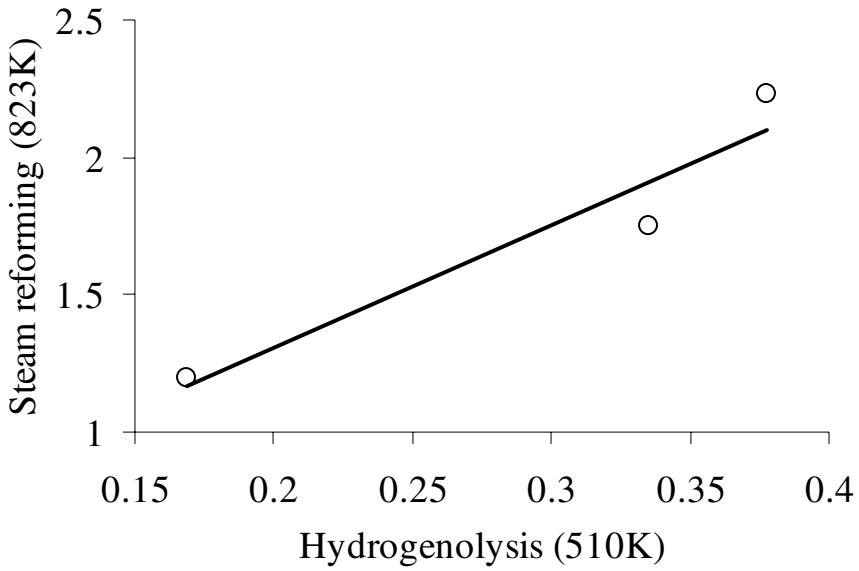

Figure 15. TOF for ethane hydrogenolysis (510K, total flow: 0.006 mol/min, $H_2/Ar/C_2H_6$ = 1.4/2.2/1) and steam methane reforming (873K, total flow: 0.009mol/min, P=20bar and S/C=0.5). Catalysts: NiO/HT30, NiO/HT50 and NiO/HT70 (873). The dots are experimental results, while the line indicates a trend.

The trend seen from Figure 15 indicates that hydrogenolysis of ethane and steam methane reforming may be strongly related for reactions over hydrotalcite supported nickel catalysts. Rostrup-Nielsen et al. [82] reported a similar relation between ethane hydrogenolysis and steam ethane reforming.

In order to compare the deactivation of the different catalysts a deactivation equation is defined (4.1).

$$\varphi = \frac{x_1}{x_2} \tag{4.1}$$

where φ is the degree of deactivation, x_1 is the conversion at a specific temperature during temperature increase and x_2 is the conversion at the same temperature during temperature decrease. One example of x_1 and x_2 is shown in figure 16.

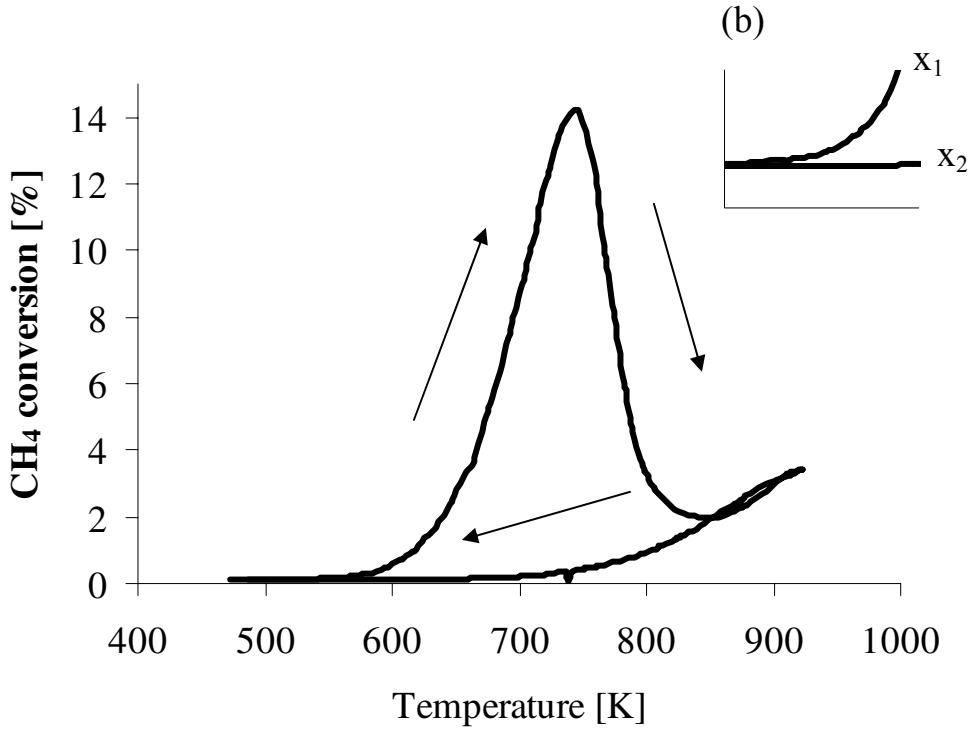

Figure 16. Ethane conversion over NiO/HT50 and at a total flow of 0.006 mol/min, $H_2/Ar/C_2H_6$ = 1.4/2.2/1. (b) The conversion in the temperature range 500-600K.

Table 6: $\varphi=x_1/x_2$ at 600K. x_1 is the conversion at a specific temperature during temperature increase, x_2 is the conversion at the same temperature during temperature decrease

Catalyst	φ
NiO/HT30	12.4
NiO/HT50	4.2
NiO/HT70 (873)	3.0
NiO/HT70 (1173)	1.9
NiO/α-Al_2O_3	1.4

From Table 6 it is seen that the catalysts with the smallest particle size deactivates the most. This is the opposite trend of what is observed for steam methane reforming, Paper I.

It is concluded that the TOF for the examined catalysts increase with increasing particle size. The catalysts with the smallest Ni particles seem to deactivate faster than the catalysts with larger Ni particles. The correlation between ethane hydrogenolysis and steam methane reforming indicates that the reactions are strongly related.

5 Summary of the papers

5.1 Paper I

Effect of Crystal Size on Carbon Formation and Sintering of Hydrotalcite Derived Ni-catalysts

Both carbon formation and sintering were studied over different nickel catalysts at steam methane reforming conditions. Hydrotalcite derived catalysts were compared with conventional catalysts. Catalyst composition and NiO crystal size are given in Table 5.

Table 5: Catalyst composition and NiO crystal size

Catalyst	NiO [%]	MgO [%]	CaO [%]	Al_2O_3 [%]	NiO crystal size [nm]
NiO/HT30	15.9	24.5	-	59.6	12
NiO/HT50	15.9	42.6	-	41.5	24
NiO/HT70 (873)	15.9	59.5	-	24.6	29
NiO/HT70 (1173)	15.9	59.5	-	24.6	29
NiO/CaO-Al_2O_3	15.9	-	39.27	44.8	32
NiO/α-Al_2O_3	15.9	-	-	84.1	60
Ni/$CaAl_2O_4$	11	-	8	81	65

Carbon formation and catalyst activity were studied using the tapered element oscillating microbalance (TEOM) at 823K, a total pressure of 20

bar and steam to carbon ratios from 0.08 to 2.4. The hydrotalcite derived catalysts were compared with NiO/α-Al_2O_3 and NiO/CaO-Al_2O_3. As seen from Table 5, nickel supported on hydrotalcite derived materials had a smaller crystal size than the conventional catalysts. Figure 17 shows a higher resistance to carbon formation for the hydrotalcite derived catalysts. (The carbon threshold value refers to the steam to carbon ratio where the carbon gasification rate equals the rate of carbon formation.)

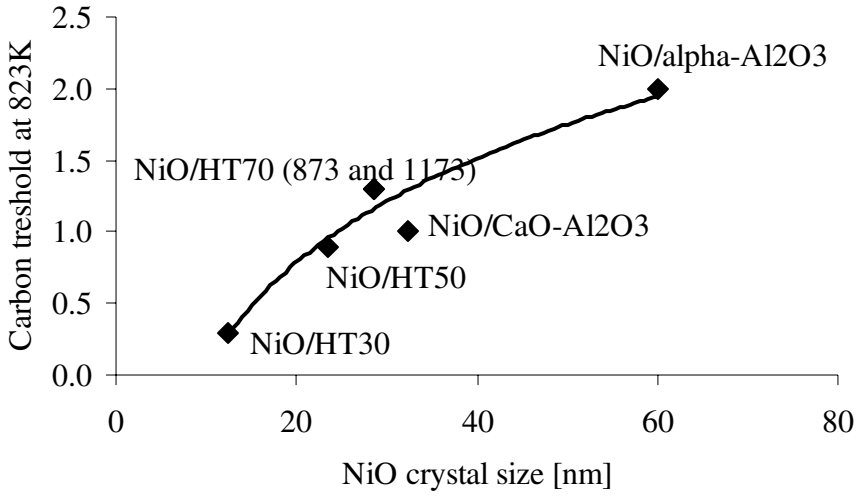

Figure 17. Carbon threshold values for steam methane reforming at a total flow of 0.009mol/min, T=823K and P=20bar. The symbols correspond to experimental data, while the line is for guidance of the eye.

The higher carbon resistance was believed to be caused by a higher saturation concentration of carbon in the smaller nickel crystals. The smallest crystals were observed on NiO/HT30.

Sintering experiments were performed at 903K and a total pressure of 20 bar. The hydrotalcite derived catalysts were compared with an industrial NiO/$CaAl_2O_4$ catalyst. Also in these experiments the hydrotalcite

derived catalysts were most stable. NiO/HT30 having the smallest size of stabilized nickel crystals showed the highest resistance towards sintering.

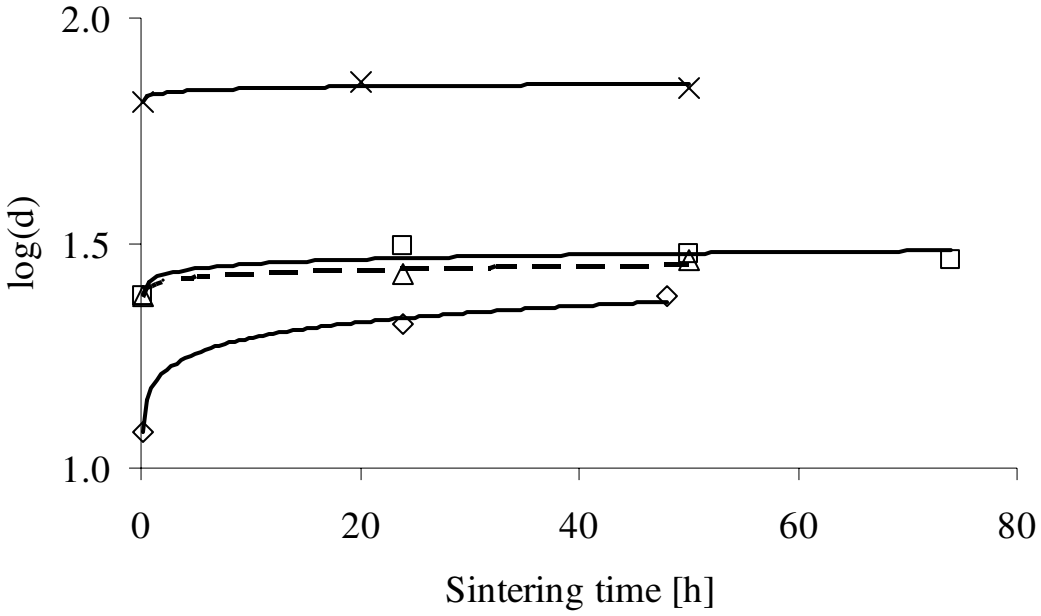

Figure 18. NiO particle size (d) as a function of sintering time. The symbols correspond to experimental data points, lines only indicate trends. T=903K, P=20bar and total flow=0.03mol/min. (x) denotes Ni/$CaAl_2O_4$ sintered at H_2O/H_2/Ar (1/0.23/0.85), (Δ) denotes NiO/HT50 sintered at H_2O/H_2/Ar (1/0.23/0.85), (□) denotes NiO/HT50 sintered at H_2O/CH_4/Ar (1/0.51/0.57) and (◊) denotes NiO/HT30 sintered at H_2O/H_2/Ar (1/0.23/0.85)

Results from temperature programmed reduction (TPR) indicated that the nickel crystals in NiO/HT30 were incorporated in the support. This could explain the high sintering resistance.

5.2 Paper II

Examination of nickel crystal size on derived hydrotalcite catalysts

In literature differences in crystal size measured by different techniques have been reported. Therefore an extensive study on determination of crystal size on hydrotalcite derived catalysts was performed. The crystal size was studied by chemisorption, X-ray diffraction (XRD), transmission electron microscopy (TEM) and scanning transmission electron microscopy (STEM). In order to compare the hydrotalcite derived catalysts prepared by different methods the catalysts were also characterized by BET and temperature programmed reduction (TPR).

The different techniques for determining the crystal size had different limitations. For chemisorption the degree of reduction was crucial. NiO crystals in hydrotalcite derived catalysts are known to bee difficult to reduce [24-27]. And an incomplete reduction would lead to a crystal size larger than the actual crystal size [97].

The Ni particle size from XRD was determined by two methods: the line broadening analysis (LBA) and the Fourier method. Small particles and an increased metal loading may result in a particle size distribution shifted towards higher particle sizes for the LBA method. Another limitation was that the Scherrer equation did not consider the line broadening caused by the microstrain. A disadvantage compared to the Fourier method was that peak overlap lead to increased tendency for errors. However, a good correlation between crystal sizes found by the two different methods was obtained.

For electron microscopy it must bee assumed that the size of the imaged particle is truly proportional to the size of the actual particle, and that the detection probability is the same for all the particles, independent of their dimensions [92]. In order to ensure that the results were representative for the catalyst sample a number of images was investigated at different parts of the sample.

The crystal size determined from chemisorption, XRD, TEM and STEM gave almost identical results for the catalysts examined. To ensure that correct crystal size is determined, it was concluded that the crystal size should be investigated by more than one technique.

Hydrotalcite derived catalysts prepared by impregnation of commercial hydrotalcite support are compared to hydrotalcite catalysts prepared by the co-precipitation method. The composition of the different catalysts is given in Table 6.

Table 6: Catalyst composition and preparation method. d_{NiO} is the NiO particle size from X-ray diffraction

Catalyst	NiO [%]	MgO [%]	Al_2O_3 [%]	Preparation method	d_{NiO} [nm]
NiO/HT30	15.9	24.5	59.6	Impregnation	12
NiO/HT50	15.9	42.6	41.5	Impregnation	24
NiO/HT70	15.9	59.5	24.6	Impregnation	29
Ni/HT	15.9	60.1	24	Co-precipitation	10
40Ni/HT	50.9			Co-precipitation	9

A low ratio of Mg/Al in the catalysts seems to yield a better dispersion of the nickel crystals. Preparation through the co-precipitation

method gave small nickel crystals even at high nickel loadings. Strong interactions between nickel and support were observed during the TPR experiments for NiO/HT30 and the catalysts prepared by the co-precipitation method. This indicated nickel incorporated in the hydrotalcite structure.

5.3 Paper III

In situ catalyst characterization by the oscillating microbalance catalytic reactor (TEOM)

The paper gives a review of *in situ* catalyst characterization in the TEOM setup. The main advantage of the TEOM is that all the feed gases pass through the catalysts bed. The TEOM offers a high mass resolution and a short response time. With an on-line gas chromatograph or mass spectrometer, catalyst activity and selectivity can be determined as a function of time. Originally the TEOM was used for measuring solid particulates in gases, but the technology has gradually been upgraded and the TEOM is now a powerful tool for *in situ* catalyst characterization.

TEOM applications generally involve:

- Adsorption studies
- Catalyst characterization
- Reaction kinetics
- Deactivation due to coke formation
- Effect of coke on adsorption, diffusion, selectivities and reaction rates
- Regeneration kinetics

A general literature survey of the use of TEOM is given. Two examples of use and TEOM characteristics are presented in detail: Methanol to olefins over SAPO-34 and steam reforming of natural gas on nickel catalysts.

5.4 Paper IV

A model for reforming on Ni catalysts with carbon formation and deactivation

In order to describe methane reforming with carbon formation and deactivation a microkinetic model with 30 elementary steps was developed. The model was based on Aparicio [38] and Chen et al. [40]. No rate determining step was assumed and the Bond Order Conservation - Morse Potential (BOC-MP) method was used to calculate the activation energies as a function of the carbon-nickel, hydrogen-nickel and oxygen-nickel bond strength. The BOC method creates a link between the bond strength and the activation energies, which can provide a direct guidance for suggesting new catalysts or of improving existing ones. Microkinetic analysis indicates that the bond strengths are strongly correlated to catalyst activity. It is possible to change the bond strength through promoters, but catalysts promoters are often also catalyst poison.

The model was fitted to experimental data for two different nickel catalysts for a wide range of experimental conditions. The elementary steps are given in Table 7.

Table 7: Microkinetic model for CH_4 reforming including carbon formation

	Reaction	Rate constant Forward reaction	Rate constant Reverse reaction
r_1	$CH_4 + 2* \leftrightarrow *CH_3 + *H$	$6.5 \cdot 10^7 \cdot e^{-57500/RT}$	$6.5 \cdot 10^7 \cdot e^{-57500/RT}$
r_2	$*CH_3 + * \leftrightarrow *CH_2 + *H$	$1.0 \cdot 10^{13} \cdot e^{-99900/RT}$	$2.0 \cdot 10^{12} \cdot e^{-49600/RT}$
r_3	$*CH_2 + * \leftrightarrow *CH + *H$	$1.0 \cdot 10^{13} \cdot e^{-97000/RT}$	$1.0 \cdot 10^{13} \cdot e^{-73700/RT}$
r_4	$*CH + * \leftrightarrow *C + *H$	$1.0 \cdot 10^{13} \cdot e^{-189700/RT}$	$1.0 \cdot 10^{13} \cdot e^{-173000/RT}$
r_5	$H_2O + * \leftrightarrow *H_2O$	$2.4 \cdot 10^6$	$1.0 \cdot 10^{13} \cdot e^{-68900/RT}$
r_6	$*H_2O + * \leftrightarrow *OH + *H$	$1.0 \cdot 10^{16} \cdot e^{-86700/RT}$	$1.0 \cdot 10^{13} \cdot e^{-42700/RT}$
r_7	$*C + *OH \leftrightarrow *CHO + *$	$1.0 \cdot 10^{13} \cdot e^{-86800/RT}$	$6.73 \cdot 10^{11} \cdot T^{-3.03} \cdot e^{-103600/RT}$
r_8	$**COOH + *O \leftrightarrow *CHO + *OH + *$	$3.38 \cdot 10^{18} \cdot T^{-0.968} \cdot e^{-108900/RT}$	$1.0 \cdot 10^{15} \cdot e^{-24900/RT}$
r_9	$*CHO + 2** \leftrightarrow **CO + *H$	$1.0 \cdot 10^{11} \cdot e^{-16800/RT}$	$1.0 \cdot 10^{11} \cdot e^{-66700/RT}$
r_{10}	$**CO \leftrightarrow CO + 2*$	$2.0 \cdot 10^{12} \cdot e^{-122400/RT}$	$5.9 \cdot 10^7$
r_{11}	$2*H \leftrightarrow H_2 + 2*$	$3.1 \cdot 10^{12} \cdot e^{-97600/RT}$	$1.1 \cdot 10^8 \cdot e^{-5600/RT}$
r_{12}	$CO_2 + 2* \leftrightarrow **CO_2$	$1.0 \cdot 10^6$	$1.0 \cdot 10^{13} \cdot e^{-27300/RT}$
r_{13}	$**CO_2 + *H \leftrightarrow **COOH + *$	$1.0 \cdot 10^{13}$	$1.0 \cdot 10^{13} \cdot e^{-18400/RT}$
r_{14}	$**C \leftrightarrow C_{Ni,f} + 2*$	eq (6.1)	
r_{15}	$C_{Ni,f} \leftrightarrow C_{Ni,r}$	eq (6.3)	
r_{16}	$C_{Ni,r} \leftrightarrow C_f$	fast	
r_{17}	$3**C \rightarrow 3\ C_{encapsulating}$	$k\theta_C^3$	

A carbon filament growth mechanism [47] with formation of adsorbed surface carbon, dissolution and segregation of surface carbon, diffusion of carbon through Ni particles and precipitation of filaments is assumed. This type of carbon formation does not deactivate the catalyst. Encapsulating carbon formation deactivates the catalyst by decreasing the total number of active sites and can be described by a site conservation equation. A Langmuir equation was used to estimate the concentration of carbon in the segregation layer (6.1) and (6.2):

$$\frac{\theta_C}{1-\theta_C} = \frac{x_b}{1-x_b}\exp\left(-\frac{\Delta G_{seg}}{RT}\right) \tag{6.1}$$

where θ_C is the surface coverage of carbon, x_b is the weight fraction of carbon in the segregation layer of the nickel and $\Delta G_{seg} = -4.52 \cdot 10^4 - 14.23T$ [J/mol]

The rate of the carbon diffusion through nickel was described as:

$$r = \frac{D_C}{d_{Ni}} a_{Ni}\left(C_{Ni,f} - C_{sat}\right) \tag{6.2}$$

where r is the rate of carbon diffusion through Ni, D_C is the effective diffusivity for carbon diffusion through Ni, d_{Ni} is the effective diffusion path and a_{Ni} is the specific surface area of Ni [40].

The activation energies were used as calculated, but some of the preexponential factors were fitted to steady-state experimental data. The

reactions, on which the preexponential factors were fitted, were chosen on basis of sensitivity analysis.

Carbon formation and sintering are believed to be the most important causes for deactivation. The deactivation from carbon formation can be described by change in the surface coverage, while deactivation by sintering can be described by change in surface area. It was found that modelling based on surface area change gave a better fit of experimental data at different conditions. The estimated changes in relative surface area can be described by a general power law as shown in (6.3).

$$-\frac{d(S/S_0)}{dt} = k_s\left(\frac{S}{S_0} - \frac{S_{eq}}{S_0}\right)^2 \tag{6.3}$$

where S/S_0 and S_{eq}/S_0 are the relative surface area and relative equilibrium surface area, respectively. k_s is the sintering rate constant.

Sensitivity analysis indicated that no single rate determining step exists in methane dry reforming. Reactions r_1-r_3 and r_7-r_{10} were sensitive to methane conversion, while r_7 and r_8 were sensitive to CO_2 conversion. It was found that the Ni-C bond strength is a sensitive parameter for both reforming and carbon deposition.

Form the microkinetic model two possible routes for lowering the carbon threshold, and hence increase the catalysts carbon resistance, was found:

- Lower the surface site coverage
- Increase the filamentous carbon solubility in nickel and thus lower the driving force for carbon deposition.

6 Final remarks and suggestion for further work

Different hydrotalcite derived catalysts have been prepared and compared with Ni/CaO-Al_2O_3, Ni/α-Al_2O_3 and Ni/$CaAl_2O_4$. Characterizations showed that the hydrotalcite derived catalysts had smaller Ni particles than the conventional catalysts. The hydrotalcite derived catalyst had a higher resistance towards coking and sintering. Hydrogenolysis of ethane was used as a probe reaction for catalysts testing. Carbon formation and sintering were studied at steam reforming conditions in the TEOM and in a high pressure fixed-bed apparatus, respectively. Both the hydrogenolysis- and TEOM experiments gave an increased TOF with increased Ni particle size. From the carbon formation study in the TEOM, it seemed that the Ni crystal size had a large effect on the carbon threshold value (S/C ratio where the carbon gasification rate equals the carbon deposition rate). Increased crystal size gave an increased carbon threshold value. It was concluded that small nickel crystals resulted in a large saturation concentration of carbon giving a low driving force for carbon diffusion and hence a lower coking rate. From the sintering experiments it was found that the sintering mechanism involving particle migration was dominating for all the examined catalysts. Due to a higher degree of wetting of the substrate by the nickel particle, the catalysts with smallest nickel particles showed the highest resistance towards sintering.

According to Cavani et al. [23] a hydrotalcite structure is defined by the ratio $x = Al^{3+}/(Mg^{2+} + Al^{3+})$. A lowered distance between the hydrotalcite layers is reported with increased x value [23, 98], and hence the layer distance is expected to increase in the following order for the hydrotalcite supports: HT30 < HT50 < HT70. After Ni impregnation and

drying the interlayer distance is reported to be greater for NiO/HT30 than for NiO/HT70 [98]. Bjørgum et al. [98] explain this with an anion exchange or incorporation of Ni^{2+} in the layers. Fornasari et al. [27] and Schulze et al. [99] also report that low Mg^{2+}/Ni^{2+} ratio, as in NiO/HT30, can give incorporation of Ni^{2+} in the layers. Testing of catalysts with a lower MgO/Al_2O_3 ratio than 3/7 is recommended in order to study the relation between Mg^{2+}/Ni^{2+} and Ni particle size.

Most of the sintering experiments were stopped after 50 hours on stream. In order to check that the particle size obtained after 50 hours of is the semi-stable particle size, it would be interesting to perform experiments with a longer time scale. More frequently catalyst outtakes would be desirable in order to determine the sintering order more accurately.

Some deactivation was observed in the TEOM experiments with $NiO/CaO\text{-}Al_2O_3$ and $NiO/\alpha\text{-}Al_2O_3$. Sintering experiments performed at the same temperature and with the same catalysts as in the TEOM experiments are recommended to describe the observed deactivation from the TEOM.

References

[1] Ministry of Petroleum and Energy, Fact sheet 2004.

[2] F. Fischer and H. Tropscii, *Brennstoff-Chemie* **9** (1928) 39

[3] J. R. Rostrup-Nielsen, *Catalysis Today* **71** (2002) 243

[4] J. R. Rostrup-Nielsen, Catalytic steam reforming, in *Catalysis - Science and Technology*. (J. R. Anderson and M. Boudart, eds.), **5** Springer-Verlag, Berlin, 1984

[5] K. Aasberg-Petersen, J. B. Hansen, T. S. Christensen, I. Dybkjaer, P. S. Christensen, C. S. Nielsen, S. E. L. W. Madsen and J. R. Rostrup-Nielsen, *Applied Catalysis A: General* **221** (2001) 379

[6] J. R. Rostrup-Nielsen, *Catalysis Today* **63** (2000) 159

[7] J. R. Rostrup-Nielsen, *Catalysis Today* **18** (1993) 305

[8] J. R. Rostrup-Nielsen, J. Sehested and J. K. Norskov, *Advances in Catalysis* **47** (2002) 65

[9] J. R. Rostrup-Nielsen, T. S. Christensen and I. Dybkjaer, *Studies in Surface Science and Catalysis* **113** (1998) 81

[10] J. R. Rostrup-Nielsen, J. Sehested and J. K. Nørskov, *Advances in Catalysis* **47** (2003) 65

[11] I. Dybkjær, *Fuel Processing Technology* **42** (1995) 85

[12] J. R. Rostrup-Nielsen, L. J. Christiansen and J. H. B. Hansen, *Applied Catalysis* **43** (1988) 287

[13] H. S. Bengaard, J. K. Nørskov, J. Sehested, B. S. Clausen, L. P. Nielsen, A. M. Molenbroek and J. R. Rostrup-Nielsen, *Journal of Catalysis* **209** (2002) 365

[14] M. A. Goula, A. A. Lemonidou and A. M. Efstathiou, *Journal of Catalysis* **161** (1996) 626

[15] T. Borowiecki, *Applied Catalysis A: General* **4** (1982) 223

[16] D. Chen, K. O. Christensen, E. Ochoa-Fernández, Z. Yu, B. Tøtdal, N. Latorre, A. Monzón and A. Holmen, *Journal of Catalysis* **229** (2004) 87

[17] T. Horiuchi, K. Sakuma, T. Fukui, Y. Kubo, T. Osaki and T. Mori, *Applied Catalysis A: General* **144** (1996) 111

[18] T. Borowiecki, A. Golebiowski and B. Stasinska, *Applied Catalysis A: General* **153** (1997) 141

[19] Borowiecki, Golebiowski, Stolecki and Stasinska, *Polish Journal of Chemical Tecnology* **1** (1999) 2

[20] B. -L. Su and S. -D. Guo, *Studies in Surface Science and Catalysis* **126** (1999) 325

[21] V. R. Choudhary, B. S. Uphade and A. S. Mamman, *Catalysis Letters* **32** (1995) 387

[22] A. Bhattacharyya, V. W. Chang and D. J. Schumacher, *Applied Clay Science* **13** (1998) 317

[23] F. Cavani, F. Trifirò and A. Vaccari, *Catalysis Today* **11** (1991) 173

[24] O. Clause, M. Gazzano, F. Trifirò and A. Vaccari, *Applied catalysis* **73** (1991) 217

[25] O. Clause, M. Goncalves Coelho, M. Gazzano, D. Matteuzzi, F. Trifiro and A. Vaccari, *Applied Clay Science* **8** (1993) 169

[26] F. Trifirò, A. Vaccari and O. Clause, *Catalysis Today* **21** (1994) 185

[27] G. Fornasari, M. Gazzano, D. Matteuzzi, F. Trifirò and A. Vaccari, *Applied Clay Science* **10** (1995) 69

[28] J. R. H. Ross, *Surface and Defect Properties of Solids* **4** (1975) 34

[29] H. Morioka, Y. Shimizu, M. Sukenobu, K. Ito, E. Tanabe, T. Shishido and K. Takehira, *Applied Catalysis A: General* **215** (2001) 11

[30] A. Bhattacharyya, V. W. Chang and D. J. Schumacher, *Applied Clay Science* **13** (1998) 317

[31] T. Shishido, M. Sukenobu, H. Morioka, M. Kondo, Y. Wang, K. Takaki and K. Takehira, *Applied Catalysis A: General* **223** (2002) 35

[32] K. Takehira, T. Shishido, P. Wnag, T. Kosaka and K. Takaki, *Physical Chemistry Chemical Physics* **17** (2003) 3801

[33] J. Rostrup-Nielsen, *Journal of Molecular Catalysis A: Chemical* **163** (2000) 157

[34] I. M. Bodrov, L. O. Apel'baum and M. I. Temkin, *Kinetika i Kataliz* **9** (1968) 1065

[35] A. A. Khomenko, L. O. Apel'baum, F. S. Shub, Y. S. Snagovskii and M. I. Temkin, *Kinetika i Kataliz* **12** (1971) 423

[36] P. B. Toettrup, *Applied Catalysis* **4** (1982) 377

[37] J. Xu and G. F. Froment, *Aiche Journal* **35** (1989) 88

[38] L. M. Aparicio, *Journal of Catalysis* **165** (1997) 262

[39] D. Chen, R. Lødeng, K. Omdahl, A. Anundskås, O. Olsvik and A. Holmen, *Studies in Surface Science and Catalysis* **139** (2001) 93

[40] D. Chen, R. Lødeng, A. Anundskås, O. Olsvik and A. Holmen, *Chemical Engineering Science* **56** (2001) 1371

[41] O. Sidjabat and D. L. Trimm, *Topics in Catalysis* **11/12** (2000) 279

[42] D. L. Trimm, *Catalysis Reviews* **16** (1977) 155

[43] J. R. Rostrup-Nielsen and D. L. Trimm, *Journal of Catalysis* **48** (1977) 155

[44] D. L. Trimm, *Catalysis Today* **37** (1997) 233

[45] D. L. Trimm, *Catalysis Today* **49** (1999) 3

[46] S. Helveg, C. Lopez-Cartes, J. Sehested, P. L. Hansen, B. S. Clausen, J. R. Rostrup-Nielsen, F. Abild-Pedersen and J. K. Norskov, *Nature* **427** (2004) 426

[47] J. W. Snoeck, G. F. Froment and M. Fowles, *Journal of Catalysis* **169** (1997) 240

[48] T. P. Beebe, D. W. Goodman, B. D. Kay and J. T. Yates, *Journal of Chemical Physics* **87** (1987) 2305

[49] J. R. Rostrup-Nielsen, *Studies in Surface Science and Catalysis* **68** (1991) 85

[50] I. Alstrup and N. T. Andersen, *Journal of Catalysis* **104** (1987) 466

[51] J. R. Rostrup-Nielsen, *Journal of Catalysis* **85** (1984) 31

[52] B. J. Cooper and D. L. Trimm, *Journal of Catalysis* **62** (1980) 35

[53] I. Alstrup, B. S. Clausen, C. Olsen, R. H. H. Smits and J. R. Rostrup-Nielsen, *Studies in Surface Science and Catalysis* **119** (1998) 5

[54] J. R. Rostrup-Nielsen, J. -H. B. Hansen and L. M. Aparicio, *Sekiyu Gakkaishi* **40** (1997) 366

[55] T. Numaguchi, K. Shoji and S. Yoshida, *Applied Catalysis A: General* **133** (1995) 241

[56] K. Ahmed, L. Kershenbaum and D. Chadwick, *Chemical Engineering Science* **44** (1989) 999

[57] L. E. Alzamora and J. R. H. Ross, *Journal of Chemical Society* **77** (1981) 665

[58] P. Marginean and A. Olariu, *Applied Catalysis A: General* **140** (1996) 59

[59] I. Chen and F. Chen, *Industrial & Engineering Chemistry Research* **29** (1990) 534

[60] A. C. S. C. Teixeira and R. Giudici, *Chemical Engineering Science* **54** (1999) 3609

[61] J. Sehested, A. Carlsson, T. V. W. Janssens, P. L. Hansen and A. K. Datye, *Journal of Catalysis* **197** (2001) 200

[62] A.C.S.C.Teixeira and R.Giudici, *Stud Surf Sc Catal* **139** (2001) 495

[63] J.Lif, M.Skoglundh and L.Lövendahl, *Applied Catalysis A: General* **228** (2002) 145

[64] C. H. Bartholomew, *Applied Catalysis A: General* **107** (1993) 1

[65] J. Sehested, J. A. P. Gelten, I. N. Remediakis, H. Bengaard and J. K. Nørskov, *Journal of Catalysis* **223** (2004) 432

[66] C. H. Bartholomew and W. L. Sorensen, *Journal of Catalysis* **81** (1983) 131

[67] J. Sehested, *Journal of Catalysis* **217** (2003) 417

[68] J. T. Richardson and J. L. Propp, *Journal of Catalysis* **98** (1986) 457

[69] T. Numaguchi, K. Shoji and S. Yoshida, *Applied Catalysis A: General* **133** (1995) 241

[70] F. B. Rasmussen, J. Sehested, H. T. Teunissen, A. M. Molenbroek and B. S. Clausen, *Applied Catalysis A: General* **267** (2004) 165

[71] K. -T. Kim and S. Ihm, *Journal of Catalysis* **96** (1985) 12

[72] H. K. Kuo and R. J. De Angelis, *Journal of Catalysis* **68** (1981) 203

[73] H. K. Kuo, P. Ganesan and R. J. De Angelis, *Journal of Catalysis* **64** (1980) 303

[74] J. T. Richardson and J. G. Crump, *Journal of Catalysis* **57** (1979) 417

[75] S. E. Wanke, *Journal of Catalysis* **46** (1977) 234

[76] P. Wynblatt and N. A. Gjostein, *Progress in Solid State Chemistry* **9** (1975) 21

[77] H. L. Gruber, *Journal of Physical Chemistry* **66** (1962) 48

[78] F. J. Bröcker, W. Dethlefsen, K. Kaempfer, L. Marosi, M. Schwarzmann, B. Triebskorn and G. Zirker, *German Patent 2,255,909* (1972), *to BASF AG*

[79] C. Komodomos, N. Parkyns and A. Williams, *UK Patent 1,550,749* (1977), *to British Gas Co*

[80] K. O. Christensen, D. Chen, R. Lødeng and A. Holmen, *Submitted.*

[81] J. R. Rostrup-Nielsen, *Journal of Catalysis* **21** (1971) 171

[82] J. R. Rostrup-Nielsen and I. Alstrup, *Catalysis Today* **53** (1999) 311

[83] J. H. Sinfelt, *Advances in Catalysis***23** (1973) 91

[84] R. D. Cortright, R. M. Watwe, B. E. Spiewak and J. A. Dumesic, *Catalysis Today* **53** (1999) 395

[85] A. V. Zeigarnik and O. N. Myatkovskaya, *Kinetics and Catalysis (Translation of Kinetika i Kataliz)* **42** (2001) 418

[86] G. C. Bond, A. D. Hooper, J. C. Slaa and A. O. Taylor, *Journal of Catalysis* **163** (1996) 319

[87] D. S. Jackson, G. J. Kelly and G. Webb, *Physical Chemistry Chemical Physics* **1** (1999) 2581

[88] W. F. Taylor, J. C. Yates and J. H. Sinfelt, *Journal of Physical Chemistry* **68** (1964) 2962

[89] D. Chen, A. Grønvold, H. P. Rebo, K. Moljord and A. Holmen, *Applied Catalysis A: General* **137** (1996) L1

[90] E. Bjørgum, D. Chen, K. O. Christensen, R. Lødeng and A. Holmen, *Submitted.*

[91] J. L. Lemaitre, P. G. Menon and F. Delannay, *Characterisation of heterogenous catalysts*. (F. Delannay, ed.), **15** Marcel Dekker inc, New York, 1984

[92] J. W. Niemantsverdriet, Spectroscopy in Catalysis. Wiley-VCH, Weinheim, 2000.

[93] E. A. Blekkan, A. Holmen and S. Vada, *Acta Chemica Scandinavica* **47** (1993) 275

[94] J. L. Carter, J. A. Cusumano and J. H. Sinfelt, *Journal of Physical Chemistry* **70** (1966) 2257

[95] D. W. Goodman, *Catalysis Today* **12** (1992) 189

[96] M. Che and C. O. Bennett, *Advances in Catalysis* **36** (1989) 55

[97] Richardson, J T, R. M. Scates and M. V. Twigg, *Applied Catalysis A: General* **267** (2004) 35

[98] E. Bjørgum, D. Chen, M. G. Bakken, K. O. Christensen, A. Holmen, O. Lytken and I. Chorkendorff, *Journal of Physical Chemistry B.* **109(6)** (2005) 2360

[99] K. Schulze, W. Makowski, R. Chyy, R. Dziembaj and G. Günter, *Applied Clay Science* **18** (2001) 59

Paper I

Effect of crystal size on carbon formation and sintering of hydrotalcite derived Ni-catalysts

Effect of Crystal Size on Carbon Formation and Sintering of Hydrotalcite Derived Ni-catalysts

K.O. Christensen[a], D. Chen[a], R. Lødeng[b] and A. Holmen[a]

[a] Department of Chemical Engineering, Norwegian University of Science and technology (NTNU), N-7491 Trondheim, Norway.

[b] SINTEF Applied Chemistry, N-7465 Trondheim, Norway.

Abstract

Steam methane reforming was studied over both conventional NiO/α-Al_2O_3 and NiO/CaO-Al_2O_3 catalysts and catalysts supported on hydrotalcite derived materials. Catalyst activity, coke formation and deactivation at steam reforming conditions were studied using the tapered element oscillating microbalance (TEOM). Steam reforming was studied at 823K, a total pressure of 20 bar and steam to carbon ratios from 0.08 to 2.4.

Nickel supported on hydrotalcite derived materials had a smaller crystal size and a higher resistance to coke formation than the conventional NiO/α-Al_2O_3 and NiO/CaO-Al_2O_3. The higher resistance to carbon formation could be due to a higher saturation concentration of carbon in the smaller nickel crystals.

Sintering experiments were performed at 903K and 20 bar on the hydrotalcite derived catalysts and compared with an industrial NiO/$CaAl_2O_4$ catalyst. The particle growth for the hydrotalcite derived catalysts was larger than for the industrial catalyst, but the hydrotalcite derived catalysts had the smallest size of stabilized Ni crystals.

1. Introduction

Methane can be converted into synthesis gas by steam reforming, CO_2 (dry) reforming or by conversion with O_2 through secondary reforming and partial oxidation [1]. When hydrocarbons are exposed to high temperatures, carbon formation might occur. In the production of synthesis gas carbon may be formed by decomposition of methane (1.1) (or higher hydrocarbons) or by the Boudouard reaction (1.2):

$$CH_4 \rightleftarrows C+2H_2 \qquad \Delta H^o_{298} = \quad 75kJ/mol \tag{1.1}$$

$$2CO \rightleftarrows C+CO_2 \qquad \Delta H^o_{298} = -172kJ/mol \tag{1.2}$$

Steam reforming reactions are usually carried out on supported nickel catalysts [1]. Nickel catalyses both the steam reforming reactions and the carbon formation reactions. Well-defined carbon structures are documented to be formed on the nickel surface. Distinguishable morphologies include filamentous carbon, encapsulating carbon and pyrolytic carbon. Filament growth causes no immediate deactivation, but may result in a mechanical breakdown of the catalyst pellets [2-4]. A high steam to carbon (S/C) ratio in the feed can be used to control the carbon formation, but in commercial operation this means higher production costs. Modifications of the catalyst by introducing alkali metals [2] or gold [5] can improve the carbon resistance of the catalyst. Hydrotalcites or mixed oxides have also shown to be more resistant to both coke formation [6] and sintering [7] than commercial catalysts supported on alumina.

Hydrotalcites are presented by the following general formula (2.1) [6]:

$$[M^{2+}_n M^{3+}_m (OH)_{2(n+m)}]^{m+} A^{x-}_{m/x} \times yH_2O \tag{1.3}$$

where: M^{2+} and M^{3+} are metal cations, A is an anion, x is the charge of the anion, n>m and y is the number of interlayer water molecules. When heated, the hydrotalcites dehydrate and loose their characteristic structure. At about 473K, the interlayer water leaves and about 723K, the layered hydroxides dehydrate. The dehydrated material retains the memory of the layered structure, but if the material is heated above 1023K an irreversible change occurs and a complex mixture of oxides, mixed oxides, spinels, etc. begins to form [6]. The mixed oxide obtained by calcination has high surface area, basic properties and form homogenous mixtures of oxides with small crystal size, which by reduction form small and thermally stable metal crystals [8].

As early as in 1975 Ross [9] published a review article where he recognized that coprecipitated Ni, Al based catalysts satisfied all the requirements for steam reforming of methane. In the review article from Cavani et al. [8] catalysts from hydrotalcite

precursors are reported to be both active and stable during steam reforming. Morioka et al. [10] reported high activity and high sustainability against coke formation during partial oxidation of methane to syngas. For the same reaction Shishido et al. [11] reported high activity for impregnated hydrotalcite catalysts and catalysts prepared by the solid phase crystallization (spc) method. Clay-derived catalysts exhibited superior activity and stability compared to Ni/Al_2O_3 and $Ni/MgAl_2O_4$ during CO_2 reforming of methane to syngas, Bhattachatyya et al. [12]. Takehira et al. [13] found that spc-Ni/MgAl catalysts were active and stable for steam reforming of CH_4 into synthesis gas. No deterioration in the catalytic activity was observed for 600 h of reaction time, while a commercial Ni/Al_2O_3 catalyst showed a clear activity decline during the same period of time on stream.

The Ni particle size seems to be an important factor for steam reforming catalyst activity. Smaller particles will provide a larger surface for reaction and hence improved catalyst activity. But also other aspects concerning the particle size are important. Smaller NiO crystals are known to have more steps and kinks on the surface than larger crystals, and hence a larger turnover rate [14-15]. Smaller particle have been reported to be more resistant to carbon formation. Carbon formation is a structure sensitive reaction and not able to proceed at all when the crystals are below a critical size [14]. Borowiecki [16] reported a higher carbon deposition rate on larger Ni particles during steam reforming of butane. The author explains the correlation between particle size and coking rate with a model where spillover of steam adsorbed on the surface of the support is the key point. Chen et al. [17] found that the size of the nickel crystal had an influence on both coking rate and the ability of initiation or nucleation of carbon nano-fibers (CNF) from methane decomposition.

In addition to carbon formation, sintering is an important mechanism for catalyst deactivation. Sintering may result from loss of catalytic surface due to crystallite growth, loss of support area due to support collapse or a combination of the two processes. Several studies on sintering of nickel particles are reported [18-25]. The most important factors that may influence the sintering process are: Particle size, structure and composition of the support, reaction temperature and the reaction atmosphere. Both increasing temperature and especially the presence of steam increase the sintering [20].

The purpose of the present work is to compare the carbon as well as the sintering resistance of conventional Ni based catalysts with Ni supported on hydrotalcite derived compounds with Al and Mg as cations. The effects of the Ni crystal size on carbon formation and sintering during steam reforming are specially addressed.

2. Experimental

2.1 Catalyst preparation

Three different commercial hydrotalcites from Condea were used as supports: HT30 (MgO/Al_2O_3 = 3/7), HT50 (MgO/Al_2O_3 = 5/5) and HT70 (MgO/Al_2O_3 = 7/3). These materials were compared with standard supports like $CaO\text{-}Al_2O_3$ and $\alpha\text{-}Al_2O_3$. $CaO\text{-}Al_2O_3$ was prepared by mechanical mixing, and the molar ratio was CaO/Al_2O_3=1/2. The mixture was calcined at 1423K at a heating-rate of 200K/h. $\alpha\text{-}Al_2O_3$ was prepared by heating $\gamma\text{-}Al_2O_3$ at a rate of 200K/h up to 1423K. The final temperature was held for 5h, in both cases.

The supports were impregnated with nickel-nitrate by the incipient wetness technique to obtain 12.5 weight present nickel on the carrier. The catalysts were dried overnight at 373K and calcined at 873 or 1173K at a heating rate of 4K/min and the final temperature was held for 4h. $Ni/CaAl_2O_4$ is an industrial reforming catalyst with 11 weight percent nickel supported on $CaAl_2O_4$. This catalyst has only been used in the sintering experiments. The composition, BET surface area and calcination temperature of the different catalysts are given in Table 1.

2.2 Sample characterisation

2.2.1 X-ray diffraction (XRD)

X-ray diffraction studies were performed in a Simens D5000 X-ray diffractometer using monochromatic Cu Kα radiation. Phase identifications were carried out by comparing the collected spectra in the database. The measurements were done on calcined catalysts and average Ni crystal sizes were calculated using the Scherrer formula based on peak broadening [26].

2.2.2 Temperature programmed reduction (TPR)

The TPR experiments were performed in a quartz micro reactor heated by an electrical furnace. The experiments involved heating of 0.2g catalyst at a rate of 4K/min to 1173K with a gas consisting of 7% H_2 in Ar. The H_2 consumption was measured by analyzing the effluent gas with a thermal conductivity detector. The steam formed during reduction was removed by a cooling trap.

2.2.3 Transmission electron microscopy (TEM) and scanning transmission electron microscope (STEM)

A JEOL 2000EXII high resolution transmission electron microscopy was used to study the diameter of the nickel particles. TEM specimens were prepared by ultrasonic dispersion of the slightly ground catalyst samples in chloroform, and then a drop of the suspension was applied to a holey carbon copper grid.

For STEM experiments the JEOL 2000EXII electron microscope was equipped with a field emission gun capable of giving a lattice resolution of 0.14 nm. Both bright field and annual dark field images of the catalysts were performed to get a better contrast of Ni particles against support materials.

2.2 Tapered element oscillating microbalance (TEOM)

Catalyst activity, carbon formation and deactivation at steam reforming conditions have been studied using the TEOM. The TEOM setup which has been described in detail previously [27], is a powerful technique for studying activity and coke formation simultaneously by coupling with on line GC [28].

The catalyst loading was about 8mg and it was diluted with approximately 100mg α-Al_2O_3. Both catalyst and diluent had a particle size in the range of 0.25-0.50mm. The catalyst bed was held in place by α-Al_2O_3 wool and the product was analyzed on-line by a HP5890 II GC with a carbosieve S-II column and TCD.

The catalyst was reduced with a mixture of 1/1 H_2/Ar at increasing temperature from ambient to 923K at a rate of 2K /min. The final reduction temperature was held for 6h and, lowered to the reaction temperatures of 823K or 873K.

Steam reforming reaction was started after first stabilizing the flow of steam in presence of a sufficient amount of H_2 to keep the catalyst reduced. At stable conditions the hydrocarbon was fed and the flow of H_2 stopped. Steam reforming was studied at 823K and 873K, a total pressure of 20 bar and steam to carbon ratios of 0.08 to 2.4.

Dynamical experiments were performed to study the effect of the S/C ratio on carbon formation at a constant temperature. Coke formation was initiated at a low S/C ratio. The S/C ratio was thereby stepwise increased until coke gasification was observed. The carbon threshold value is defined as the steam to carbon ratio that gives no observed carbon formation; the gasification rate equals the rate of the carbon formation [29]. From the carbon threshold values, found from the dynamic experiments, the relative carbon resistance for each catalyst could be found.

2.3 High pressure sintering

Catalyst activity and deactivation have been studied in a high pressure fixed-bed reactor. The set-up consists of three main sections: the feed section, the reactor section and the analyzing section. In the feed section water from a tank is pressurized by a pump, diluted by Ar and led in to a vaporizer before it mixes with the rest of the feed gasses. The reactor section consists of a stainless steel tube reactor (length: 410 mm, inner diameter: 7 mm and outer diameter: 10 mm) heated by an electrical furnace. The catalyst bed is positioned in the middle of the tube reactor. A catalyst loading of about 3g with particle size in the range of 0.25-0.50mm was used. The catalyst was held in place by Al_2O_3 wool and the product was analyzed by an on line GC with TCD.

Prior to the sintering experiments the catalyst was reduced in a mixture of 1/1 H_2/Ar at increasing temperature from ambient to 943K. The heating rate was 3K/min and the final reduction temperature was held for about 14h before lowering to the reaction temperature at 903K. Sintering experiments were performed both with and without methane in the reaction mixture, at a total pressure of 20 bar and a partial

pressure of steam equal to 9.6 bar. Sintering condition I: $H_2O/CH_4/Ar$ (1/0.51/0.57) and sintering condition II: $H_2O/H_2/Ar$ (1/0.23/0.85)

1g catalyst was removed from the reactor 20/24, 48/50 and 74h after the sintering was started, respectively. After each catalyst removal, the remaining catalyst was reduced and sintered at the conditions described above. The sintered catalysts were examined by XRD in order to determine the NiO crystal size. Prior to the XRD experiments the catalysts were oxidized in air at 723K for 2h. The heating rate from ambient to 723K was 10K/min.

3. Results and discussion

3.1 X-ray diffraction

The NiO crystal sizes calculated from the Scherrer equation are presented in Table 2. The crystal size measured by XRD is in accordance with the crystal size measured by chemisorption and TEM, the results are reported elsewhere [17, 30, 31]. The results from Table 2 show that $NiO/\alpha\text{-}Al_2O_3$ and $Ni/CaAl_2O_3$ have remarkably larger NiO crystals than the other catalysts. An increase in the crystal size with increasing MgO/Al_2O_3 ratio in the mixed oxide support is observed. Chen et al. [17] reported that, with exception of NiO/HT30, the surface area of Ni on different catalysts was proportional to the surface area of the supports. The Ni surface area for NiO/HT30 is much higher than on the other catalysts. Chen et al. proposed that the incorporation of Ni in the hydrotalcite structure, which has also been reported by Bjørgum et al. [31], causes the formation of smaller Ni particles and hence a larger Ni surface area.

The XRD profiles of the hydrotalcite supports have been discussed in detail by Bjørgum et al. [31]. It was reported that the XRD profile for HT70 fitted nicely a hydrotalcite structure, while the XRD profiles for HT50 and HT30 fit better to a hydrotalcite derived compound.

After calcination at temperatures of 873 and 1173K, NiO/HT30, -50 and –70 have all lost their hydrotalcite structure and become mixed oxides [12]. The XRD profiles in Figure 1 indicate that neither Al_2O_3, MgO nor Al_2MgO_4 exists in NiO/HT50 and NiO/HT70 (873). In the NiO/HT30 profile there are double peaks at 45 and 65°, indicating mixed metallic oxides or a spinel phase ($NiAl_2O_4$ or $MgAl_2O_4$). The large

peak at 45˚ could also be Ni metal. The peaks at 45 and 65˚ for NiO/HT70 (1173) give indication of a spinel phase, either $NiAl_2O_4$ or $MgAl_2O_4$. Overlapping peaks makes it difficult to distinguish between NiO, MgO and Ni/MgO at 37, 43, 63 and 79˚.

The XRD profile for NiO/CaO-Al_2O_3 is affected by noise, but it is possible to mark out peaks for NiO, Al_2O_4, CaO and Ca-Al-O spinel. The characteristic NiO peaks are found at 37, 63, 75 and 79˚. It seems that most of the Al_2O_3 has formed a spinel phase with the CaO. This formation has suppressed the formation of $NiAl_2O_4$ and hence indication of a spinel phase, either $NiAl_2O_4$ or $MgAl_2O_4$. Overlapping peaks makes it difficult to distinguish between NiO, MgO and Ni/MgO at 37, 43, 63 and 79˚.

The XRD profile for NiO/CaO-Al_2O_3 is affected by noise, but it is possible to mark out peaks for NiO, Al_2O_4, CaO and Ca-Al-O spinel. The characteristic NiO peaks are found at 37, 63, 75 and 79˚. It seems that most of the Al_2O_3 has formed a spinel phase with the CaO. This formation has suppressed the formation of $NiAl_2O_4$ and hence no indication of $NiAl_2O_4$ is observed in this catalyst.

The NiO/α-Al_2O_3 profile has NiO peaks at 37, 63, 75 and 79˚ and $NiAl_2O_4$ peaks at 45, 60, and 66˚. The remaining peaks are probably from Al_2O_4. The NiO peak at 43˚ is sharp and narrow, indicating rather large crystals.

3.2 Temperature programmed reduction

TPR profiles for the different catalysts are shown in Figure 2. NiO/HT30, NiO/HT50 and NiO/HT70 (873) have two reduction peaks. The low temperature peaks are in the area of 690-775K, while the high temperature peaks are located at 1080-1115K. The low temperature reduction peaks increase in size with increasing Mg/Al ratio in the catalysts. The high temperature peak is of the same size for NiO/HT70 (873) and NiO/HT50, but much larger for NiO/HT30. Compared to NiO/HT70 (873) and NiO/HT50, the low temperature peak for NiO/HT30 appears at a higher temperature whereas the second peak is located at a lower temperature.

NiO/HT70 (1173), NiO/CaO-Al_2O_3 and NiO/α-Al_2O_3 have several overlapping reduction peaks. NiO/HT70 (1173) has main peaks at 700K, with a shoulder to the left at 630K, and at 1100K. The peak at 700K has. Between the two main peaks there is also a top at 873K. The TPR profile for NiO/CaO-Al_2O_3 shows at least four overlapping peaks with the first peak at about 675K and the last at 1000K. NiO/α-Al_2O_3 has the

most complex TPR profile with at least six different peaks. The first peak has a maximum at 530K and the last at 1100K.

For the NiO/HT30, -50 and -70 the low temperature peak results from reduction of Ni^{2+} in the NiO phase [11], while the high temperature peak most likely corresponds to the Ni^{2+} in the mixed metal oxide phase ($Mg_xN_{1-x}O$) [32]. However, it could also be that the high temperature peak corresponds to $NiAl_2O_4$ [33]. The XRD profiles of NiO/HT30 and NiO/HT50 do not give any indication of $NiAl_2O_4$ in the catalysts, but such compounds could be present as very finely divided spinel phases that are to small to be detected by X-ray diffraction [34]. Schulze et al. [32] found that calcined hydrotalcites containing Al, Mg and Ni had only one reduction peak, corresponding to the Ni^{2+} in the mixed metal oxide phase. They also reported that the reduction peak shifted towards lower temperatures as the nickel / magnesium ratio in the hydrotalcites was decreasing, in agreement with the slightly lower temperature for the high temperature reduction peak for NiO/HT30.

Figure 2 shows that NiO/HT30 is more difficult to reduce than the other HT catalysts, and that the fraction of NiO is much lower. This could be explained by incorporation of Ni into the hydrotalcite structure [17, 31]. Richardson [35] observed a decrease in the NiO crystal size with increasing reduction temperature. NiO/HT30 has smaller NiO crystal size than the other catalysts, which might result in a higher temperature required to reduce it.

As shown in Figure 2 an increase in the calcination temperature form 873K to 1173K results in a more complex reduction profile. If the shoulder on the first peak for NiO/HT70 (1173) is ignored, NiO/HT70 (873) and NiO/HT70 (1173) seem to be reduced in the same temperature range. The main difference is the number of peaks which indicates that the NiO in NiO/HT70 (1173) is bounded to the support at different strengths.

The first peak in the TPR profile of NiO/CaO-Al_2O_3 indicating the presence of Ni^{2+} in the NiO phase [11], while the last peaks give indication of different calcium-alumina oxides [36]. It is known that the reduction of $NiAl_2O_4$ occurs at slightly higher temperatures than what is observed from the TPR profile [7]. In agreement with the results from XRD, the TPR profile gives no indication of $NiAl_2O_4$ in NiO/CaO-Al_2O_3. Jung et al. [37] found that CaO had no effect on the reduction of nickel species.

The interaction between NiO and NiO/α-Al_2O_3 is normally weak, but as observed in Figure 2 the high calcination temperature at 1173K has lead to severe interactions. For NiO/α-Al_2O_3 the first peak indicates NiO while the last peak indicates $NiAl_2O_4$. The temperature maxima for these two peaks are close to the reduction temperature for bulk NiO and $NiAl_2O_4$ [38]. The other peaks may correspond to dissolution of Al^{3+} into the NiO crystals, which increase the reduction temperature for NiO [38, 39]. Another explanation could be that the NiO crystals vary in size, and that the smaller crystals are more difficult to reduce [35]. The α-Al_2O_3 was prepared from γ-Al_2O_3. Due to a possible temperature gradient in the reactor during preparation of α-Al_2O_3, some of the γ-Al_2O_3 could still be present in the catalyst after the preparation. γ-Al_2O_3 in the catalyst could lead to formation of $NiAl_2O_4$ during calcination of the impregnated catalyst.

3.3 Steam methane reforming in TEOM

The CH_4 conversion and carbon formation at 823K and different steam to carbon ratios are given for NiO/HT70(1173) in Figure 3. The figure shows that the carbon formation is easily initiated at S/C=0.3 and that the rate for carbon formation decreases with increasing S/C ratio from S/C=0.3 to S/C=1.0. At a S/C ratio of 1.25 gasification of the carbon is observed. It was more difficult to initialize carbon formation on NiO/HT30 than on the other catalysts. A low S/C ratio of 0.08 has been used to initialize the carbon formation on NiO/HT30, but for the other catalysts carbon growth could be initialized at S/C=0.3. For both NiO/HT50 and NiO/CaO-Al_2O_3 an induction period were observed.

It has been found that carbon formation depends significantly on the catalyst properties [16, 17]. As pointed out previously the Ni crystal size has a dominating effect on the carbon formation. Coking rates are presented in Figure 4 as a function of the Ni crystal size at different S/C ratios. The relation between the nickel crystal size and the carbon formation rate is in agreement with the results from steam reforming of butane reported by Borowiecki [16]. Borowiecki explains the correlation between the crystal size and the coking rate with a model where spillover of steam adsorbed on the surface of the support is the key point. According to Borowiecki hydrocarbons undergo chemisorption on the metal, while steam chemisorbs on the carrier. The chemisorption

of steam occurs in the vicinity of metal crystals on the carrier surface. The amount of chemisorbed steam is a function of the surface affinity of the carrier towards steam and the partial pressure of the latter in the gas phase. As the partial pressure of steam increases with increased S/C ratio, the amount of water chemisorbed in the vicinity of the nickel crystals also increases. Borowiecki suggests that a certain surface concentration of steam (p^s_{min}) over the nickel crystals is needed in order to ensure gasification of the hydrocarbon intermediates over transformation of these intermediates into carbon deposits. When the S/C ratio increases, the surface concentration of steam reaches the p^s_{min} value and the size of the crystals, on which coking can be inhibited, simultaneously increases.

The effect of crystal size on filamentous carbon growth has been observed by Rostrup-Nielsen [40] who has reported an equation for the free energy, ΔG_C, deviation from graphite. The value reflects the excess energy of the carbon formed compared to that of graphite (3.1).

$$\Delta G_C = \frac{\gamma \times M}{\rho} \times \frac{1}{D} + \mu^* \qquad (3.1)$$

where γ is the surface tension, M is the molecular weight, ρ is the density, D is the diameter of the carbon filament and μ^* is the contribution from structural defects compared to graphite. The deviation between graphite and the carbon filament becomes smaller as the diameter increases. Geus et al. [41-43] have reported that the deviation from the graphite equilibrium is explained by the formation of unstable carbide intermediates. At a surface with smaller crystals the average energy barrier for filament formation will be higher than on a surface with larger crystals. It must also be noted that the carbon formation reaction is structure sensitive and not able to proceed at all when the crystals are below a critical size [14].

The mechanism for carbon whisker growth involves several steps [4, 44, 45]. Methane is adsorbed on the surface, and is through surface reaction converted into adsorbed carbon. These steps are followed by segregation of surface carbon into the layers near the surface. The carbon diffuses through the Ni and precipitates on the rare

side of the Ni crystal. The growing whisker will lift the Ni particle at the tip. Recently, Helveg et al. [46] suggested that the carbon is transported along the graphene-Ni interface. They performed *in situ* transmission electron microscopy (TEM) studies of the formation of carbon nanofibers from methane decomposition over supported nickel nanocrystals. An elongation/contraction of the nickel crystal during the carbon growth was observed. Graphene layers were formed around the nickel crystal leading to a change in the adsorption energy of C and Ni adatoms. The graphene overlayer helped the formation of Ni steps, and hence, the release of Ni adatoms, which could diffuse along the interface towards the free surface. C adatoms at the interface were destabilized. The transport of C adatoms from the free surface to sites at the graphene-Ni interface was described by the following steps: Breaking of the C-bond to the Ni-step on the free surface, incorporation under the graphene sheet and diffusion at the graphene-Ni interface.

Chen et al. [17] found that the size of the nickel crystal had an influence on both the coking rate and the ability of initiation or nucleation of carbon nanofibers (CNF) from methane decomposition. Indication of lower coking rate on the smaller sized Ni crystals was observed. They also reported that initiation or nucleation of CNF was more difficult on the smaller sized Ni crystals. Chen et al. [17] discussed the growth of CNF and calculated the equilibrium constant for carbon precipitation as a function of the Ni crystal size. The results indicated that the effect of the Ni crystal size, especially for crystals less than 60nm, was strong. Chen et al. [17] also suggested that a small crystal size of Ni will provide a large surface area for the surface reactions, a higher diffusion flux and a shorter diffusion length. This would lead to a high coking rate. On the other hand will a small crystal size also result in a large saturation concentration leading to a low driving force of carbon diffusion and hence a lower coking rate. Goula et al. reported that smaller crystals have a more open metal surface [15] which would lead to higher coking rates.

The relation between the crystal size and the coking threshold shown in Figure 5 is a result of all the factors mentioned above. Figure 4 shows that an increasing coking rate is observed as the crystal size increases. This indicates that the large saturation concentration of CNF is the most dominating factor for the growth of carbon fibers. The increasing turnover frequency (TOF) with increasing crystal size reported in Figure 6,

supports the above statement. According to the H_2O spillover theory, smaller crystals would have a higher partial pressure of steam on the surface. This would lead to an increased conversion of methane, and hence an increased TOF. The opposite of what is shown in Figure 6. In addition, a strong dependence of coking rate on the Ni crystal size in the absence of steam indicates that the spillover theory is unlikely.

From the above discussion it is reasonable to assume that the saturation concentration of carbon in the nickel crystals is the main contribution to the difference in the coking threshold. It also explains well our observation of difficult nucleation of filamentous carbon on the smallest Ni crystals of NiO/HT30. On the other hand, effects from the support could not completely be excluded. MgO in the support material could favor coke gasification and hence decrease the carbon formation. This would be in accordance with results from Houruchi et al [47] who reported that basic metal oxides make the catalyst suppress the carbon deposition.

With time on stream the catalysts may sinter or the carbon deposit on the catalyst may lead to reconstructions of the active nickel. Beebe et al. [48] found that the activation energy for dissociative adsorption of methane was structure sensitive, with an activation energy on Ni(110) and Ni (111) being higher than on Ni (100). A change like this in the catalyst structure could affect the carbon threshold value. Therefore the reported carbon threshold value might only be valid for a narrow range for the time on stream. As shown in Figure 5 the carbon threshold value depends on the NiO crystal size. If the catalysts sinter it is likely to assume that the NiO crystal size increases and hence the carbon threshold value also increases.

As shown in Figure 6 increasing S/C ratios give increasing TOF values for the HT-catalysts. However, deactivation may contribute to the observed TOF for NiO/CaO-Al_2O_3 and NiO/α-Al_2O_3. For these catalysts an increase in the S/C ratio gives a decrease in TOF. Explanations for the deactivation could be encapsulating coke formation, sintering, nickel oxidation, change in bulk- and surface site defects. High saturation concentration level of carbon in the Ni crystals may lead to formation of encapsulating coke due to high surface coverage of carbon. This will result in a deactivation for the HT-catalysts, which have the smallest crystal sizes. According to the results form steam methane reforming in the TEOM this was not the case. No deactivation is observed for these catalysts. The Tamman temperature for nickel, about 690K [20], is considered to

be a critical temperature for the nickel stability in an inert atmosphere. In the presence of steam, however, the critical temperature is significantly lowered [20]. It is likely to assume that sintering is the main deactivation cause, but a combination of the deactivation factors mentioned above could not be excluded. A surprising result was that turnover frequency increased with increasing particle size of NiO. Smaller NiO crystals have more steps and kinks on the surface than larger crystals, and hence a larger turnover rate [14]. Rostrup-Nielsen [49], also reported increasing TOF with increasing particle size and suggests that some surface inhomogeneities may have occurred on the large crystals. Frusteri et al. [50] reported an exponential increase in TOF as the NiO particle size increased during steam reforming of bio-ethanol and it was suggested that this coud be caused by a structure-sensitive ethanol dehydrogenation. For a dispersion of 60% or higher, Notheisz et al. [51] observed a decreased TOF with increasing dispersion for hydrogenolysis of methyloxirane. They concluded that this was due to structure sensitivity related to the clean metal surface and to the metal-hydrogen system.

When the reaction temperature for the steam methane reforming was increased from 823K to 873K the carbon threshold value for NiO/HT50 increased from 0.8 to 1.1, while the carbon threshold value for NiO/HT30 decreased from 0.4 to 0.2. At steady-state, the coking rate equals the rate of carbon diffusion through the Ni particles described by the following expression:

$$r = \frac{D_C}{d_{Ni}} a_{Ni} \left(C_{C\_Ni,f} - C_{C\_Ni,r} \right) \tag{3.2}$$

where D_C is the effective diffusivity for carbon diffusion through the nickel particle, d_{Ni} is the effective length of carbon diffusion in the Ni particles, a_{Ni} is the specific surface area of Ni, $C_{C\_Ni,f}$ is the carbon concentration on the front side of the Ni particles and $C_{C\_Ni,r}$ is the carbon concentration on the rare side of the Ni particles. Both $C_{C\_Ni,f}$ and $C_{C\_Ni,r}$ are functions of the temperature and the final dependence of carbon formation on the temperature is a combination of those two factors. Different temperature dependence on carbon formation and carbon threshold on NiO/HT30 and NiO/HT50 could then be explained by the different trends on the driving force of carbon diffusion when the temperature was increased from 823K to 873K.

3.4 High pressure sintering

The NiO crystal size was calculated from XRD using the Scherrer equation and XRD profiles for the sintered catalysts are given in Figure 7 (a) to (d). It is reported in literature that the dispersion and particle size generally approach a limiting value with time on stream [18-20, 22, 52], in accordance with the results presented here. Figure 8 shows that all the experiments seem to give the same trend for the increase in particle size with time on stream. Initially a rather rapid particle growth is observed, but the growth levels out with time. However, the increase in particle size varies form catalyst to catalyst and also with the sintering atmosphere.

Generally speaking, small Ni crystals and the presence of steam enhance the sintering. Ni/$CaAl_2O_4$ has originally the largest particles, but the particles increase the least during sintering most probably due to the large original particle size of Ni/$CaAl_2O_4$ [53]. After 50h in H_2O/H_2/Ar (1/0.23/0.85) (condition I, Table 3), an 8% increase in the particle size is observed. NiO/HT30 has originally the smallest particles and the particle size on this catalyst doubles after 50h at condition I. On fresh catalysts the NiO particle size are 12, 24 and 65 for NiO/HT30, NiO/HT50 and Ni/$CaAl_2O_4$, respectively. After 50h at condition I, the NiO particle size had increased to 24, 29 and 70 for NiO/HT30, NiO/HT50 and Ni/$CaAl_2O_4$, respectively.

Different sintering behavior can be caused by difference in particle size, surface area or metal-support interactions. According to Bartholomew [20] and Richardson et al [54] well dispersed catalysts show a higher ability to sinter because small particles are more mobile. A higher surface area of the support will provide more surface for emission of metal atoms, and hence more sintering. From Table 1 and Figure 8 it is shown that increasing the initial surface of the support and decreasing the NiO particle size give increased sintering. The BET surface areas reported in Table 3 show that the surface area for NiO/HT30 and NiO/HT50 sintered in a H_2O/H_2/Ar (1/0.23/0.85) (condition I) for 50h is almost identical, 30m^2/g (10% of the initial BET surface area) and 26m^2/g (15% of the initial BET surface area), respectively. Ni/$CaAl_2O_4$ has the smallest BET surface area after 50h at condition I, 3.3m^2/g (60% of the initial BET surface area). Neither the particles size nor the BET surface area changes dramatically during the sintering experiments over Ni/$CaAl_2O_4$. The reason for this could be that the

surface area is already so small that a further area-reduction is difficult. The size of the NiO particles on Ni/$CaAl_2O_4$ indicates that the particles are rather immobile [53]. Higher dispersion or higher BET surface area gives increased sintering, but after 50h NiO/HT30 (with initial highest dispersion and BET surface area) still have the highest dispersion. This could be due to stronger metal-support interactions for this catalyst, and will be further discussed later in this section.

From the XRD profiles of the sintered catalysts, Figure 7, it is observed a larger change of the $NiAl_2O_4$ / Al_2MgO_4 peaks during sintering of NiO/HT30 than for NiO/HT50. The peaks are much larger for NiO/HT30 already after 24h of sintering. This could indicate formation of $NiAl_2O_4$. As discussed earlier it is difficult to distinguish between $NiAl_2O_4$ and Al_2MgO_4. NiO/HT30 has an excess of Al compared to NiO/HT50 and it is therefore assumed that the large peaks for $NiAl_2O_4$ and Al_2MgO_4 are caused by $NiAl_2O_4$. The catalysts were all calcinated in air without an observed formation of $NiAl_2O_4$. It could therefore be assumed that the formation of $NiAl_2O_4$ is activated by the steam. The BET surface area decreases more during sintering for NiO/HT30 than for the other tested catalysts.

NiO/HT50 has been sintered both at condition I: $H_2O/H_2/Ar$ (1/0.23/0.85) and at condition II: $H_2O/CH_4/Ar$ (1/0.51/0.57). Sintering at condition II seems to give a higher particle growth. Schaper et al. [55] reported that the melting point of metal particles saturated with carbon decreases as the concentration of carbon in the particle increases. CH_4 in the sintering atmosphere would increase the concentration of carbon in the nickel particle and thereby increase the sintering.

STEM and TEM examination have been performed on NiO/HT50 sintered at condition II. Characterizations have been made on fresh catalyst and on catalysts sintered at 24, 50 and 74h. The NiO crystal size found from TEM and STEM pictures agrees well with the results from XRD and the exact numbers are given in Table 4. Examples of STEM images and energy dispersive spectroscopy (EDS) maps of NiO/HT50 sintered for 24 and 50h are given in Figure 9 and 10, respectively. All the TEM and STEM pictures indicate that the NiO particles have migrated to form larger particles. The NiO crystal size distribution, given in the upper right corner of the TEM image in Figure 11, is based on several TEM and STEM images. The EDS map of carbon in Figure 10 clearly shows formation of carbon whiskers on NiO/HT50 sintered

for 50h. Also images of catalyst sintered for 74h show carbon formation. Based on the TEOM results discussed in section 3.3, a S/C ratio of 2 should not yield carbon formation on NiO/HT50, even with the increased mean particle size due to sintering. However, the particle diameters referred to in section 3.3 are average particle diameters. As the particle size distribution in Figure 11 shows, some large particles are also present on the catalyst. The size of the nickel particle at the tip of the carbon whisker in Figure 10 is around 90 nm and from Figure 5 it could be found that carbon formation would occur on particles larger than around 60 nm. This explains the carbon formation observed on the NiO/HT50 sintered for 50h at condition II.

Migration of particles to concave regions in the pore structure has been suggested to be the process associated with the initial rapid sintering rates [56]. The migration process continues as long as migrating particles are available or until the growing particle fills the portion of the pore cavity in which it resides [20]. At this point the growth rate decreases substantially and the particle size stabilizes [56]. This explanation for stabilized particle sizes has been challenged by Sehested et al. [19] and will be discussed later in this section.

Generally, two mechanisms are proposed for the sintering of metal particles on ceramic supports [57]: Atom migration (Ostwald ripening) and particle migration (coalescence). Ostwald ripening refers to a process where metal atoms are emitted from one metal particle and captured by another metal particle [57]. In the particle migration process, the particles themselves move over the support and collide to form larger particles. The coalescence process is rapid and hence the migrating process becomes the rate determining step. At elevated temperatures adatoms diffusing on the particle surface will accumulate on one side, causing it to advance by one atomic diameter. A repetition of this step results in Brownian motion of the particles on the substrate and the velocity of the Brownian motion is dependent on the particle diffusivity, D_p. When the particles are small and particle migration is rate controlling, the important parameters determining the growth rate are surface initial average particle density and diffusion [57]. The particle diffusivity (D_p) for spherical particles can be expressed by the following formula (3.3) [57].

$$D_p = 0.301 D_S \left(\frac{a}{R}\right)^4 \quad [cm^3/s] \qquad (3.3)$$

where D_S is the surface diffusion coefficient, a is the atomic diameter and R is the radius of the particle. The average distance (X_p) a particle travels is given by (3.4) [57]

$$X_p = 2\sqrt{D_p t} \qquad (3.4)$$

where t is time. From the above equation it could be found that a 24nm particle travels in average 7.3 longer than a 65nm particle and 1.5 longer than a 29nm particle. This clearly points out that the probability for two nickel particles to collide on NiO/HT30 (24nm) or NiO/HT50 (29nm) is much higher than the probability for two nickel particles to collide on $Ni/CaAl_2O_4$ (65nm). The reduced mobility of large particles could also explain why the sintering slows down after some time.

Substrate morphology has according to Wynblatt et al. [57] the same effect on both sintering mechanisms. A pore structure with narrow pores enhances the stability of the catalyst.

In the review of Bartholomew [20] a sintering rate equation involving dispersion was described (2.17).

$$-d(D/D_0)/dt = k_s(D/D_0)^n \qquad (3.5)$$

where k_s is the sintering rate constant, D_0 the initial dispersion and (n+1) is the sintering order. Lower values for n indicate atomic migration, while $2<n<8$ usually indicates particle migration. A higher value for n could also indicate particle migration if the diffusion controlled process is assumed [56]. The sintering order for NiO/HT30, NiO/HT50 and $Ni/CaAl_2O_4$ is around 10. From this it could be assumed that particle migration is the dominating sintering mechanism.

The crystal size distribution of NiO calculated on basis of TEM and STEM pictures are given in Figure 13 for fresh catalyst, and for catalysts sintered for 50 and 74h. The catalyst sintered for 24h is not included in Figure 13 due to the resemblance

with the catalyst sintered for 50h. The peak of the log-normal lines in Figure 12 shifts towards higher particle sizes as the sintering time increases, which is descriptive for the particle migration mechanism [54]. Fresh catalyst has a peak around 22nm, the catalyst sintered for 50h has a peak around 27nm, while the catalyst sintered for 74h has a peak around 32nm. As seen from Figure 13 the NiO particle size distribution are narrower for the fresh catalyst than for the sintered catalysts, meaning that the sintered catalysts have both smaller and larger particles than the fresh catalyst. The smaller particles may have been formed by redispersion during reduction [56]. The log-normal fits of the sintered catalysts clearly show a tail towards larger particles. This agrees well with sintering via the particle migration mechanism [19, 56].

As mentioned above, the BET surface areas have decreased remarkably for the hydrotalcite derived catalysts. Based on the mechanism of particle migration, a collapse of the support can significantly enhance the sintering. It is reasonable to believe that the reduction in support surface area is an important factor to the sintering.

Sehested et al. [19] found that nickel particles on different catalysts reach a limiting size within a narrow range independent of nickel loading and surface area of the support. The stabilizing size follows the order for initial crystal size, namely $Ni/CaAl_2O_4$ > NiO/HT50 > NiO/HT30. This could be explained by the difference in particle-surface interactions. The TPR profile of NiO/HT30, Figure 2, indicates a strong metal-support interaction. As discussed in the TPR section the metal particles are probably incorporated in the hydrotalcite structure, which should make the catalysts quite stable towards sintering. In Figure 11 the shape of the nickel particles on NiO/HT50 seem to deviate from the spherical shape which could give indications of particles incorporated in the support [58]. The TEM picture of $Ni/CaAl_2O_4$ in Figure 13 clearly shows that the nickel particles are on top of the support, with a large contact angle. The particles on this catalyst seem to have a spherical shape which gives indication of poor particle-surface interactions. Wetting of the substrate by the metal particle is an important feature to the sintering resistance, an illustration of wetting is given in Figure 14. Wynblatt et al. [57] states that increased wetting of the substrate reduces particle growth both by the atom migration and the particle migration process. As described earlier in this section, the particle migration results in diffusion of metal monomers over the particle surface and hence a dependence of the particle diffusivity

on the particle size occurs. According to Wynblatt et al. [57] the effective particle size increases as wetting increases, which again leads to a decrease in diffusivity and hence a decreased sintering. The sintering rate reaches maximum as $\theta \rightarrow \pi$ and minimum as $\theta \rightarrow 0$ [57], which gives decreased sintering with increased wetting. This explains the observed stabilized Ni particle size.

Prior to the XRD experiments the catalysts were oxidized in order to remove coke deposit from the catalyst, and to oxidize the metallic Ni to NiO. As seen in Figure 7 (a) to (d) the XRD profiles give no indications of metallic nickel. From the XRD profile of NiO/HT50 sintered for 74h at condition II in Figure 7 (b) it is shown that not all the carbon has been burned off during the oxidizing process. This XRD profile gives a clear indication of carbon on the catalyst.

4. Conclusion

TEOM experiments have been performed on hydrotalcite derived catalysts and conventional NiO/α-Al_2O_3 and NiO/CaO-Al_2O_3 at 823 and 873K and a total pressure of 20 bar. The experimental results indicate a strong correlation between the nickel crystal size and the carbon resistance. It is suggested that smaller crystals have a larger saturation concentration level than larger nickel crystals. This result in a higher resistance to coke formation for the hydrotalcite like catalysts (with small crystal sizes) compared to the conventional NiO/α-Al_2O_3 and NiO/CaO-Al_2O_3 catalysts. The hydrotalcite derived catalysts show no deactivation during the TEOM experiments, while NiO/α-Al_2O_3 and NiO/CaO-Al_2O_3 show indication of deactivation.

Sintering experiments have been performed on NiO/HT30, NiO/HT50 and Ni/$CaAl_2O_4$ at 903K, 20 bar and H_2O/H_2/Ar (1/0.23/0.85). The particle growth for the different catalysts increased in the following order: NiO/HT30>NiO/HT50> Ni/$CaAl_2O_4$, while the order of the mean NiO particle size remained unchanged: NiO/HT30<NiO/HT50< Ni/$CaAl_2O_4$. Both particle size distribution from TEM and STEM images and sintering kinetics indicated that particle migration mechanism is dominating.

The initial nickel particles for NiO/HT30 are the smallest, the carbon threshold value is the lowest and NiO/HT30 has also the smallest particles after sintering. But a formation of $NiAl_2O_4$ is observed as a result of the sintering and it is concluded that the

collapse of the BET surface of NiO/HT30 is contributing to the observed sintering on this catalyst. Therefore NiO/HT50 is considered to be the most promising catalyst for steam methane reforming. The NiO particles of this catalyst are quite small and the catalyst seems to be resistant to carbon formation and sintering.

Acknowledgement

The Norwegian Research Council (NFR), Norsk Hydro and Statoil are acknowledged for the financial support. John Walmsley is acknowledged for the TEM/STEM images.

References

[1] J. R. Rostrup-Nielsen, *Catal. Today* **18** (1993) 305

[2] J. R. Rostrup-Nielsen and I. Alstrup, *Catal. Today* **53** (1999) 311

[3] J. De Deken, G. Haemers, P. G. Menon and G. F. Froment, *J. Catal.* **70** (1981) 225

[4] D. L. Trimm, *Catal. Today* **37** (1997) 233

[5] F. Besenbacher, I. Chorkendorff, B. S. Clausen, B. Hammer, A. M. Molenbroek, J. K. Nørskov and I. Stensgaard, *Science* **279** (1998) 1913

[6] A. Bhattacharyya, V. W. Chang and D. J. Schumacher, *Appl. Clay Sci.* **13** (1998) 317

[7] G. Fornasari, M. Gazzano, D. Matteuzzi, F. Trifirò and A. Vaccari, *Appl. Clay Sci.* **10** (1995) 69

[8] F. Cavani, F. Trifirò and A. Vaccari, *Catal. Today* **11** (1991) 173

[9] J. R. H. Ross, *Surface and Defect Properties of Solids* **4** (1975) 34

[10] H. Morioka, Y. Shimizu, M. Sukenobu, K. Ito, E. Tanabe, T. Shishido and K. Takehira, *Appl. Catal.* **215** (2001) 11

[11] T. Shishido, M. Sukenobu, H. Morioka, M. Kondo, Y. Wang, K. Takaki and K. Takehira, *Appl. Catal.* **223** (2002) 35

[12] A. Bhattacharyya, V. W. Chang and D. J. Schumacher, *Appl. Clay Sci.* **13** (1998) 317

[13] K. Takehira, T. Shishido, P. Wnag, T. Kosaka and K. Takaki, *Phys. Chem. Chem. Phys.* **17** (2003) 3801

[14] H. S. Bengaard, J. K. Nørskov, J. Sehested, B. S. Clausen, L. P. Nielsen, A. M. Molenbroek and J. R. Rostrup-Nielsen, *J. Catal.* **209** (2002) 365

[15] M. A. Goula, A. A. Lemonidou and A. M. Efstathiou, *J. Catal.* **161** (1996) 626

[16] T. Borowiecki, *Appl. Catal.* **4** (1982) 223

[17] D. Chen, K. O. Christensen, E. Ochoa-Fernández, Z. Yu, B. Tøtdal, N. Latorre, A. Monzón and A. Holmen, *J. Catal.* **229** (2004) 87

[18] A. C. S. C. Teixeira and R. Giudici, *Chem. Eng. Sci.* **54** (1999) 3609

[19] J. Sehested, A. Carlsson, T. V. W. Janssens, P. L. Hansen and A. K. Datye, *J. Catal.* **197** (2001) 200

[20] C. H. Bartholomew, *Appl. Catal.* **107** (1993) 1

[21] J. Sehested, J. A. P. Gelten, I. N. Remediakis, H. Bengaard and J. K. Nørskov, *J. Catal.* **223** (2004) 432

[22] C. H. Bartholomew and W. L. Sorensen, *J. Catal.* **81** (1983) 131

[23] J. Sehested, *J. Catal.* **217** (2003) 417

[24] J. T. Richardson and J. L. Propp, *J. Catal.* **98** (1986) 457

[25] C. H. Bartholomew, R. B. Pannel and R. W. Fowler, *J. Catal.* **79** (1983) 34

[26] J. W. Niemantsverdriet, Spectroscopy in Catalysis. Wiley-VCH, Weinheim, 2000.

[27] D. Chen, A. Grønvold, H. P. Rebo, K. Moljord and A. Holmen, *Appl. Catal.* **137** (1996) L1

[28] D. Chen, R. Lødeng, A. Anundskås, O. Olsvik and A. Holmen, *Chem. Eng. Sci.* **56** (2001) 1371

[29] J. W. Snoeck, G. F. Froment and M. Fowles, *J. Catal.* **169** (1997) 240

[30] K. O. Christensen, E. Ochoa-Fernández, D. Chen, R. Lødeng and A. Holmen, *Submitted*

[31] E. Bjørgum, D. Chen, M. G. Bakken, K. O. Christensen, A. Holmen, O. Lytken and I. Chorkendorff, *J. Phys. Chem. B* **109** (2005) 2360

[32] K. Schulze, W. Makowski, R. Chyy, R. Dziembaj and G. Günter, *Appl. Clay Sci.* **18** (2001) 59

[33] L. Chmielarz, P. Kustrowski, A. Rafalska-Lasocha and R. Dziembaj, *Thermochim. Acta* **395** (2003) 225

[34] M. V. Twigg and J. T. Richardson, *Appl. Catal.* **190** (2000) 61

[35] J. T. Richardson, R. M. Scates and M. V. Twigg, *Appl. Catal.* **267** (2004) 35

[36] Goula, Lemonidou and Efstathiou, *J. Catal.* **161** (1996) 626

[37] K. S. Jung, H. Moon and H. Lee, *Res. Shem. Intermed.* **26** (2000) 45

[38] C. Li and Y. Chen, *Thermochim. Acta* **256** (1995) 457

[39] J. T. Richardson, M. Lei, B. Turk, K. Forster and M. V. Twigg, *Appl. Catal.* **110** (1994) 217

[40] J. R. Rostrup-Nielsen, *J. Catal.* **27** (1972) 343

[41] P. K. Bokx, A. J. H. M. Kock, E. Boellaard, W. Klop and J. W. Geus, *J. Catal.* **96** (1985) 454

[42] A. J. H. M. Kock, P. K. Bokx, E. Boellaard, W. Klop and J. W. Geus, *J. Catal.* **96** (1985) 468

[43] E. Boellaard, P. K. Bokx, A. J. H. M. Kock, W. Klop and J. W. Geus, *J. Catal.* **96** (1985) 481

[44] J. R. Rostrup-Nielsen and D. L. Trimm, *J. Catal.* **48** (1977) 155

[45] D. L. Trimm, *Catal. Today* **49** (1999) 3

[46] S. Helveg, C. Lopez-Cartes, J. Sehested, P. L. Hansen, B. S. Clausen, J. R. Rostrup-Nielsen, F. Abild-Pedersen and J. K. Norskov, *Nature* **427** (2004) 426

[47] T. Horiuchi, K. Sakuma, T. Fukui, Y. Kubo, T. Osaki and T. Mori, *Appl. Catal.* **144** (1996) 111

[48] T. P. Beebe, D. W. Goodman, B. D. Kay and J. T. Yates, *J. Chem. Phys.* **87** (1987) 2305

[49] J. R. Rostrup-Nielsen, *Catalysis - Science and Technology*. (J. R. Anderson and M. Boudart, eds.), **5** Springer-Verlag, Berlin, 1984

[50] F. Frusteri, S. Freni, V. Chiodo, L. Spadaro, O. Di Blasi, G. Bonura and S. Cavallaro, *Appl. Catal.* **270** (2004) 1

[51] F. Notheisz, A. Zsifmond, D. Ostgard, M. Bartók and G. V. Smith, *Catal. Lett.* **26** (1994) 315

[52] Å. Slagtern, U. Olsbye, R. Blom, I. M. Dahl and H. Fjellvår, *Appl. Catal.* **165** (1997) 379

[53] J. R. Rostrup-Nielsen, J. Sehested and J. K. Nørskov, *Adv. Catal.* **47** (2003) 65

[54] J. T. Richardson and J. G. Crump, *J. Catal.* **57** (1979) 417

[55] A. K. Schaper, H. Hou, A. Greiner and F. Phillipp, *J. Catal.* **222** (2004) 250

[56] H. K. Kuo, P. Ganesan and R. J. De Angelis, *J. Catal.* **64** (1980) 303

[57] P. Wynblatt and N. A. Gjostein, *Prog. Solid State Chem.* **9** (1975) 21

[58] J. Soria, M. T. Blasco and J. C. Conesa, *Surf. Sci.* **251-252** (1991) 1018

[59] D. Chen, E. Bjørgum, R. Lødeng, K. O. Christensen and A. Holmen, *Stud. Surf. Sci. Catal.* **147** (2004) 139

Table 1: Catalyst composition and BET surface area (S_{BET}) and calcination temperature (T_C). HT30, HT50 and HT70 are commercial hydrotalcites with a ratio between MgO and Al_2O_3 of 30/70, 50/50 and 70/30, respectively. (873) and (1173) refers to calcination temperatures.

Catalyst	NiO [%]	MgO [%]	CaO [%]	Al_2O_3 [%]	S_{BET} [m^2/g_{cat}]	T_C [K]
NiO/HT30[a]	15.9	24.5	-	59.6	271[b]	873
NiO/HT50[a]	15.9	42.6	-	41.5	201[b]	873
NiO/HT70 (873)[a]	15.9	59.5	-	24.6	228[b]	873
NiO/HT70 (1173)[a]	15.9	59.5	-	24.6	-	1173
NiO/CaO-Al_2O_3	15.9	-	39.27	44.8	-	1173
NiO/α-Al_2O_3	15.9	-	-	84.1	-	1173
Ni/$CaAl_2O_4$	11	-	8	81	5.5[b]	-

[a] Composition of HT30, HT50 and HT70 was supplied by Condea

[b] Data from Chen et. al [59]

Table 2: Particle size of different Ni catalysts from XRD. HT30, HT50 and HT70 are commercial hydrotalcites with a ratio between MgO and Al_2O_3 of 30/70, 50/50 and 70/30, respectively. (873) and (1173) refers to calcination temperatures.

Catalyst	NiO crystal size [nm]
NiO/HT30	12
NiO/HT50	24
NiO/HT70 (873)	29
NiO/HT70 (1173)	29
NiO/CaO-Al_2O_3	32
NiO/α-Al_2O_3	60
Ni/$CaAl_2O_4$	65

Table 3: BET surface area for different sintered catalysts. HT30 and HT50 are commercial hydrotalcites with a ratio between MgO and Al_2O_3 of 30/70 and 50/50, respectively. Sintering condition I: $H_2O/H_2/Ar$ (1/0.23/0.85), sintering condition II: $H_2O/CH_4/Ar$ (1/0.51/0.57). T=903K and P=20bar in all experiments

Catalyst	Sintering condition	Sintering time [h]	BET [m^2/g]
NiO/HT50	-	-	201
NiO/HT50	I	50	30
NiO/HT50	II	50	27
NiO/HT50	II	74	20
NiO/HT30	-	-	271
NiO/HT30	I	48	26
$Ni/CaAl_2O_4$	-	-	5.5
$Ni/CaAl_2O_4$	I	50	3.3

Table 4: Crystal size of NiO/HT50 sintered in H_2O/CH_4/Ar (1/0.51/0.57) at a total flow of 0.03mol/min, T=903K and P=20bar. HT50 is a commercial hydrotalcite with a ratio between MgO and Al_2O_3 of 50/50. Comparison between XRD and TEM

Sintering time [h]	XRD [nm]	TEM [nm]
Fresh catalyst	24	22
24	31	33
50	30	27
74	29	32

Figure captions

Figure 1. XRD profiles where (●) denotes reflection of nickel oxide, (○) denotes reflection of magnesium nickel oxide, (■) denotes reflection of nickel aluminum oxide / aluminum magnesium oxide (□) denotes reflection of alumina and (X) denotes reflection of spinel calcium aluminum oxide. (a) NiO/HT30, (b) NiO/HT50, (c) NiO/HT70 (873), (d) NiO/HT70 (1173), (e) NiO/CaO-Al_2O_3, (f) NiO/α-Al_2O_3

Figure 2. TPR profiles. H_2/Ar (7/50), total flow=0.002mol/min (a) NiO/HT30, (b) NiO/HT50, (c) NiO/HT70 (873), (d) NiO/HT70 (1173), (e) NiO/CaO-Al_2O_3, (f) NiO/α-Al_2O_3

Figure 3. Coking profile and CH_4 conversion for NiO/HT70 (1173) at a total flow of 0.009mol/min, T=823K and P=20bar

Figure 4. The influence of particle size on coking rate in wt%/h at S/C ratios from 0.3 to 1.25, total flow=0.009mol/min, T=823K and P=20bar. The symbols correspond to experimental data points, lines only indicate trends. (◊) S/C=0.3, (□) S/C=0.5, (Δ) S/C=0.76, (X) S/C=0.3, (○) S/C=0.3.

Figure 5. Carbon threshold values for steam methane reforming at a total flow of 0.009mol/min, T=823K and P=20bar. The symbols correspond to experimental data, while the line is for guidance of the eye.

Figure 6. Turnover frequency (TOF) for steam methane reforming at a total flow of 0.009mol/min, T=823K and P=20bar. The symbols correspond to experimental data points, lines only indicate trends. Catalysts: (○) NiO/HT30, (X) NiO/HT50, (Δ) NiO/HT70 (873) and (▲) NiO/HT70 (1173)

Figure 7. XRD profiles of sintered catalysts where (●) denotes reflection of nickel oxide, (○) denotes reflection of magnesium nickel oxide, (■) denotes reflection of nickel

aluminum oxide / aluminum magnesium oxide (Δ) denotes aluminum oxide, (▼) denotes calcium aluminum oxide and (C) denotes reflection of some carbon structure. (a) Catalyst: NiO/HT50. Sintering condition: $H_2O/H_2/Ar$ (1/0.23/0.85), F_{tot}=0.03mol/min (b) Catalyst: NiO/HT50. Sintering condition: $H_2O/CH_4/Ar$ (1/0.51/0.57), F_{tot}=0.03mol/min (c) Catalyst: NiO/HT30. Sintering condition: $H_2O/H_2/Ar$ (1/0.23/0.85), F_{tot}=0.03mol/min (d) Catalyst: $Ni/CaAl_2O_4$. Sintering condition: $H_2O/H_2/Ar$ (1/0.23/0.85), F_{tot}=0.03mol/min.

Figure 8. (a) Catalyst dispersion (D) as a function of sintering time, (b) NiO crystal size (d) as a function of sintering time. The symbols correspond to experimental data points, lines only indicate trends. x: $Ni/CaAl_2O_4$, Δ: NiO/HT50, □: NiO/HT50 and ◊: NiO/HT30. Sintering conditions: T=903K, P=20bar and total flow=0.03mol/min. x, Δ, ◊: $H_2O/H_2/Ar$ (1/0.23/0.85), □: $H_2O/CH_4/Ar$ (1/0.51/0.57)

Figure 9. EDS images of Ni/HT50 sintered in $H_2O/CH_4/Ar$ (1/0.51/0.57)
for 24 hours at a total flow of 0.03mol/min, T=903K and P=20bar. (a) STEM, dark field image, (b) EDX analysis. Right side: EDS maps of magnesium, aluminium and nickel.

Figure 10. EDS images of Ni/HT50 sintered in $H_2O/CH_4/Ar$ (1/0.51/0.57)
for 50 hours at a total flow of 0.03mol/min, T=903K and P=20bar. (a) STEM, dark field image, (b) EDX analysis. Right side: EDS maps of magnesium, aluminium, nickel and carbon.

Figure 11. Bright field TEM image of Ni/HT50 sintered in $H_2O/CH_4/Ar$ (1/0.51/0.57)
for 24 hours at W/F_0=6.9g cat,h/molC, T=903K and P=20bar

Figure 12. Distribution of NiO crystal size measured by TEM/STEM. Catalyst: NiO/HT50 sintered in $H_2O/CH_4/Ar$ (1/0.51/0.57) at a total flow of 0.03mol/min, T=903K and P=20bar. (◊) denotes fresh catalyst, (Δ) denotes catalyst sintered for 50 hours and (X) denotes catalyst sintered for 74 hours. The points are experimental data, while the lines are log normal trend-lines.

Figure 13. STEM picture of $Ni/CaAl_2O_4$ sintered for 24hours at $H_2O/H_2/Ar$ = (1/0.23/0.85), total flow: 0.03mol/min, T=903K and P =20bar

Figure 14. Illustration of different degrees of wetting by a metal on a surface, where θ is the contact angle. (a) represent $Ni/CaAl_2O_4$ and (b) represent NiO/HT30

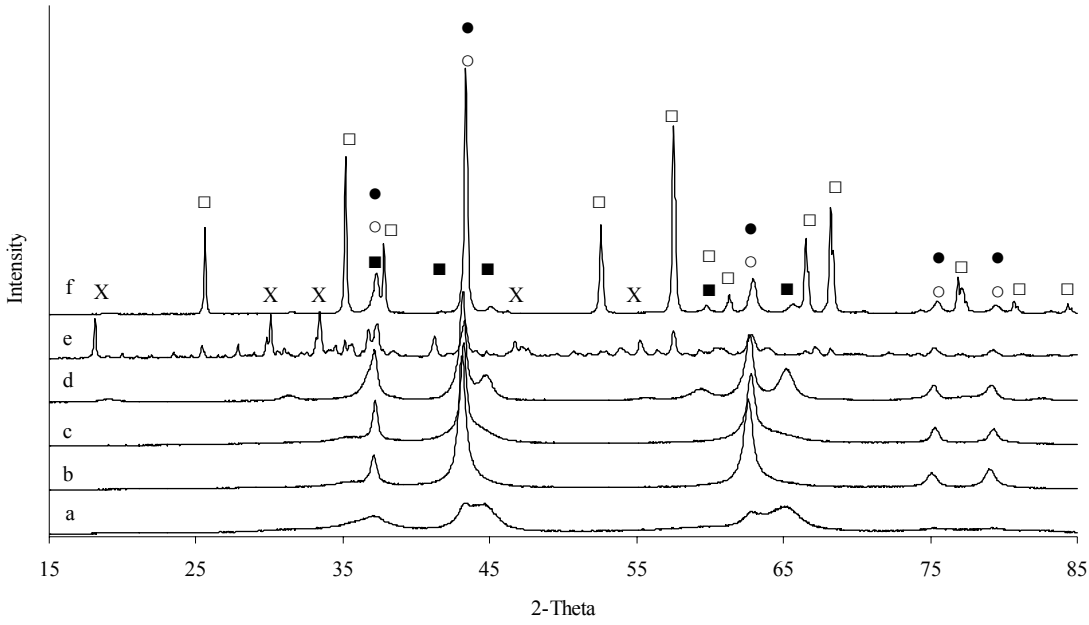

Figure 1

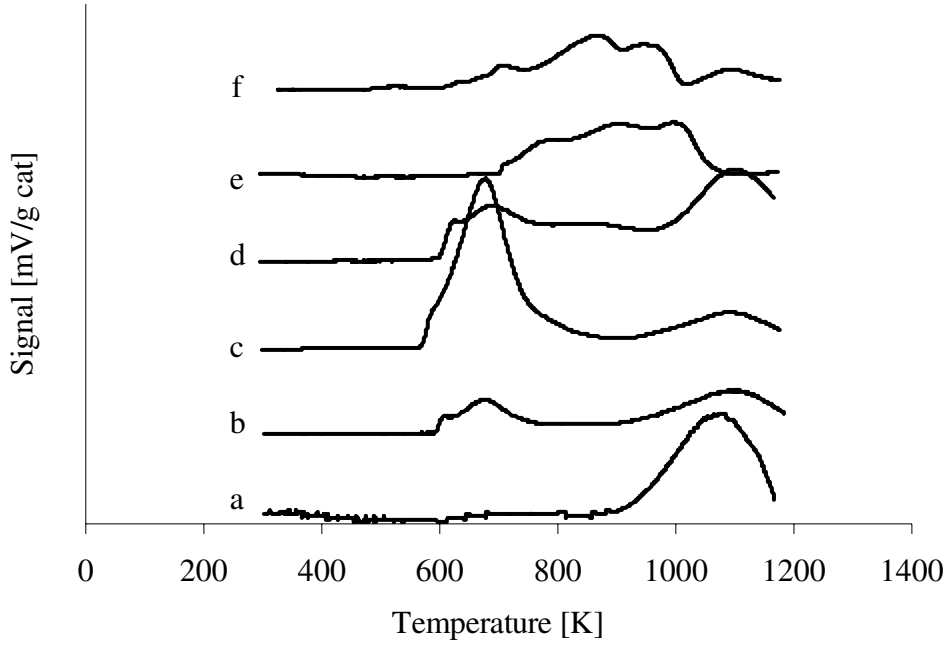
Signal [mV/g cat]
f
e
d
c
b
a
0
200
400
600
800
1000
1200
1400
Temperature [K]

Figure 2

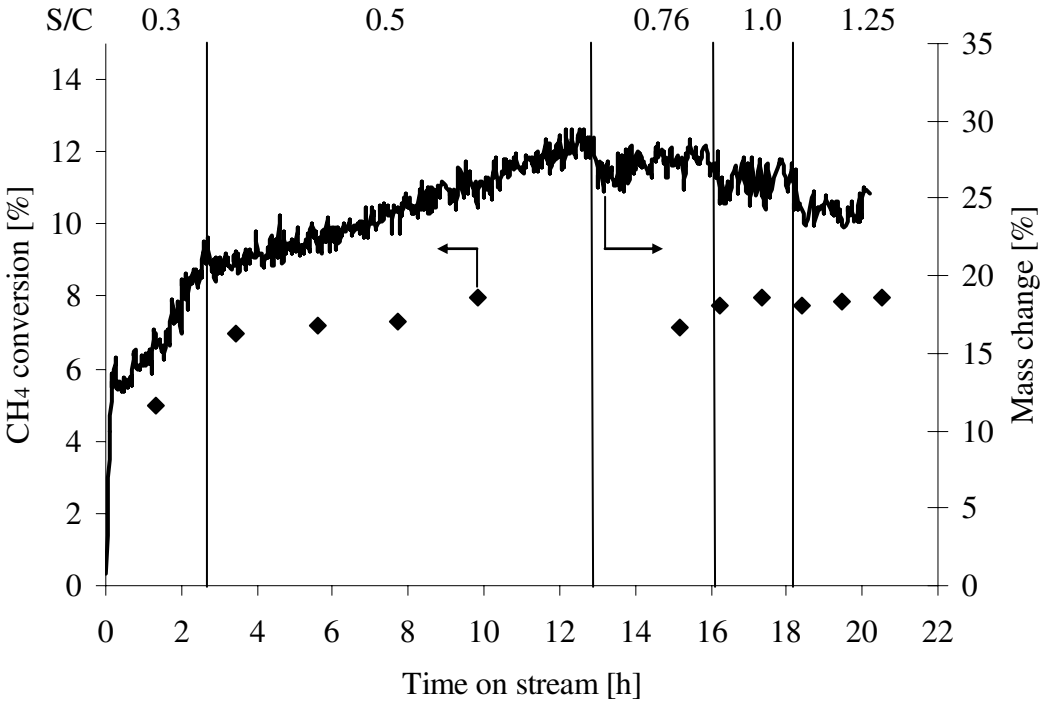
S/C
0.3
0.5
0.76
1.0
1.25
CH4 conversion [%]
Mass change [%]
Time on stream [h]
0
2
4
6
8
10
12
14
16
18
20
22
5
15
25
30
35

Figure 3

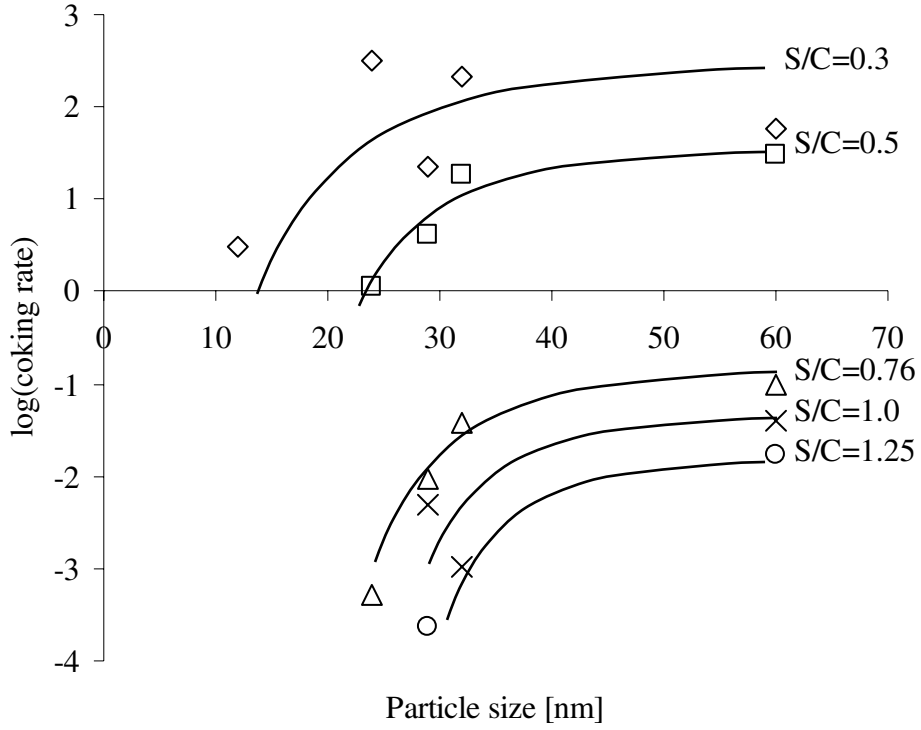
3
2
1
0
-1
-2
-3
-4
0
10
20
30
40
50
60
70
log(coking rate)
Particle size [nm]
S/C=0.3
S/C=0.5
S/C=0.76
S/C=1.0
S/C=1.25

Figure 4

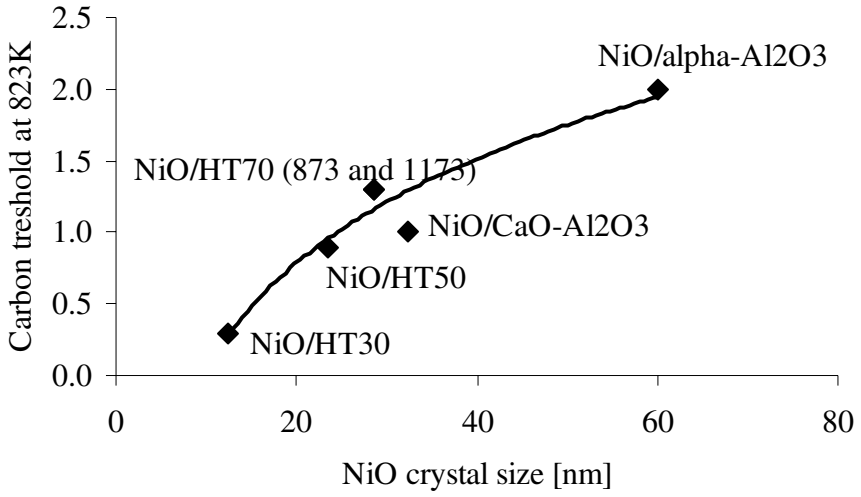
Carbon treshold at 823K
2.5
2.0
1.5
1.0
0.5
0.0
0
20
40
60
80
NiO crystal size [nm]
NiO/alpha-Al2O3
NiO/HT70 (873 and 1173)
NiO/CaO-Al2O3
NiO/HT50
NiO/HT30

Figure 5

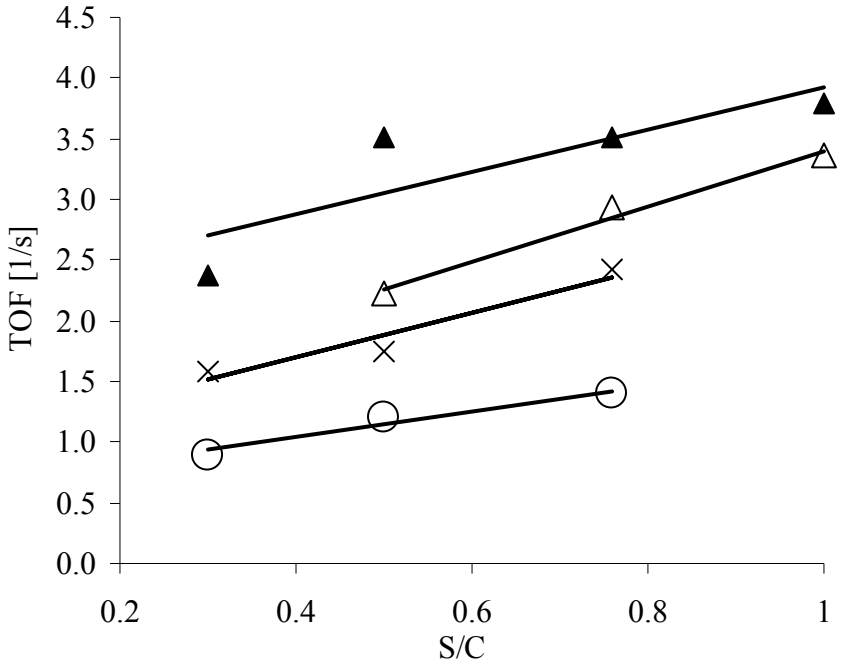

Figure 6

(a)

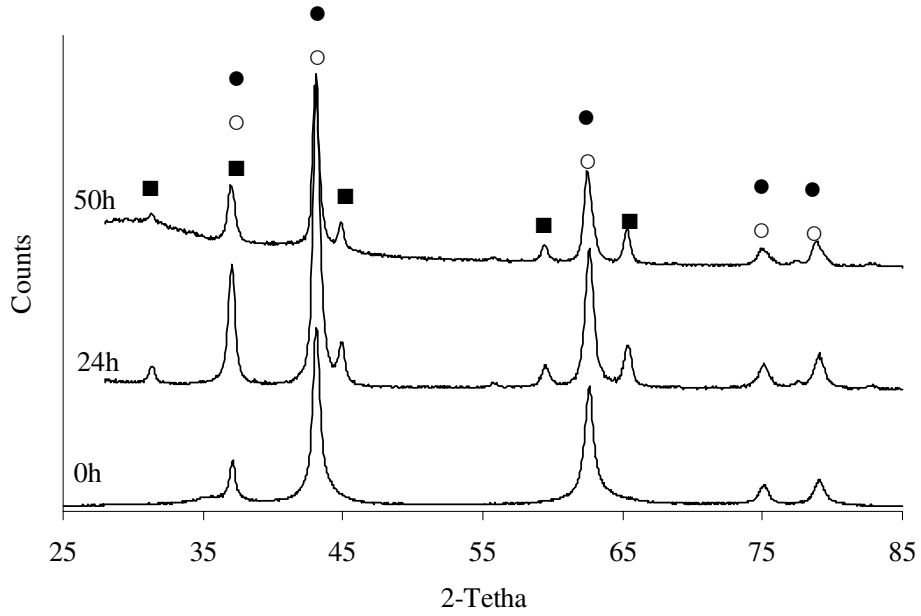
50h
24h
0h
Counts
25
35
45
55
65
75
85
2-Tetha

(b)

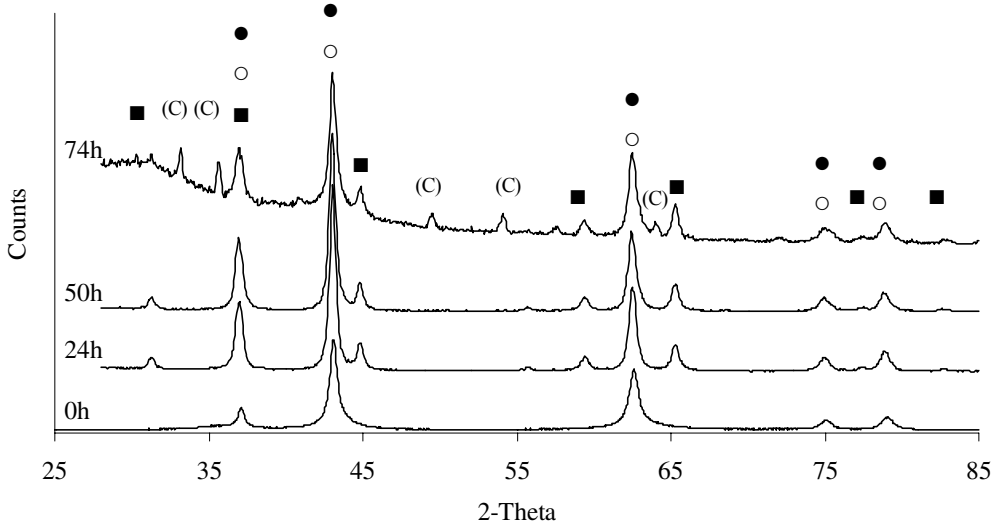
(C) (C)
74h
(C)
(C)
(C)
50h
24h
0h
Counts
25
35
45
55
65
75
85
2-Theta

Figure 7

(c)

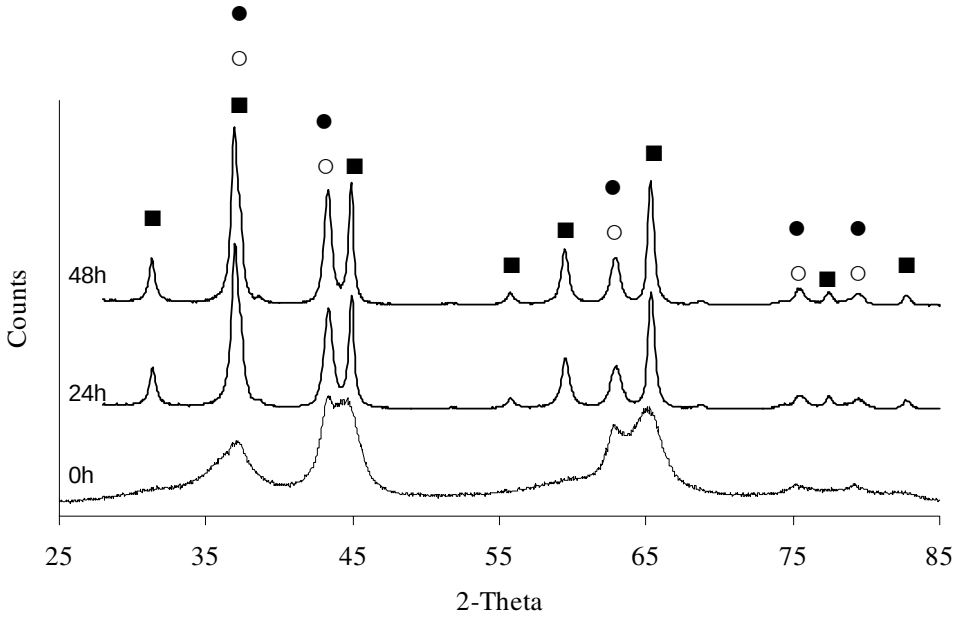
Counts
48h
24h
0h
25
35
45
55
65
75
85
2-Theta

(d)

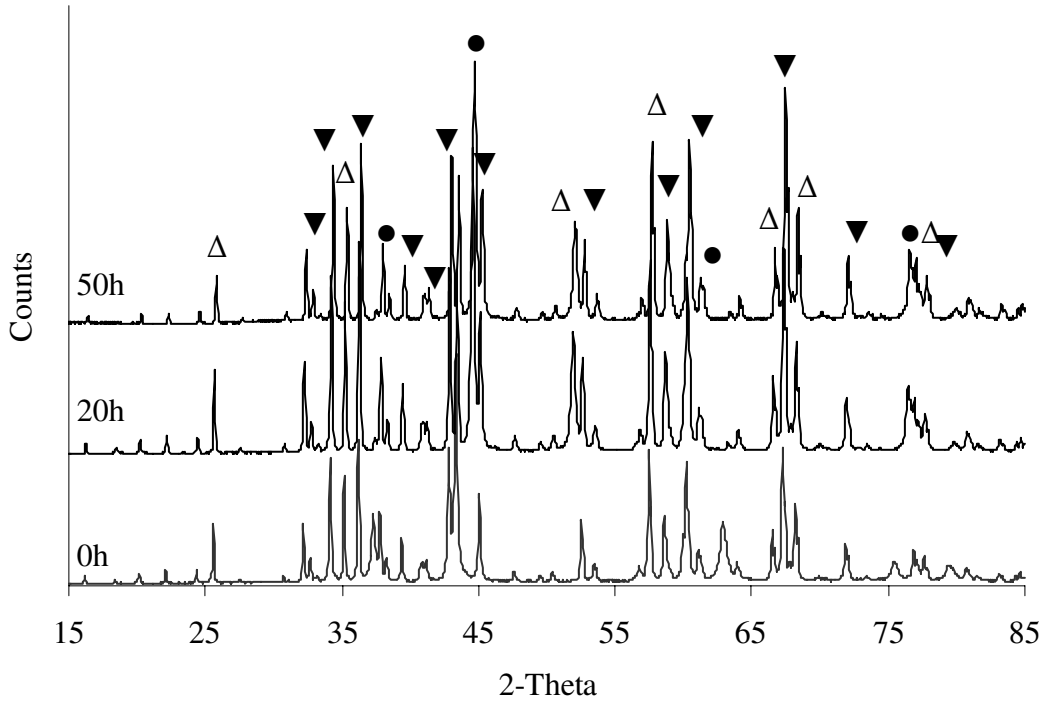
Counts
50h
20h
0h
15
25
35
45
55
65
75
85
2-Theta

Figure 7

(a)

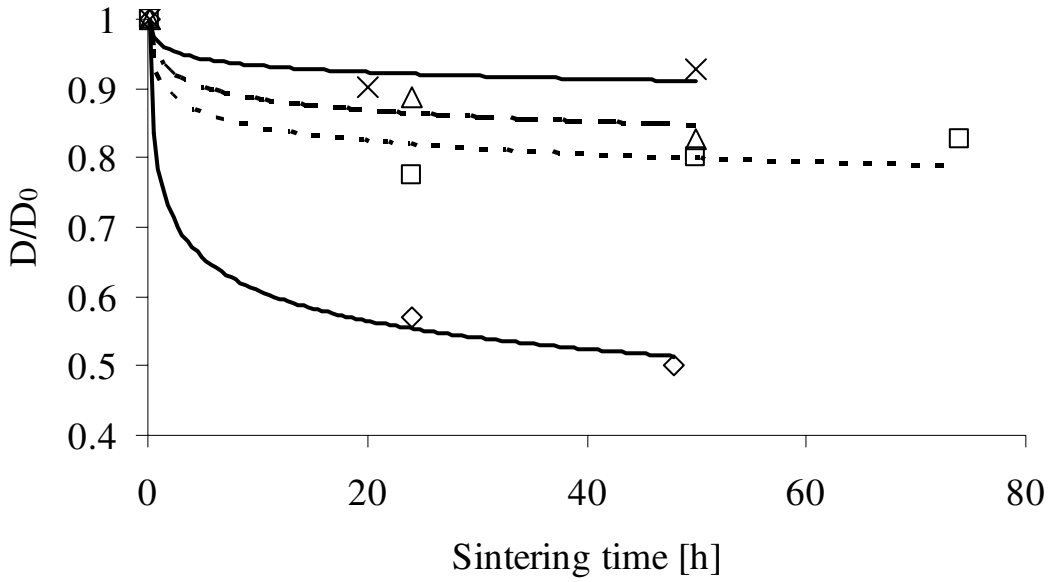
1
0.9
0.8
0.7
0.6
0.5
0.4
D/D0
0
20
40
60
80
Sintering time [h]

(b)

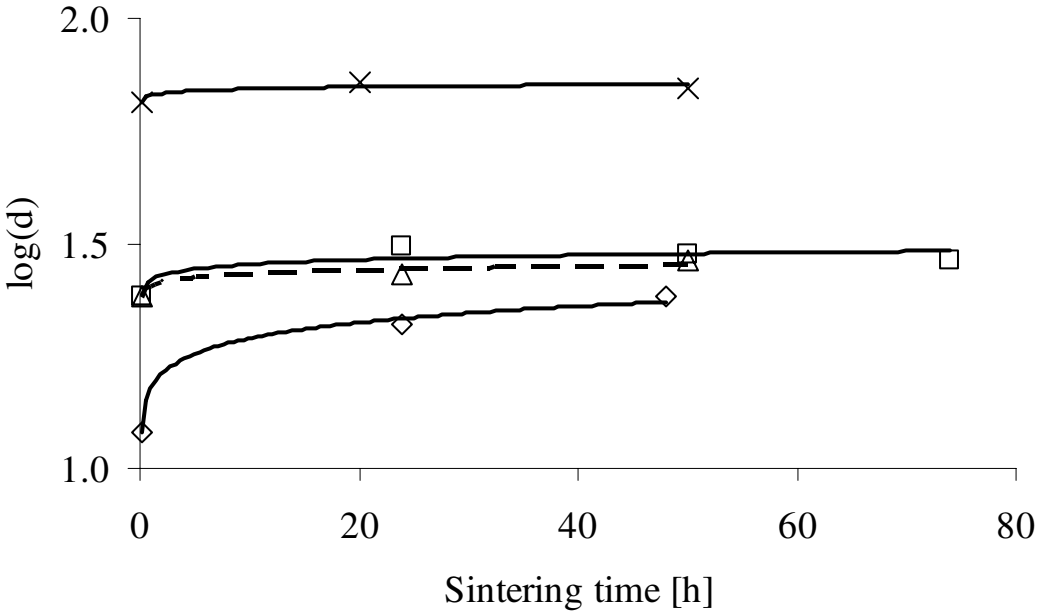
2.0
1.5
1.0
log(d)
0
20
40
60
80
Sintering time [h]

Figure 8

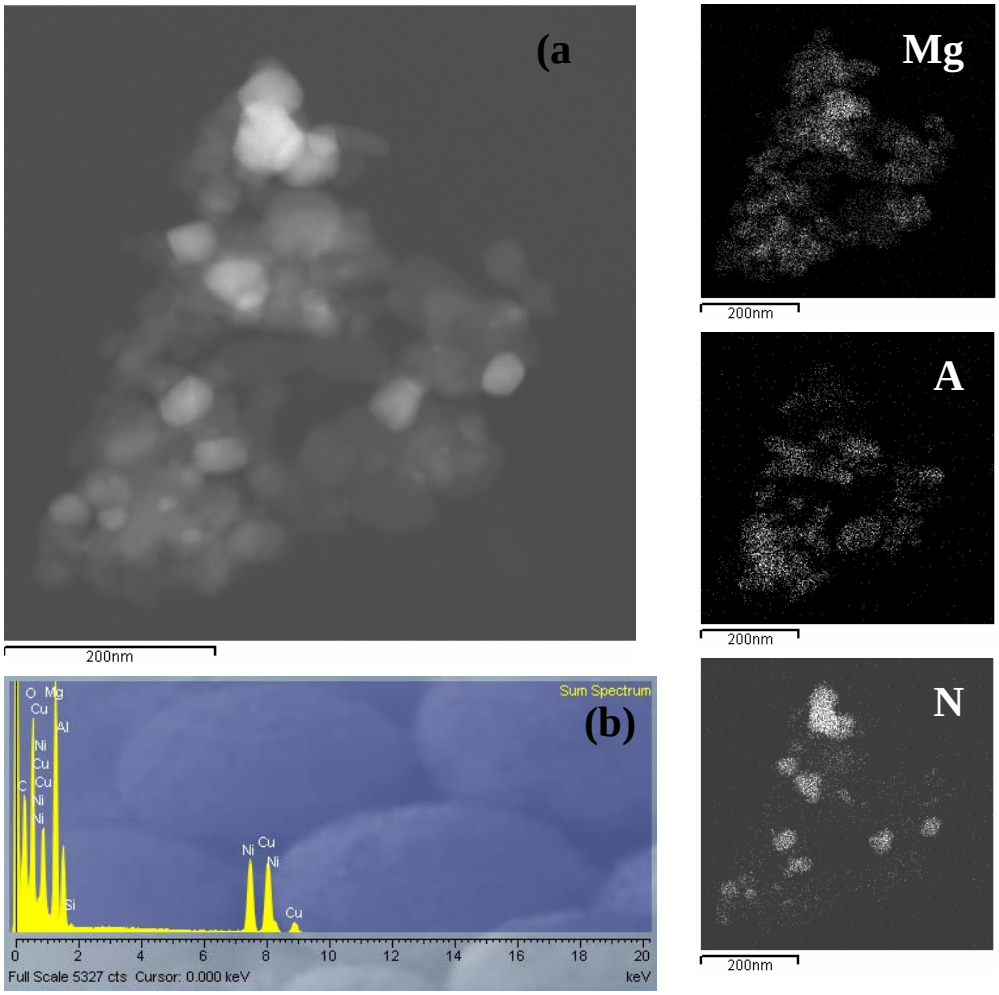
(a
200nm
Mg
200nm
A
200nm
N
200nm
Sum Spectrum
(b)
O Mg
Cu
Al
Ni
Cu
O Cu
Ni
Ni
Si
Ni Cu
Ni
Cu
0 2 4 6 8 10 12 14 16 18 20
Full Scale 5327 cts Cursor: 0.000 keV
keV

Figure 9

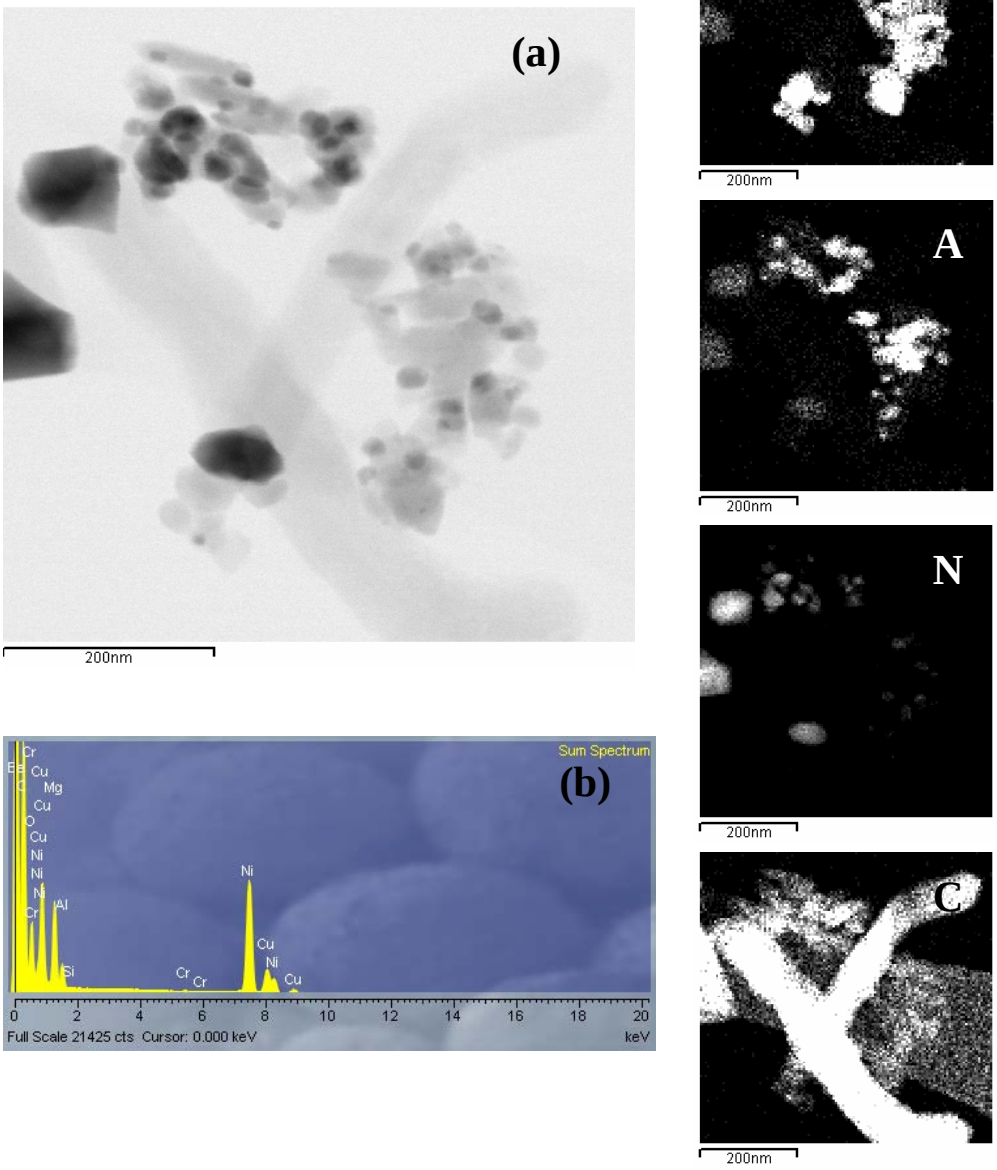
(a)
200nm
(b)
Sum Spectrum
Cr
Cu
Mg
Cu
O
Cu
Ni
Ni
Ni
Cr
Al
Si
Cr
Cr
Ni
Cu
Ni
Cu
0
2
4
6
8
10
12
14
16
18
20
Full Scale 21425 cts Cursor: 0.000 keV
keV
M
200nm
A
200nm
N
200nm
C
200nm

Figure 10

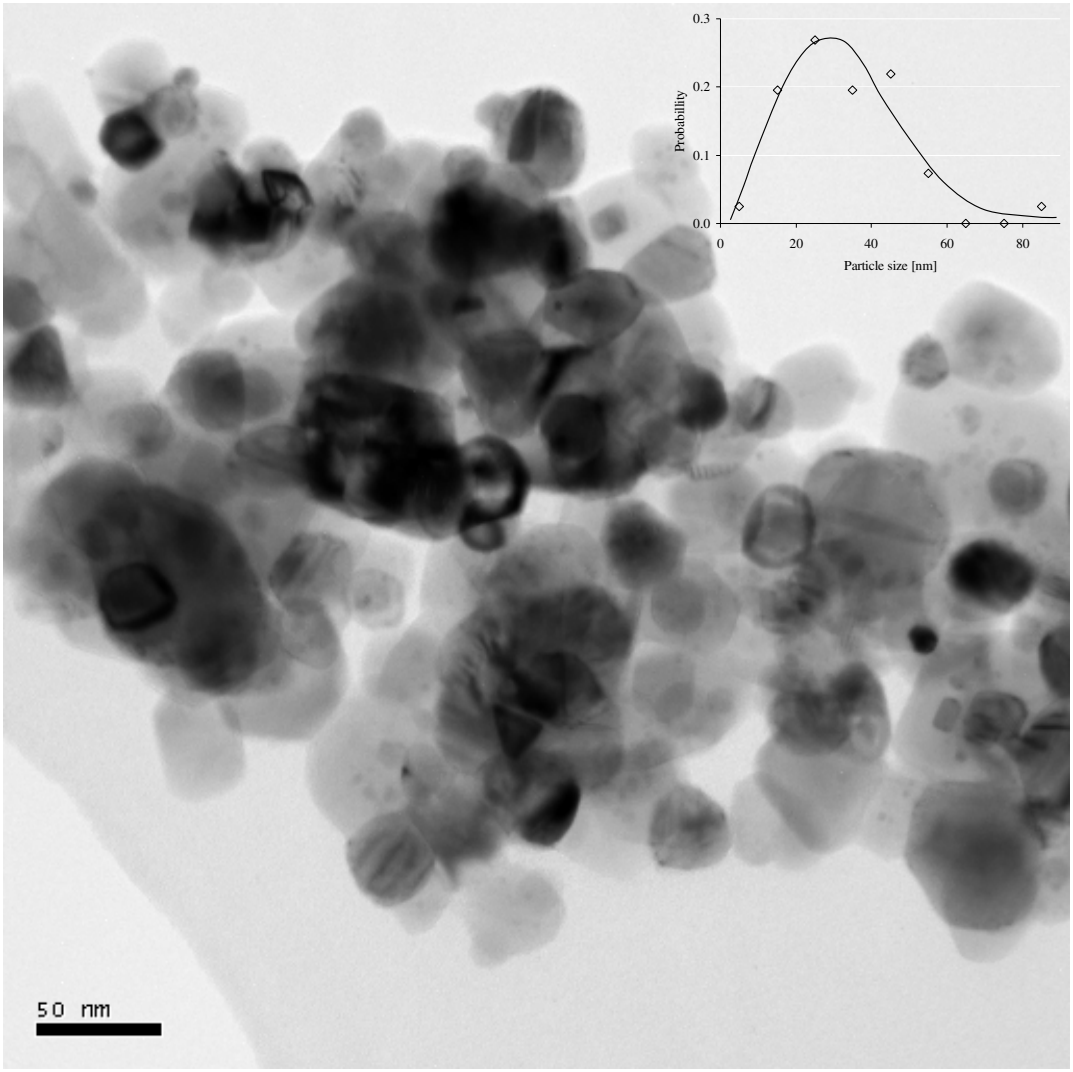

Figure 11

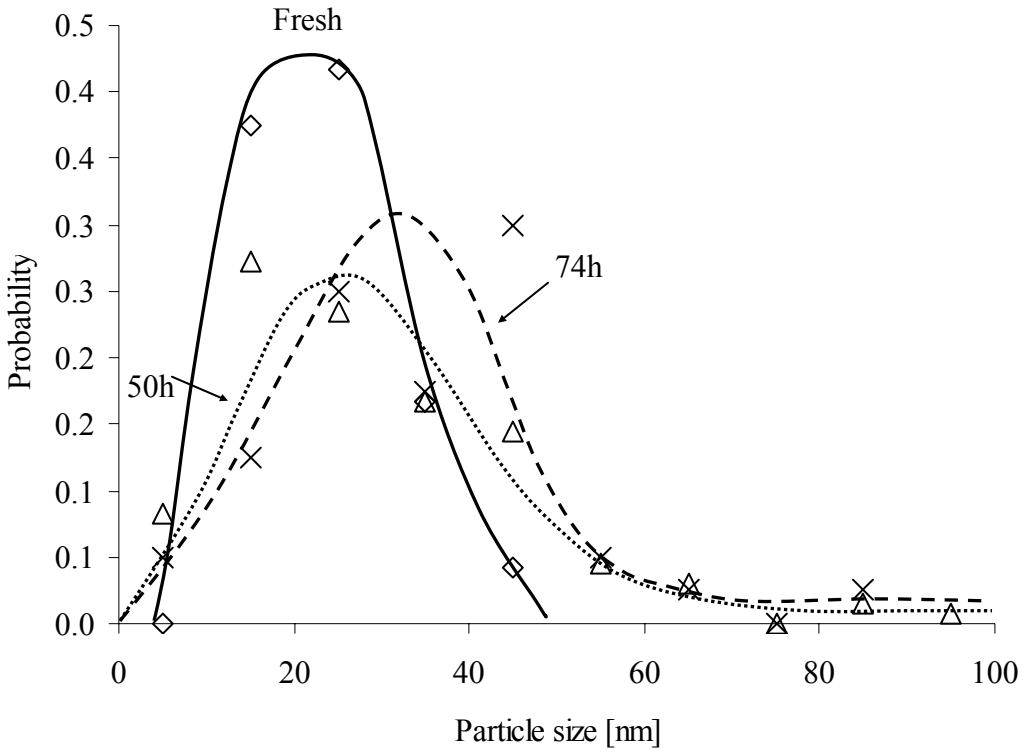
Fresh
74h
50h
Probability
Particle size [nm]
0.5
0.4
0.4
0.3
0.3
0.2
0.2
0.1
0.1
0.0
0
20
40
60
80
100

Figure 12

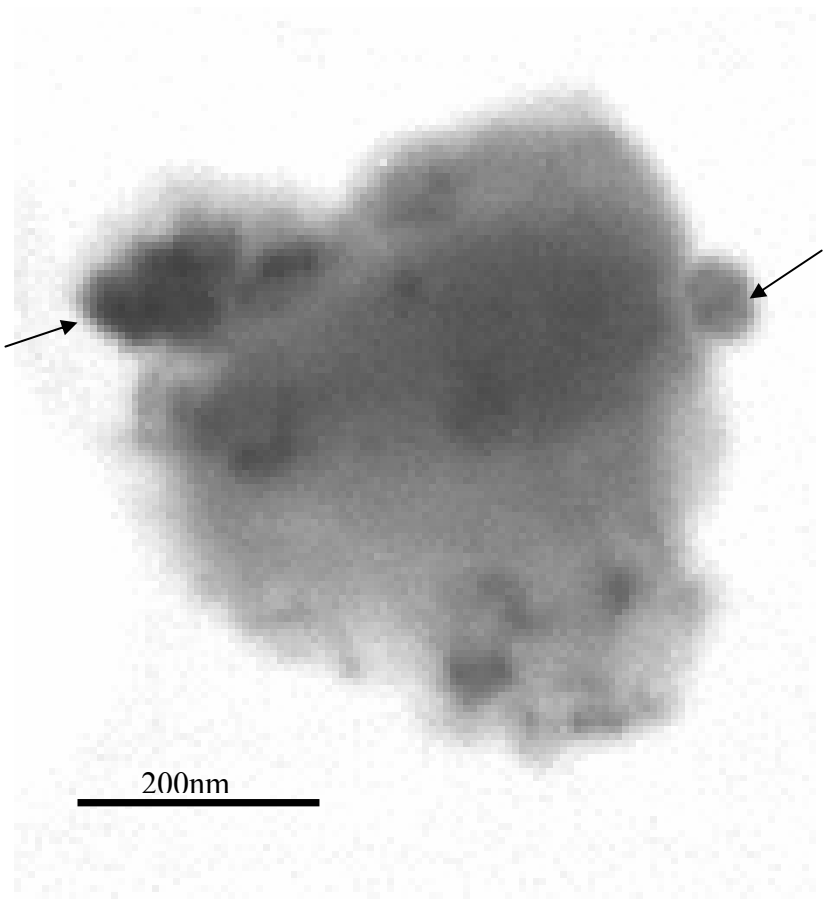

Figure 13

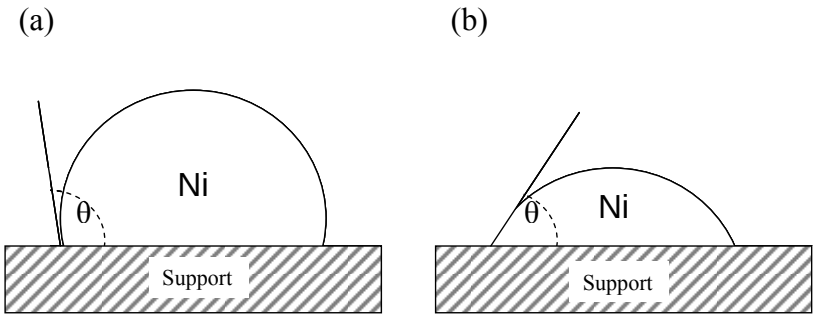

Figure 14

Paper II

Nickel crystal size and distribution of hydrotalcite derived catalysts prepared by different methods

Nickel crystal size and distribution of hydrotalcite derived catalysts prepared by different methods

Kjersti Omdahl Christensen[a], Esther Ochoa-Fernández[a], De Chen[a], Rune Lødeng[b] and Anders Holmen[a]

[a] Department of Chemical Engineering, Norwegian University of Science and Technology (NTNU), N-7491 Trondheim, Norway.

[b] SINTEF Applied Chemistry, N-7465 Trondheim, Norway.

Abstract

Different hydrotalcite derived catalysts have been prepared by impregnating commercial hydrotalcite supports and by the co-precipitation method. It is shown that hydrotalcite derived oxide mixtures are good supports where efficient anchoring sites for the Ni nanoparticles exist. The Ni crystal sizes were determined by chemisorption, XRD and TEM/STEM. Similar results for the crystal size were observed from the different techniques. However, due to the experimental limitations of the techniques involved it is concluded that determination of the crystal size should be based on more than one technique. The Mg / Al ratio in the support seems to have an effect on the dispersion of the Ni particles, and a low ratio yields a better dispersion of Ni. The co-precipitation route gave an even stronger interaction between the support and the nickel providing smaller crystals.

1. Introduction

Nickel catalysts are used in many different industrial processes, but a common problem for most commercial processes is deactivation. Ni supported on hydrotalcites or mixed oxides has shown to be more resistant to both coke formation and sintering than other Ni catalytic systems [1-3]. Features that make hydrotalcite promising for use as catalysts are: High surface area, basic properties and homogonous mixtures of oxides with small crystal size [4]. The following formula [1] describes the structure of hydrotalcites (2.1)

$$[M_n^{2+}M_m^{3+}(OH)_{2(n+m)}]^{m+}A_{m/x}^{x-}\times yH_2O \quad (1)$$

where: M^{2+} and M^{3+} are metal cations, A is an anion, x is charge of the anion, n>m and y is the number of interlayer water molecules. Hydrotalcites have a layered structure with interlayer water. This water leaves when the hydrotalcite is heated above 473K. At about 723K the layered hydroxides dehydrate. However, this material retains the memory of the layered structure, which allows reconstruction of the hydrotalcite structure when adding a water solution containing various anions to the product. If the material is heated above 1023K the hydrotalcite structure is lost and the material becomes a mixture of oxides, mixed oxides and spinels [1, 4].

A large number of commercial catalysts contain nickel in the oxide form or in the reduced form as metallic nickel. An important characteristic of these catalysts is the crystal size. The crystal size can in principle be measured by different methods including chemisorption, x-ray diffraction (XRD), transmission electron microscopy (TEM) and scanning transmission electron microscope (STEM). Due to a number of reasons, reported particles sizes from these techniques usually give different results. Sehested et al. [5] reported that the particle sizes obtained by sulphur chemisorption, XRD and TEM/STEM gave the same trends, but that there was a discrepancy between the values found by the different techniques. For sintered catalysts the values obtained from XRD were smaller than the particle sizes determined from sulphur chemisorption and TEM/STEM. According to the Sehested et al. [5] this was due to polycrystalline particles. It was also observed that for fresh catalysts measurements by XRD, TEM/STEM and sulphur chemisorption, respectively, gave increasing particle diameter. The differences were explained by the oxide layer on the Ni metal surface during XRD and TEM/STEM, and Ni atoms at the metal support interface in the case of sulphur chemisorption. Panpranot et al. [6] and Sanquin et al. [7] recently published results were the particle size obtained from H_2 and CO chemisorption was higher than the particle size from TEM and XRD, the latter two was in good agreement. Yin et al. [8] also found that the particle size obtained from chemisorption was larger than the particle size from TEM. Several groups have also reported that slightly larger values for the particle

size are observed from TEM than XRD [9-11]. The hydrotalcite derived Ni catalysts have been applied in steam methane reforming [3], carbon nanofibers synthesis [12] and ethane hydrogenolysis in our laboratory. It was found that Ni crystal size had a significant effect on the TOF. Therefore, an accurate determination of Ni crystal size is important to achieve a deep understanding of the relationship between the catalytic structure and the activity. The present work deals with a comparatively study for determining Ni crystal size and distribution by means of different techniques, and in particular the effect of preparation method on the Ni structure and distribution.

2. Experimental

2.1 Catalyst preparation

A series of hydrotalcite-based Ni catalysts has been prepared by two different methods: (a) incipient wetness impregnation using different commercial hydrotalcites as supports and (b) co-precipitation of nickel together with the different hydrotalcite precursor salts. Catalyst composition and BET surface area are given in Table 1.

(a) Three different commercial hydrotalcites from Condea were used as supports: HT30 (MgO/Al_2O_3 = 30/70), HT50 (MgO/Al_2O_3 = 50/50) and HT70 (MgO/Al_2O_3 = 70/30). The supports were impregnated with nickel-nitrate by the incipient wetness technique to obtain 12.5 wt% nickel on the carrier. The catalysts were dried for 16h at 373K and calcined at 873K for 4h after being heated at a rate of 4K/min.

(b) Two different catalyst were prepared by co-precipitation of $Mg(NO_3)_3$, $Al(NO_3)_3$ and $Ni(NO_3)_2$ to obtain 12.5 wt% Ni (Ni/HT) and 40 wt% Ni (40Ni/HT), respectively. The atomic ratio, $M^{2+}/(M^{2+}M^{3+})$, was fixed at 0.25. The samples were prepared according to following procedure. A 1l, three-neck flask equipped with a thermometer, a reflux condenser, and mechanical stirrer was charged with 400 ml deionized water and the calculated amounts of Na_2CO_3 and NaOH. A second solution containing calculated amounts of the Ni, Mg and Al precursor salts and 400 ml of deionized water was prepared. The second solution was added dropwise to the first solution while stirring for a period of about 2 hours. After the addition was completed, the pH value of the mixture was adjusted to between 8 and 9 and the mixture was then heated for about 15 hours at 353-358 K. The resultant gel was cooled, filtered and thoroughly washed. The catalysts

were dried overnight under vacuum at 343 K, heated to 873K at 4K/min and calcined at 873K for 6 h.

2.2 BET surface area

The BET surface area of the supports was measured by N_2 adsorption at 77K in Coulter^{TM} SA 3100. Prior to the measurements the samples were dried under vacuum at 423K for 1 hour.

2.3 H_2 chemisorption measurements

H_2 adsorption isotherms were measured at 308K in ASAP 2000. Before measurements, the catalysts were reduced in flowing H_2 at 903K for 12h (10K/min from ambient to 903K). The samples were evacuated for 0.5h at 903K before cooling to 308K and the adsorption isotherm between 5 and 300 Torr was measured. Assuming spherical Ni crystals, the crystal size (d) was determined from the dispersion (D) of the Ni particles [13]:

$$d = 101/D \qquad \text{where } [d = nm,\ D = \%] \qquad (2)$$

2.4 X-ray diffraction (XRD)

X-ray diffraction studies were performed in a Simens D5000 X-ray diffractometer. Phase identifications were carried out by comparing the collected spectra with spectra in the database. The measurements were done on calcined catalysts. The particle sizes were calculated in two ways, (a) using the Scherrer formula [14] based on peak broadening, providing average particle sizes and neglecting the strain and (b) using Fourier methods based on the shape of the peak, providing particle size and strain distributions. For this last purpose, the analysis of the experimental data was performed in two steps. The experimental XRD peaks were first simulated by means of the software *Profile* [15], where several models can be selected to fit the experimental data. The Pearson VII-Lm model gave the best fit. This model is a combination of two basic peak profiles: Gaussian and Cauchy. The Gaussian broadening is due to the strain in the crystal, whereas the Cauchy broadening is due to the crystallite size. The program

Crysize [16] was then used to estimate the crystallite size and microstrain distributions based on the data obtained from *Profile.* LaB_6 was used as a standard reference to take into account the equipment contribution. LaB_6 does not exhibit any line broadening from the crystallite size or strain, and the width of the peaks is hence solely due to instrumental broadening.

2.5 Transmission electron microscopy (TEM)

The diameter of the Ni-particles was measured by a JEOL 2000EXII high resolution transmission electron microscopy. TEM specimens were prepared by ultrasonic dispersion of the slightly ground catalyst samples in ethanol, and a drop of the suspension was applied to a holey carbon copper grid.

2.6 Scanning transmission electron microscope (STEM)

The Ni catalysts have also been examined by means of STEM, which was performed with the JEOL 2000EXII electron microscope equipped with a field emission gun capable of giving a lattice resolution of 0.14 nm. Both bright field and annual dark field image were performed in order to obtain a better contrast of the Ni particles against support materials.

2.7 Temperature programmed reduction (TPR)

The TPR experiments were performed in a quartz micro-reactor heated by an electrical furnace. The experiments involved heating of 0.2g catalyst at a rate of 4K/min to 1173K with a gas consisting of 7% H_2 in Ar. The H_2 consumption was measured by analyzing the effluent gas with a thermal conductivity detector. The steam formed during the reduction was removed by a cooling trap.

3. Results and discussion

3.1 Temperature programmed reduction

TPR profiles for the different Ni catalysts are shown in Figure 1. The Ni catalysts exhibit very different reduction behavior. The temperatures of the larger peak in the TPR spectra are found at 690, 690, 1080, 1047 and 1110 K for NiO/HT70, NiO/HT50,

NiO/HT30, Ni/HT and 40Ni/HT, respectively. However, all the catalysts have two reduction peaks. The low temperature peaks are in the area of 600-775K, while the high temperature peaks are at 1047-1115K. The low temperature reduction peak increases in size with increasing Mg/Al ratio in the catalysts prepared by impregnation of the commercial supports. The high temperature peak is of the same size for NiO/HT30, Ni/HT and 40Ni/HT, but much smaller for NiO/HT50 and NiO/HT70. For the first peak the opposite trend is observed.

The low temperature peak results from reduction of Ni^{2+} in the NiO phase [17], while the high temperature peak most probably corresponds to the Ni^{2+} in the mixed metal oxide phase ($Mg_xN_{1-x}O$) [18]. Schulze et al. [18] found that calcined hydrotalcites containing Al, Mg and Ni had only one reduction peak, corresponding to the Ni^{2+} in the mixed metal oxide phase. They also reported that the reduction peak shifted towards lower temperature with decreasing nickel / magnesium ratio in the hydrotalcites. This is in agreement with the slightly lower temperature of the high temperature reduction peak for NiO/HT30. Fornasari et al. [2] also found that Mg-rich samples had reduced reducibility due to the formation of NiO/MgO solid solution.

NiO crystals in hydrotalcite derived catalysts are known to be difficult to reduce [2, 19-21]. Figure 1 shows that NiO/HT30 and the samples prepared by coprecipitation are much more difficult to reduce than NiO/HT50 and NiO/HT70. Isotherm reduction in 50% H_2 in Ar, at a total flow of 100ml/min and a temperature of 1123K was performed in the Tapered Element Oscillating Microbalance (TEOM). These experiments also showed that NiO/HT70 (873) is more easily reduced than NiO/HT30 (Figure 2). The different reduction behavior could be explained by the incorporation of Ni into the hydrotalcite structure [12, 22]. Chen et al. [12] proposed that Ni^{2+} ions might penetrate into the space between two layers of the hydrotalcite during the preparation and replace part of Mg^{2+}. The chemically bonded Ni in the hydrotalcite structure is then more difficult to reduce. This theory is supported by the XRD study, where the mixed metal oxide diffraction peaks are identified as the main phase ($NiAl_2O_4$, Ni-MgO) and will be discussed in detail later in this section. In addition, Richardson [23] found a decrease in the NiO crystal size with increasing reduction temperature. Accordingly, NiO/HT30, Ni/HT and 40Ni/HT catalysts with crystal sizes of 12, 10 and 10 nm respectively, present the highest maximum reduction temperatures.

The TPR results is an indication of the strong interaction between the catalyst and the hydrotalcite derived support in the case of incorporation of Ni into the hydrotalcite structure itself. For example, commercial Ni based catalysts with α-Al_2O_3 as the support present low reduction temperatures, close to the maximum reduction temperature of bulk NiO [24]. Higher temperatures are found for Ni in hydrotalcites (>1000 K) because of the mixed oxide phase. This results in stronger interactions and as hence smaller metallic particles. Bulk NiO and $NiAl_2O_4$ give reductions peaks at 493 and 1063K, respectively [25].

3.2 X-ray diffraction

Due to the high calcination temperature at 873K, the hydrotalcite-based catalysts have lost their hydrotalcite structure and become mixed oxides [26]. The XRD profiles in Figure 3 indicate that neither Al_2O_3, MgO nor Al_2MgO_4 exists in NiO/HT50 and NiO/HT70. For NiO/HT30 and Ni/HT the peaks for NiO at 43° and 63° are much lower and broader. It is assumed that this is an indication of the incorporation of NiO into the hydrotalcite structure. NiO looses its nature and results in a mixed metallic oxide or a spinel phase ($NiAl_2O_4$ or $MgAl_2O_4$). However, overlapping diffraction peaks make it difficult to distinguish between NiO, MgO and Ni/MgO at 37, 43, 63 and 79°. NiO/HT30 shows broader peaks with a higher degree of noise than NiO/HT50 and NiO/HT70. This indicates relatively lower degree of crystallinity. Indication of an MgAl spinel phase was not found for any of the catalysts.

3.3 Scanning transmission electron microscope and transmission electron spectroscope

Several of the catalysts were examined by STEM and TEM. As examples STEM and TEM examinations of 40Ni/HT prepared by coprecipitation are given in Figure 4 and 5. According to Figure 4, a relatively good contrast is obtained by the annular dark field image. The visible spots in Figure 4A were confirmed to be Ni particles by Energy Dispersive Spectroscopy (EDS) maps as shown in Figure 4. The EDS maps also indicate that Mg and Al are well distributed on the surface of the catalysts prepared by

the co-precipitation route. As reported elsewhere [12], the same results were obtained for catalyst prepared by impregnation of the commercial hydrotalcite support. An annular dark field TEM picture of 40Ni/HT is shown in Figure 5. The average crystal size is 10 nm, which is in good agreement with the size measured by chemisorption and XRD as shown in Table 2. A good contrast is also obtained for annular dark field images for NiO/HT50, but due to smaller crystal size [12] the contrast obtained for NiO/HT30 is not as good. The average Ni crystal size on NiO/HT30 and NiO/HT50 is 12nm and 22nm, respectively, which is also in good agreement with the size observed from chemisorption and XRD (Table 2).

3.4 Particle size and distribution

The estimated Ni particle size based on chemisorption, XRD and TEM/STEM is presented in Table 2. In the XRD study an effort has been made to determining the Ni crystal size. The samples have been prereduced and passivated in an air/Ar (10/90) atmosphere at room temperature. Two peaks, Ni and NiO, respectively were observed making it difficult to determine a precise crystal size. The Ni particle size determined from chemisorption is in good agreement with the NiO crystal size measured by XRD and TEM/STEM, except from Ni/HT that shows a considerable larger diameter from H_2 chemisorption than expected from the XRD and TEM investigation. As already discussed TPR indicates that the incorporation of Ni in the hydrotalcite structure in Ni/HT makes the NiO very difficult to reduce. An incomplete reduction of nickel oxide could therefore be the reason for the low dispersion. Chen et al. [12] reported that reduced Ni crystals were only slightly smaller than the NiO crystals. Therefore, Ni and NiO crystal sizes are not clearly distinguished in the discussion. The Table 2 shows an increase in the particle size with increasing MgO/Al_2O_3 ratio in the support. A possible explanation could be the influence of the surface area of the supports. Larger surface areas provide more surface active sites, resulting in a larger dispersion and as consequence smaller crystal sizes. However, this explanation is not valid for the Ni catalysts that were prepared by coprecipitation. Ni/HT and 40Ni/HT exhibit the lower surface area but they have the smallest crystal sizes.

The crystal size determined from chemisorption strongly depends on the degree of reduction. As discussed in the TPR part, the largest particles will be reduced first [23]. Incomplete reduction would therefore give a too large average particle sizes from chemisorption measurements. The effect of the degree of reduction is illustrated in Table 3 where the particle size from chemisorption of the catalysts reduced for only 2h at 903K is given. The difference in reduction regime in Table 2 and Table 3 is the time kept at 903K, 12h in Table 2 and 2h in Table 3. Table 2 and 3 show that shorter reduction time gives remarkably larger Ni particle sizes. Another disadvantage concerning H_2 chemisorption is that the adsorption time can influence on the amount of H_2 adsorbed. Stockwell et al. [27] have reported that for H_2 chemisorption on Ni/Al_2O_3 the isobars pass through a maximum at about 373K, meaning that at 298K kinetic factors (adsorption time) have an important influence on the amount of H_2 adsorbed. According to Che et al. [28] it is very difficult to calibrate the H_2 chemisorption for particles smaller than 3nm.

In this study the Ni particle size from XRD is determined by two methods: The line broadening analysis (LBA) and the Fourier method. LBA is considered to be a reliable method for particles in the range of 1.5 to 100nm [28]. For very small particles the reflections from the different solid phases might be superimposed due to overlapping of neighboring reflections such as the (111) and (200) lines in fcc metals [28]. With increasing amount of metal the wings of the line profiles become weak and the smaller particles are not taken into account. As a result the LBA becomes less accurate and the particle size distribution shifts towards larger particle size [28]. Another limitation of the use of the Scherrer equation is that it does not consider the line broadening caused by the microstrain. Strain is defined as the deformation of an object divided by its ideal length. In crystals two types of strain can be observed. Uniform strain causes the unit cell to expand/contract in an isotropic way. This leads to a change in the unit cell parameters and a shift of the peaks. There is no broadening associated with this type of strain. However, non-uniform strain leads to systematic shifts of atoms from their ideal positions and to peak broadening. The advantage of the Fourier method is that, in addition to produce a crystallite size distribution, it can separate more accurately the instrumental broadening and the sample broadening effects. However, the disadvantage of the Fourier method is that it is more prone to errors when peak overlap

is significant. In this case, it is more difficult to determine the entire peak shape accurately than it is to determine the full width at half maximum (FWHM). As discussed above, overlapping peaks make it difficult to distinguish between NiO, MgO and NiMgO phases in the case of Ni based hydrotalcite. However, similar crystallite sizes were calculated by the Scherrer equation and by the Fourier method. Figure 6 shows a typical crystal size and strain distribution for one of the studied catalysts. The average crystal size in this case was 11 nm, in accordance with the crystal size calculated by Scherrer equation. As shown in Figure 6 the catalyst also presents some strain, indicating the strong interaction of Ni with the support in the hydrotalcite structure. A comparison between the Ni particle size distributions obtained from XRD and TEM (Figure 6) shows a that the particle size distribution from XRD is shifted towards smaller particles compared to the distribution from TEM. One reason for this could be that neighboring reflections from the same crystal are detected as different crystals, and hence a smaller crystal size will be observed from XRD.

The development over the last years in electron microscopes has been tremendously. TEM can achieve magnifications on the order of one million times and reveal details with a resolution of about 0.1 nm [14]. The advantages from the use of electron microscopy are many [28]:

- Particle size distribution can be obtained
- Average particle size can be derived
- Electron microscope can be used to determine whether the particles are evenly distributed of paced up in larger aggregates
- For large particles, shape and crystal structure can be determined

Determination of particle sizes and particle size distributions by TEM has become a matter of routine for many systems. However, it rests on the assumption that the size of the imaged particle is truly proportional to the size of the actual particle and that the detection probability is the same for all the particles, independent of their dimensions [14]. In order to ensure that the results are representative for a sample a number of images must be investigated at different parts of the sample. This is time consuming. Small metal particles may be affected by the support crystallinity [29],

orientation of particles and imaging conditions. For particles smaller than 2.5nm an increasing unreliability appears from the bright-field technique [29, 30].

3.5 Effect of preparation method

A comparison of the two preparation methods, impregnation and co-precipitation, can be done by a simple comparison between Ni/HT and Ni/HT70. As shown in Table 1 the catalysts have the same composition, but were prepared by a different route. The catalyst prepared by coprecipitation (Ni/HT) has a surface area of 134 m^2/g, significantly lower than the catalyst impregnated on commercial support (NiO/HT70), 228 m^2/g. However, the dispersion of metallic Ni is better on Ni/HT, resulting in much smaller particles. As discussed above, direct coprecipitation of the Ni together with the Mg and Al oxides, results in Ni ions incorporated into the hydrotalcite structure and dispersed in octahedral sites in the layered hydrotalcite. This is in accordance with the XRD results which showed a mixed metallic oxide phase. The strongly interacted Ni in the hydrotalcite structure is more difficult to reduce and hence the Ni crystals are much smaller. In addition, catalysts with high Ni loading can also be prepared by the coprecipitation route. Dispersion and crystal size remained unchanged as the Ni loading was increased up to 40% (40Ni/HT) indicating that the direct synthesis of Ni based hydrotalcite is a promising way for preparation of small sized nanocrystals, which is also in accordance with other reports [4].

3.6 Structure of support

In those cases were Al_2O_3 and MgO exists, a good crystallinity of such monoxides is expected at the calcination temperature used in the present work. However, only a week signal was detected at 35˚ indicating Al_2O_3. The results suggest that the Al_2O_3 and MgO mixture exists as an amorphous structure. The EDX analysis in Figure 4 clearly shows that the Al and Mg oxides are very well mixed, indicating a solid solution. The strong bond between Al and Mg in the solid solution makes it difficult to form separate phases of Al_2O_3 and MgO. In addition the calciation temperature is not high enough to form a crystalline Al_2MgO_4 phase. In conclusion, combined XRD and

EDX clearly suggests that hydrotalcite derived supports exists as an amorphous solid solution. This might be the reason for the significant sintering observed in the sintering experiment at steam reforming conditions [3].

4. Conclusions

Chemisorption, XRD and TEM/STEM gave almost identical Ni crystal sizes for the different catalysts examined. Nevertheless, all the different techniques present some limitations. Due to apparatus restrictions particles smaller than 2nm are difficult to measure in XRD. Such small particles are also difficult to reduce and hence seldom detected in chemisorption. TEM and STEM seem to be the most promising techniques for determining the Ni crystal size, especially for the smallest crystal sizes. Several catalyst samples must be examined to ensure a representative selection. In order to find the correct crystal size, it is advantageous to examine the crystal size by more than one technique.

Hydrotalcite derived oxide mixtures are good supports providing efficient anchoring sites for Ni nanoparticles. The Mg / Al ratio seems to have an effect on the dispersion, and a low ratio yields a better dispersion of Ni nanoparticles. The co-precipitation route results in an even stronger interaction between the support and the nickel providing smaller crystals. The co-precipitation route also gives stable particle sizes at increasing Ni loadings.

Acknowledgments

The Norwegian Research Council (NFR), Norsk Hydro and Statoil are acknowledged for the financial support. John Walmsley is acknowledged for the TEM/STEM images.

References

[1] A. Bhattacharyya, V. W. Chang and D. J. Schumacher, *Appl. Clay Sci.* **13** (1998) 317

[2] G. Fornasari, M. Gazzano, D. Matteuzzi, F. Trifirò and A. Vaccari, *Appl. Clay Sci.* **10** (1995) 69

[3] K. O. Christensen, D. Chen, R. Lødeng and A. Holmen, *Submitted*

[4] F. Cavani, F. Trifirò and A. Vaccari, *Catal. Today* **11** (1991) 173

[5] J. Sehested, A. Carlsson, T. V. W. Janssens, P. L. Hansen and A. K. Datye, *J. Catal.* **197** (2001) 200

[6] J. Panpranot, K. Pattamakomsan, P. Praserthdam and J. G. J. Goodwin, *Ind. Eng. Chem. Res.* **43** (2004) 6014

[7] C. D. Saquing, T. Cheng, M. Aindow and C. Erkey, *J. Phys. Chem. B* **108** (2004) 7716

[8] S. Yin, Q. -H. Zhang, B. -Q. Xu, W. -X. Zhu, C. -F. Ng and C. Au, *J. Catal.* **224** (2004) 384

[9] S. Lambert, C. Cellier, P. Grange, J. Pirard and B. Heinrichs, *J. Catal.* **221** (2004) 335

[10] J. M. Jablonski, J. Okal, D. Potoczna-Petru and L. Krajczyk, *J. Catal.* **220** (2003) 146

[11] W. Zhou, Z. Zhou, S. Song, W. Li, G. Sun, P. Tsiakaras and Q. Xin, *Appl. Catal. B* **46** (2003) 273

[12] D. Chen, K. O. Christensen, E. Ochoa-Fernández, Z. Yu, B. Tøtdal, N. Latorre, A. Monzón and A. Holmen, *J. Catal.* **229** (2004) 87

[13] J. L. Lemaitre, P. G. Menon and F. Delannay, *Characterisation of heterogenous catalysts*. (F. Delannay, ed.), **15** Marcel Dekker inc, New York, 1984

[14] J. W. Niemantsverdriet, Spectroscopy in Catalysis. Wiley-VCH, Weinheim, 2000.

[15] Diffracplus Profile, Profile fitting program. User's manual, Siemens.

[16] Diffracplus Win-crysize, Crystallite Size and Microstrain. User's manual, Analytical X-Ray Siemens.

[17] T. Shishido, M. Sukenobu, H. Morioka, M. Kondo, Y. Wang, K. Takaki and K. Takehira, *Appl. Catal.* **223** (2002) 35

[18] K. Schulze, W. Makowski, R. Chyy, R. Dziembaj and G. Günter, *Appl. Clay Sci.* **18** (2001) 59

[19] F. Trifirò, A. Vaccari and O. Clause, *Catal. Today* **21** (1994) 185

[20] O. Clause, M. Gazzano, F. Trifirò and A. Vaccari, *Appl. Catal.* **73** (1991) 217

[21] O. Clause, M. Goncalves Coelho, M. Gazzano, D. Matteuzzi, F. Trifiro and A. Vaccari, *Appl. Clay Sci.* **8** (1993) 169

[22] E. Bjørgum, D. Chen, M. G. Bakken, K. O. Christensen, A. Holmen, O. Lytken and I. Chorkendorff, *J. Phys. Chem.* B **109** (2005) 2360

[23] Richardson, J T, R. M. Scates and M. V. Twigg, *Appl. Catal.* **267** (2004) 35

[24] M. V. Twigg and J. T. Richardson, *Appl. Catal.* **190** (2000) 61

[25] C. Li and Y. Chen, *Thermochim. Acta* **256** (1995) 457

[26] A. Bhattacharyya, V. W. Chang and D. J. Schumacher, *Appl. Clay Sci.* **13** (1998) 317

[27] D. M. Stockwell, A. Bertucco, G. W. Coulston and C. O. Bennett, *J. Catal.* **113** (1988) 317

[28] M. Che and C. O. Bennett, *Adv. Catal.* **36** (1989) 55

[29] G. R. Millward, *J. Catal.* **64** (1980) 381

[30] P. C. Flynn, S. E. Wanke and P. S. Turner, *J. Catal.* **33** (1974) 233

Table 1: Catalyst composition and BET surface area (S_{BET}). HT30, HT50 and HT70 are commercial hydrotalcites with a ratio between MgO and Al_2O_3 of 30/70, 50/50 and 70/30, respectively. Ni/HT and 40 Ni/HT are prepared by co-precipitation as described in the text.

Catalyst	NiO [%]	MgO [%]	Al_2O_3 [%]	Calcination temperature [K]	S_{BET} [m^2/g_{cat}]
NiO/HT30	15.9	24.5	59.6	973	271
NiO/HT50	15.9	42.6	41.5	973	201
NiO/HT70	15.9	59.5	24.6	973	228
Ni/HT	15.9	60.1	24	873	134
40Ni/HT	50.9			873	134

Table 2: Particle size of different Ni catalysts. HT30, HT50 and HT70 are commercial hydrotalcites with a ratio between MgO and Al_2O_3 of 30/70, 50/50 and 70/30, respectively. Ni/HT and 40 Ni/HT are prepared by co-precipitation as described in the text.

Catalyst	Particle size [nm]		
	Chemisorption, Ni	XRD, NiO	TEM/STEM, NiO
NiO/HT30	12	12	12
NiO/HT50	24	24	22
NiO/HT70	24	29	-
Ni/HT	20	10	10
40Ni/HT	11	9	10

Table 3: Particle size of Ni determined from H_2 chemisorption. The catalysts have been reduced for 2h at 903K for 2h, using a heating rate of 10K/min from ambient to 903K. HT30, HT50 and HT70 are commercial hydrotalcites with a ratio between MgO and Al_2O_3 of 30/70, 50/50 and 70/30, respectively. Ni/HT and 40 Ni/HT are prepared by co-precipitation as described in the text.

Catalyst	Particle size [nm]
NiO/HT30	20
NiO/HT50	62
NiO/HT70	32

Figure captions

Figure 1. Temperature programmed reduction spectra of the different Ni catalysts. Heating rate: 4K/min, Reduction gas: 7% H_2 in Ar

Figure 2. Isotherm reduction of NiO/HT30 and NiO/HT70 (873) in the TEOM. Reduction gas: 50% H_2 in Ar, at a total flow of 100ml/min. Reduction temperature: 853K

Figure 3. XRD profiles of (a)NiHT, (b) NiO/HT30, (c) NiO/HT50 and (d) NiO/HT70. Phases identified: (●) nickel oxide, (○) magnesium nickel oxide, (■) nickel aluminum oxide and (□) alumina

Figure 4. EDS images of 40Ni/HT. A: STEM, dark field image, B: Energy dispersive X-ray (EDX) analysis. Right side: EDS maps of magnesium, aluminum and nickel.

Figure 5. Dark field TEM image of 40Ni/HT

Figure 6. (a) Crystal size distribution calculated by the Fourier method and from TEM / STEM measurements (dotted line) (b) Microstrain distribution of NiO/HT30 calculated by the Fourier method

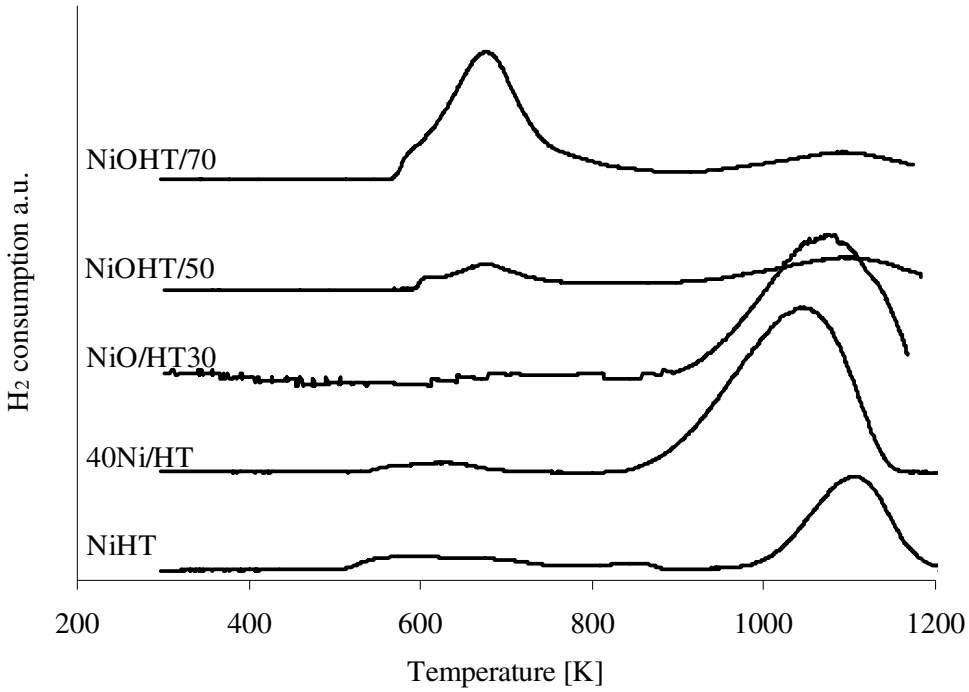
NiOHT/70
NiOHT/50
NiO/HT30
40Ni/HT
NiHT
H2 consumption a.u.
200
400
600
800
1000
1200
Temperature [K]

Figure 1

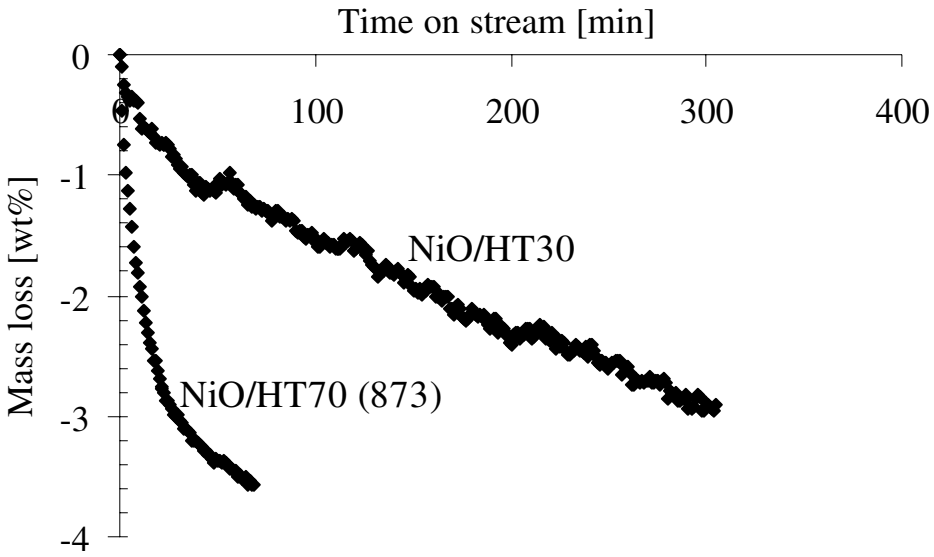
Time on stream [min]
0
100
200
300
400
0
-1
-2
-3
-4
Mass loss [wt%]
NiO/HT30
NiO/HT70 (873)

Figure 2

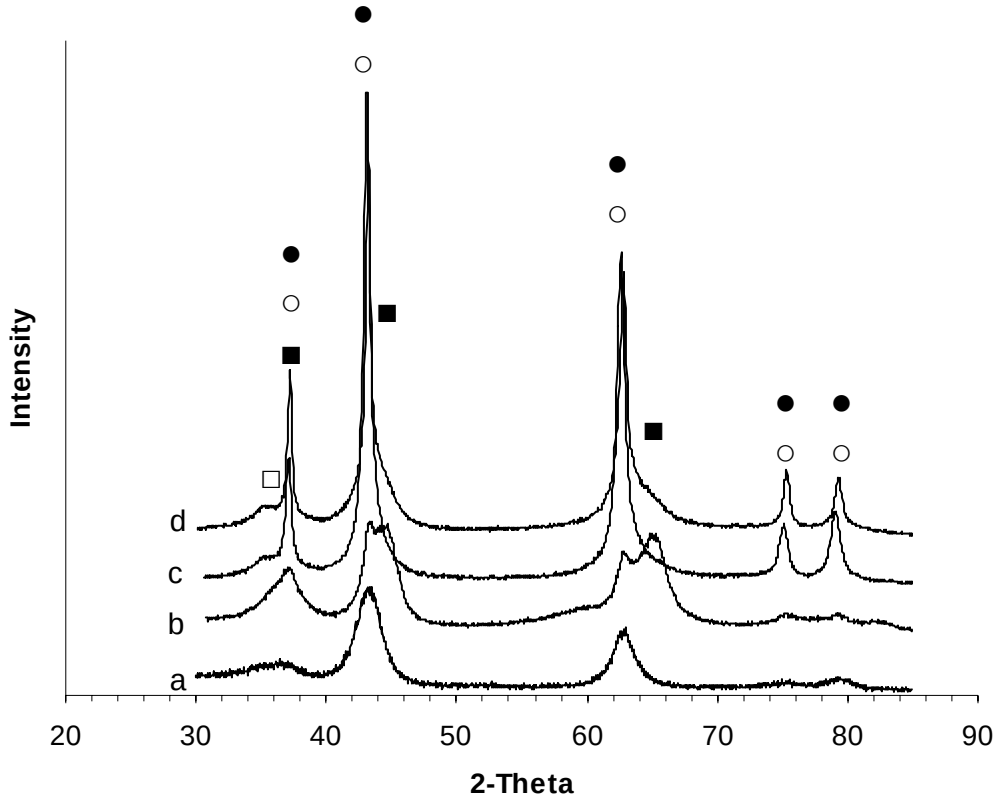

Figure 3

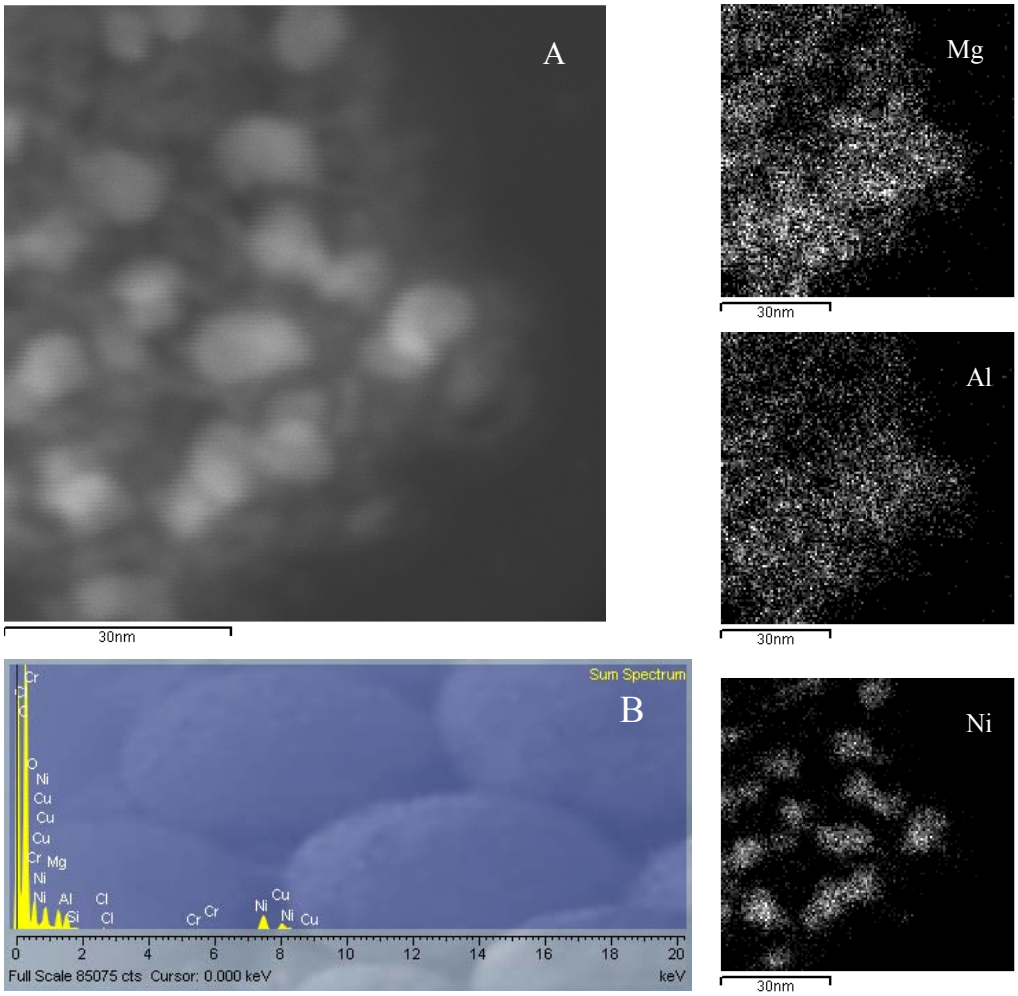
A
30nm
Mg
30nm
Al
30nm
Ni
30nm
Sum Spectrum
B
Cr
O
Ni
Cu
Cu
Cu
Cr
Mg
Ni
Ni
Al
Si
Cl
Cl
Cr
Cr
Ni
Cu
Ni
Cu
0
2
4
6
8
10
12
14
16
18
20
Full Scale 85075 cts Cursor: 0.000 keV
keV

Figure 4

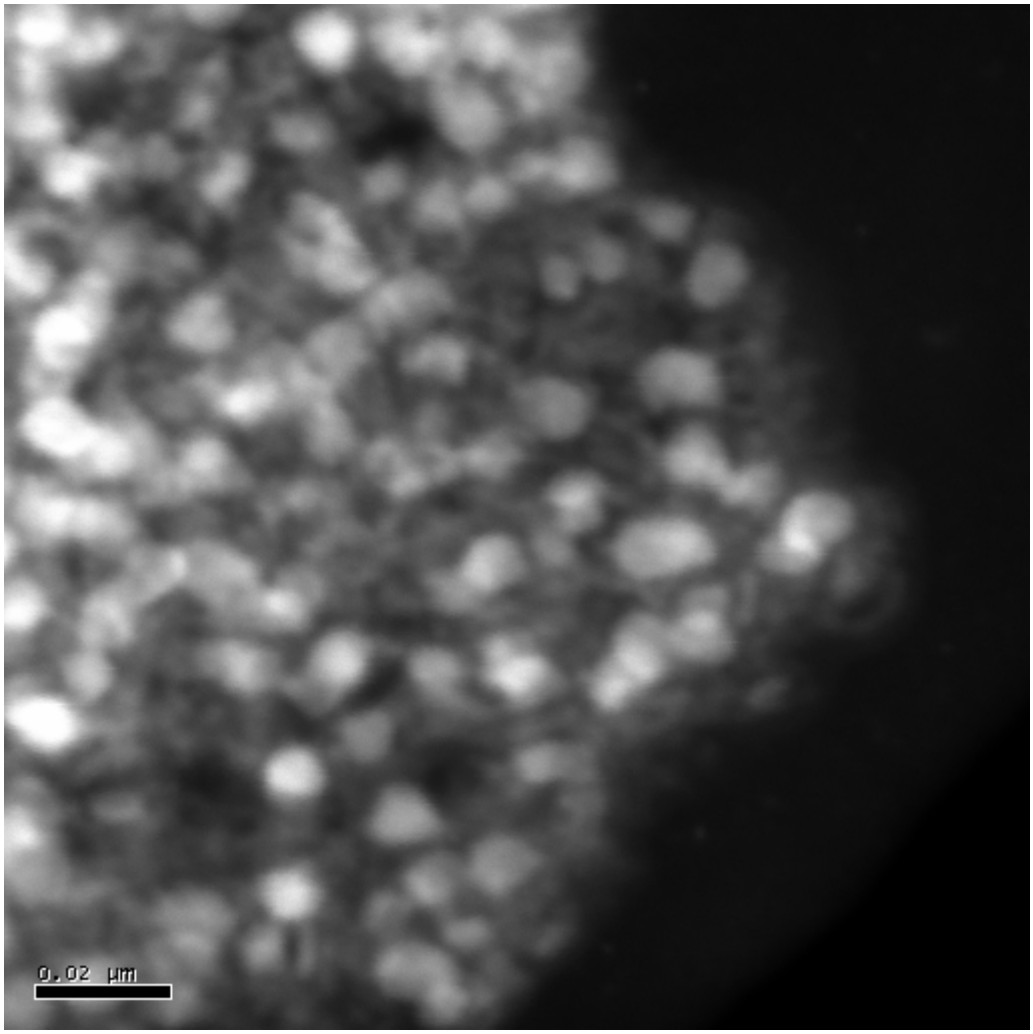

Figure 5

(a)

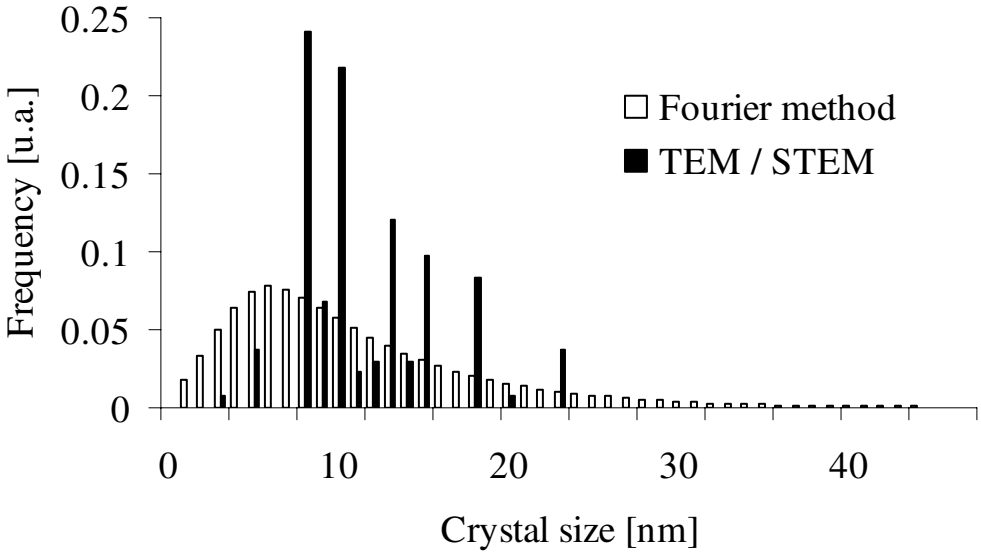
0.25
0.2
0.15
0.1
0.05
0
Frequency [u.a.]
Fourier method
TEM / STEM
0
10
20
30
40
Crystal size [nm]

(b)

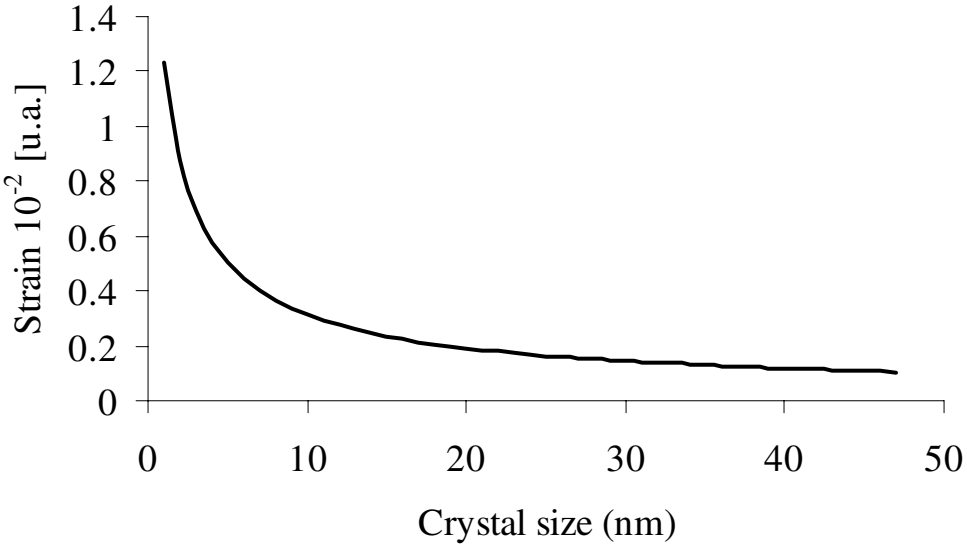
1.4
1.2
1
0.8
0.6
0.4
0.2
0
Strain 10^{-2} [u.a.]
0
10
20
30
40
50
Crystal size (nm)

Figure 6

Paper III

In situ catalyst characterization by the oscillating microbalance catalytic reactor (TEOM)

In situ Catalyst Characterization by the Oscillating Microbalance Catalytic Reactor (TEOM)

Erlend Bjørgum[1], Kjersti Omdahl Christensen[1], Rune Lødeng[2], De Chen[1] and Anders Holmen[1]

[1]Department of Chemical Engineering, Norwegian University of Science and Technology (NTNU), N-7491 Trondheim, Norway. [2]SINTEF Materials and Chemistry, N-7465 Trondheim, Norway.

Table of contents

Abstract

The present review deals with the use of the Tapered Element Oscillating Microbalance for *in situ* studies of catalytic reactions. It combines the advantage of a microbalance for measuring mass changes in the catalyst bed and the fixed-bed micro reactor for performing kinetic studies. In the TEOM the mass is detected as a change in its vibrational frequency thus avoiding the problem of bypassing in a conventional microbalance. It is shown that the TEOM is a powerful tool for *in situ* studies by using two examples: Methanol to olefins over SAPO-34 and steam reforming of natural gas on Ni catalysts. A comprehensive literature survey of the use of TEOM is also given.

Abbrevations

DTO	Dimethylether to olefins
GC	Gas chromatograph
MS	Mass spectrograph
MTO	Methanol to olefins
PR-F	Fresh prereforming catalyst
PR-S	Stabilized prereforming catalyst
SAPO-34	Silica alumina-phosphate
SMR	Steam methane reforming
SR-F	Fresh steam reforming catalyst
TEOM	Tapered element oscillating microbalance

ZLB	Zero length bed
ZLC	Zero length column
C	Concentration
D	Diffusivity
D_{SS}	Steady-state diffusivity
f	Natural frequency of the spring-mass system
K	Equilibrium constant
K_0	Spring constant
m	Mass
m_t	Adsorbed amount at time t
m_∞	Adsorbed amount at infinite time
p	Partial pressure in the gas phase
q	Concentration in adsorbed phase
S	Selectivity (hydrocarbon basis)
S0	Initial selectivity (hydrocarbon basis)
t	Time
WHSV	Weight hourly space velocity
X	Conversion

1. Introduction

Many catalytic processes involving hydrocarbons are accompanied by deactivation as a result of coke formation. In quantifying the effect of coke on the catalyst activity, knowledge about the rate of coke deposition is necessary. By using a microbalance the coke content on the catalyst can be measured continuously during reaction. Combining such *in situ* measurements of the coke formation by on-line gas chromatography or mass spectroscopy, the catalyst activity and selectivity can be determined as a function of time on stream, and thus also as a function of the coke content.

Unfortunately, a main disadvantage of the conventional microbalance is that a large part of the feed bypasses the catalyst basket. The large bypass makes it very difficult to

confirm differential operation in the conventional microbalance. In order to obtain a uniform coke level and to measure the catalyst activity gradientless operation is necessary. The development of the inertial microbalance (TEOM – Tapered Element Oscillating Microbalance), however, avoids the problems of bypass [1, 2]. In the inertial microbalance the mass located at the tip of an oscillating tapered quartz element is detected as a change in its vibrational frequency. The new design provides a packed bed of catalyst through which all the gas is forced to flow. The classical methods of testing for differential operation in a fixed-bed reactor can therefore also be used with this new inertial microbalance.

TEOM was originally developed for measuring concentrations of solid particulates in gases [1]. In addition to particulate measurements in different environments (in space, in air, in exhaust streams) the technology has been gradually extended into a very powerful tool for *in situ* studies of catalytic reactions [2, 3, 4]. Processes involving mass changes such as carbon formation, can very conveniently be studied. The high mass resolution and the short response time make this technique also particularly suitable for studying adsorption and diffusion in porous catalytic materials.

2. The principle of mass measurement by TEOM

The reactor (Fig. 1) is made up of a hollow quartz ("engineered glass") tube with a material test bed located at the tip of the quartz element. Catalyst particles held in place by packed quartz wool and a metal cap, fill up the material test bed. As gas flows through the tapered element and the catalyst bed, the system records changes in the mass of the catalyst bed as a result of interactions with the gas stream.

The principle of operation and the equations governing the TEOM are those of a cantilever beam mass-spring system [5]:

$$f^2 = K_0 / m \qquad (1)$$

where f = natural frequency of the spring-mass system, K_0 = spring (tapered element) constant and m = total oscillating mass consisting of the material bed mass (m_s), the mass of the tapered element (m_t) and the changes in mass (Δm):

$$m = m_s + m_t + \Delta m \tag{2}$$

If an experiment starts with a given catalyst mass in the test bed:

$$m_1 = K_0 \cdot \frac{1}{f_1^2} \tag{3}$$

If mass is lost or increased during the course of an experiment, the following applies:

$$m_2 = K_0 \cdot \frac{1}{f_2^2} \tag{4}$$

The change in mass in the catalyst test bed between time 1 and 2 is then simply:

$$\Delta m = m_2 - m_1 = K_0 \left(\frac{1}{f_2^2} - \frac{1}{f_1^2} \right) \tag{5}$$

In order to determine the change in mass, only the frequencies and the spring constant are required. Equation (5) is independent of the mass of the catalyst bed (m_s) and the mass of the tapered oscillating tube (m_t). The spring constant (K_0) is unique for each tapered element and must be determined by calibration using known masses.

Changes in the natural frequency of the fixed-bed reactor element are thus correlated to changes in the mass as described by Equation (5).

Since the tapered element has to vibrate freely, it is impossible to connect the sample cell outlet directly to a gas chromatograph (GC) or a mass spectrometre (MS) for

analysis. A purge gas is passed along the outside of the tube to collect and sweep the reactor effluent as it exists from the tapered element.

The major features of the TEOM reactor can be summerized as follows:

- Direct, real-time mass change measurement of the sample bed.
- 1 μg mass sensitivity.
- 0,1 sec time resolution capability.
- 700 ^{o}C or 900 ^{o}C temperature capability for mass measurements.
- Pressures up to 50 bars.
- 50 to 200 mg sample capabilities.
- The reactant gases are forced to flow through the packed sample bed.
- The gas streams are in contact with only stainless steel and glass

3. Description of a TEOM experimental set-up

Fig. 2 represents a flow diagram of an oscillating microbalance reactor used for studying steam reforming catalysts at high pressures (< 40 bars) using steam and high temperatures (< 700 ^{o}C) [6]. The experimental set-up in Fig. 2 has also been used for *in situ* low pressure studies such as methanol to olefins [7], catalytic dehydrogenation [8], formation of carbon nanofibers [9].

The set-up consists of a feeding system, the reactor section, a GC and a MS for product analysis.

A Rupprecht and Patashnick TEOM 1500 PMA (Pulse Mass Analyzer) was used in the experimental set-up shown in Fig. 2. The reactor tube is constructed of proprietary glass ("engineered glass") [5] material with a high mechanical quality factor. The reactor material has proved to be sufficiently inert for a number of applications. The catalyst bed is held in place by quartz, α-alumina or carbon wool depending on the conditions.

The metal cap may influence the measurements. Different metal caps are used including the standard Ni cap, a gold plated Ni cap or more recently a Si coated Ni cap. Ni is a good catalyst for carbon formation and the measurements may thereby be falsified by carbon formation on the metal cap. Oxidation of reduced Ni results in similar problems. The experience with the recent developed Si coated caps is, however, very promising.

The reaction temperature can normally not be measured directly inside the catalyst bed during an experiment without disturbing or lowering the sensitivity of the mass measurements considerably. The reactor in Figs. 1 & 2 is equipped with two thermocouples, one is positioned outside the reactor for measuring the wall temperature of the catalyst bed and one immediately below the reactor exit. An alternative approach for measuring the reaction temperature is to perform preliminarily experiments with a thermocouple inserted through the reactor feed line and down into the catalyst bed, aimed solely at obtaining a calibration between the catalyst bed temperature and the reactor wall temperature measured by the thermocouple on the outside of the reactor wall. Subsequent experiments should then normally be performed without a thermocouple inserted in the sample.

The experimental set-up in Fig. 2 is equipped with a gas manifold with mass-flow controllers for supplying feed and carrier gases. Water or other liquids are supplied from a 5 l storage cylinder which is pressurized by nitrogen to a level sufficiently above the test conditions. A liquid flow controller is regulating the amount which is subsequently injected into an evaporator. The set-up includes the possibility to preheat all the feed lines and the exit line up-stream of the condensation cylinders. Cryogenic baths are also included as an option to increase the efficiency of taking out the liquid product.

A GC or a MS is used for analysing the product gas. The unit described in Fig. 2 is largely controlled by a PC/Labview application via an interface controller unit (CU). This encompasses controlling a number of feed lines, performing optional valve switching, regulating a number of temperature zones as well as pressure. The unit has been especially modified to allow for on line MS (in addition to on line GC). A

capillary tube can be inserted from below and be positioned immediately below the oscillating element.

Due to the operating principles of TEOM, the mass of the gas occupied in the void volume of the tapered element affects the vibrational frequency of the balance. A mass change is detected when switching from one gas to another at isothermal conditions and the mass change is proportional to the density difference between the two gases. The apparent mass change as a result of switching between He and N_2 at different temperatures can be used to calculate the effective volume as reported by Fung et al [4]. The effective volume is defined as the total void space in a tapered element including the sample cell and can be used to account for the mass change due to the density change in the void space when switching from an inert gas to a feed gas or adding a feed gas into a stream. The effective volume change with the flow rates of the carrier gas as well as of the purge gas and the measurements of the density change must therefore be performed at exactly identical temperature, purge gas and carrier gas flow rates. R&P recommend [5] 200 ml/min purge and 100 ml/min carrier gas when He is used as purge gas to obtain correct void volumes.

The spring constant (K_0) in Equation (1) is temperature dependent, but fortunately only to a small extent. However, the oscillating frequency changes significantly with temperature due to gas density variations and changes in material properties. The TEOM is therefore not immediately suitable for temperature programmed experiments, but based on careful calibrations such experiments can be carried out.

Conversion and coke formation of ethene oligomerisation over HZSM-5 have been studied in the TEOM and in a conventional gravimetric microbalance at similar conditions [2]. The results clearly show that the TEOM is a very powerful tool to study deactivation kinetics with a design making true space time easy to obtain. The TEOM combine the advantage of the conventional microbalance and the fixed bed reactor and the same criteria can be used to check for differential operation.

4. A literature survey of the application of the inertial microbalance for *in situ* catalyst studies

In general, the applications of the TEOM involve:

- Adsorption studies. (Equilibrium data, uptake rates, adsorption kinetics, intracrystalline diffusivity).
- Catalyst characterization. (Oxidation/reduction of metallic catalysts as well as oxides, chemisorption, desorption).
- Reaction kinetics.
- Deactivation due to coke formation. (Coking rate, kinetics of deactivation, coke location).
- Effect of coke on adsorption, diffusion, selectivities and reaction rates.
- Regeneration kinetics. (Removal of coke).

The use and the characteristics of the TEOM will be presented in some detail by using two quite different examples:

- Methanol to olefins (MTO) over SAPO-34.
- Steam reforming of natural gas on Ni catalysts

However, first a literature survey of the use of TEOM is presented.

Initially the inertial microbalance was developed for the quantification of particulates in air [1], but in 1993/1994 the first reports on the use of TEOM for studying catalytic reactions appeared [3, 4, 10, 11]. A number of TEOM studies have since then been published and in the following a short presentation of these studies is given. Although the focus of the present review is on *in situ* studies, a relatively complete review of the use of the TEOM is given in the following.

4.1 Adsorption/diffusion studies

The Tapered Element Oscillating Microbalance is a very promising tool to study adsorption and diffusion as a function of coke. The technique minimizes the external

mass and heat transfer limitations in transient experiments due to a high flow rate of the carrier gas through the sample bed without affecting the measurements. The experimental data are not influenced by factors such as buoyancy and flow patterns, which are encountered with conventional methods.

Equilibrium adsorption of light hydrocarbons and aromatics in zeolites has been studied by many groups. Examples of adsorption studies are given by Rebo et al. [12] and by Zhu et al. in a series of papers [13-18]. Adsorption of aromatics on ZSM-5 was studied at low temperatures (<200 ^{o}C) and the adsorption isotherms could very well be described by the Langmuir equation [12]:

$$q = q_{sat} \frac{K \cdot p}{1 + K \cdot p} \qquad (6)$$

where q is the adsorbed phase concentration in the zeolite, p is the gas phase partial pressure of the probe molecule and K is an equilibrium constant.

Zhu et al. [17], however, used a dual-site Langmuir model to describe the equilibrium amounts of alkanes in silicalite-1. Following the work of Hershkowitz et al. [3, 10, 11] uptake rates of hydrocarbons on FCC catalysts have been studied by Alpay et al. [19] and Lee et al./Barrie et al. [20-22]. Other adsorption studies involve adsorption phenomena in zeolite membranes (Baldwin et al. [23], Zhu et al. [24]), adsorption of 1,2 dichloropropane on activated carbon (Zhang et al. [25]), studies on a novel adsorbent for the separation of propane/propene mixtures (Zhu et al. [26]), adsorption of butane isomers and SF_6 on Kureha activated carbon (Zhu et al. [27]), adsorption on single-walled carbon nanotubes (Bittner et al. [28], Smith et al. [29]), adsorption and hydrogenation of C_5 hydrocarbons on solid catalysts (McGregor and Gladden [30]) and nonisothermal adsorption with vapours on organic/inorganic porous materials (Larsen et al. [31]). Giaya and Thompson [32] characterized the hydrophobicity of microporous materials and obtained adsorption isotherms of chlorinated volatile organic compounds on these materials.

The experimental method used in TEOM for diffusion measurements is similar to the uptake and chromatographic methods, i.e. a step injection is made and the response curve is recorded. It is recommended to operate with dilute systems and low zeolite loadings. For an isothermal system where the uptake rate is controlled by intracrystalline diffusion with only a small concentration gradient for the adsorbed phase (constant diffusivity), solutions of the transient diffusion equation for different geometries have been given [33]. For adsorption and diffusion of o- xylene, p-xylene and toluene in HZSM-5, the one-dimensional model for a slab geometry represented by Eq. (7) turned out to fit the experimental data best [12]:

$$\frac{m_t}{m_\infty} = 1 - \frac{8}{\pi^2} \sum_{n=o}^{\infty} \frac{1}{(2n+1)^2} \exp\left(-\frac{(2n+1)^2 \pi^2 D t}{4L^2}\right) \qquad (7)$$

Adsorption and diffusion of linear and branched C_6 alkanes in silicalite-1 was studied by Zhu et al. [34] and by Vlugt et al. [35]. Van Donk et al. [36] did transient uptake measurements to study the diffusivity of n-hexane in Pt/H-Mordenite. The effect of coke deposition on transport and adsorption in zeolites was studied by Chen et al. [37, 38].

4.2 Studies of carbon formation and catalyst deactivation

TEOM can continuously monitor the mass of the catalyst sample. The fixed-bed characteristics of the microbalance coupled with the online GC (and/or MS) measurements therefore allow the rates and the selectivities to be studied simultaneously (Chen et al [2]). Consequently, the TEOM can provide continuous measurements of the coking rate and the determination of the reaction kinetics at temperatures up to 700 ^{o}C and pressures up to 60 bar.

Hershkowitz et al. [3, 10, 11] studied FCC catalysts and they measured *in situ* adsorption and coke deposition on zeolite catalysts during short contact-time interactions with the reactants. Activity and deactivation measurements were also included.

In a series of papers Chen et al. [7, 37, 38, 39, 40] studied the conversion of methanol to light olefins (MTO) using TEOM. The studies include the influence of coke deposition on the selectivity, the effect of the crystal size of SAPO-34 on the selectivity and the deactivation of the MTO reaction and also kinetic modelling of the MTO reaction. Fung et al [4] have also used the TEOM to study adsorption and reaction of methanol on SAPO-34.

Coke formation and catalyst deactivation on zeolites have been the subject of many studies. Van Donk et al. [41, 42] performed combined adsorption, diffusion and reaction studies of n-hexane hydroisomerization ocer Pt/H-Mordenite. Van Donk et al. [43] combined TEOM with *in situ* IR studies to characterize the carbonaceous deposits and the location of Brønsted acid sites when working with butene skeletal isomerization over H-ferrite. A recent review article deals with generation, characterization and impact of mesopores in zeolite catalysts [44]. Gomm et al. [45] performed *in situ* observations of coke deposition on zeolite catalysts using a TEOM-GC setup. Other examples involve oligomerization of n-butenes on ferrierite catalysts (Petkovic and Larsen [46]), interaction of isobutene with different solid acids (Petkovic and Larsen [47])

n-heptane reforming on Pt-Re/Al_2O_3 catalysts has also been studied by TEOM. In a series of papers Liu et al. [48, 49, 50, 51] studied the kinetics of catalyst coking and catalyst deactivations. Deactivation and coke formation over PtSn/Al_2O_3 in propane dehydrogenation (Rebo et al. [8]) and hydrodechlorination of 1,2–dichloropropane over Pt-Cu/C catalysts (Zhu et al. [52]) have also been studied. Several groups have studied carbon formation during steam an CO_2 reforming of methane (Lødeng et al. [6, 52, 53, 54], Zheng et al. [55], Srimat et al. [56], Stasinska et al. [57] , Armor and Martenak [58]).

Examples of other studies include carbon formation during hydrogenation of C_5 over Ni and Pd catalysts (Canning et al. [59]), interaction of N_2O with a hydrotalcite-derived multimetallic mixed oxide catalyst (Roman-Martinez et al. [60, 61]), *in situ* mass change measurements in solid oxides (Hartley et al [62]), methanol sorption in Nafion-117 (proton-exchange membranes) (Jalani et al. [63]), vanadyl pyrophosphate catalyst

for butane oxidation (Wang et al [64, 65, 66]) and dynamic studies of deactivation/regeneration of RbO_x/SiO_2 catalyst for methylene valerolactone synthesis (Lemondidou et al. [67]). Rekoske and Barteau [68] used TEOM in scaling-up surface science results to higher pressure. The same authors studied reduction kinetics and reaction on titanium oxide [69, 70]. Recent applications also include the study of carbon nanofibers (Chen et al. [9]) and hydrogen adsorption properties of single-walled carbon nantubes (Smith et al. [71]).

4.3 Air pollution studies

A main use of the inertial microbalance is to monitor air pollution. The technique can continuously measure the change of mass of an exchangeable filter cartridge as dust laden air or gas is drawn through it. Patashnick et al. [1, 72-74] used the TEOM to monitor high and low particulate concentration in real time focusing on diesel emissions and smoke measurements. Customized TEOM instrumentation has been made for monitoring particulate concentration in coal-fired power plants, TEOM detectors for NASA comet mission and for monitoring workplaces. Even particles in the air of an underground station in Stockholm have been studied by TEOM [75].

5. Methanol conversion to light olefins over SAPO-34: A TEOM study.

UOP/HYDRO has developed a Methanol-to-Olefin (MTO) process which combines complete conversion of methanol with 90 % or more selectivity to C_2-C_5 olefins in the hydrocarbon fraction [76]. The key to the UOP/HYDRO process was the discovery of the molecular sieve catalyst SAPO-34 (a silica alumina-phosphate) [77, 78].

SAPO-34 has a very high activity for the MTO reaction, but unfortunately it is accompanied by very fast deactivation due to coke formation [79, 80, 81]. However, detailed knowledge of the kinetics [82] and the reaction mechanism [83, 84, 85] is important and necessary for process development of MTO. The MTO reaction serves as a case study for illustrating the use of TEOM for *in situ* measuring of mass changes during reactions with very fast deactivation. The following problems are addressed by means of this *in-situ* technique:

- Mechanism and kinetics of coke formation and deactivation [7, 38-40, 86, 87).
- Diffusion effects on the reaction, coke formation and deactivation [38, 87-89].
- Effect of coke formation on the olefin selectivity [38, 39].
- The effects of adsorption on the reactions including the coking reactions [86, 88, 89].

TEOM provides the sole possibility to study deactivation and adsorption/diffusion effects as a function of the coke content. In addition, it makes it possible to study the kinetics directly as a function of the concentration inside the pores instead of in the gas phase.

5.1 Coke formation and deactivation studied by pulse mass analysis

The MTO reaction has been studied on a calcined SAPO-34 with a unit cell composition of $(Si_{2.88}Al_{18}P_{15.12})O_{72}$ supplied by SINTEF Materials & Chemistry, Norway [90]. The catalyst particles (52-140 mesh) were dried *in situ* at 500 °C for more than three hours. Quartz particles (52-140 mesh) were placed between the quartz wool and the catalyst particles (Fig. 1) in order to avoid temperature gradients and to improve the distribution of the flowing gas in the catalyst bed.

The MTO reaction was studied at 425 ^{o}C, WHSV =57-384 (g/g_{cat},h) using a methanol partial pressure of 7.2 kPa. Due to rapid catalyst deactivation, the MTO reaction was studied using 3 min interrupted pulses with GC analysis taken after 2 min for each pulse (integrated pulse method). The time between each pulse was about 40 min, allowing for completion of the GC analysis of each pulse. The reactant mixture of methanol was replaced by pure helium after the 3 min pulses and the possible effect of stripping in helium must be considered. In principle, the coke precursor may crack to smaller molecules during the stripping process. These effects were checked out by comparing pulse and steady-state experiments, and experiments with different pulse lengths [40].

Fig. 3 shows the changes in conversion and coke formation with time on stream for both 3 minute pulses and steady-state experiments. The data describing the steady-state experiments were obtained from two separate runs. It was also found that stripping in

helium did not influence neither coking nor the deactivating effect of coke. Experiments have also been performed with different sized pulses (3, 1, 0.5 and 0.15 min pulses) and the results clearly indicate that the size of the pulses [40] do not affect the coking and the deactivation. These results also indicate that the reproducibility of the experiments in the TEOM reactor is good.

In the study of the effect of methanol partial pressure on coke formation, both space velocity and partial pressure were adjusted to keep a constant conversion of methanol. It was found that the coke formation was proportional to the total amount of methanol injected into the catalyst bed during each pulse [40]. Therefore, the pulse length has to be selected according to the methanol partial pressure and the WHSV used in the study. For example, a WHSV of 2558 $g/g_{cat},h$ has to be used at a methanol partial pressure of 83 kPa where the life time of the catalyst is less than one minute. A pulse length as short as 0.15 min must be used.

Typical mass response curves for 3 min pulses are shown in Fig. 4. A rapid increase was observed initially caused by both adsorption and gas density change in the microbalance reactor. The density change was accounted for by subtracting a blank run with inert quartz particles as shown in Fig. 4. The weight increase following the initial period was caused by coking and was almost linear with time on stream. After switching back to pure He after three minutes, the weight curves decreased first rapidly due to the density change from the reactant mixture to pure helium, followed by a slow decrease caused by desorption and diffusion of products out of the pore system. However, the effect of cracking of coke precursors in the zeolite cages on the slow decrease in weight should also be considered. Anyhow, the fact that the rate of coke formation was identical for different pulse lengths (from six seconds to three minutes) as well for continuous experiments [40, 88] showed that the effect of cracking could be neglected. After about thirty minutes, the mass response curves were stable, and the permanent mass increase during the 3 min pulses, which is defined as coke in the present work, could be obtained. By assuming a linear change in the weight with time on stream during the 3 min pulses, the coking rate could be calculated.

The effect of space velocity, partial pressure, temperature and crystal size on the coke formation and the resulting deactivation could easily be obtained in the TEOM [39, 40, 86]. In addition, the desorbed amount from the catalysts can be obtained by the transient mass response, which is an important parameter for the design of the stripping process in such processes as FCC and MTO.

A typical mass response curve for a six-second pulse is shown in Fig. 5. Curve B in Fig. 5 shows the adsorption and desorption with time on stream, which was obtained from the raw data (A) after correction for the mass response of a pulse over a nonadsorbing quartz bed at identical conditions (C). Fig. 5 shows that the rate of desorption is very slow. It should be pointed out that the correction of density change by a blank run is not necessary if the interest is only related to coke formation, since the composition is identical after switching of the pulse. However, a corrected mass response curve can provide informative data on
adsorption-desorption during reaction.

5.2 Model of coke formation

5.2.1 Nature of coke

The effect of coke deposition on the MTO reaction is rather complex. Coke deposition influences either the formation of dimethyl ether (DME) or the DME conversion inside the pores during MTO. However, the effect of coke deposition on the dimetylether conversion to light olefins (DTO) over SAPO-34 is much simpler and can allow us to focus on the effect of intracrystalline coke on the olefin formation from DME.

A set of experiments with DTO and MTO on SAPO-34 precoked with propene were performed at 425°C to determine the role of coke formed from olefins. Due to a low coking rate from propene, a relatively high partial pressure of propene (>30 kPa) was used to reach similar coking rates as in MTO. It may be

important to keep the time on stream (TOS) similar for the desired coke amounts obtained in both methanol and propene conversion, since this might influence the nature of coke. Propene is expected to form mainly intracrystalline coke in similar locations as

in MTO or DTO. The yield of olefins over the precoked samples was lower than over a sample without pretreatment at a given coke content (including coke formed from pretreatment and MTO/DTO) in both DTO (Fig.6) and MTO (Fig. 7). This indicates that the nature of the coke formed from oxygenates is different from the coke formed directly from olefins, and that the coke formed from olefins is inactive for the MTO and the DTO reactions.

Another possible explanation for the lower conversion over pre-coked SAPO-34 is that the coke formed from propene would be of such a nature that it would result in a more significant decrease in the void space of the cavities. This was examined by porosity experiments using water adsorption and the results showed [7, 89] that the difference in pore volume was quite small. Therefore, it can be concluded that the lower activity of precoked SAPO-34 is mainly caused by the inactive nature of coke formed from olefins.

As a result, the coke in MTO and DTO should be divided into two categories: Inactive coke formed from adsorbed olefins (surface carbonium ions) having a deactivating effect and active coke formed from oxygenates having a promoting effect. The activity at different coke contents depends on the ratio of active to inactive coke [7].

5.2.2 Reaction pathway for coke formation.

Yield-conversion plots have long been used to identify the product type and the reaction network. It has been identified that DME is an unstable primary product and that all the olefins are stable secondary products. It has also been shown that simultaneous studies of conversion and coke formation are an efficient way to identify reaction pathway for coke formation. The coke yield and methanol conversion is presented in Fig. 8, where the solid line presents the trend of changes in coke yield with the methanol conversion on fresh catalysts. It indicates that coke is a stable secondary product plus stable tertiary products at high conversion. It means that most coke is formed directly from oxygenates, and that a small part is formed from olefins at high conversion. It is in good agreement with the separate experiment above, indicating a much slower coke formation from propene. In addition, the selectivity of coke on coked samples is lower than on fresh samples, which has been explained by a transient state shape selective

reaction for coke formation [38]. The coke molecule formed inside the pores lowered the possibilities for coke molecule growth.

5.3 Effect of coke deposition on product selectivity

The change in selectivity of different hydrocarbons with the coke content is shown in Fig. 9 for WHSV = $57h^{-1}$. The change in relative selectivities is shown in Fig. 10 where the initial selectivity was obtained by extrapolation to zero coke content from Fig. 9. These results clearly show that the selectivity to ethene increases with increasing coke content, whereas the C_4 selectivity is almost constant.

Changes in the product selectivity in zeolites due to coke deposition for a complex reaction have previously been discussed in a systematical way [88, 91]. The main feature of the method is to specify the effect of coke on the selectivity by comparing the yield at each conversion obtained by varying the contact time as well as by varying the degree of deactivation due to coke formation. The concepts of non-selective and selective deactivation have been proposed and MTO is a typical case of selective deactivation [38]. Changes in conversion, acidity (including density and strength distribution) and shape selectivity are the main factors contribute to the selectivity changes. A sophisticated method is needed for distinguishing the mechanism for selectivity change with coke deposition. It can, however, be demonstrated that the *in-situ* characterization by TEOM combined with yield-conversion (selectivity) plots is an efficient way for this purpose [38].

Coke formation influences not only the catalyst activity but also the selectivity of olefins as described above. It is of particular interest that the selectivity to ethene increases with coke formation (Figs. 9, 10), and the selectivity to the longer chain olefins decreases, except for C_4 for which the selectivity is relative stable. This study has been further explored to the MTO reaction on differently sized crystals [38, 39] and it was found that changes in the product selectivities caused by coke deposition were independent of the crystal size. It has been concluded that changes in product selectivities caused by coke deposition are a result of changes in the transition-state shape selectivity. The sharp decrease in olefin formation at high coke content could be explained by the strong effects of the transition-state shape selectivity. The small decrease in the free space inside the pores at high coke content

seems to suppress significantly the olefin formation [92, 93, 94]. The formation of methane seems not to be influenced probably due to its small molecular size. However, the effect of pore blocking due to external coke at the high coke content can not be excluded.

5.4 *In situ* study of adsorption at reaction conditions

The kinetics of reaction on zeolites is conventionally related to the reactant concentration in the gas phase. The reaction inside the pores of zeolites, however, involves adsorption and diffusion into the pores and reactions of adsorbed species inside the pores [92]. Therefore, intrinsic kinetics based on the adsorbed concentration inside the pores will be very useful for catalyst development. TEOM is an excellent technique to measure adsorption of reactant at reaction conditions, as well as to measure it as a function of the coke content [3, 88]. It makes it possible to obtain intrinsic activity of each acidic active site in a direct way, and to understand deactivation mechanism in great detail.

The practical problem in measurement of adsorption at reaction conditions is to minimize the coke formation during the pulse. The size of the pulse has been varied in the MTO reaction, and a six-second pulse has been selected, as shown in Fig. 5. The concentration of methanol in the pores was estimated from the adsorbed amount. Assuming that the methanol partial pressure of 7.8 kPa is low enough to operate in the Henry's law region, the Henry's law constant under reaction conditions was calculated to be 0.035 mmol/g,kPa. The adsorption measurements at reaction conditions has also been compared to the adsorption parameters found at low temperatures, where the isotherms for methanol adsorption over SAPO-34 at 348 K, 373 K and 398 K were measured in the TEOM [88]. It is interesting to note that the directly measured adsorbed amount of methanol at reaction conditions is in good agreement with the predicted values by the Langmuir model, which was obtained at low temperatures. Based on adsorbed amount and conversion measured by *in situ* GC analysis, the turnover frequency, site coverage and rate constant for the MTO reaction and propene conversion have been analysed [88].

It is interesting to note that the conversion decreased more rapidly than adsorption, as shown in Fig. 11, similar to the observations of Hershkowitz [3] in catalytic cracking of

decane over zeolite Y. In general, coke deposition in the zeolite pores influences the accessibility of active sites by blocking the sites directly and by blocking the pores, thus affecting the diffusion, adsorption and the reactions. The results shown in Fig. 11 indicate that rate constant decreases with increasing coke content. It can again be a result of transition state shape selective reaction. The gradually decrease in pore volume due to coke formation [89] suppresses the formation of the transition state towards to the products.

5.5. Diffusion and reaction in SAPO-34

As discussed above, MTO reactions might be influenced by diffusion, especially on coked samples. In general, the way molecules move inside a zeolite and how the intracrystalline channel network of a zeolite influence the movement and the reaction pathway of organic molecules are obviously very important questions in the design and application of shape selective catalysts.

Diffusion and reaction in porous heterogeneous catalysts have been a subject of intensive investigations for almost a half century and general treatments on this subject are available [95, 96]. Quantitative methods for deciding the extent of mass transport or diffusion limitation for a reaction in a porous catalyst have been developed on the premise that molecular diffusion within a porous solid obeys Fick's first law of diffusion. However, the applicability of this general reaction and diffusion model for zeolite catalyzed reaction is still a matter of debate.

Molecular diffusion in zeolites takes place in a different regime from the Knudsen regime [97, 98]. Because mass transport in the intracrystalline space of a zeolite is strongly influenced by interactions between the molecules and the walls of the zeolite channels, the term configurational has been used to characterize this regime [98]. Although the diffusion in zeolites has been investigated intensively by experimental and theoretical approaches during the past twenty years, disagreements still occur [33]. A large number of experimental techniques have been employed to measure the diffusivity in zeolites at the micro- or at the macro-scale. Uptake diffusivity is the most often used technique due to its simplicity in the experiments. However, it appears to be large inconsistencies between reported zeolite diffusivities, often by several orders of magnitude [33].

Although different techniques have be developed, direct measurement of the diffusivity of hydrocarbons is still a difficult task, mainly due to the fact that different techniques yield different results. Moreover, very few successful examples can be found in literature for directly applying independently measured diffusivity to the reaction model. The present section will illustrate that TEOM provides a unique opportunity to measure diffusivity directly and to study changes in diffusion and the effects of such diffusion on the MTO reaction for the first time. Diffusion of methanol has been studied by uptake diffusivity measurement at inert conditions, and by kinetic studies on differently sized crystals at real reaction conditions.

Uptake diffusivity is a measurement of the response of a step function change in gas phase concentration of probe molecule to be adsorbed on the sample. Different techniques have been developed to follow such response, like gravimetric measurement of the weight change of the adsorbents [99, 100], volumetric measurement of the pressure change in a constant volume of the probe molecule due to adsorption [101].

Both gravimetric and volumetric experiments are relative simple in design and operation for diffusion measurements in zeolites. In practice, however, there are a number of experimental problems related to these methods. Rate processes other than intracrystalline zeolite diffusion and thermal effects have to be carefully eliminated. The conventional microbalance is often used for gravimetric uptake measurement, where most part of gas flows via bypass. The flow through the sample is small and almost close to molecular diffusion [2]. The volumetric measurement is often carried out in a static system. As a consequence, the heat of adsorption generated during the transient uptake of adsorbate has for long been recognized as a potential source of error in the determination of diffusivity using transient uptake methods [102].

With the assurance of sample isothermality and the absence of other transport resistance, the solution of Fick's second law equation may be used to calculate the transient uptake diffusivity. Different solutions for different cases have been developed [33].

The method which has been developed using TEOM combines the advantages of both the gravimetric uptake method and zero length column (ZLC) method [103, 104]. Due to a high sensitivity, a small amount of sample can be installed in the sample carrier. High flow rate of gas containing probe molecules forced through the samples makes the concentration of probe molecule almost constant in the bed. Also as a result, external diffusion and thermal effect can be relatively easily eliminated. In addition, the response time can be as short as 0.1 s, which makes it possible to study a fast diffusion process. The measurable diffusivity by TEOM is much higher than one measured by conventional gravimetric method, and similar to one measured by ZLC. The diffusion measurement by TEOM can be called zero length bed - TEOM (ZLB-TEOM) method.

The effect of bed length in the diffusion measurements by ZLB-TEOM has been studied by varying catalyst loading from 5 mg to 20 mg at 298 K and constant total flow of 250 ml/min, for the following systems: Ethane/HZSM-5, n-hexane/HZSM-5, toluene/HZSM-5 and methanol/SAPO-34. Much lower diffusion was observed for catalyst loadings larger than 10 mg for all the systems studied. This is illustrated in Fig. 12 for n-hexane/HZSM-5. A sample as small as 5 mg has to be used indicating the importance of “zero length bed” in the diffusion measurements.

In many instances adsorbent particles are not uniform spheres and it is therefore pertinent to consider the extent to which the solution of the diffusion equation may be affected by particle shape. The expressions for a parallel sided slab, an infinite cylinder, and a cube have previously been summarized [33].

A typical uptake curve for methanol diffusion in SAPO-34 at 373 K and a methanol partial pressure of 0.75 kPa is shown in Fig. 13. The transient diffusion equation for a slab geometry (Eq. (7)) for sorbate uptake was found to give the best fit to the experimental data, although SAPO-34 appears a typical cubic ship.

The uptake diffusivities or diffusion times are estimated from uptake curves based on the concentration in the adsorbed phase, in contrast to the reaction rate in a diffusion/reaction equation which is based on the gas phase concentration. The uptake diffusivity is therefore

multiplied by a Henry's law constant to transform to the effective diffusivity based on the gas phase concentration [105]. A similar approach was used by Garcia and Weisz [106], where the steady-state diffusivity has been defined. If all the molecules internally sorbed are assumed to be equally mobile, the definition of the steady-state diffusivity is given by Eq. (8):

$$D_{SS} = D_C C_\infty / C_0 \qquad (8)$$

where D_{SS} is the steady-state diffusivity, C_∞ is the concentration inside the pores at infinite time and C_0 is the concentration of probe molecules in the gas phase. The steady-state diffusivity is then identical to the effective diffusivity in Post's approach [105]. Due to the large adsorption capacity of zeolites, the steady-state diffusivity could be 2-5 orders of magnitude larger than the uptake diffusivity.

In agreement with other results [12, 106], the steady-state diffusion over SAPO-34 was found to be a non-activated process, as shown in Fig. 14. It means that the steady-state diffusivity can directly be put into the Weisz-Prater criterion at reaction conditions.

Intracrystalline diffusion is normally assumed to be rate limiting step in the diffusion measurements, but it may be questioned for diffusion in zeolites. It has been known that the diffusional resistences rather than intracrystalline diffusion could exist for diffusion in zeolites. The complete dimension variation of the zeolite sample (i.e., also of the zeolite crystal size) has to be investigated in order to prove that intracrystalline mass transport is rate-limiting. If the sorption process reflects intracrystalline mass transport, then its time dependence must be a function of D/L^2, with D representing a diffusion coefficient independent of the crystal size.

In order to determine the rate limiting step, the sorption process was studied on SAPO-34 with crystal sizes of 0.25, 0.5, 2.5 and 25 μm at temperature from 75-125 °C and methanol partial pressure from 0.75 to 7 kPa. The steady-state diffusivity was found to increase when crystal size increased from 0.25 μm to 2.5 μm (Fig.14). This can be

explained by an additional resistance namely the surface barrier, which varied with the crystal size. It has previously been observed that the effect of surface barrier was smaller at a higher temperature, suggesting that the surface barrier depends on the energetic heterogeneity of the zeolite crystal surface. It has been pointed out [107] that entrance through the pore opening may involve a surface barrier phenomena. The molecular size is comparable to the pore opening, and this barrier is possibly significant. This should increase when the crystallite size decreases since the number of openings increases shapely.

However, similar diffusivity was found on the 2.5 μm and 25 μm crystals, indicating that intracrystalline diffusion is a rate-limiting step. Therefore, the proper uptake and steady-state diffusivities can be measured on the 2.5 μm crystals (Fig. 14). The steady-state diffusivity of methanol is about 1.65 10^{-9} m^2/s.

Steady-state measurement of diffusivity can be done indirectly from the reaction kinetics on two differently sized crystals. The 0.25 and 2.5 μm crystals were used for quantitative studies [89].

The classical reaction and diffusion model was adopted to describe the effect of diffusion on zeolite catalysis. Changes in the intrinsic rate constant and methanol diffusivity are illustrated in Fig. 15. The methanol diffusivity decreased almost three orders of magnitude from fresh catalyst to a coke content of 15 wt%. Such decrease in methanol diffusivity with coke content has
been perfectively described by percolation theory [89].

This approach separated the effects of diffusion limitation and poisoning of the active sites on the total deactivation rate. It is of particular interest that the effect of diffusion limitation caused by coking probably was more significant than the other factors. It is necessary to use relatively small crystals to obtain large catalyst capacity.

The measured steady-state diffusivity is comparable with that obtained indirectly from reactions on differently sized crystals, which is in good agreement with the results of Post et al. (105) and Garcia and Weisz (106). It does not only lead to confidence in diffusion measurement by ZLD-TEOM, but also indicates that the steady-sate diffusivity is an excellent bridge between the measured uptake diffusivities and the reactive diffusivities at reaction conditions. It can be concluded that reactive diffusivity can be estimated from the uptake diffusivity which is carefully measured on the relative large crystal sizes to confirm that the intracrystalline diffusion being rate-limiting step. In addition, the measured steady state diffusivity can be directly used in the classical Weisz-Prater criterion to predict the importance of diffusion during the conversion of methanol over SAPO-34.

6. Steam reforming of natural gas

Conversion of natural gas to fuels, chemicals and hydrogen depends on synthesis gas as an intermediate product and steam reforming is the main process for production of synthesis gas. Steam reforming and in particular carbon formation during steam reforming is used as an example of *in situ* TEOM studies at high pressures and high temperatures.

Prereforming (low temperature steam reforming) of C_1-C_3 natural gas mixtures at 400-550^{o}C, as well as steam methane reforming (SMR) at higher temperatures (< 680 ^{o}C) have been studied at total pressures between 15 and 20 bars. Two different commercial nickel based catalysts have been used.

- A fresh SMR catalyst designed for high temperature service (SR-F) containing 11 wt% Ni on α-Al_2O_3 with 9 wt% CaO. The nickel and BET surface areas are rather low, 0.33 m^2/g (dispersion 0.46%) and 5.5 m^2/g, respectively.
- A fresh prereforming catalyst (PR-F), 45wt% Ni Al_2O_3 (10wt%) and MgO (10wt%). The BET area is 155 m^2/g and the Ni area has been measured by H_2 chemisorption to 31.5 m^2/g (dispersion 10.5%).

● A stabilized prereforming catalyst (PR-S) with BET surface area of 26 m^2/g. and Ni area of 7.8 m^2/g. (dispersion 2.8%).

Catalyst particles of about 0.3-0.6 mm were found to be suitable to avoid transport limitations influencing the results. Stabilization of the PR-F catalyst was performed by running the prereforming reaction at a high steam to carbon ratios (> 2, i.e. carbon free conditions) at 490^{o}C and 40 bars over 582 hours.
SEM-EDX indicated that the surface was sulfur and carbon-free after this treatment.

The main interests have been to establish the relationship between catalyst properties and intrinsic reaction and carbon formation kinetics, deactivation (carbon, sintering, poisoning) as well as determining practical (via intrinsic kinetic) carbon thresholds for carbon free operation. Different natural gas feedstock compositions have been studied with varying levels of C_2-C_3 alkanes, including trace levels of olefins, hydrogen, carbon dioxide and steam.

When feeding steam at high temperature and pressure it is particular important to avoid SiO_2 containing materials due to the instability of SiO_2 and subsequent
deposition and deactivation of the catalyst. A comparison between quartz and carbon wool used during studies of steam reforming of methane on a Ni catalyst is shown on Fig. 16. It is evident from the figure that the materials containing SiO_2 have a strong effect on the catalyst activity. The carbon fiber wool, however, gave only the normal activity loss at 550 and 650 ^{o}C. It has also been shown that α-alumina wool is a suitable material at the conditions used in Fig. 16.

Fig. 17 shows a comparison of the time on stream behaviour of the three nickel catalysts. The propane conversion and corresponding mass change observed is shown. It is obvious that the initiation of carbon formation is proceeding especially easily on the PR-S catalyst at these conditions. In contrast, no carbon was observed on PR-F at similar conditions during a 30 hour time frame. The actual gas composition in the experiment with SR-F, also indicated in the figure, had a much lower carbon potential than for the two other catalyst (no C_2 was present). Still the carbon formation initiated

readily, supporting a view that the nickel crystallite size could be of importance (since SR-F necessarily contains the largest nickel crystallites of the three catalysts studied).

Fig. 17 illustrates that a rather large amount of carbon could be deposited without loosing too much catalyst activity. The conversion of both ethane and propane is at a similar degree gradually declining, possibly indicating that some encapsulating carbon is forming in parallel to the weakly or non-deactivating filamentous carbon (Fig. 18). At higher steam to carbon ratio at otherwise similar conditions the conversion curves are close to stable, indicating that carbon is the main reason for deactivation in this case.

The results show that small amounts of both C_2 and C_3 olefins were formed at 450^{o}C. This could very well provide an important clue to the actual deactivation mechanism. It is likely that the olefins can polymerize to carbon structures on the surface and thus cover and block the active reforming sites. The effect of adding small amounts of olefins in the feed on the carbon formation rates and carbon thresholds has also been studied. Fig. 19 indicates that olefins, and in particular propene increases the rate of carbon formation. However, this is not a generally applicable result because the stronger deactivation effect of olefins over time can cause the observed carbon formation rates also to be lower than without olefins present. Thus, it is important to consider also time derived effects when concluding about the effect of additives. It is not so obvious from this figure, but olefins, and propene to a stronger degree than ethene, increases the carbon threshold conditions considerably.

Fig. 20 shows typical time-on-stream behaviour for the SR-F catalyst. The conversion level and deactivation rate are highly dependent upon the temperature. It is also interesting to note that the deactivation characteristics are rather similar for conditions with and without carbon formation. Thus, it seems to be a rather high selectivity to non-deactivating carbon filaments at these conditions. The main reason for deactivation at these conditions is believed to stem from sintering of nickel. Experimental evidence that sintering can proceed at similar conditions are provided by Bartholomew [108],

illustrating the strong effect of even small amounts of steam, and Sehested [109], showing that sintering can proceed well below the Tammann temperature of 592^{o}C.

The effect of addition of various hydrocarbons in the feed has been studied. Fig. 21 shows a comparison of the effect of 4% C_3H_8 relative to CH_4 compared to a case with similar total C_3 concentration containing ¼ propene. The effect of propylene is very pronounced, causing both considerably higher carbon formation rates and also a considerably stronger deactivation of the reforming, which can be seen by comparing the conversion at a similar carbon amount.

The experimental results have been used for building kinetic models [110, 111, 112, 113]. Carbon formation kinetics has also been included in the microkinetic models, though mainly described by algebraic equations. This model assumes that the carbon filaments are formed by carbon atoms diffusing through bulk nickel crystallites. Recent studies have also indicated that surface diffusion processes can be more important than believed so far in the filament formation mechanism [114]. When the irreducible heat transfer limitation was taken into account, providing an improved estimate of the real catalyst surface temperature, the model was able to predict both our own kinetic data as well as the intrinsic kinetic data that has earlier been reported by Xu and Froments [115] over a similar catalyst (Ni on Mg-Al_2O_3 spinel).

7. Conclusion

The Tapered Element Oscillating Microbalance is a powerful tool for *in situ* studies of catalytic reactions. It combines the advantage of the conventional microbalance and the fixed-bed reactor. Processes involving mass changes such as carbon formation can very conveniently been studied at reaction conditions. The literature survey shows that the TEOM has already been applied for a larger number of different applications in catalysis.

The MTO case study clearly demonstrates that the TEOM reactor is a excellent *in-situ* technique for studying reactions, coke formation and deactivation in zeolites,

simultaneously. The effects of coke formation on changes in selectivity and activity can be studied in a straightforward way, namely as a function of the coke content. The TEOM is also a powerful tool for studying adsorption and diffusion in zeolites both at inert and reaction conditions. By means of short pulse injection in TEOM, absorption and desorption has been studied *in-situ* at reaction conditions, which provides a possibility to determine the activity of each active site relating the real concentration of reactants inside pores. High sensitivity, fast response and well-defined flow pattern make TEOM an excellent tool for determining diffusivity of hydrocarbon in the zeolites. Moreover, TEOM has provided the sole possibility for gaining knowledge about the effect of coke deposition on adsorption and diffusion *in situ* at reaction conditions. A sophisticated application of TEOM in zeolite catalysis by combining different approaches as mentioned above can lead to a much more detailed understanding of the catalytic processes, including the mechanisms of reaction, coke formation and deactivation. The steam reforming case also demonstrates the ability of TEOM to operate at relatively high pressures and temperatures for studying reactions, coke formation and deactivation simultaneously.

References

1. Patashnick, H., Rupprecht, G. and Wang, J.C.F. *Preprints – Am. Chem. Soc., Div. Petr. Chem.,* **25,** 188 (1980).
2. Chen, D., Gronvold,A., Rebo, H.P., Moljord, K. and Holmen, A. *Appl. Catal., A: General* **137**, L1 (1996).
3. Hershkowitz, F. and Madiara, P.D. *Ind. Eng. Chem. Res.,* **32**, 2969 (1993).
4. Fung, S.C., Querini, C.A., Liu, K., Rumschitzki, D.S. and Ho, T.C. *Stud. Surf. Sci. Catal.,* **88**, 305 (1994).
5. Rupprecht, H. and Patashnick, G. Operating Manual TEOM Series Pulse Mass Analyzer, R&P, Albany, N.Y. 1996
6. Lødeng, R., Chen, D., Jacobsen, C.K. and Holmen, A. *Stud. Surf. Sci. Catal*., **130D**, 3639 (2000).
7. Chen, D., Rebo, H.P., Moljord, K. and Holmen, A. *Stud. Surf. Sci. Catal.,* **126**, 159 (1997).
8. Rebo, H.P., Chen, D., Blekkan, E.A. and Holmen, A. *Stud. Surf. Sci. Catal.* **119**, 617 (1998).
9. Chen, D., Christensen, K.O., Ochoa-Fernandez, E., Yu, Z., Tøtdal, B. Latorre, N., Monzon, A. and Holmen, A. *J. Catal*. **229**, 87 (2004).
10. Hershkowitz, F., Kheshgi, H.S. and Madiara, P.D. *Preprints–Am. Chem. Soc., Div. Petr. Chem* **38**, 619 (1993).
11. Hershkowitz, F., Kheshgi, H.S. and Madiara, P.D. *ACS Symp. Ser.* **571**, 178 (1994).
12. Rebo, H.P., Chen, D., Brownrigg, M.S.A., Moljord, K. and Holmen, A. *Collect. Czech. Chem. Commun,* **62**, 1832 (1997).
13. Zhu, W., van de Graaf, J.M., van den Broeke, L.J.P., Kapteijn, F. and Moulijn, J.A. *Ind. Eng. Chem. Res.* **37**, 1934 (1998).
14. Zhu, W., Kapteijn, F., Moulijn, J.A. and Jansen, J.C. *Phys. Chem. Phys.* **2**, 1773 (2000).
15. Zhu, W., Kapteijn, F., Moulijn, J.A., den Exter, M.C. and Jansen, J.C. *Langmuir* **16**, 3322 (2000).

16. Zhu, W., Kapteijn, F. and Moulijn, J.A. *Phys. Chem. Chem. Phys*. **2**, 1989 (2000).
17. Zhu, W., Kapteijn, F. and Moulijn, J. A. *Adsorption* **6**, 159 (2000).
18. Zhu, W., Kapteijn, F., van der Linden, B. and Moulijn, J. A. *Phys. Chem. Chem. Phys.* **3**, 755 (2001).
19. Alpay, E., Chadwick, D., Kershenbaum, L.S., Barrie, P. J., Sivadinarayana, C. and Gladden, L. F. *Chem. Eng. Sci.* **58**, 2777 (2003).
20. Lee, C.K., Ashtekar, S., Gladden, L.F. and Barrie, P.J. *Chem. Eng. Sci.* **59**, 1131 (2004).
21. Barrie, P. J., Lee, C. K. and Gladden, L. F. *Chem.Eng. Sci.* **59**, 1139 (2004).
22. Lee, C.K., Gladden, L.F. and Barrie, P.J. *Appl. Catal. A: General* **274**, 269 (2004).
23. Baldwin, R.M., van de Graaf, J.M., Zhu, W., Kapteijn, F. and Moulijn, J.A. *Book of Abstracts, 214th ACS National Meeting, Las Vegas, NV, September.* **7-11**, PMSE-P172 (1997).
24. Zhu, W., Kapteijn, F. and Moulijn, J.A. *Sep. Purif. Technol.* **32**, 223 (2003).
25. Zhang, J., Zhu, W., Makkee, M., van der Linden, B., Kapteijn, F. and Moulijn, J.A. *J. Chem. Eng. Data* **46**, 662 (2001).
26. Zhu, W., Kapteijn, F. and Moulijn, J. A. *Stud. Surf. Sci. Catal.* **135**, 2961 (2001).
27. Zhu, W., Groen, J.C., Kapteijn, F. and Moulijn, J.A. *Langmuir* **20(5)**, 1704 (2004).
28. Bittner, E. W., Smith, M. R. and Bockrath, B. C. *Carbon* **41**, 1231 (2003).
29. Smith, M.R.J., Bittner, E.W., Shi, W., Johnson, J.K. and Bockrath, B.C. *J. Phys. Chem. B* **107**, 3752 (2003).
30. McGregor, J. and Gladden, L. F. *13th International Congress on Catalysis.* Paris, France, 2004.
31. Larsen, G., Silva, H. S. and de Silva, R. V. *J. Colloid Interface Sci.* **224**, 205 (2000).
32. Giaya, A. and Thompson, R. W. *Micropor. Mesopor. Mater.* **55**, 265 (2002).
33. Kärger, J. and Ruthven, D.M. Diffusion in zeolites and other microporous solids. John Wiley & Sons, Inc. 1992.

34. Zhu, W., Kapteijn, F. and Moulijn, J. A. *Micropor. Mesopor. Mater.* **47**, 157 (2001).

35. Vlugt, T.J.H., Zhu, W., Kapteijn, F., Moulijn, J.A., Smit, B. and Krishna, R. *J.Am. Chem. Soc.* **120**, 5599 (1998).

36. van Donk, S., Broersma, A., Gijzeman, O.L.J., Bitter, J.H. and de Jong, K.P. *Stud. Surf. Sci. Catal.* **135**, 3112 (2001).

37. Chen, D., Rebo, H.P., Moljord, K. and Holmen, A. *Chem. Eng. Sci.* **51**, 2697 (1996).

38. Chen, D., Rebo, H.P., Moljord, K. and Holmen, A. *Ind. Eng. Chem. Res.* **36**, 3473 (1997).

39. Chen, D., Moljord, K., Fuglerud, T. and Holmen, A. *Micropor. Mesopor. Mater.* **29**, 191 (1999).

40. Chen, D., Rebo, H. P., Gronvold, A., Moljord, K. and Holmen, A. *Micropor. Mesopor. Mater.* **35**, 121 (2000).

41. van Donk, S., Broersma, A., Gijzeman, O.L.J., van Bokhoven, J.A., Bitter, J.H. and de Jong, K.P. *J. Catal.* **204**, 272 (2001).

42. van Donk, S., Bitter, J.H., Versluijs-Helder, M., Verberckmoes, A. and de Jong, K.P. *EuropaCat VI Innsbruck, Austria* (2003)

43. van Donk, S., Bus, E., Broersma, A., Bitter, J.H. and de Jong, K.P. *Appl. Catal. A: General* **237**, 149 (2002).

44. van Donk, S., Janssen, A. H., Bitter, J. H. and de Jong, K. P. *Catal. Rev.* **45**, 297 (2003).

45. Gomm, S., Glaser, R. and Weitkamp, J. *Chem. Eng. Techn.* **25**, 962 (2002).

46. Petkovic, L.M. and Larsen, G. *Ind. Eng. Chem. Res.* **38**, 1822 (1999).

47. Gill, R., Petkovic, L.M. and Larsen, G. *J. Catal.* **179**, 56 (1998).

48. Liu, K., Fung, S.C., Ho, T.C. and Rumschitzki, D.S. *J. Catal.* **169**, 455 (1997).

49. Liu, K., Fung, S. C., Ho, T. C. and Rumschitzki, D. S. *Ind. Eng. Chem. Res.* **36**, 3264 (1997).

50. Liu, K., Fung, S.C., Ho, T.C. and Rumschitzki, D.S. *Stud. Surf. Sci. Catal.* **111**, 625 (1997).

51. Liu, K., Fung, S.C., Ho, T.C. and Rumschitzki, D.S. *J. Catal.* **206**, 188 (2002).

52. Zhu, W., Zhang, J., Kapteijn, F., Makkee, M. and Moulijn, J. A. *Stud. Surf. Sci. Catal.***139**, 21 (2001).

53. Lødeng, R., Chen, D., Christensen, K. O., Andersen, H. S., Rønnekleiv, M. and Holmen, A. *225th ACS National Meeting, New Orleans, LA, USA, March 23-27,* FUEL-F172 (2003).

54. Lødeng, R., Chen, D., Christensen, K. O., Rønnekleiv, M., Andersen, H.S. and Holmen, A. *EuropaCat VI Innsbruck, Austria* (2003).

55. Zheng, J., Song, C., Pan, W., Sun, L., Nataraj, S., Wilhelm, F. and Armor, J. N. *226th ACS National Meeting, New York, NY, United States, September 7-11, 2003* FUEL-F138 (2003).

56. Srimat, S., Pan, W., Song, C. and Armor, J. N. *Preprints Am. Chem. Soc.,Div. Fuel Chem.* **46**, 92 (2001).

57. Stasinska, B., Golebiowski, A., Stolecki, K. and Borowiecki, T. *Adsorption Science & Technology* **19**, 441 (2001).

58. Armor, J. N. and Martenak, D. J. *Appl. Catal. A: General* **206**, 231 (2001). 59. Canning, A., Jackson, D. S., Doyle, A., Shaikhutdinov, S., Freund, H.J., Gladden, L. and McGregor, J. *EuropaCat VI Innsbruck, Austria, (*2003).

59. Roman-Martinez, M.C., Kapteijn, F., Overeijnder, J. and Moulijn, J. A. *Greenhouse Gas Control Technologies, Proceedings of theInternational Conference on Greenhouse Gas Control Technologies, 4th,Interlaken, Switz, Aug 30-Sept 2, 1998.* 343 (1999).

60. Roman-Martinez, M. C., Kapteijn, F., Cazorla-Amoros, D., Perez-Ramirez, J. and Moulijn, J. A. *Appl. Catal. A: General* **225**, 87 (2002).

61. Hartley, A., Mantzavinos, D., Sahibzada, M. and Metcalfe, I. S. *Solid State Ionics* **136, 127** (2000).

62. Jalani, N. H., Choi, P. and Datta, R. *Abstracts of Papers, 226th ACS National Meeting, New York, NY, United States, September 7-11, 2003.* POLY-P549 (2003).

63. Wang, D., Kung, H. H. and Barteau, M. A. *Appl.Catal. A: General* **201**, 203 (2000).

64. Wang, D. and Barteau, M. A. *J. Catal.* **197**, 17 (2001).

65. Wang, D. and Barteau, M. A. *Appl. Catal., A: General* **223**m, 205 (2002).

66. Lemonidou, A.A., Lopez, L., Manzer, L.E. and Barteau, M.A. *EuropaCat VI,* Innsbruck, Austria (2003).

67. Rekoske, J. E. and Barteau, M. A. *Preprints-Am. Chem. Soc., Div. Petr. Chem.* **40**, 187 (1995).

68. Rekoske, J. E. and Barteau, M. A. *J. Phys. Chem. B.* **101**, 1113 (1997).

69. Rekoske, J.E. and Barteau, M.A. *Langmuir* **15**, 2061 (1999).

70. Smith, M.R., Bittner, E.W., Shi, W., Johnsen, J.K. and Bockrath, B.C. *J.Phys. Chem. B.* **107**, 3752 (2003).

71. Patashnick, H. and Rupprecht, E. G. *J. Air Waste Manag.Assoc.* **41**, 1079 (1991).

72. Patashnick, H. and Rupprecht, G. *Am. Lab.* **18**, 59 (1986).

73. Patashnick, H. and Rupprecht, G. *Technical Publishing.**June*** (1986).

74. Johansson, C. and Johansson, P.A. *Atmosph. Environ.* **37**, 3 (2003).

75. Vora, B.V., Marker, T.L., Barge, P.T., Fullerton, H.E., Nilsen, H.R., Kvisle, S. and Fuglerud, T. *Stud. Surf. Sci. Catal.* **107**, 87 (1997**)**.

76. Lok, B.M., Messina, C.A., Patton, R.L., Gajek, R.T., Cannan, T.R. and Flanigen, E.M. *J. Am. Chem. Soc.* **106**, 6092 (1984**)**.

78. Liang, J., Li, H., Zhao, S., Guo, W., Wang, R. and Ying, M. *Appl.Catal.* **64**, 31 (1990).

79. Froment, G.F., Dehertog, W.J.H. and Marchi, A.J. *Catalysis* **9**, 1 (1992).

80. Marchi, A.J. and Froment, G.F. *Appl. Catal.* **71**, 139 (1991).

81. Grønvold, A.G., Moljord, K., Dypvik, T. and Holmen, A. *Stud. Surf. Sci. Catal.* **81**, 399 (1994)**.**

82. Bos, R.A., Tromp, P.J.J. and Akse, H.N. *Ind. Eng. Chem. Res.* **34**, 3808 (1995).

83. Chang, C.D. *Cat. Rev. Sci. Eng.* **26**, 323 (1984).

84. Dahl, I. and Kolboe, S. *J. Catal.* **149**, 458 (1994).

85. Salehirad, F. and Anderson, M.W. *J. Catal.* **164**, 301 (1996).

86. Chen, D., Rebo, H.P., Moljord, K. and Holmen, A. *Stud. Surf. Sci. Catal*. **119**, 521 (1998).

87. Chen, D., Moljord, K. and Holmen, A. *Stud. Surf. Sci. Catal.* **130^{C}**, 2651 (2000).

88. Chen, D., Moljord, K., Rebo, H.P. and Holmen, A. *Ind. Eng. Chem. Res.* **38**, 4242 (1999).

89. Chen, D., Rebo, H.P., Moljord, K. and Holmen, A. *Chem. Eng. Sci.* **54**, 3465 (1999).

90. Dahl, I.M., Wendelbo, R., Andersen, A., Akporiaye, D., Mostad, H.B. and Fuglerud, T. *Micropor. Mesopor. Mater.* **29**, 158 (1999).

91. Best, A.N and Wojciechowski, B.W. *J. Catal.* **47**, 11 (1977).

92. Chen, N.Y., Degnan, T.F. and Smith, C.M. Molecular transport and reaction in zeolites, design and application of shape selective catalysts, VCH Publishers: New York, 1994.

93. Dadyburjor, D.B. *Catalysis,* **9**, 229 (1992).

94. Xu, W.Q., Yin, Y.G., Suib, S.L. and O'Young, C.L. *J. Phys.Chem.* **99**, 758 (1995).

95. Satterfield, C.N. Mass Transfer in Heterogeneous Catalysis. Robert Krieger publishing Co.:Malabar, FL, 1980.

96. Rosner, D.E. Transport Processes in Chemically Reaction Flow Systems. Butterworth: Stoneham, MA, 1986.

97. Wheeler, A. *Adv. Catal.* **3**, 249 (1951).

98. Weisz, P.B. and Prater, C.D. *Adv. Catal*. **6**, 143 (1954).

99. Cavalcante, C.L.Jr. and Ruthven, D.M. *Ind.Eng. Chem. Res.* **34**, 185 (1995).

100. Wu, P., Debrbe, A., Ma, Y.H. *Zeolites* **3**, 118 (1983).

101. Bülow, M., Struve, P., Finger, G., Redszus, C., Ehrhardt, K. and Schirmen, W. *J.C.S. Faraday* **76**, 597 (1980).

102. Lee, L-K. and Ruthven, D.M. *J. Chem. Soc. Faraday Trans. I.* **75**, 2406 (1979).

103. Eic, M. and Ruthven, D.M. *Zeolites* **8**, 40 (1988).

104. Eic, M. and Ruthven, D.M. Intracrystalline diffusion of linear paraffins and benzenes in silicalite studied by the ZLC method, Jacobs, P.A. van Santen, R- A. Zeolites: Facts, Figures, Future. p. 897 Elsevier, Amsterdam 1987.

105. Post, M.F.M., van Amstel, J. and Kouwenhoven, H.W. *Proceedings of 6th international zeolite conference*, Reno, USA, 1984, 517.

106. Garcia, S.F. and Weisz, P.B. *J. Catal.* **121**, 294 (1990).

107. Lin, D., Ducarme, V. and Vedrine, J.C. Asorption and diffusion of different hydrocarbon in MFI zeolite of varying crystallite sizes. Zeolites as Catalysts, Sorbents and Detergent Builders. (Karge, H.G. Weitkamp, J. eds) p. 615, 1989.

108. Bartholomew, C.H. *Appl. Catal.* **107**, 1 (1993).

109. Sehested, J., Carlson, A., Janssens, T.V.W., Hansen, P.L. and Datye, A.K. *J. Catal.* **197**, 200 (2001).

110. Chen, D., Lødeng, R., Omdahl, K., Anundskås, A., Olsvik, O. and Holmen, A *Stud. Surf. Sci. Catal.* **139**, 93 (2001).

111. Chen, D., Lødeng, R., Omdahl, K., Anundskås, A., Olsvik, O. and Holmen. Microkinetic modeling of steam reforming in the presence of transport limitations. Presented at *ISCRE17*, Hong Kong, 2002.

112. Chen, D., Svendsen, H., Lødeng, R., Omdahl, K., Anundskås, A., Olsvik, O. and Holmen, A. A multiscale approach to steam methane reforming: Carbon potential mapping in a steam reforming reactor. Presented *ISCRE17*, Hong Kong, 2002.

113. Chen, D., Bjørgum, E., Lødeng, R., Christensen, K.O. and Holmen, A. *Stud. Surf. Sci. Catal*. **147**, 139 (2004).

114. Helveg, S., Lopez-Cartes, C., Sehested, J., Hansen, P.L., Clausen, B.S., Rostrup-Nielsen, J.R., Abild-Pedersen, F. and Nørskov, J.K. *Nature* **427**, 6973 (2004).

115. Xu, J. and Froment, G.F. *AIChE Journal* **35,** 88 (1989).

Figure Captions

Figure 1. The Tapered Element Oscillating Microbalance Reactor from Patashnick and Rupprecht (TEOM Series 1500 PMA Reaction Kinetics Analyzer).

Figure 2. Flow diagram of a TEOM experimental set-up for high pressure operations.

Figure 3. Comparisons between 3 min pulse experiments and steady-state experiments for the conversion of methanol and the coke deposition over SAPO-34S. Conditions: T=425°C, WHSV=57h^{-1}, partial pressure of methanol=7.2 kPa. Coke formation: Line: Steady-state experiments and •: 3 min pulses. Conversion: ■: steady-state experiments and ○: 3 min pulses [40].

Figure 4. Transient mass response during 4 subsequent 3 min pulses of methanol on 5.5 mg SAPO-34 at T=698 K, WHSV=385 h^{-1} and P_{MeOH}=7.2 kPa. For comparison the mass response from a pulse (3 min) on quartz is shown. The frequency gate time for recording: 0.8 sec [88].

Figure 5. Transient mass response curves for a six-second pulse of methanol over the catalyst bed (A), over a quartz bed (C) and the corrected curve for the mass response over SAPO-34 (B). Catalyst loading=5.5 mg, T=698 K, WHSV=283 h^{-1} and P_{MeOH}=7.2 kPa. The frequency gate time for recording: 0.8 sec [88].

Figure 6. Yield of olefins versus the coke content on the catalyst during DTO (dimethylether-to-olefins) over SAPO 34F (0.25 μm) with different amounts of coke deposited from propene before the experiment: ▲ 0 wt%, ● 2.4 wt% and ■ 4.7 wt% coke from propene on the catalyst [7].

Figure 7. Yield of olefins versus coke content during MTO over SAPO-34F with different amounts of coke deposited from propene before the experiment: ○: no pretreatment, □: 3.4 wt% coke [7].

Figure 8. Coke yield versus methanol conversion during MTO over SAPO-34 at P_{MeOH}=7.2 kPa and T=425°C. Symbols with lines represent experimental results at different WHSV (g/gcat,h): 384 (□), 253(x), 114(+), 82(Δ), 57 (◊). Solid lines: OPE curves [38].

Figure 9. Changes in the distribution of hydrocarbons during MTO on SAPO-34 at different coke contents. T=425 °C, WHSV=57 h^{-1}, methanol partial pressure= 7.2 kPa. ■: methane,● ●: ethene, ♦: propene, ▲: butene, ×: C_5, +: C_6 [38]

Figure 10. Changes in relative hydrocarbon distribution with the content of coke. T=425 °C, WHSV=57 h^{-1} and the methanol partial pressure 7.2 kPa.

■: methane,● ●: ethene, ♦: propene, ▲: butene, ×: C_5, +: C_6 [38].

Figure 11. Relative activity and adsorption of methanol versus coke content on SAPO-34 at WHSV=283 h^{-1}, 698 K and a methanol partial pressure of 7.2 kPa. ■: relative adsorption (K/K_0), ●: relative conversion (X/X_0). K_0 and X_0 are the initial Henry's Law constant and the initial conversion, respectively [88].

Figure 12. The effect zeolite loading on the diffusion process for n-hexane on HZSM-5 at T= 298 K, identical total flow rate 250 ml/min and n-hexane partial pressure of 22.7 mbar. □: 20 mg, ○: 10 mg, +: 5 mg.

Figure 13. Uptake curve for methanol over SAPO-34 with a crystal size of 2.5 μm at 373 K and a methanol partial pressure of 0.75 kPa. ○: experimental data, line: predicted by Equation (7) for a slab geometry [88].

Figure 14. Steady-state diffusivity of methanol on 0.25 μm, 0.5 μm, 2.5 μm and 25 μm SAPO-34 crystals at different temperatures and partial pressures of methanol: ♦0.8: kPa, □: 2.2 kPa, ○: 10 kPa [89].

Figure 15. Methanol diffusivities and intrinsic reaction rate constants with coke content estimated indirectly from reactions on 0.25 and 2.5 μm crystals [89].

Figure 16. Steam reforming of methane on Ni (11wt%) supported on α-Al_2O_3 (BET surface 5.5 m^2/g) studied in the TEOM. S/C is the steam carbon ratio and the catalyst bed is held in place using quartz, Fiberfrax (90% Al_2O_3, 10% SiO_2) or carbon fiber wool.

Figure 17. Steam reforming of C_1-C_3 mixtures at 460 ^oC, 20 bar and P_{H2}=1.46 bar. On catalyst SR-F: P_{CH4}=3.8 bar, P_{C3H8}=0.15 bar and P_{H2O}=1.2 bar. On PR-F and PR-F: P_{CH4}=3,3 bar, P_{C2H6}=0.4 bar, P_{C3H8}=0,18 bar and P_{H2O}=1,46 bar.

Figure 18. Steam reforming of CH_4 containing either C_2H_6 or C_3H_8 at 580 ^oC and 20 bar on catalyst PR-F. T=450 ^oC, P_{tot}=15 bar, P_{CH4}=3.36 bar, P_{C2H6}=0.42 bar, P_{C3H8}=0.19 bar, P_{H2O}=4.7 bar, S/C_{tot}=1, P_{H2}=o.25 bar.

Figure 19. Effect of adding C_2H_4 and C_3H_6 on steam reforming of C_1-C_3 at 520 ^oC and 20 bar on catalyst PR-S. P_{CH4}=3.36 bar, P_{C2H6}=0.4 bar, P_{C3H8}=o.18 bar, P_{H2}=0.08 bar, P_{H2O}=1.46, 2.8, 4.6 bar.

Figure 20. Steam reforming of CH_4 on catalyst SR-F. P_{tot}=20 bar, P_{CH4}=3,9 bar, P_{H2O}=3.1 bar, P_{H2}=0.1 bar, S/C=0.8 bar.

Figure 21. Effect of C_3H_6 addition on steam reforming of CH_4 + C_3H_8 on catalyst SR-F. P_{tot}=20 bar, P_{HC}=3.9 bar, P_{H2}=0.1 bar and T=670 ^oc

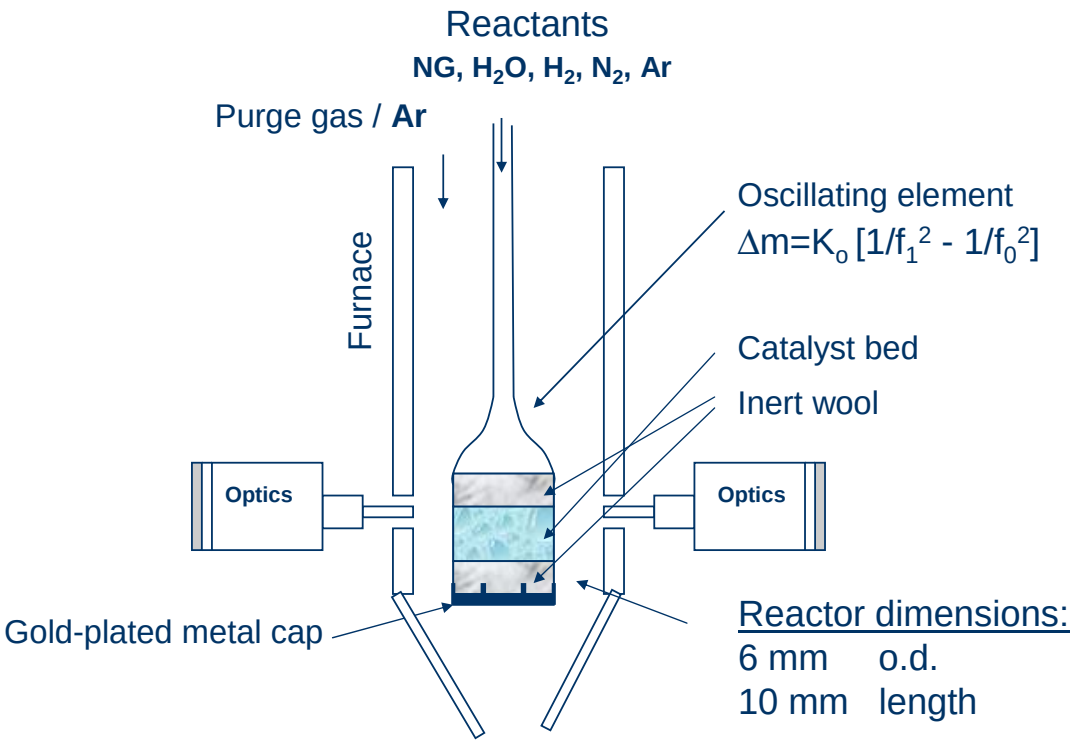
Reactants
NG, H_2O, H_2, N_2, Ar
Purge gas / Ar
Furnace
Oscillating element
$\Delta m=K_o [1/f_1^2 - 1/f_0^2]$
Catalyst bed
Inert wool
Optics
Optics
Gold-plated metal cap
Reactor dimensions:
6 mm o.d.
10 mm length

Figure 1

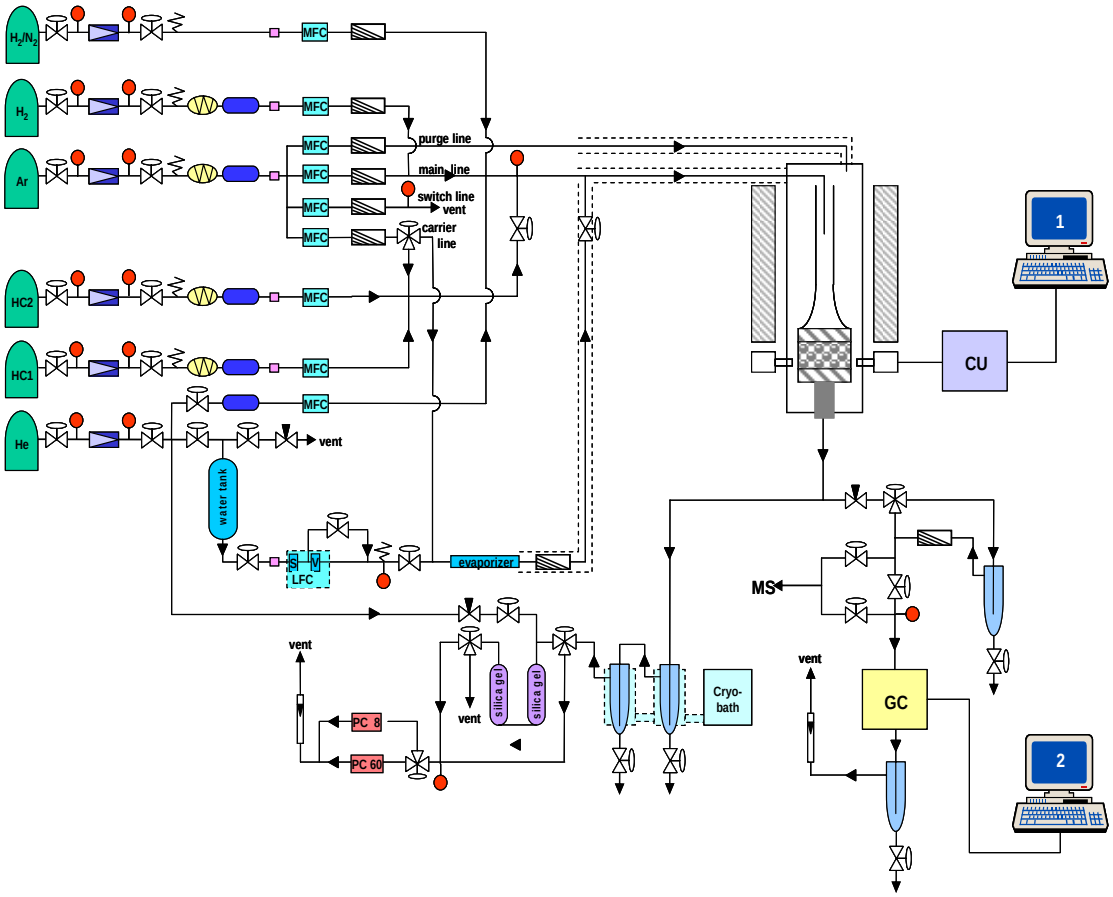
H2/N2
H2
Ar
HC2
HC1
He
MFC
purge line
main line
switch line
vent
carrier line
water tank
LFC
evaporizer
vent
CU
1
MS
GC
2
Cryo-bath
silica gel
silica gel
PC 8
PC 60
vent

Figure 2

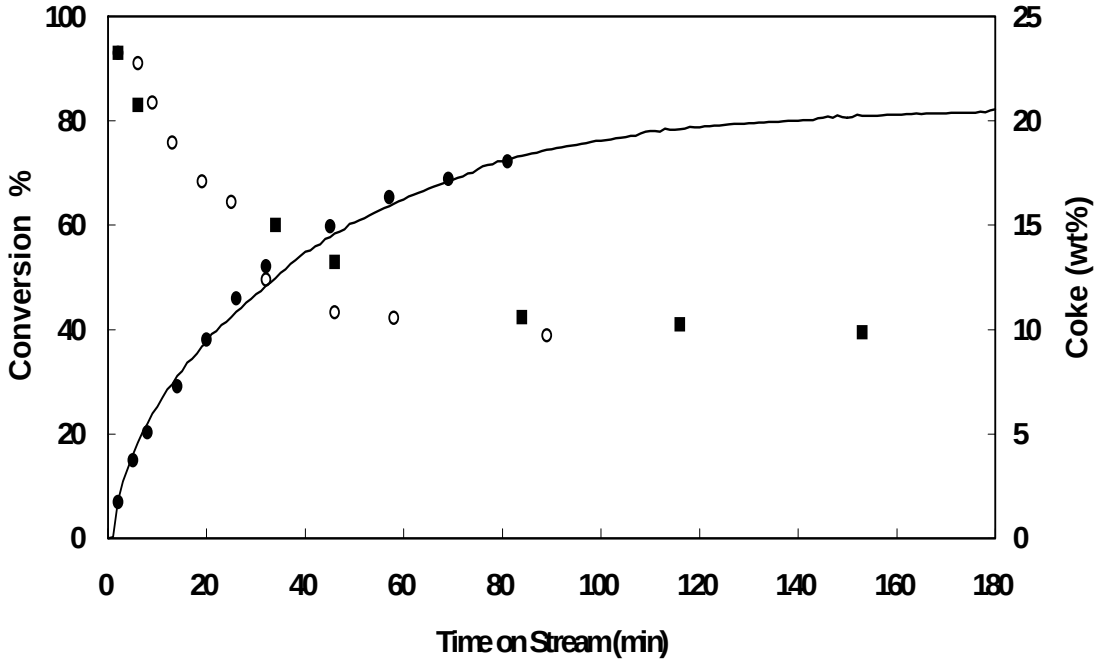
100
80
60
40
20
0
Conversion %
25
20
15
10
5
0
Coke (wt%)
0
20
40
60
80
100
120
140
160
180
Time on Stream (min)

Figure 3

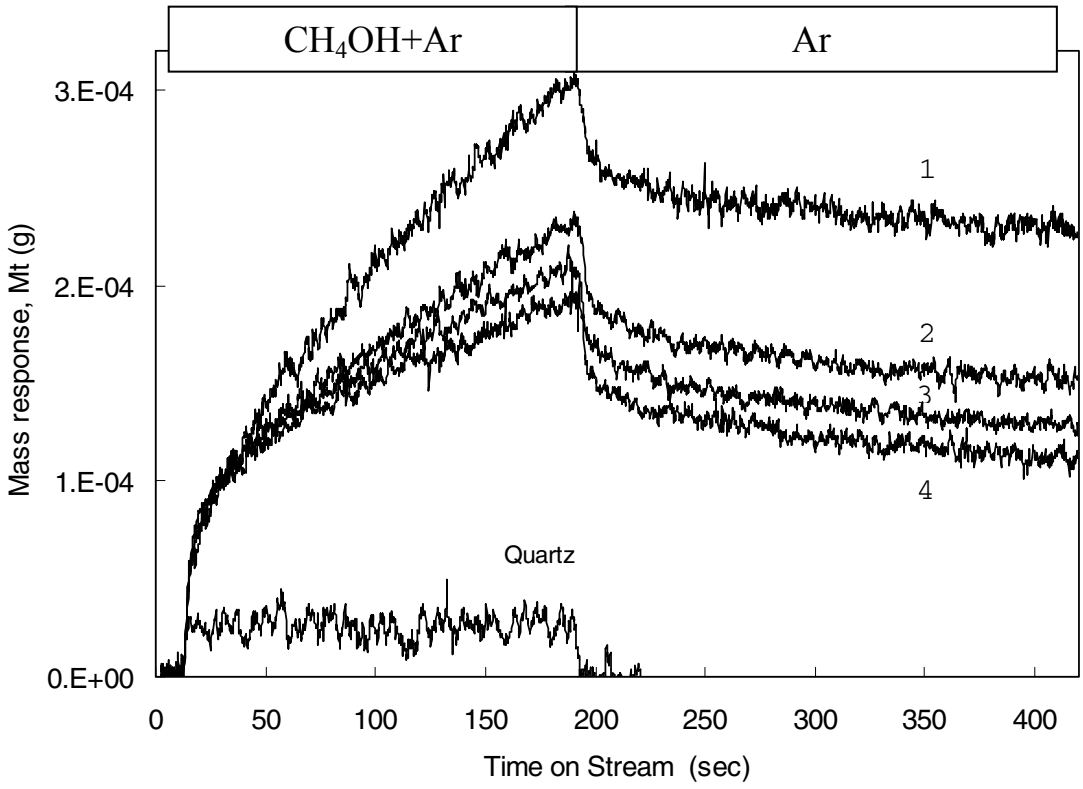
CH4OH+Ar
Ar
3.E-04
2.E-04
1.E-04
0.E+00
Mass response, Mt (g)
1
2
3
4
Quartz
0
50
100
150
200
250
300
350
400
Time on Stream (sec)

Figure 4

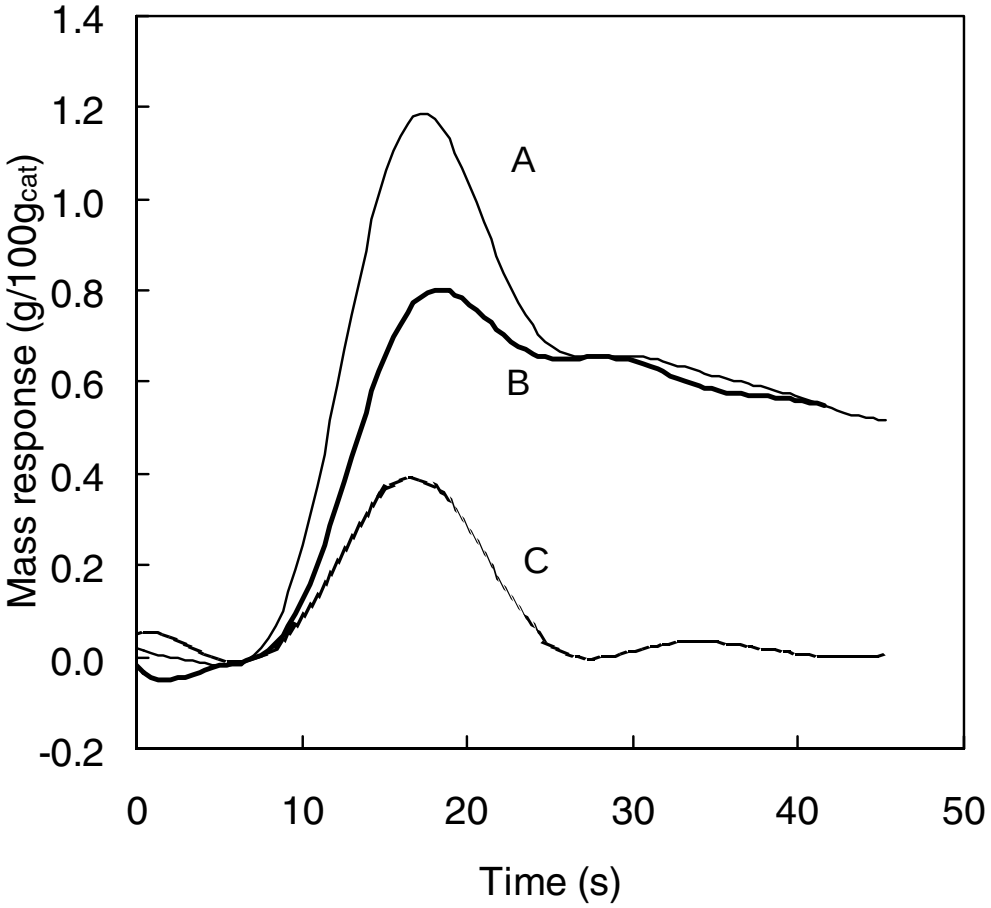
1.4
1.2
1.0
0.8
0.6
0.4
0.2
0.0
-0.2
Mass response (g/100g$_{cat}$)
A
B
C
0
10
20
30
40
50
Time (s)

Figure 5

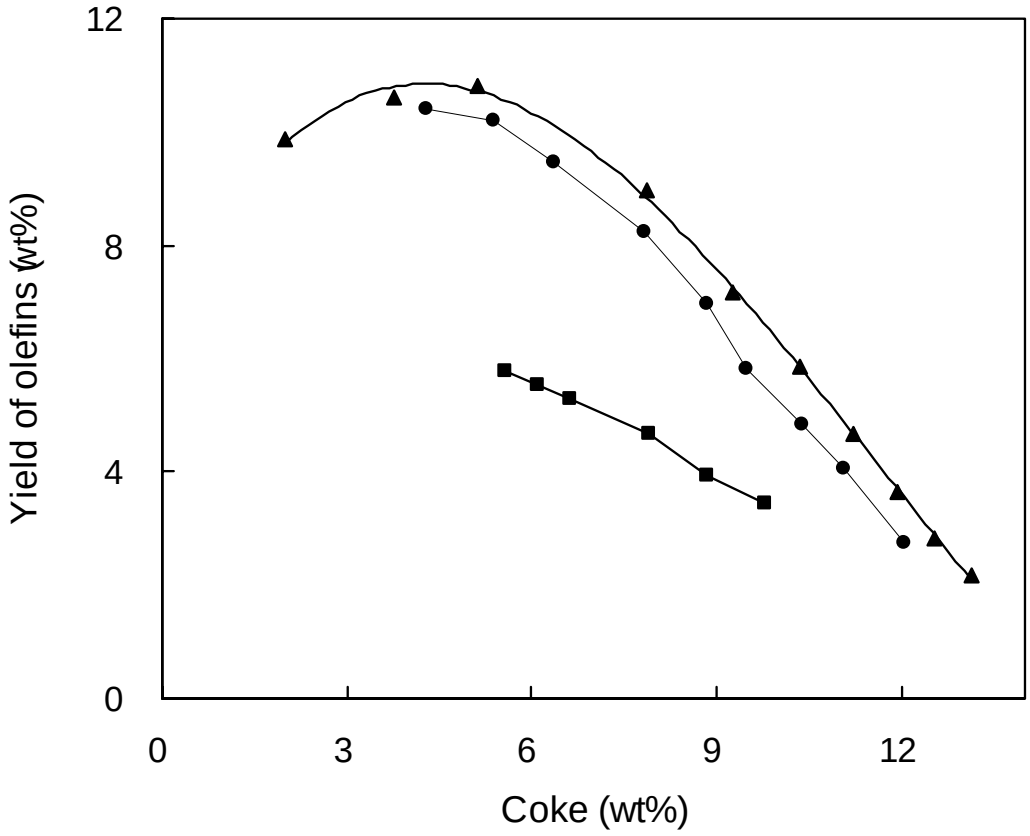

Figure 6

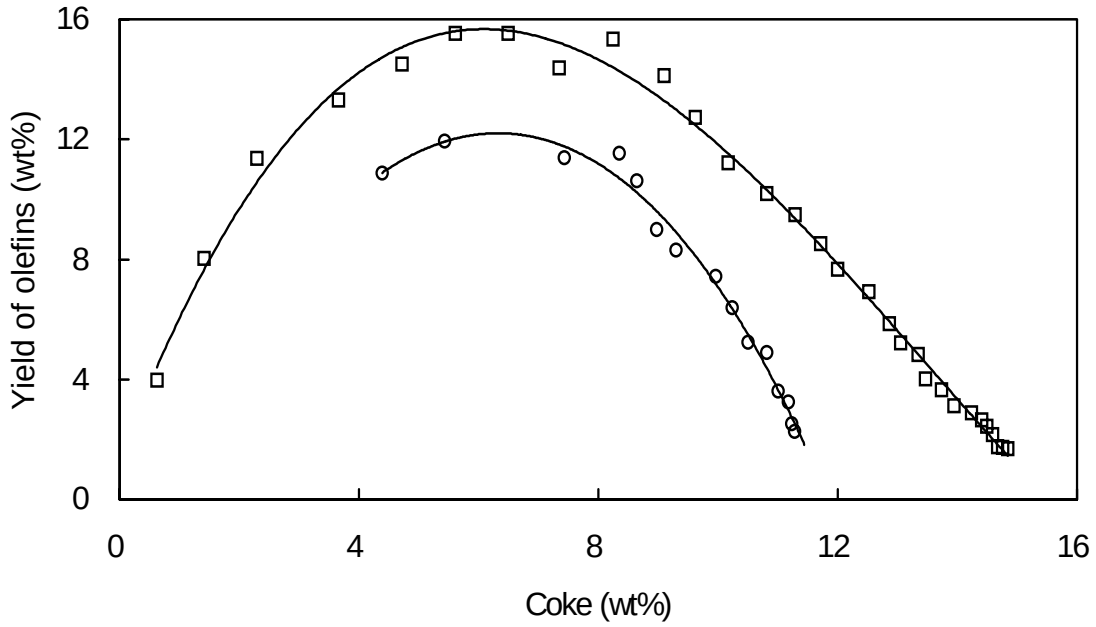

Figure 7

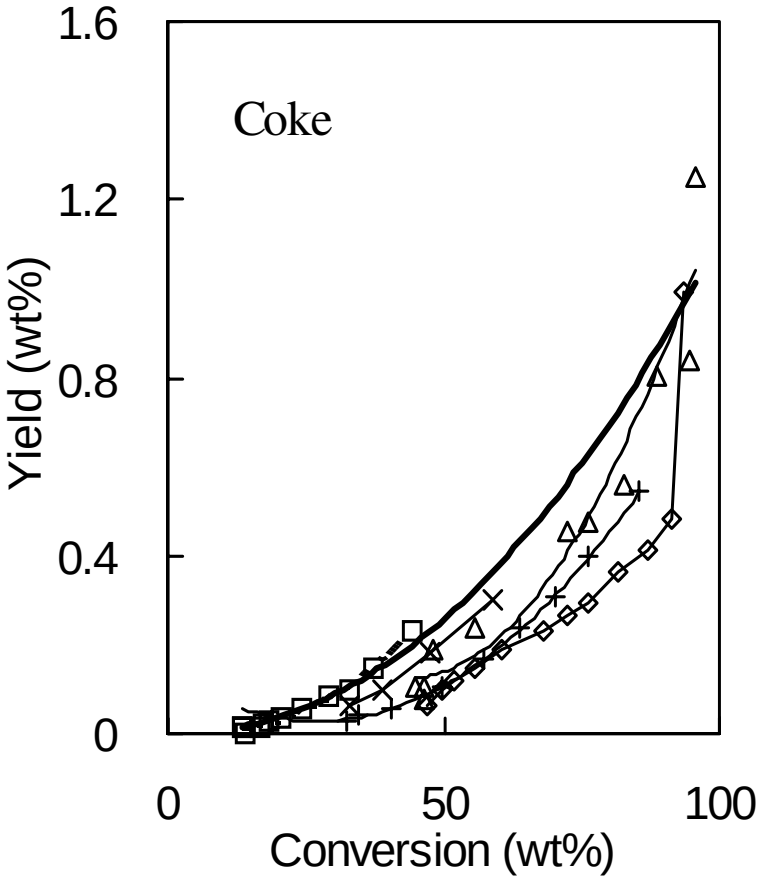

Figure 8

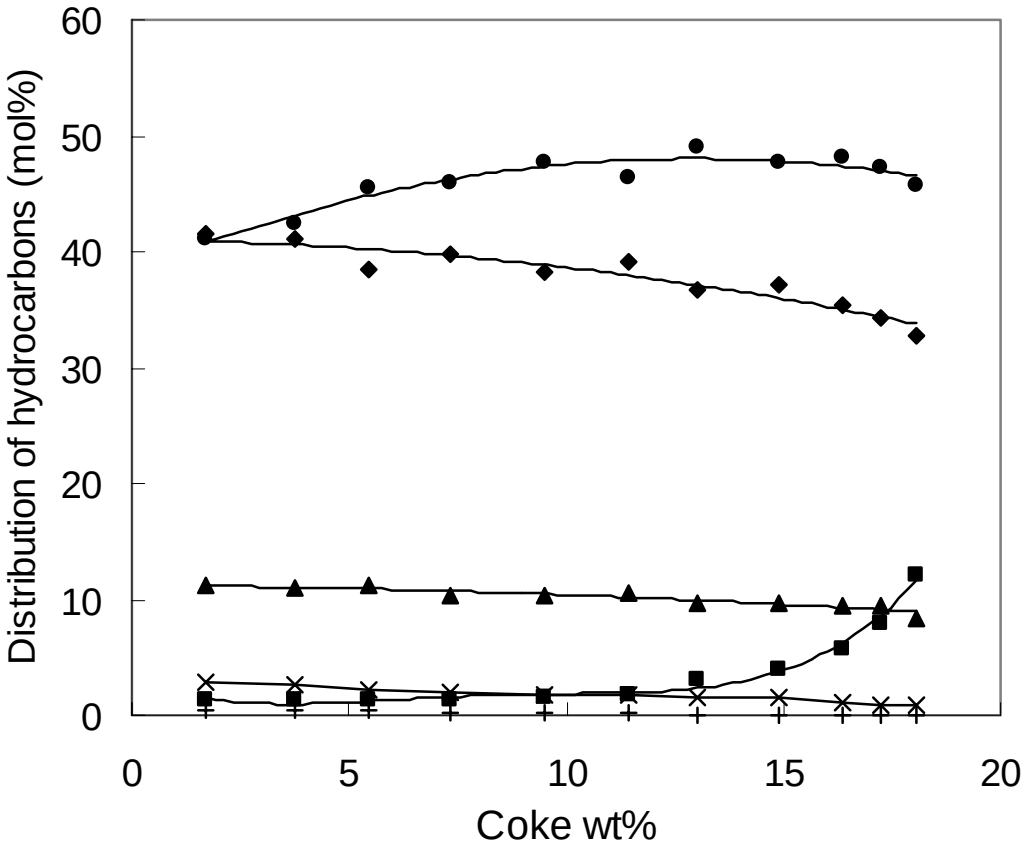
Distribution of hydrocarbons (mol%)
60
50
40
30
20
10
0
0
5
10
15
20
Coke wt%

Figure 9

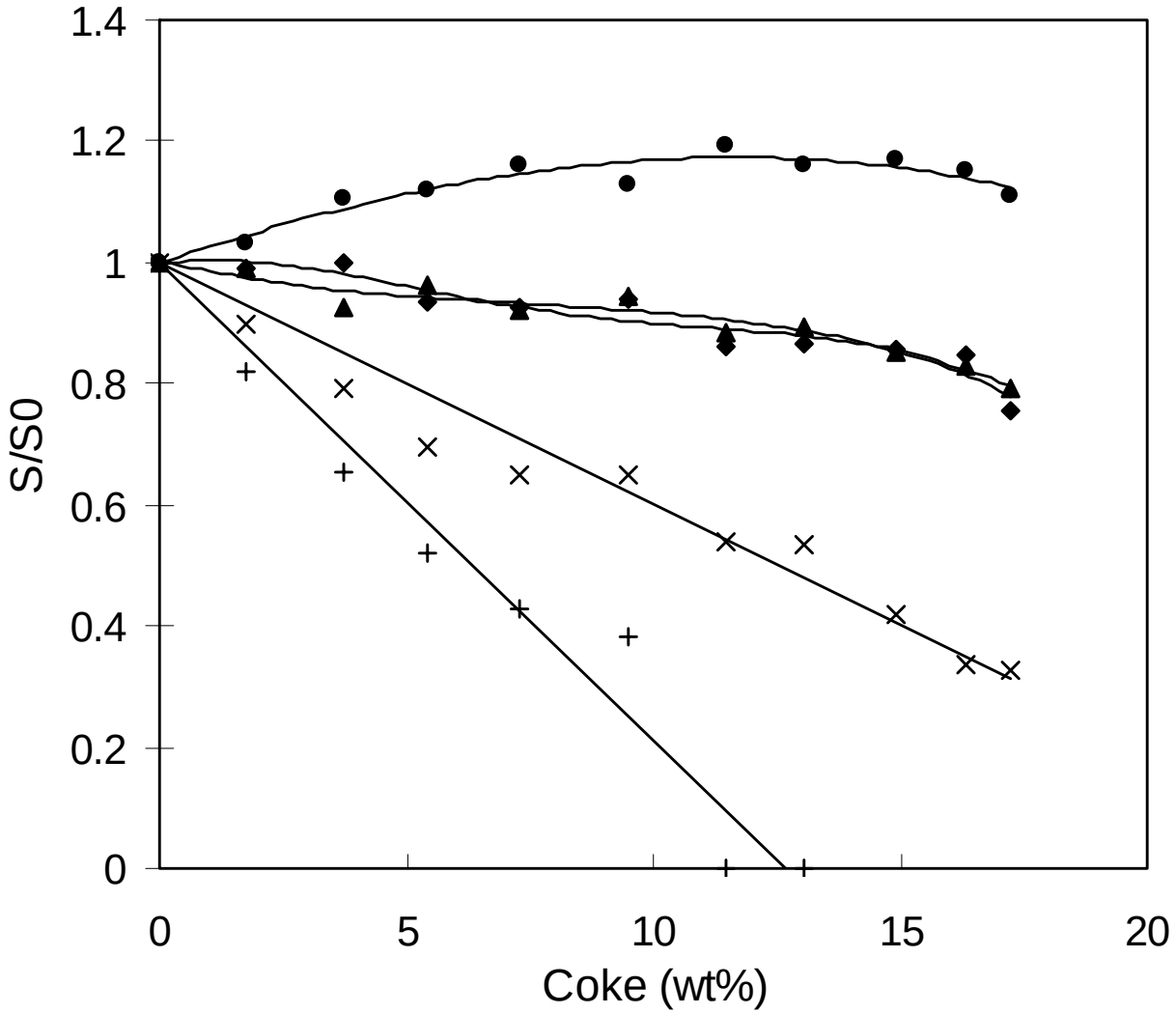

Figure 10

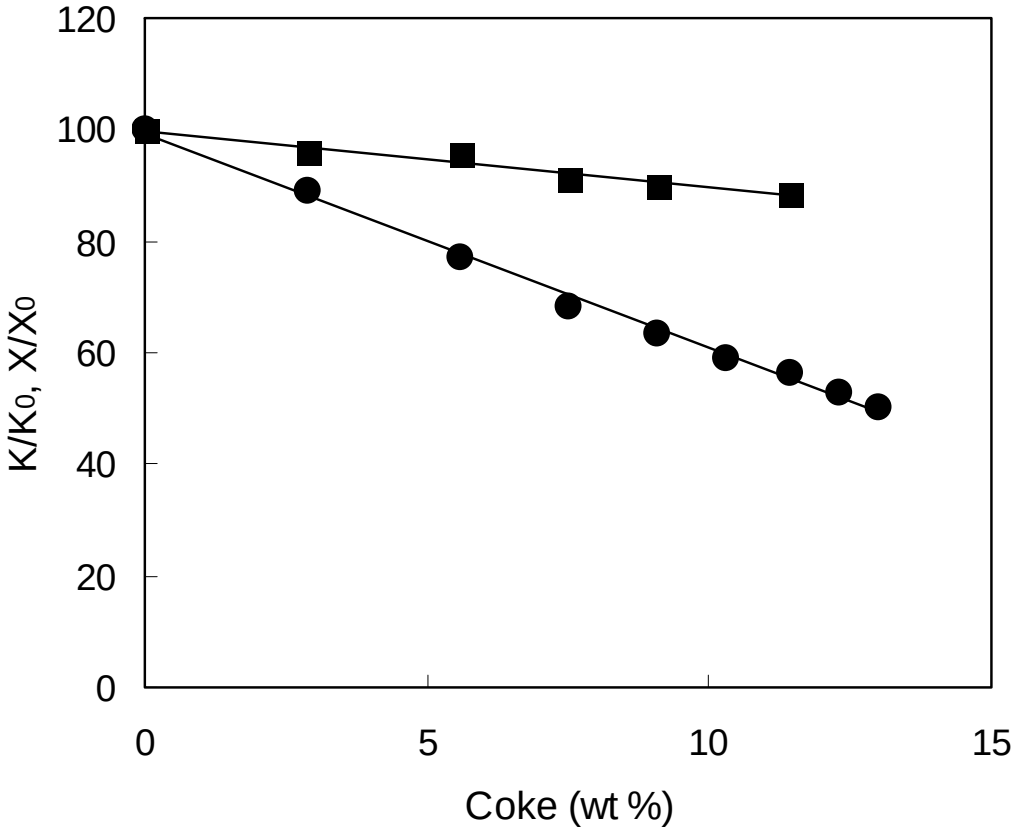

Figure 11

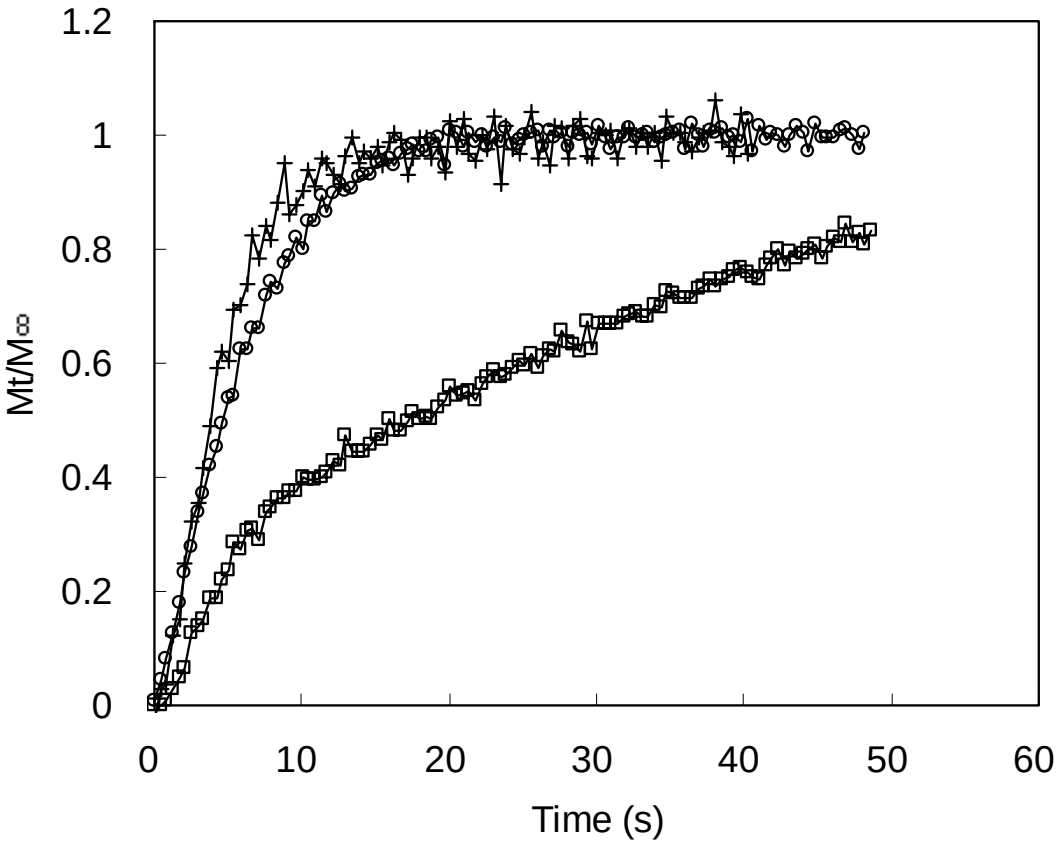

Figure 12

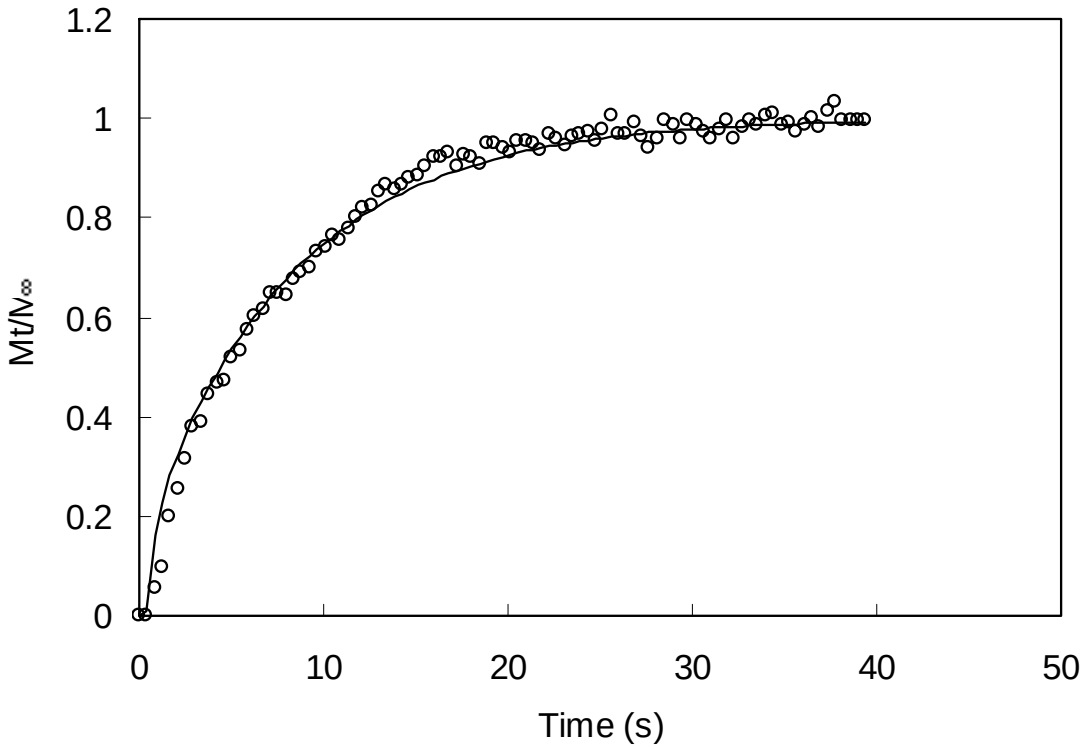

Figure 13

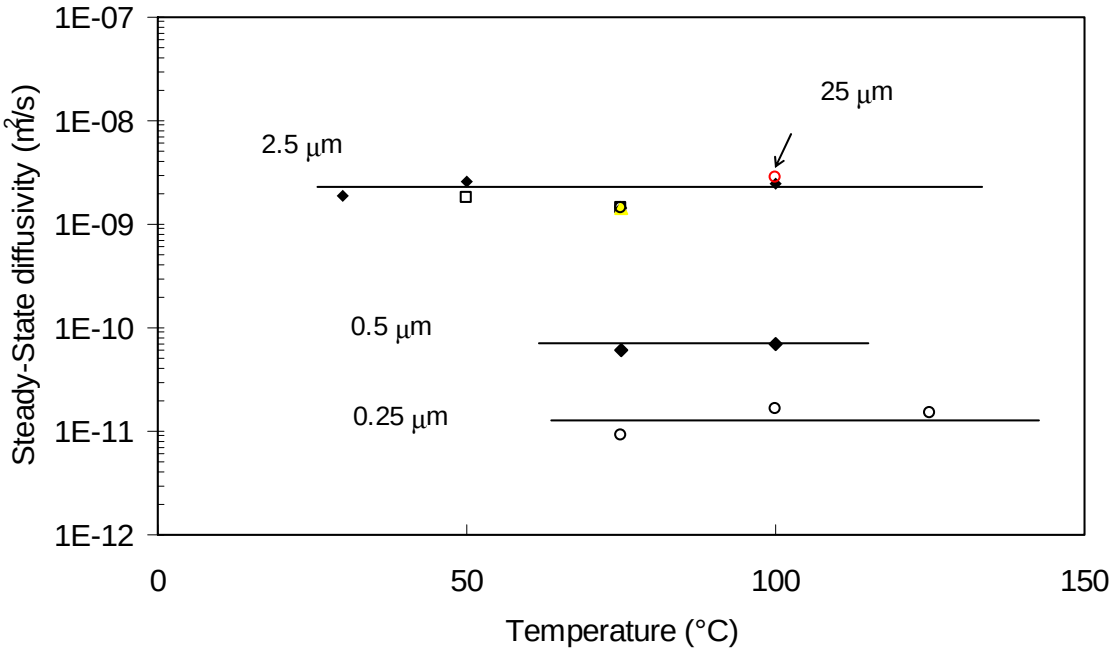
1E-07
1E-08
1E-09
1E-10
1E-11
1E-12
Steady-State diffusivity (m²/s)
25 μm
2.5 μm
0.5 μm
0.25 μm
0
50
100
150
Temperature (°C)

Figure 14

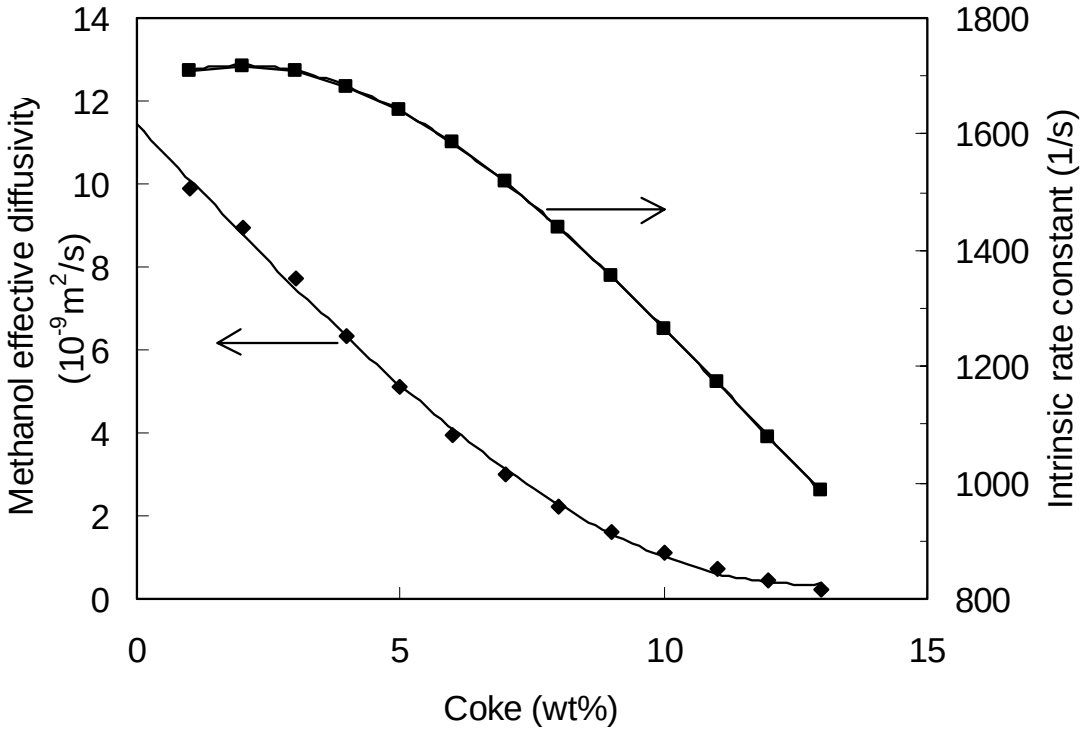
Methanol effective diffusivity
(10^{-9} m^2/s)
Intrinsic rate constant (1/s)
Coke (wt%)
0
2
4
6
8
10
12
14
800
1000
1200
1400
1600
1800
0
5
10
15

Figure 15

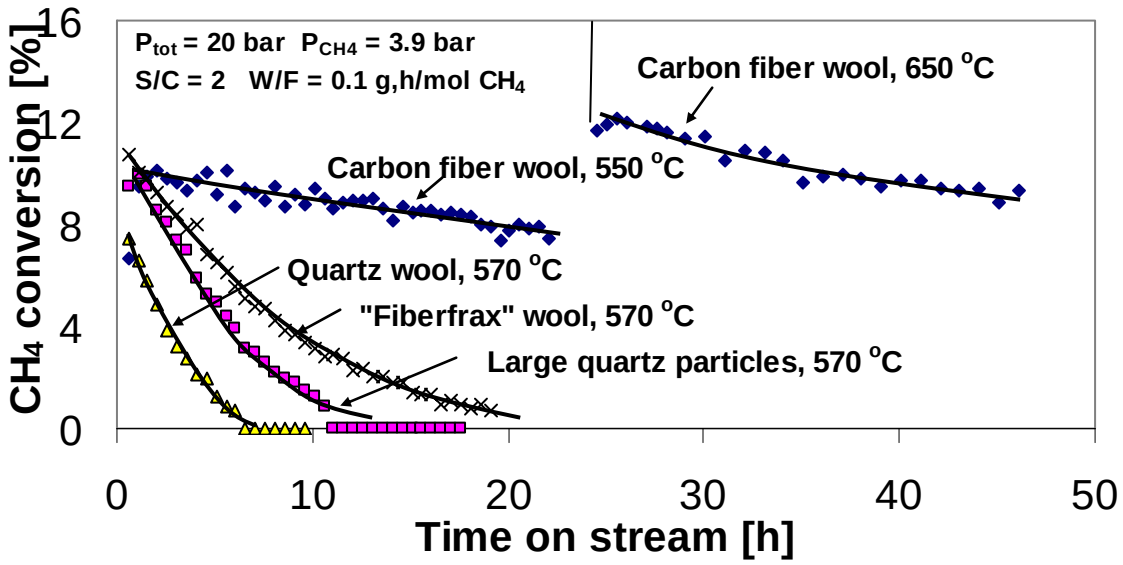
P_{tot} = 20 bar P_{CH4} = 3.9 bar
S/C = 2 W/F = 0.1 g,h/mol CH_4
Carbon fiber wool, 650 °C
Carbon fiber wool, 550 °C
Quartz wool, 570 °C
"Fiberfrax" wool, 570 °C
Large quartz particles, 570 °C
CH_4 conversion [%]
0
4
8
12
16
0
10
20
30
40
50
Time on stream [h]

Figure 16

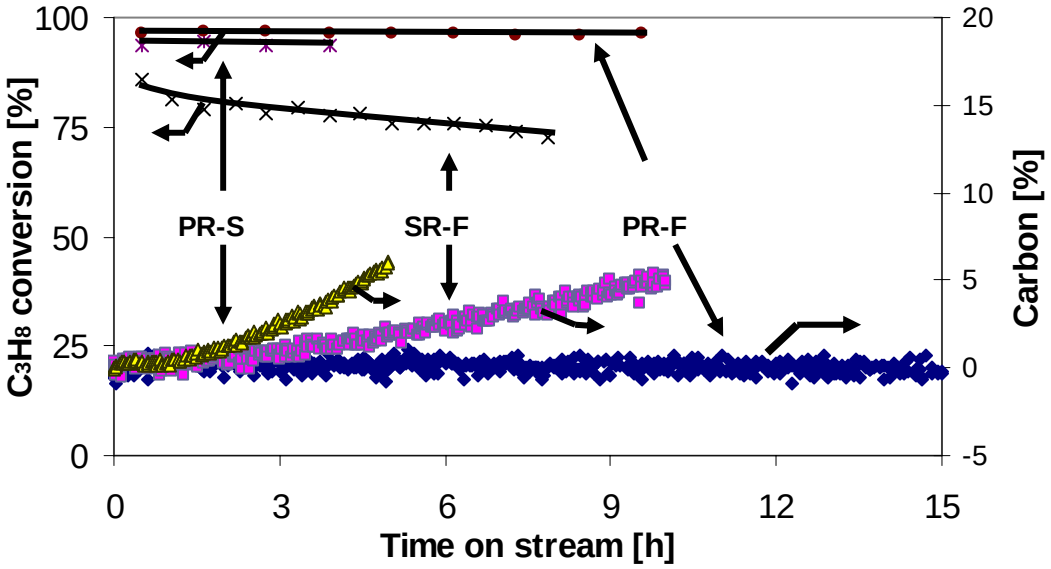
100
75
50
25
0
20
15
10
5
0
-5
0
3
6
9
12
15
C3H8 conversion [%]
Carbon [%]
Time on stream [h]
PR-S
SR-F
PR-F

Figure 17

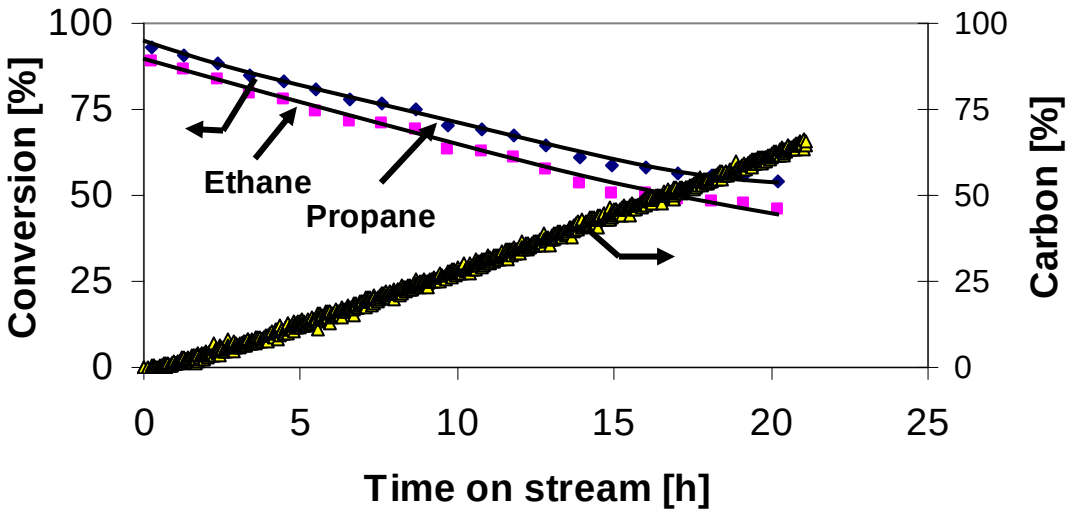
100
75
50
25
0
Conversion [%]
Ethane
Propane
Carbon [%]
0
5
10
15
20
25
Time on stream [h]

Figure 18

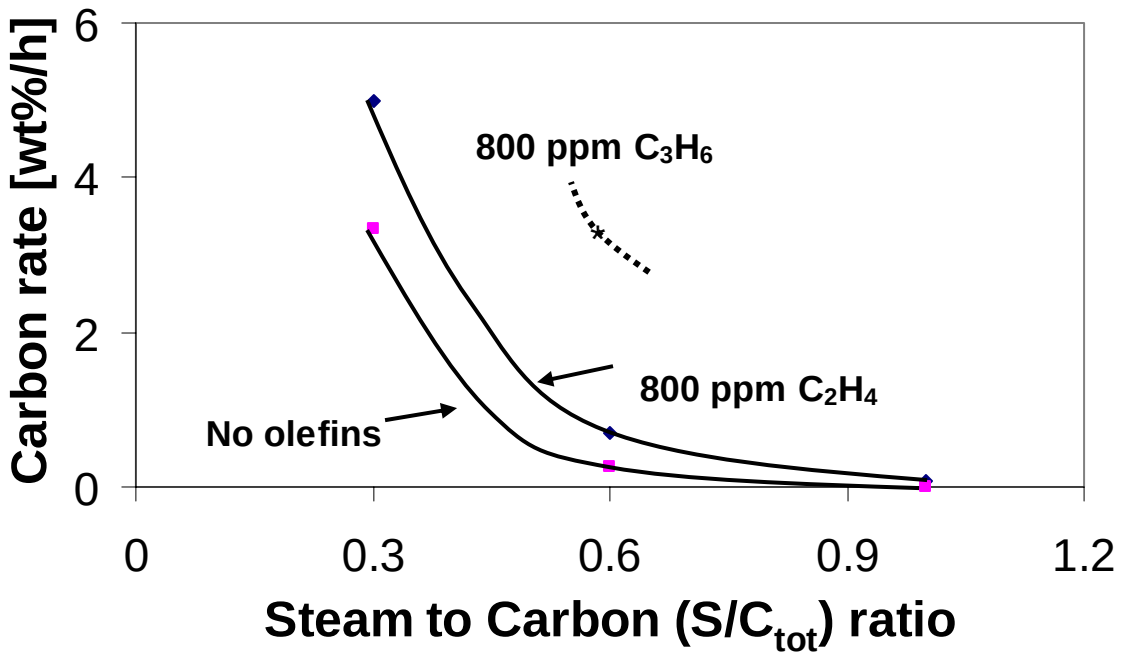
Carbon rate [wt%/h]
6
4
2
0
800 ppm C_3H_6
800 ppm C_2H_4
No olefins
0
0.3
0.6
0.9
1.2
Steam to Carbon (S/C_{tot}) ratio

Figure 19

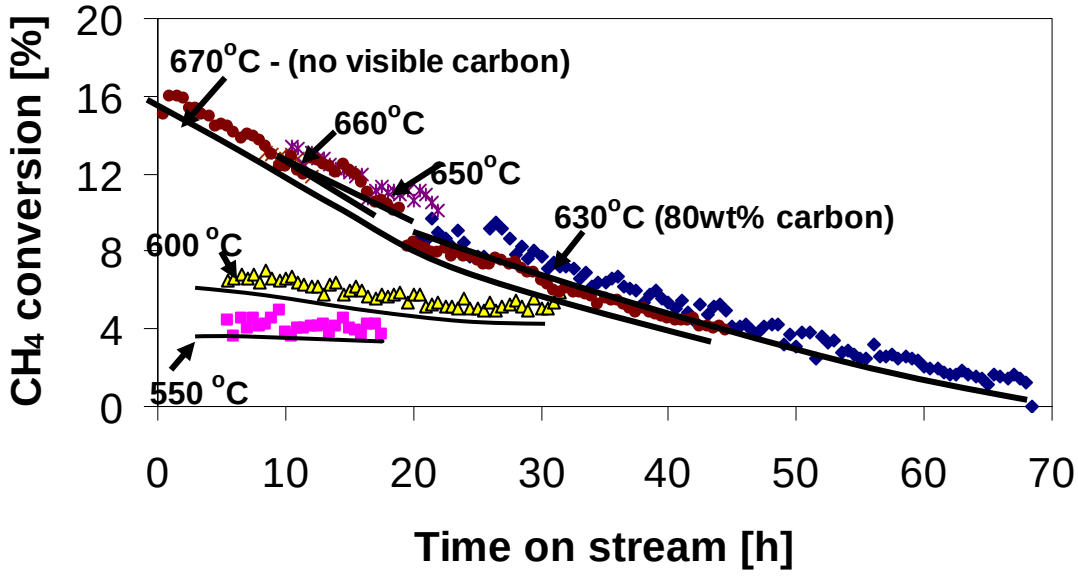
20
16
12
8
4
0
CH4 conversion [%]
670°C - (no visible carbon)
660°C
650°C
630°C (80wt% carbon)
600 °C
550 °C
0
10
20
30
40
50
60
70
Time on stream [h]

Figure 20

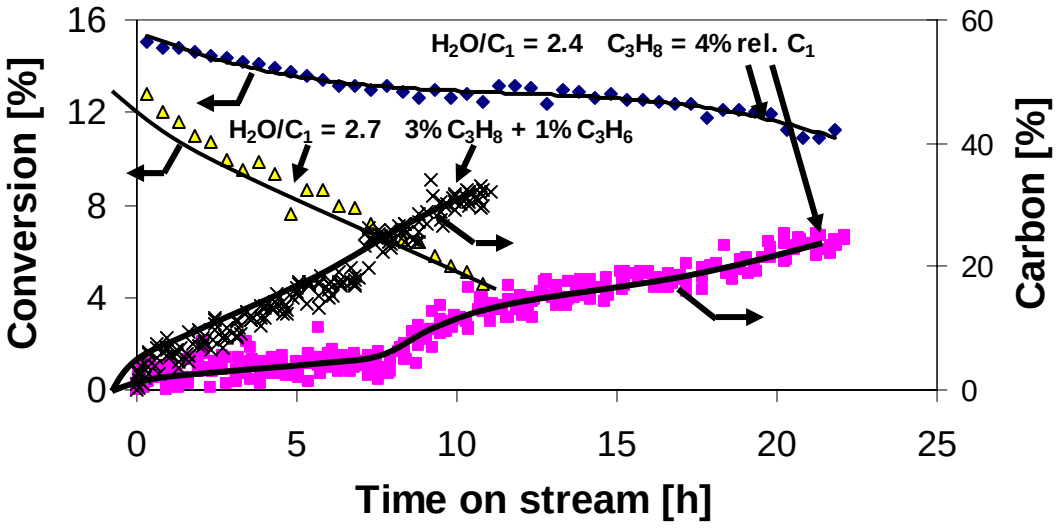
16
12
8
4
0
Conversion [%]
60
40
20
0
Carbon [%]
0
5
10
15
20
25
Time on stream [h]
H2O/C1 = 2.4 C3H8 = 4% rel. C1
H2O/C1 = 2.7 3% C3H8 + 1% C3H6

Figure 21

Paper IV

A model for reforming on Ni catalysts with carbon formation and deactivation

Studies in Surface Science and Catalysis, Vol. 139
J.J. Spivey, G.W. Roberts and B.H. Davis (Editors)

A Model for Reforming on Ni Catalyst with Carbon Formation and Deactivation

De Chen[a], Rune Lødeng[b], Kjersti Omdahl[a], Arne Anundskås[c], Ola Olsvik[d] , Anders Holmen[a]

[a]Department of Chemical Engineering, Norwegian University of Science and Technology (NTNU), N-7491 Trondheim, Norway.
[b]SINTEF Applied Chemistry, N-7465 Trondheim, Norway.
[c]Norsk Hydro, Research Center, Box 2560 N-3907 Porsgrunn, Norway.
[d]Statoil Research Center, Postuttak, N-7004 Trondheim, Norway.

A microkinetic model with 30 elementary steps has been developed to describe methane reforming including carbon formation and deactivation. No rate-determining step is assumed in the model. The Bond Order Conservation (BOC) method was used to calculate activation energies as a function of bond strength of carbon-nickel, hydrogen-nickel and oxygen-nickel. The simulation of gas composition, surface coverages and carbon formation is shown and compared with experimental values. The model is able to properly describe both dry and steam reforming of methane on Ni/MgO-Al_2O_3 and on Ni/CaO-Al_2O_3 at a pressure range of 0.1 to 2 MPa and a temperature range of 500 to 650 °C.

1. Introduction

Coke formation, sintering, poisoning and solid-state transformations are major causes of catalyst deactivation. Kinetic modeling of such processes has attracted much interest from both academy and industry (1,2). The quantitative formulation of deactivation as a function of coke content derived by Froment and coworkers (2) was a major breakthrough in this field. However, a fundamental kinetic expression for metal catalyzed reactions is by no means easy to arrive at since the morphology and location of the coke on the metal surface can be an even more important parameter than the coke content itself. Moreover, the kinetic expressions for the main and the coking reactions are normally derived by the Langmuir-Hinshelwood approach, where a rate-determining step (RDS) is assumed. However, the possible effect of coke formation on the RDS has usually been ignored. Dumesic et al. (3) have clearly demonstrated that RDS can change with the reaction conditions or that no single rate-determining step exists. It should also be expected that the RDS might change with carbon deposition, sintering and poisoning. Therefore, a more fundamental kinetic model is required for describing such effects in catalyst deactivation.

Since the pioneering work of Dumesic et al. in 1993 (3) there has been a substantial effort in microkinetic modeling based on knowledge about elementary steps and their energetics, where the parameters reflect the physical meaning and no rate-determining step is assumed. A review of recent developments is given by Broadbelt and Snurr (4). Dumesic et al. (3) also proposed a method for catalyst design through microkinetic modeling. The catalyst surface properties are reflected in the rate constants of the elementary steps, determined either experimentally or estimated theoretically. The BOC-MP (Bond Order Conservation-Morse Potential) approach (5) provides such a tool to estimate activation energies. More interestingly, it creates a link between bond strength (between absorbed atoms and the metal) and activation energies, which can provide a direct guidance for suggesting new catalysts or improving existing ones.

The conversion of natural gas to synthesis gas will continue to play an important role also in the years to come. Methane reforming on Ni catalysts is a main process for production of synthesis gas. However, the process suffers from the possible risk of carbon formation and deactivation. Aparicio (6) has established a microkinetic model for methane steam reforming with kinetic parameters determined from transient kinetic experiments, as well as from Xu's steady-state experimental results of steam reforming and CO_2 methanation (15). We have previously extended Aparicio's model to apply also for methane dry reforming (7). Since no RDS is assumed in microkinetic modeling, it might provide the best opportunity to describe deactivation kinetics. It can also provide a good framework for understanding the deactivation mechanism and the effect of the individual elementary reaction steps on deactivation at a molecular level.

However, a direct link between catalyst properties and kinetics is missing in Aparicio's model (6) and our previous work (7). The present work deals with the development of a microkinetic model for syngas production including carbon formation and deactivation, where the activation energies are related to C-Ni, O-Ni and H-Ni bond strengths determined by the BOC-MP method.

2. Experimental

The experiments were performed in the Tapered Element Oscillating Microbalance (TEOM) reactor (7,8), in which carbon formation and deactivation could be measured simultaneously by coupling with on-line GC analysis. The dry reforming of methane was studied on an industrial Ni (11 wt%)/(CaO)α-Al_2O_3 catalyst at temperatures of 500 °C and 650 °C, total pressures of 0.1 MPa and 0.5 MPa and a CO_2/CH_4 ratio of 1. The BET surface area of the catalyst was 5.5 m^2/g, and the Ni surface area 0.33 m^2/g. The detailed experimental procedures were similar to that reported previously (7).

3. Microkinetic modeling

The reaction mechanisms of methane steam reforming (6,9) and dry reforming (10) have been studied extensively. It is commonly agreed that activation of methane on Ni surfaces involves dissociative adsorption followed by a series of dehydrogenation steps. No dissociative adsorption of CO_2 and CO is assumed in the model. Based on our previous work (7), we have assumed an ensemble size of 2 for adsorption of carbon on a Ni surface, giving a maximum carbon site coverage of 0.5. This is in good agreement with experimental results (11). All the elementary reaction steps are summarized in Table 1.

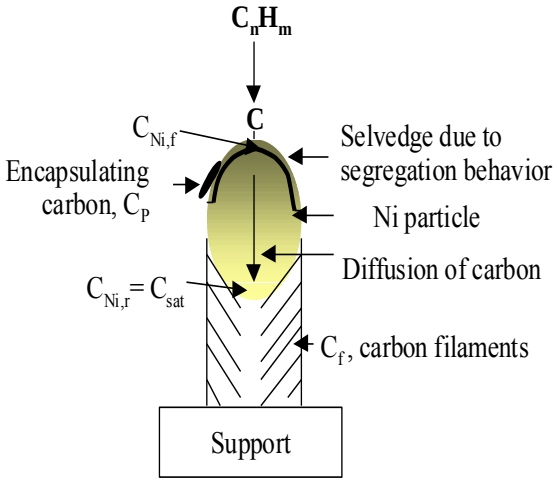

Fig. 1 Mechanism of formation of filamentous carbon (13).

Atomic carbon, encapsulating and filamentous carbon are the most important types of carbon formed. It is generally accepted that filament carbon formation (13) involves the formation of adsorbed surface carbon, dissolution and segregation of surface carbon, diffusion of carbon through Ni particles and precipitation of filaments. The mechanism of carbon formation (12,13) is illustrated in Fig. 1. $C_{Ni,f}$ is the concentration of carbon dissolved in nickel at the front of the particle, just below the selvedge, and $C_{Ni,r}$ is the concentration of carbon dissolved in nickel at the rear of the particle (support side). The properties of the carbon on the front side and the filamentous carbon on the rear side are rather different. The different chemical potential of these carbon materials result in different

solubility in the front and rear side of the Ni crystal, thus creating a driving force for the diffusion of carbon through nickel.

Table 1. Microkinetic model for CH_4 reforming including carbon formation.
The model is based on Aparicio (6), Chen et al. (7), the mechanism in Fig. 1, BOC model calculations and experimental data. R=8.314 J/mol,K

	Reaction	Rate constant Forward reaction	Rate constant Reverse reaction
r_1	$CH_4 + 2* \rightleftarrows *CH_3 + *H$	$6.5\cdot10^{7}\cdot e^{-57500/RT}$	$1.5\cdot10^{10}\cdot e^{-80900/RT}$
r_2	$*CH_3 + * \rightleftarrows *CH_2 + *H$	$1.0\cdot10^{13}\cdot e^{-99900/RT}$	$2.0\cdot10^{12}\cdot e^{-49600/RT}$
r_3	$*CH_2 + * \rightleftarrows *CH + *H$	$1.0\cdot10^{13}\cdot e^{-97000/RT}$	$1.0\cdot10^{13}\cdot e^{-73700/RT}$
r_4	$**CH + * \rightleftarrows **C + *H$	$1.0\cdot10^{13}\cdot e^{-189700/RT}$	$1.0\cdot10^{13}\cdot e^{-173000/RT}$
r_5	$H_2O + * \rightleftarrows *H_2O$	$2.4\cdot10^{6}$	$1.0\cdot10^{13}\cdot e^{-68900/RT}$
r_6	$*H_2O + * \rightleftarrows *OH+*H$	$1.0\cdot10^{16}\cdot e^{-86700/RT}$	$1.0\cdot10^{13}\cdot e^{-42700/RT}$
r_7	$**C + *OH \rightleftarrows **CHO + *$	$1.0\cdot10^{13}\cdot e^{-86800/RT}$	$6.73\cdot10^{11}\cdot T^{-3.03}\cdot e^{-103600/RT}$
r_8	$**COOH+*O \rightleftarrows **CHO+*OH$	$3.38\cdot10^{18}\cdot T^{-0.968}\cdot e^{-108900/RT}$	$1.0\cdot10^{15}\cdot e^{-24900/RT}$
r_9	$**CHO + * \rightleftarrows **CO + *H$	$1.0\cdot10^{11}\cdot e^{-16800/RT}$	$1.0\cdot10^{11}\cdot e^{-66700/RT}$
r_{10}	$**CO \rightleftarrows CO + 2*$	$2.0\cdot10^{12}\cdot e^{-122400/RT}$	$5.9\cdot10^{7}$
r_{11}	$2*H \rightleftarrows H_2 + 2*$	$3.1\cdot10^{12}\cdot e^{-97600/RT}$	$1.1\cdot10^{8}\cdot e^{-5600/RT}$
r_{12}	$CO_2 + 2* \rightleftarrows **CO_2$	$1.0\cdot10^{6}$	$1.0\cdot10^{13}\cdot e^{-27300/RT}$
r_{13}	$**CO_2 + *H \rightleftarrows **COOH + *$	$1.0\cdot10^{13}$	$1.0\cdot10^{13}\cdot e^{-18400/RT}$
r_{14}	$**C \rightleftarrows C_{Ni,f} + 2*$	eq (2)	
r_{15}	$C_{Ni,f} \rightarrow C_{Ni,r}$	eq (4)	
r_{16}	$C_{Ni,r} \rightleftarrows C_f$	fast	
r_{17}	$3**C \rightarrow 3\ C_{encap}$	$k\theta_C^{3}$	

Shustorovich (5) has reviewed the detailed method and the equations for calculating heat of chemisorption and activation barriers by BOC. The multidimensional activation energies were calculated in the present work and the activation energies are listed in Table 1. The initial preexponential factors were estimated by transition-state theory, employing reasonable chemical assumptions about surface mobility. Dumesic et al. (3) summarized typical ranges of these values used in microkinetic analysis studies. For the reaction A*+B*→C*+D* the preexponential factor is typically 10^{13} s^{-1}, assuming immobile surface intermediates without rotation.

The TEOM reactor is modeled as an ideal plug flow reactor. For reactions without carbon deposition and deactivation, 12 surface species and 5 gas phase components were solved from 12 surface species mass balance equations, two mass balance equations for the reactor (CH_4 and CO_2 or CO) and three element mass balance equations.

Based on the mechanism of carbon formation presented in Fig. 1, carbon filaments do not deactivate the catalyst as encapsulating carbon does. The encapsulating carbon deactivates the

catalysts by decreasing the total number of active sites. This is described by a site conservation equation (Eq. (1)) in the present work:

$$\theta_H + \theta_{CH3} + \theta_{CH2} + \theta_{CH} + 2\theta_C + \theta_{H2O} + \theta_{OH} + \theta_{CHO} + 2\theta_{CO} + 2\theta_{CO2} + 2\theta_{COOH} + \theta_* + \theta_{Cp} + \theta_{other} = 1 \quad (1)$$

where θ_{other} is the effective site coverage of other species such as promoters and poisons.

Snoeck et al. (13) suggested that segregation is a fast process and that a segregation/dissolution equilibrium exists at the gas side of the nickel particle. A simple Langmuir equation (Eq. (2 and 3)) was used to estimate the concentration of carbon in the segregation layer (7):

$$\frac{\theta_C}{1-\theta_C} = \frac{x_b}{1-x_b}\exp(-\frac{\Delta G_{seg}}{RT}) \text{ where } \Delta G_{seg} = -4.52\cdot10^4 - 14.23T \text{ (J/mol)} \quad (2)$$

In Eq. (2) θ_C is the surface coverage of carbon and x_b is the weight fraction of carbon in the segregation layer of Ni (g carbon/g Ni). The concentration of carbon dissolved in Ni at the support side of the particle equals the saturation concentration of filamentous carbon in Ni during steady-state carbon filament growth ($C_{Ni,r} = C_{sat}$) (7, 13).

The rate of carbon diffusion through nickel is described as:

$$r = \frac{D_C}{d_{Ni}} a_{Ni}(C_{Ni.f} - C_{sat}) \quad (3)$$

where D_C is the effective diffusivity for carbon diffusion through nickel, d_{Ni} is the effective diffusion path (7) and a_{Ni} is the specific surface area of Ni. More details about modeling of diffusion in a Ni particle have been presented previously (7).

4. Results and Discussion

For Ni (1 1 1) the typical bond strength of C-Ni, H-Ni and O-Ni are 716, 264 and 482 kJ/mol, respectively (5). These values obtained from single crystals were used in the modeling. However, such bond strengths is principally catalyst dependent, and might be a function of the support, promoter and crystal size. In the present work BOC is used to calculate activation energies of the elementary steps, instead of using experimental data from different sources. It should be expected that rather accurate data can be obtained, since BOC provides a very good framework to estimate heat of chemisorption of intermediates with an error range of 15-20% (5,6). The activation barrier for methane dissociation used in the present work is 57 kJ/mol, which is in good agreement with experimental observations. The experimental activation energy is 52.7, 55.7 and 26.8 kJ/mol for Ni (1 1 1), Ni(1 1 0) and Ni (1 0 0), respectively (14). In addition, one should keep in mind that BOC provides only zero coverage activation energies. All the coverages are relatively low at the dry reforming condition, and thus ignoring effects of the surface coverage

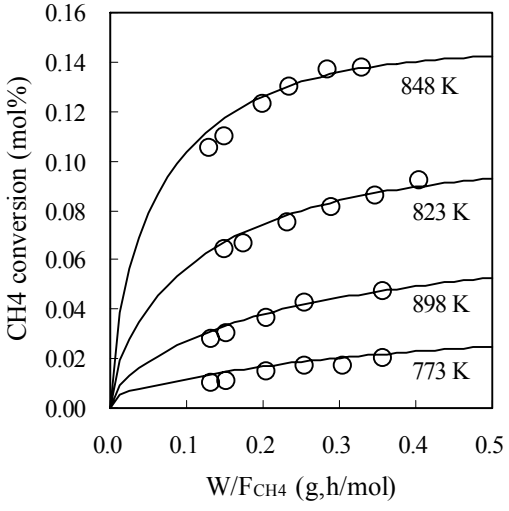

Fig. 2 Comparison of microkinetic model calculation with previously published data for methane steam reforming at 1 MPa. Markers are experimental data from ref. (15), lines are data from the microkinetic model.

on the activation energy is not expected to create a large error.

The activation energies were used as calculated, but some preexponential factors were fitted to steady-state experimental data.

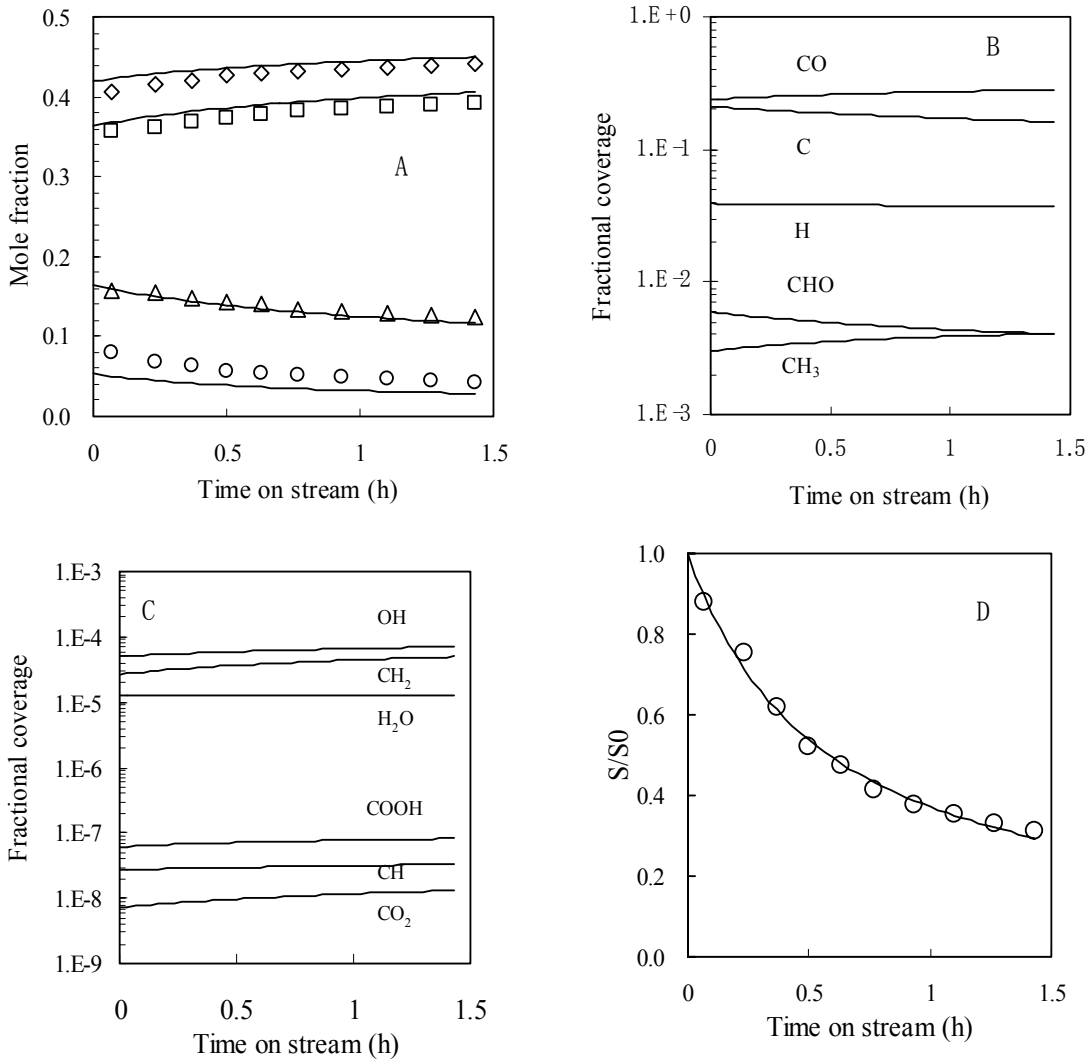

Fig. 3 (A) Calculated (line) and experimental (symbol) exit mole fractions of CH_4 (◊), H_2 (○), CO (Δ) and CO_2 (□) on dry basis; (B) (C) Estimated site coverage (D) estimated changes in relative surface area. Line simulated by Eq (4). Reaction conditions: T= 650 °C; W/F_{CH4} = 0.15 g·h/mol , $CH_4/CO_2/N_2$+Ar = 1/1/1.89, P_{tot} = 0.5 MPa.

The preexponential factors in forward and reverse steps of reactions r_1-r_2 and r_{11} were selected as adjustable based on sensitivity analysis. It was found that the estimated values deviated only slightly from the initial values estimated by transition-state theory. The kinetic data of methane steam reforming from Xu (15) and our data of methane dry reforming were used for the above adjustment. The reverse step of r_7 and forward step of r_8 were forced to meet thermodynamic consistence (6,7).

The microkinetic model in Table 1 describes very well the kinetic behavior of steam reforming of methane on Xu's catalyst (Ni/MgO-Al_2O_3) and Fig. 2 shows one example of steam

reforming at 1 MPa. It was found that all preexponential factors must be multiplied by a factor of 0.35 in order to describe methane reforming on Ni/CaO-Al_2O_4 at a pressure range of 0.1 to 2 MPa and a temperature range of 500 to 650 °C. It is possibly a result of heterogeneous surface of Ni. A study taking into account the heterogeneous surface is in progress. However, it is also worth mentioning that the mechanism for syngas production in this model is by no means unique (6,7).

Carbon formation (9) and sintering (16) are the most likely causes for deactivation of syngas catalysts. Deactivation can be described by changes in the surface coverage through Eq. (1) or by changes in the surface area. The change in site coverage can be a result of the formation of encapsulating carbon or other reasons, and the modeling has been discussed previously (7). The change in surface area can possibly be caused by sintering and encapsulating carbon formation. At each time on stream the surface area or dispersion was estimated as the only parameter in the microkinetic model. It was found that modeling based on surface area change gave a better fit of the experimental data at different conditions. One example of estimated changes in mole fraction and site coverage resulted from the decrease in relative surface area is shown in Fig. 3 during methane dry reforming at 0.5 MPa and 923 K. The estimated changes in relative surface area can be described by a general power law (1), as presented in Eq. (4). Microkinetic analysis was then based on Eq. (4).

$$-\frac{d(S/S_0)}{dt} = k_s\left(\frac{S}{S_0} - \frac{S_{eq}}{S_0}\right)^2 \tag{4}$$

In Eq (4) S/S_0 and S_{eq}/S_0 are the relative surface area and relative equilibrium surface area, respectively, k_S is the sintering rate constant. $S_{eq}/S_0 = 0.018$ and k_S=1.81 1/hr are estimated from the calculated changes in relative surface area by the microkinetic model (Fig. 3D). Although the data fitted well the typical sintering kinetic model of general power law, the possible effect of encapsulating carbon deposition on the decrease in the surface area can not simply be excluded.

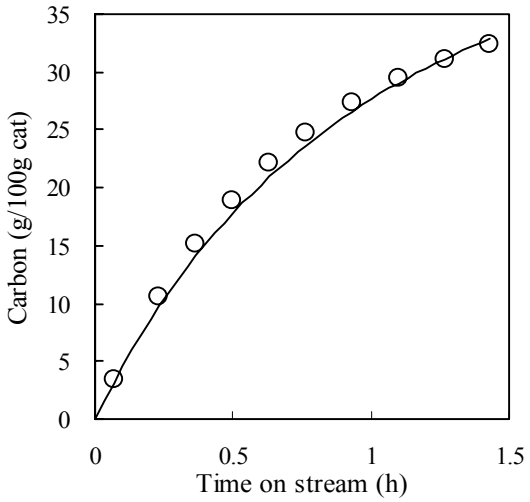

Fig.4 Experimental (○) and simulated filamentous carbon deposition at the same conditions as in Fig. 3.

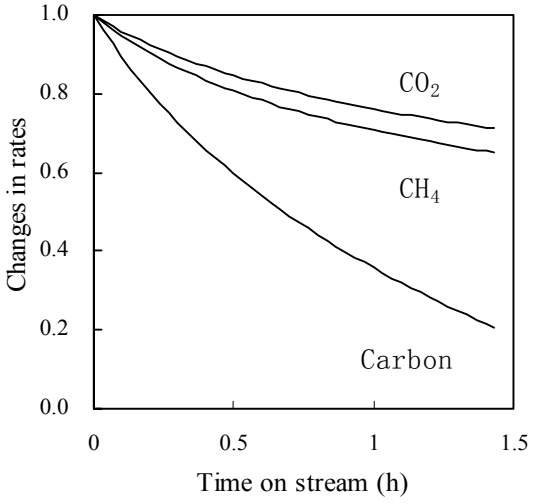

Fig. 5 Calculated changes in relative reaction rates of CH_4 and CO_2 as well as filamentous carbon deposition.

Sensitivity analysis indicated that no single RDS exists in methane dry reforming. Reactions r_1-r_3, and r_7-r_{10} were sensitive to methane conversion, while r_7 and r_8 were sensitive to CO_2 conversion. At $S/S_0 = 0.2$, the adsorption and desorption steps of CO and H_2 (r_{10} and r_{11})

were most sensitive to methane reforming and only the reverse reaction of r_9 and forward reaction of r_{10} were most sensitive to CO_2 conversion. This clearly demonstrates the limitation of conventional kinetic modeling. On the other hand, it reveals remarkably the advantage of microkinetic modeling for catalyst deactivation.

Since diffusion and dissolution of filamentous carbon in Ni particles are less well known, the diffusivity of carbon through Ni and the saturation concentration of filamentous carbon in Ni were estimated from experimental data. The estimated diffusivity is $1.3 \cdot 10^{-13}$ m^2/s, which is rather close to the experimental value of $8.6 \cdot 10^{-14}$ m^2/s at 923 K (17). The experimental (TEOM) and simulated carbon deposition are presented in Fig. 4.

The estimated C_{sat} is 64 mol/m^3 at 0.5 MPa. However, it was found that the solubility of carbon filaments depends on reaction conditions even at constant temperature. The solubility is about 120 mol/m^3 at 0.1 MPa during methane dry reforming and 263 mol/m^3 during methane decomposition at 0.13 MPa methane partial pressure. The possible reason is that the experimental conditions might affect the diameter of the growing filaments. Experimental results have shown that the property of filamentous carbon is a function of its diameter (9). Modeling indicates that carbon filaments with smaller diameters have higher solubility in Ni.

Fig. 5 shows that filamentous carbon deposition deactivates much faster than the main reactions. Ensemble size control by sulfur addition has been used as a tool to suppress carbon deposition in the industrial SPARG process (18). The basic principle is that the ensemble size for carbon formation is larger than the ensemble size needed for syngas formation. However, the present model also suggests an alternative explanation. The faster decrease in driving force for carbon diffusion, namely $C_{Ni,f}$-C_{sat} in Eq. (3) compared to the decrease in carbon site coverage, can result in a fast decrease in the carbon deposition. As shown in Fig. 4, the predicted decrease in the coking rate is about 3 times larger than to the decrease in the rates of the main reactions. This value is almost identical to the ratio of ensemble size of methane reforming to carbon formation reported by Rostrup-Nielsen (18).

Microkinetic analysis suggests two possible ways to lower the carbon threshold. The first is to lower the surface carbon site coverage, resulting also in lower activity to syngas formation. The second is to increase the filamentous carbon solubility in Ni and thus lower the driving force for carbon deposition. This means that smaller crystal sizes of Ni will suppress filamentous carbon deposition without lowering the activity for syngas formation.

Microkinetic analysis indicates that the bond strengths are strongly correlated to catalyst activity. In practice, it is possible to change the bond strength through promoters. However, catalyst promoters are often also poisons for the catalyst. Poisons and promoters affect catalysts not only through geometric modification but also through electronic modification. Both effects can be taken into account in the present model quantitatively. It has recently been reported (19) that potassium increased the energy barrier for dissociation of methane on Ni surface by 20 kJ/mol at θ_K=0.125ML. It has been shown that the same conclusion may be drawn from model calculations assuming that potassium electronically affects only the C-Ni bond strength. The model estimated about 20 kJ/mol lower C-Ni bond strength correspondingly, and predicted almost 10 times lower activity of methane conversion and no carbon formation at the conditions presented in Fig. 3. It indicates the way potassium affects the activity and carbon deposition.

5. Conclusions

A microkinetic model has been developed for methane reforming including carbon formation and deactivation. The activation energies of elementary steps are related to the bond strength by the BOC method. No assumption about rate determining steps is made. Both steam and dry reforming were well simulated by the model at a broad range of operating conditions on two Ni catalysts. The model could also serve as a tool providing input for the design of new catalysts. The C-Ni bond strength is a sensitive parameter for both reforming and carbon deposition.

Moreover, the method and principle used in the present work is not limited to methane reforming, but can possibly be applied to many other metal catalyzed reactions.

Acknowledgments

The support of this work by the Norwegian Research Council, STATOIL and Norsk Hydro ASA is gratefully acknowledged.

References

(1) C. H. Bartholomew. Stud. Surf. Sci. Catal. 88 (1994) 1.
(2) G. F. Froment and K. B. Bischoff. Chemical reactor analysis and design. Wiley, New York, 1990.
(3) J. A. Dumesic, D. F. Rudd, L. M. Aparicio, J. E. Rekoske and A. A. Treviño. The microkinetics of heterogeneous catalysis. ACS, Washington, 1993.
(4) L. J. Broadbelt and R. Q. Snurr. Appl. Catal. 200 (2000) 23.
(5) E. Shustorovich, Adv. Catal. 37 (1990) 101.
(6) L. M. Aparicio, J. Catal. 165 (1997) 262.
(7) D. Chen, R.Lødeng, A. Anundskås, O. Olsvik and A. Holmen. Chem. Eng. Sci. 56 (2001) 1376.
(8) D. Chen, A. Grønvold, H. P. Rebo, K. Moljord, A. Holmen. Appl. Catal. 137 (1996) L1.
(9) J .R.Rostrup-Nielsen, Steam reforming catalysts. Danish Technical Press, Copenhagen, 1975.
(10) M. C. J. Bradford and M. A. Vannice. Catal. Rev.-Sci. Eng. 41 (1999) 1.
(11) J. H. Onuferko, D. P. Woodruff, B. W. Holland. Stud. Surf. Sci. Catal. 87 (1979) 357.
(12) I. Alstrup. J. Catal. 109 (1998) 241-251.
(13) J. W. Snoeck, G. F. Froment and M. J. Fowles. J. Catal. 169 (1997) 240.
(14) T. V. Choudhary and D. W. Goodman. Catal. Today. 163 (2000) 9.
(15) J. Xu, Ph. D Thesis, University of Gent. Belgium. 1989.
(16) J. Sehested, A. Carlsson, T. V. W. Janssens, P. L. Hansen, and A. K. Datye. J. Catal. 197 (2001) 200.
(17) M. Hoogenraad. Ph.D. Thesis, University Utrecht, The Netherlands. 1995.
(18) J. R. Rostrup-Nielsen. Stud. Surf. Sci. Catal. 68 (1991) 85.
(19) H. S. Bengaard, I. Alstrup, I. Chorkendorff, S. Ullmann, J. R. Rostrup-Nielsen. J. K. Nørskov. J. Catal. 187 (1999) 238.